Transition metal dichalcogenide single photon emitters and nano-photonic structures

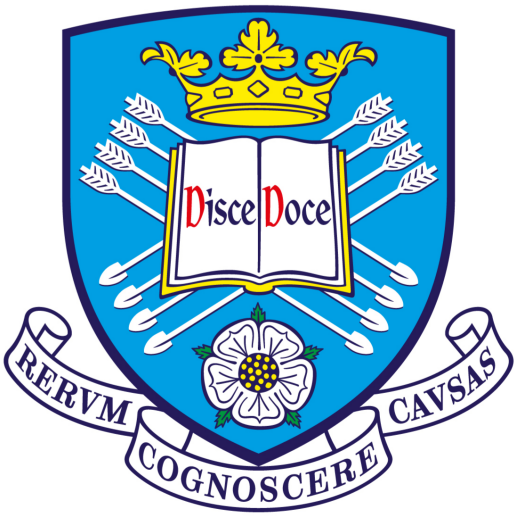

Panaiot Zotev

Department of Physics and Astronomy
University of Sheffield

This thesis is submitted for the degree of
Doctor of Philosophy

June 2021

Declaration

I hereby declare that except where specific reference is made to the work of others, the contents of this dissertation are original and have not been submitted in whole or in part for consideration for any other degree or qualification in this, or any other university. This dissertation is my own work and contains nothing which is the outcome of work done in collaboration with others, except as specified in the text and Acknowledgements.

Panaiot Zotev
June 2021

Acknowledgements

I would like to acknowledge those who helped me in this work and those who supported me through the tough times over the past four years as well as the many people I met during my PhD in the UK and throughout Europe. First, I would like to thank Prof. Sasha Tartakovskii who gave me the opportunity to be a part of his group, to study the topics which I found interesting and grow during my PhD. Next, I would like to thank the Marie Skłodowska-Curie Actions for funding my project and allowing me to be a part of a great network where I met some wonderful people. I would then like to thank those members of my group who helped and guided me including Eugene, Armando and in particular Luca who helped me in terms of experiments for this thesis as well as guidance and pushing me to do better than I though I could. Next I would like to thank Toby who also took part in many experiments presented in this thesis. I cannot forget to acknowledge and thank Catherine and Alistair for their help with the interferometry measurements as well as Andrew for his help with anti-bunching experiments. I would also like to thank the support of others from the LDSD group who made the work environment not only friendly but fun and entertaining including Tom, Pambos, Alessandro, Mostafa, Joe, Dan, Dom, Ruggiero, Gau, Kyriakos, Rahul and many more. For the work presented in this thesis, I would like to acknowledge Riccardo Sapienza's group and in particular Javier who fabricated gallium phosphide dimer nano-antennas. I would also like to thank the group of Thomas Krauss for their support in writing up much of this work with a particular mention for Christina and her fabrication of WS_2 nano-antennas as wells Donato for his simulations of optical trapping forces. I must also acknowledge Single Quantum for hosting my secondments which were very enjoyable even if they were cut short by the pandemic. Last but definitely not least, I would like to thank my wonderful family and my wonderful Gabi for their tremendous support through difficult times and their ability to always put a smile on my face. Without them, there is no way I could have accomplished so much.

Abstract

The integration of single photon sources with resonators for Purcell enhancement of spontaneous emission has drawn tremendous research efforts from many researchers around the world over the past 20 years. The desire to increase the radiative emission rate of quantum light sources arises due to new and exciting applications in quantum information processing which require emitters with ideal properties. Most light sources characterized as exhibiting single photons, however, do not meet many of the requirements of these new applications and so the enhancement of their emission rate via the Purcell effect is one method of suppressing unwanted properties and improving desired functions. Previous works involving micrometer-scale cavities fabricated from one material system have been integrated with quantum emitters from another, which has presented many new challenges. The use of transition metal dichalcogenides (TMDs) may provide a solution as these materials not only host single photon emission, but also exhibit a large refractive index and transparency window in the visible making them ideal for the fabrication of resonant structures. As 2D material, TMDs are also intrinsically compatible with a wide variety of substrates due to their weak van-der-Waals attractive forces.

In this work, we demonstrate an approach to precisely position strain-induced single photon sources in WSe_2 monolayers ($g^{(2)}(0) = 0.26 \pm 0.03$) and simultaneously couple their emission to broad Mie resonances of high refractive index gallium phosphide (GaP) dimer nano-antennas. This leads to large quantum efficiency enhancements yielding values of 21% on average when compared to 4% for emitters formed on SiO_2 nano-pillars. A maximum value of 86% corresponds to a 69 MHz single photon emission rate. The GaP substrate also enables more stable emission over time as well as reduced non-radiative recombination channels leading to lifetime values of up to 200 ns, which suggests much longer radiative decay times than previously reported. The enhanced quantum efficiency allows the study of the emission rise time which enables the first report of a dark exciton dwelling time before trapping into a 0D state in WSe_2 to be $\tau_t \approx 1.7$ ns. Increased excitation powers are shown to lead to efficient exciton-exciton annihilation rates which may lead to photoluminescence saturation that does not occur as a result of the filling of the quantum state but instead represents a depletion of the dark exciton population. We also perform the first systematic

study of the coherence time of WSe_2 single photon emitters (SPEs) yielding values of 3.12 ± 0.4 ps which we assert to be limited by pure dephasing via phonon interactions.

In order to complete the system of TMD single photon emitters coupled to nano-photonic resonators in the same material family, our work leads to the fabrication of monomer and dimer nano-antenna Mie resonators in bulk crystals of WS_2. The unique crystal symmetry of TMDs allows the fabrication of circular, hexagonal and square nano-antenna geometries with potentially atomically sharp vertices for the latter two. The high refractive index and large transparency window of the material enable the formation of highly confined anapole resonances which we show to enhance second harmonic generation (SHG) in nano-meter scale monomer and dimer nano-antennas with the latter yielding linearly polarized signal. The weak van-der-Waals forces responsible for the compatibility with a wide variety of substrates also enable the use of atomic force microscopy (AFM) for the repositioning of constituent nano-pillars in dimer nano-antennas. This enables a reduction of the dimer gap to values as low as 10 ± 5 nm which has so far only been achieved in plasmonic bowtie antennas or in dielectric structures using non-repeatable and damadging methods such as focused ion beam milling.

We study the applications enabled by these TMD nano-resonators numerically. A near unity degree of linear polarization of the SHG enhancement factor is expected for WS_2 dimer nano-antennas with small gaps. For the minimum achieved dimer gap of 10 nm, we simulate electric field hotspots with intensities of more than 10^3 when compared with vacuum for the novel hexagonal and square dimer geometries. This large enhancement leads to single photon emission Purcell enhancements of more than 150 for emitters positioned at the inner top vertices of the hexagonal and square dimer nano-antennas. The AFM repositioning technique and to a lesser degree the fabrication procedure enables the modulation of the electric field intensity and the Purcell enhancement through increases in the dimer gap as well as the rotation of individual nano-pillars in the dimer. Another application expected to benefit from such large electric field intensities is the optical trapping of nano-particles which we show to yield attractive forces of more than 350 fN for colloidal quantum dots and more than 70 fN for polystyrene beads, the latter of which closely resembles the refractive index and size of a large protein. The stable trapping which we simulate surpasses previous reports by a factor of more than 80 for quantum dots and more than 40 for polystyrene beads.

Publications and conference presentations

Publications

- L. Sortino, **P. G. Zotev**, S. Mignuzzi, J. Cambiasso, D. Schmidt, A. Genco, M. Aßmann, M. Bayer, S. A. Maier, R. Sapienza, A. I. Tartakovskii

  "Enhanced light-matter interaction in an atomically thin semiconductor coupled with dielectric nano-antennas"

  Nature Communications **10**:5119, (2019)

- L. Sortino, Matthew Brooks, **P. G. Zotev**, A. Genco, J. Cambiasso, S. Mignuzzi, S. A. Maier, G. Burkard, A. I. Tartakovskii

  "Dielectric Nanoantennas for Strain Engineering in Atomically Thin Two-Dimensional Semiconductors"

  ACS Photonics **7**(9):2413-2422, (2020)

- L. Sortino, **P. G. Zotev**, C. Phillips, A. Brash, J. Cambiasso, E. Marensi, A. M. Fox, S. A. Maier, R. Sapienza, A. I. Tartakovskii

  "Bright single photon emitters with enhanced quantum efficiency in a two-dimensional semiconductor coupled with dielectric nano-antennas"

  Nature Communications **12**:6063, (2021)

- **P. G. Zotev**, Y. Wang, L. Sortino, T. Sevars Millar, N. Mullin, D. Conteduca, M. Shagar, A. Genco, J. K. Hobbs, T. F. Krauss, A. I. Tartakovskii

  "Transition metal dichalcogenide dimer nano-antennas with ultra-small gaps"

  (Submitted)

Conference presentations

- Quantum dot day (poster) Sheffield, UK, January 2018

  "Localized exciton emission from WSe_2 strain induced defects on GaP nanoantennas"

- TMD-UK (poster) Sheffield, UK, July 2018

  "Exciton funneling and narrow linewidth emission in monolayer transition metal dichalcogenides"

- TMD-UK (poster) Sheffield, UK, July 2019

  "Photoluminescence dynamics of single photon emitters in WSe_2"

- LaserLab Symposium (poster) Sheffield, UK, June 2019

  "Single photon sources in transition metal dichalcogenides"

- Quantum dot day (poster) Sheffield, UK, January 2020

  "Strain-induced single photon emitters in WSe_2 on gallium phosphide nano-antennas"

- Nanophotonics Winter school (poster) Sheffield, UK, January 2020

  "Strain-induced single photon emitters in monolayer TMDs"

- QD2020 (presentation) Munich, DE, January 2020

  "Single photon emitters with enhanced quantum efficiency in WSe_2 coupled to dielectric nano-antennas"

Table of contents

List of figures

Chapter 1

Introduction

In this chapter, I will give a brief introduction into 2D materials, single photon emitters as well as photonic resonators all of which will hold a central place throughout this thesis. I will also discuss the motivation behind enhancement of single photon emission through coupling to nano-antenna resonances which is a central theme in this thesis and the aim of most of my work. I will end the chapter with a brief description of the subsequent chapters outlining the entire thesis.

1.1 Two dimensional materials

The field of two dimensional materials began in 2004 when the isolation of single layers of graphite, called graphene [1], was reported even though it had previously been judged to be impossible by Landau et al. [2]. The surprising result that a semiconducting material can be separated into atomically thin sheets with metallic properties changed the way we see a large group of materials which similar to graphene are often referred to as van-der-Waals crystals. Each layer consists of covalently bonded atoms, however, inter-layer adhesion is attained by much weaker van-der-Waals forces which permits the separation of single or multiple layers from a bulk crystal using surprisingly trivial mechanical means. The "scotch tape" method pioneered by Novoselov et al., which consists of peeling off single layers from a crystal using simple tape led to a broad range of discoveries and the expansion of the field of two-dimensional (2D) physics, ultimately leading to the Nobel Prize in 2010. As the study of 2D crystals became more accessible, materials with not only metallic but also those exhibiting properties ranging from semiconducting to insulating were discovered, as shown in Fig.1.1. These properties are all due to the general nature of quantum confinement which changes the properties of van-der-Waals crystals as they are thinned down to monolayers. Some of the

most often studied layered materials include hexagonal boron nitride and transition metal dichalcogenides in addition to graphene.

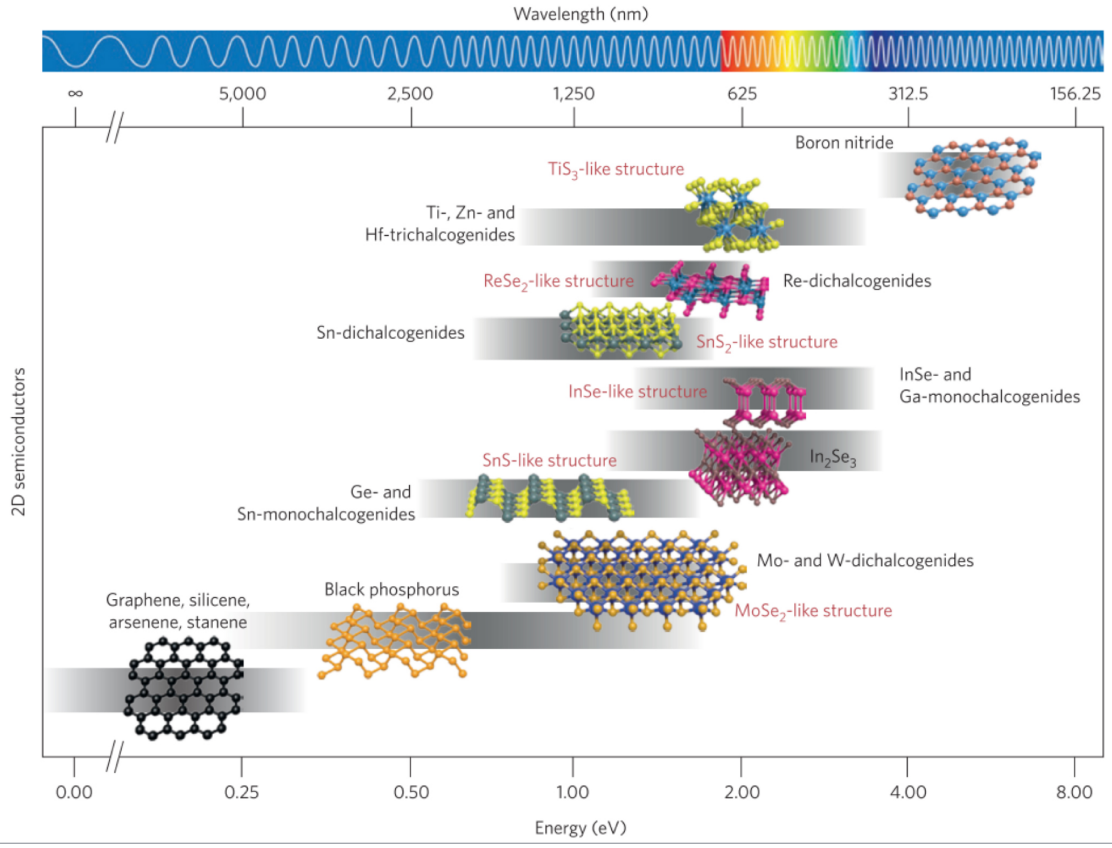

Fig. 1.1 Comparison of bandgap values and crystal structure for different families of 2D materials. Gray bars represent the range that can be spanned by changing either the number of layers, straining or alloying. The wide range of bandgaps accessible in 2D materials highlights the potential for their use in a broad variety of applications. Adapted from [3].

Beginning with graphite, a single layer of this crystal exhibits radically different properties than its bulk form mainly due to the closing of the band gap leading to a very high electron mobility (>11000 $\frac{cm^2}{V \cdot s}$ [4]) and therefore a conductive nature. A somewhat recent discovery has shown that graphene can exhibit negative local resistance due to viscous electron flow ($\nu \approx 0.1 \frac{m^2}{s}$), forming vortices [5]. The tensile strength of the single layer is also a record breaker (130 Gigapascals [6]) making it the strongest material ever discovered. In addition, the 3.45Å[6] thickness of a monolayer is very attractive for small-scale contact applications.

Semiconducting 2D materials emerged from subsequent research into suspected layered materials. The family of transitional metal dichalcogenides (TMD) are the most often studied and most exciting of the semiconducting two dimensional materials. The excitement surrounding these stems from the fact that similar to graphene their electronic band structure radically changes when thinning down the crystal from bulk to monolayer form. Bulk TMD

crystals, studied in the 1970s [7], exhibit an indirect band gap with a valence band edge at the Γ point of the Brillouin zone and a conduction band edge nearly halfway between the Γ and K symmetry points making light emission an inefficient process [8, 9]. Since the isolation of single layers of these materials, researchers have discovered that the band gap now appears at the K symmetry point, therefore, light emission becomes much more efficient [8]. Their band gaps also shift to visible energies qualifying them for use in light emission applications. TMDs have also been studied for the formation of quantum emitters [10–13] which are yet to be fully understood.

Insulating 2D materials research has been led by studies of hexagonal boron nitride (hBN) which exhibits a bandgap ≈ 6 eV [14]. Some of the first applications of mono- or multi-layers of this material was to protect other semiconducting or metallic monolayers from the environment and improve their optical qualities [15, 16]. Since the hBN monolayers are dielectric, mostly transparent in the visible, and mechanically strong, they are often sought after in order to cover TMD monolayers and improve their optical properties by shielding from environmental effects such as adsorbates or stray electric fields from a charged substrate. Other uses of thin hBN mono- and multilayers have been found in gating applications such as FET transistors using metallic graphene, semiconducting TMDs, and insulating hBN spacers [17]. Another exciting discovery associated with hexagonal boron nitride has taken the form of single photon emitters (SPEs) attributed to anti-site complexes with a nitrogen vacancy ($N_B V_N$) [18] as well as shelved states [19]. The large amount of interest in these SPEs has been in part due to the discovery of room temperature quantum emission [18, 20].

1.2 Single photon emitters

Single photon emitters (SPEs) are sources of single quanta of light often emitted from a two level system. In layman's terms this translates to a source of light which emits exactly one photon upon request as opposed to classical light emission which yields a large density of photons per excitation. Research into such systems started nearly 50 years ago with the discovery of single photon emission from trapped atoms in opto-magnetic fields [21]. More recent work on quantum dots in III-V semiconductors [22] has expanded the field due to the relative ease of fabricating artificial atoms as opposed to isolating real ones. Further studies into defect states such as color centers in diamond [23] have increased the number of easily accessible single photon emitting systems with the addition of two dimensional material SPEs in transition metal dichalcogenides [11] and hexagonal boron nitride [18].

Research into single photon sources may have originally been fueled by a simple interest into the physics of these systems, however, this changed after the seminal paper by David DiVincenzo [24] despite an earlier proposal by Richard Feynman [25]. The popularization of the idea to build a quantum computer in 2000 has since lead many funding bodies to aggressively pursue this goal and greatly increased research efforts in the field of single photon emitting devices which play a central role.

A quantum computer, as defined by DiVincenzo's criteria, consists of a network of quantum bits or qubits which function as the quantum version of logic gates in a computer and have the advantage of storing larger quantities of information than classically possible. A network of n such qubits can store 2^n states while a network of classical bits can only store binary information. Therefore, the advent of a quantum computer would not only allow faster computing, but would also allow the solution of problems which would be impractical for a classical computer due to the necessary computation time. Examples of this so called quantum supremacy are realizations of Grover's search algorithm [26] and Shor factorization [27] which is exponentially slower for a classical computer to implement thereby prohibiting its use due to the impossibly long computation time.

Another exciting application which is mentioned in the last two DiVincenzo criteria and pushes the field of single photon sources further is quantum communication. An example of this is quantum key distribution which has already been realized, if not with the use of single photon sources. This method of communication implements a cryptographic technique which is impermeable to attack by unwanted outside observers. The method of utilizing encryption keys which are randomly formed by a quantum entangled system such as that by an entangled pair of photons allows two end users of the network to immediately learn of a third party listening in due to the change that this outside attack would have on the quantum system.

In order to realize a quantum emitter which can satisfy many or all of the conditions set by the above applications it must exhibit certain properties. These include spectral stability, short emission lifetimes, indistinguishability, maximal brightness, high single photon purity and scalability. In order for a single photon source to function in the above mentioned applications as well as others, the emission wavelength of single photon source must not change within a time required for its use. Short emission times are important for applications which would require a large rate of excitation and emission such as the previously mentioned quantum computers. Indistinguishability is often necessary for any application, such as quantum key distribution, which would require entanglement between emitted photons. Without identical photons, this quantum effect would not be possible. Brightness is related to the amount of light emitted from a source within a given timescale. Ideal SPEs emit a single photon after

each excitation, however, this is not guaranteed for the systems under current study and therefore there is still much to do in order to maximize the number of emitted photons. High photon purity is a must for all applications as this defines how close this light source is to emitting no more than one photon each time. Lastly mentioned is the ability to scale up the fabrication of single photon sources which would be a necessity for most applications and in particular quantum computation in which a dense array of qubits or SPEs used to manipulate qubits would be required.

Examples of single photon emitting systems under active research include but are not limited to III-V quantum dots, color centers in diamond, and quantum emitters in 2D materials. The first mentioned source, namely quantum dots or zero dimensional structures grown in III-V compound semiconductors, has so far proven the most promising candidate for many applications. These consist of artificial atoms of a low band gap material grown within a high band gap material, therefore confining electron hole pairs to a small volume hosting a two-level state. These sources have a large quantum yield yet their emission is often not collected due to the high refractive index material surrounding the zero dimensional emitter. Color centers in diamond are also fairly promising candidates due to their ability to emit single photons at room temperature which has proved difficult in many other systems. These consist of defect centers in diamond [28]. Their relatively inexpensive fabrication is balanced by the difficulty of deterministically inducing emitters at desired wavelengths or spatial positions. Lastly, SPEs forming in 2D materials come in two varieties. Defect centers in hexagonal boron nitride often suffer from similar disadvantages to color centers in diamond, however, they have also been shown to emit single photons at room temperature. The other option for 2D single photon sources is emitters in transition metal dichalcogenides which emit only at liquid helium temperatures yet allow precise spatial positioning and exhibit a reduced range of emission wavelengths. Schematics of the geometry of the above mentioned single photon emitting systems can be seen in Fig. 1.2.

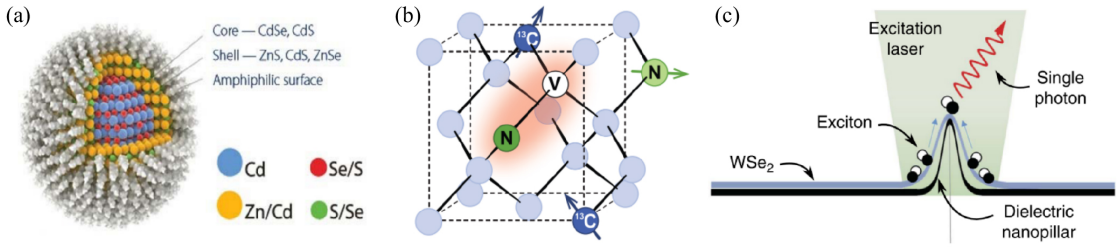

Fig. 1.2 Schematic illustration of **(a)** quantum dots adapted from [29], **(b)** color centers in diamond adapted from [30] and **(c)** quantum emitters in TMDs adapted from [31].

1.3 Nano-photonic cavities and antennas

Electromagnetic resonators have been of great interest in physics for more than 100 years with early uses of LC circuits in radio transmission and filtering as well as microwave cavities which are now used in microwave ovens, radar equipment and satellite communication. These cavities require rather long wavelengths of electromagnetic radiation. Optical cavities or cavities which confine visible light have also been sought after since the first laser systems [32] in which a Fabry-Perot cavity provides the necessary feedback to induce a population inversion in a laser gain material. The size of these is smaller than the previously mentioned resonators, however, is still within centimeter to meter size.

Moving down in scale, we reach micro-cavities or cavities formed by distributed Bragg reflectors which are often micrometers in size with uses in laser systems [33], polariton research [34] and formation of Bose-Einstein condensates [35].

Even smaller resonators have now been achieved at the nano-scale. The largest example of these is a photonic crystal cavity in which light is confined to a nano-meter sized defect in an array of holes etched into a high refractive index material and suspended in air [36]. Other similar systems named nano-beams [37] use a photonic crystal cavity in only one dimension while relying on total internal reflection for confinement in the other two. Whispering gallery mode resonators [38] are another example of light confined to nanoscale regions of a micrometer sized structure. All of these optical resonators are often used in lasing applications as well as single photon emission enhancement. Examples of photonic crystal cavities, nanobeams and whispering gallery mode resonators are shown in Fig. 1.3.

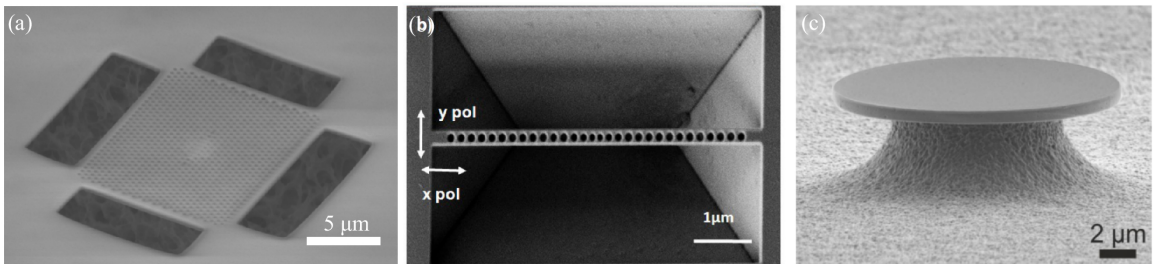

Fig. 1.3 SEM images of **(a)** photonic crystal cavity, **(b)** nanobeam cavity adapted from [39] and **(c)** whispering gallery mode resonator adapted from [38].

The resonators which this thesis will heavily focus on consist of nano-meter scale antennas which can be described as Mie resonators. Gustav Mie provided an analytical solution to the problem of scattering plane waves from small (comparable to the wavelength) particles of any dielectric function [40]. Metallic Mie resonators have been realized using colloidal gold nano-particles which are often placed over a metallic surface in order to form plasmonic

resonances with a strong electric field confinement within a nano-scale volume between particle and surface [41]. A more generalized version of Mie's solutions to Maxwell's equations now provides the opportunity to model dielectric nano-particles using the same equations.

The most recent developments have slowly moved away from the spherical nano-particle geometry in favor of cylindrical shaped antennas patterned into a substrate [42]. Some of these structures have also relied on plasmonic resonances, however, a new development in the field of nano-photonics has seen the realization of high-index dielectric nano-antennas such as those defined in gallium phosphide (GaP) [43] or silicon (Si) [44]. These have been shown to confine light to similar dimensions as plasmonic structures with the additional advantage of virtually lossless resonances below the band gap of the material as well as magnetic resonances which cannot be induced in a metallic structure [45].

As researchers are still discovering the uses for high-index dielectric nano-antennas a new material platform has joined this field in the form of 2D materials. Transition metal dichalcogenide nano-antennas have recently been reported with Mie-like dipolar magnetic and electric modes [46]. The use of these antennas and their resonances has already proven versatile. Strong coupling between TMD excitonic resonances and anapole modes within the antenna has been shown [46]. Similarly, the use of the anapole has been applied to enhancement of second and third harmonic generation [47]. This thesis will focus heavily on more complicated resonances using these TMD nano-antennas which have exciting applications in single photon emission rate enhancement as well as optical trapping.

1.4 Summary of Thesis

As briefly mentioned in the previous sections of this chapter, this thesis will focus on single photon emitters in transition metal dichalcogenides as well as resonant nano-antennas fabricated from the same material family. At first glance, these two fields seem to be independent, yet the integration of single photon sources with resonant structures is the aim of the research that has been carried out and is also sought after by many researchers around the world. The use of single photon emission in many applications requires large emission rates with low spectral diffusion, and long coherence times and the generally used approach to guarantee these characteristics is to utilize the Purcell effect.

First discovered by Edward Purcell in 1946 [48], the so-called Purcell effect is a change in the radiative spontaneous emission rate of a source of electromagnetic radiation due to the photonic environment surrounding it. Until this time, researchers believed the spontaneous

emission rate of any source to be an intrinsic property of the system. What Purcell discovered, was that the local density of optical states surrounding the source played a vital part in determining the emission rate. In later years, it has been discovered that with careful designs of the refractive index of the materials surrounding the source, one could either enhance the emission rate or reduce it.

The next chapter of this thesis will introduce and give an overview of transition metal dichalcogenides as well as a more detailed look into some particularly pertinent properties of these materials to the work discussed in later chapters. The discussion will begin with the crystal symmetry of the material family and continue with implications of this to the stability of the lattice and its resistance to chemically etching reactions. Next, implications of the crystal symmetry and the breaking of symmetries at the monolayer limit will be discussed in terms of the band structure of the material. Moving from this topic, the discussion will shift to the presence of strongly bound excitons and their spin-orbit and valley properties as well as the presence of optically dark excitons in the tungsten based materials.

Chapter 3 will begin with a general discussion of single photon emitters and their theoretical formulation. The discussion will then shift to optical properties of realistic single photon systems such as spatial localization, power saturation, linear polarization, fine structure splitting, long lifetimes, brightness as well as single photon purity and coherence. Examples of TMD based SPEs will be discussed with an emphasis on WSe_2 emitters. At this point, several theories put forth to describe the formation of 2D material quantum emitters will be discussed in order to give an overview of the possible mechanisms which give rise to single photon emission in transition metal dichalcogenides and give context for many of their optical properties. The discussion of strain, which has been found to be a necessary component in the formation of SPEs in tungsten based TMDs will be emphasized.

General Mie theory will be discussed in the first section of chapter 4. The focus will then shift to Mie solutions for high refractive index nano-particles in a homogenous environment and encompass the multi-polar expansion of the scattered plane wave which gives rise to near field charge currents. Examples of studied systems will be provided by GaP monomer and dimer nano-antennas. The discussion will focus on their scattering cross sections and electric field enhancement. The Purcell effect will also be introduced theoretically in both photonic cavity and Green's functions formalism, the latter of which will be used to study enhanced single photon emission. The last section of this chapter will also discuss the formation of a non-radiative anapole mode in cylindrical nano-antenna with examples from gallium phosphide, silicon and WS_2. This section will also briefly introduce non-linear processes such as second and third harmonic generation and explain the utility of anapole resonances to enhance these phenomena.

The experimental methods used throughout this work will be discussed in chapter 5 focusing on 2D material fabrication, nano-antenna fabrication, optical spectroscopy, time-resolved photoluminescence, anti-bunching and interferometry. Dark field spectroscopy and second harmonic generation will also be discussed. Finally, FDTD simulation methods of the scattering cross section, the spatial distribution of the electric and magnetic field intensity, the confinement of electric energy, Purcell factor calculation and collection efficiency enhancement by nano-antennas will be described.

Experimental work will be reported in the following chapters starting with the use of gallium phosphide nano-antennas to enhance the quantum efficiency of single photon emitters in WSe_2 in chapter 6. The discussion will begin with a description of the sample geometry and the photonic resonances of the two nano-structures used to form SPEs in monolayer WSe_2, namely GaP dimer nano-antennas and SiO_2 nano-pillars. Next, the optical properties of the SPEs forming on these nanostructures will be presented such as spatial localization, linear polarization, power saturation and single photon purity. The next section will focus on comparing the photoluminescence enhancement and the lifetimes of emitters forming on the two material systems and show the presence of quantum efficiency enhancement. The discussion will then shift to the insight gained into the zero dimensional state filling time due to the increase quantum efficiency. The final sections of this chapter will show the first systematic study of the coherence time of SPEs formed on gallium phosphide dimer nano-antennas. The discussion will focus on two attempts to discern the dominant decoherence mechanism of the emission.

Chapter 7 will focus on the fabrication and optical characterization of WS_2 monomer and dimer nano-antennas as well as their repositioning using atomic force microscopy. The fabrication and geometry of three different nano-antenna shapes will be discussed first. The focus of the next section will be on dark field spectroscopy characterization of monomer nano-antennas with a study on radial and height dependence with a correlation to simulations. The multi-polar contributions will be discussed in order to identify the resonant modes. The discussion will then shift to the dark field spectroscopy characterization of dimer nano-antennas including the identification of a dimer anapole resonance. Second harmonic generation enhancement in the monomer and dimer WS_2 nano-antennas will be explored as well as the linear polarization dependence of the second harmonic signal due to the enhancement of the hybridized anapole mode. Finally, the use of AFM for the reduction of the separation in a dimer nano-antenna as well as the rotation of constituent nano-pillars will be discussed along with dark field spectroscopy characterization.

The final experimental chapter focuses on the simulation of WS_2 dimer nano-antennas with ultra-small gaps achieved using the AFM repositioning discussed in the previous

chapter. The simulations start with calculating the degree of linear polarization of the SHG enhancement from the dimer anapole mode. Second, the electric field intensity enhancement induced by the dimer nano-antennas is discussed for the three different geometries available for fabrication and the optimization procedure is described. After this, the measurement and simulation of the radius of curvature in dimer nano-antennas is presented. Next, the Purcell factor for an SPE-like dipole placed onto the nano-antennas at different positions is compared for the three different geometries. Modulation of these properties was explored through two separate methods, namely spatial separation of the individual nano-pillars in the dimer and relative rotation of two designs. The sections on optical trapping study the force applied to two different nano-particles within the dimer gap or positioned onto the nano-antennas. Comparisons for different dimer gaps were also performed.

A final chapter of the thesis will summarize the experimental work carried out and provide an outlook for future research directions which may lead to very appealing applications in quantum communication and information processing.

Chapter 2

Transition metal dichalcogenides

In this chapter I will discuss a special family of two dimensional materials which are semiconducting in nature, namely transition metal dichalcogenides. I will firstly discuss the crystal structure focusing on the symmetry properties which form the Brillouin zone as well as briefly mention the stability of the crystal axes. Next, I will move onto the electronic properties of TMDs in bulk and subsequently monolayer form. I will discuss the mechanism which leads indirect band gap bulk TMDs to transition into direct gap monolayer semiconductors. I will then explore the spin-orbit splitting which is responsible for many of the interesting properties of these materials including spin-valley locking and valley coherence. Lastly, I will provide a description of the excitonic properties of monolayer TMDs which define the absorption and emission spectra and yield unique properties not found in any other semiconducting materials. Lastly I will finish the chapter with a brief discussion of dark excitons in W-based TMDs which may prove to be very important for the formation of single photon emitters in these materials.

Firstly, in order to begin the study of 2D material semiconductors, a small discussion of the methods by which these materials are grown or exfoliated for their study is warranted. Most of the Group IV transition metal dichalcogenides are grown into bulk crystals through chemical vapor deposition and subsequently provided for research purposes or applications. While there is a growing community which focuses on large-area monolayer growth through chemical vapor deposition (CVD) [49] and most recently CVD van der Waals epitaxy [50], most single or few-layer crystals are mechanically exfoliated following the "scotch tape" method pioneered for graphene [1]. Another rarely used method of separating single layers is chemical exfoliation [51] which, unfortunately, often affects the optical properties of the material through formation of defects. In fact, the optical properties of mechanically exfoliated mono- and few-layers are still considered optimal.

2.1 Crystal Structure

Group IV transition metal dichalcogenides (TMDs), similar to graphene and boron nitride, consist of in-plane covalently bonded atomically thin crystal layers which are held together by out-of-plane weaker van-der-Waals forces. Each layer is of the form MX_2 where M represents a transition metal (W, Mo) and X represents a group IV chalcogen (S, Se, Te). These form a three-atom thick (0.5 - 0.7) [52] crystal of the form X-M-X with a plane of transition metal atoms located between two planes of chalcogen atoms as shown in Fig. 2.1(a). The symmetry of the resulting crystal as well as the Brillouin zone is hexagonal as shown in Fig. 2.1(b). An important property of these materials is the breaking of inversion symmetry at the single layer (monolayer) limit which has consequences for many electronic and optical properties which are discussed further in the chapter. To form a bulk crystal, single layers are stacked atop each other in two stacking orders, namely 2H and 3R [7]. The 2H stacking order, which is most prevalent due to its lower energy, consists of layers stacked atop each other with a 180° relative rotation, therefore restoring the inversion symmetry for even layer numbers. The 3R stacking order on the other hand has no such rotation of subsequently stacked layers but consists of a lateral translation of each layer with respect to the last, leading to no reintroduction of inversion symmetry and therefore subtly different electronic and optical properties with relation to the 2H stacking order.

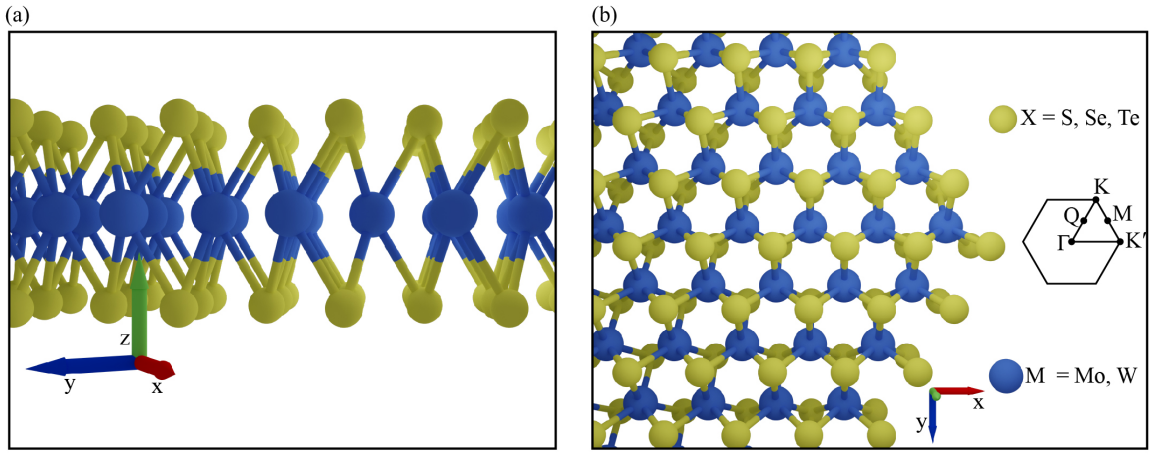

Fig. 2.1 **(a)** Side view of monolayer TMD crystal structure. **(b)** Top view of monolayer TMD crystal structure with zigzag terminated edges. Adapted from reference [53]. Inset illustrates the Brillouin zone with labels at important symmetry points.

Despite the stability of single layers of TMDs in air over a period of months and their lack of dangling bonds, the stability of the crystals is not uniform. It has been predicted that nano-ribbons of TMDs along the zig-zag axis would exhibit metallic properties while a nano-ribbon along the armchair direction would maintain semiconducting properties thereby

implying that one axis is more stable than the other [54, 55]. A simple observation which reasserts this fact can be seen in Fig. 2.1(b) where each chalcogen atom along the armchair axis is bonded to one transition metal atom as opposed to the two bonds along the zig-zag axis. This has surprising results for any application which aims to etch structures out of TMD crystals during which chalcogen atoms in that crystal are selectively removed based on the strength of their bond to the transition metals. Other applications which might benefit from the difference in stability between the crystal axes include those which require fabrication of van-der-Waals hetero-structures. This relies on the alignment and relative twist of individual layers where knowledge of the orientation of the crystal axes is paramount.

2.2 Electronic properties

Bulk transition metal dichalcogenides have been known to exhibit an indirect band gap since early studies in the 1970s [7] with a valence band edge at the Γ high symmetry point and a conduction band edge at the Q point as shown in Fig. 2.2(a) [8, 56]. The band gaps vary over a range of 1.09 - 1.32 eV [8, 57] for the different TMDs. Only a few further studies of these materials were carried out due to a lack of interest.

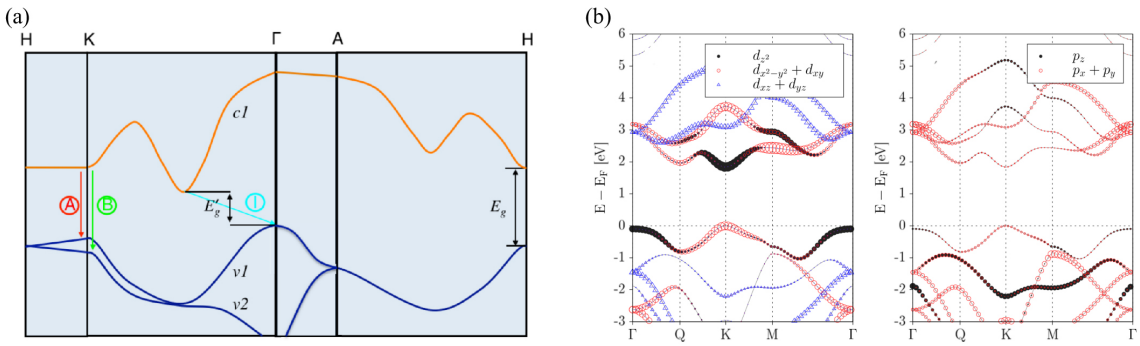

Fig. 2.2 **(a)** Band structure of bulk MoS_2 showing the lowest conduction band (c1) and the highest split valence bands (v1 and v2). A (red) and B (green) define the smallest direct-gap transitions and I defines the lowest indirect-gap transition, the energy of which corresponds to the bandgap E_g'. Adapted from reference [8]. **(b)** Calculated band structure of monolayer TMD crystals. The weights of each electronic orbital on the band structure is shown with symbols where the size of the symbol is proportional to the weight. Adapted from reference [58].

After the discovery of graphene, many researchers renewed their interest in old materials which had the potential to consist of separable van-der-Waals crystals. The discovery of MoS_2 in 2010 [56] provided the necessary interest for the discovery of the entire family of transition metal dichalcogenides as layered semiconducting crystals which showed very

interesting results when thinned down to a monolayer. The indirect band gap dictates that any decay of excited states leading to the emission of light would require the additional momentum of a phonon for an electron in the conduction band to recombine with a hole in the valence band making the entire process inefficient. However, as the crystal is cleaved from two layers to monolayer, a quantum confinement effect leads to a direct band gap transition which allows for a far more efficient light-emitting recombination, increasing the quantum yield of the material by a factor of 10^3 when compared to few layer crystals [8].

The monolayer electronic states of the valence band in the center of the Brillouin zone (Γ) and those of the conduction band at a vertex (K), as displayed in Fig. 2.2(b), contain contributions from the out of plane p_z electronic orbitals of the chalcogen atoms and d_{z^2} orbitals of the transition metal atom [59–61]. The states of the conduction band at the Q point and the valence band at the K high symmetry point, however, are largely governed by in plane electronic orbitals including chalcogen atom p_x and p_y as well as transition metal d_{xy} and $d_{x^2-y^2}$ orbitals [58, 61, 62]. Upon reduction of layer number, quantum confinement mostly affects the electronic states stemming from out of plane orbitals which mainly leads to a reduction in the valence band energy at the Γ point together with a smaller reduction of the conduction band energy at the K symmetry point leaving the conduction and valence band edges to shift to the K symmetry point at the monolayer limit therefore leading to a direct band gap which can efficiently emit light.

2.2.1 Spin-orbit splitting

Due to the fact that these materials incorporate heavy metal atoms, the spin and orbital angular momentum of the transition metal d orbitals interact and mainly contribute to form an energy splitting in both conduction and valence band edges. The spin-orbit splitting induced in the valence band of molybdenum based TMDS is on the order of 200 meV and the tungsten based materials give rise to a splitting on the order of 400 meV [9, 58, 63] which leads to two valence sub-bands at the K symmetry point with different spins. The conduction band is also split by this interaction to a smaller degree due to the partial compensation of the p and d states leading to two conduction sub-bands which are several tens of meV apart with different spins [58, 62, 64]. The band structure near the K valleys including the spin-splitting is shown in Fig. 2.3. An interesting note is that the W-based TMDs have spin flipped conduction sub-bands compared to the Mo-based [58]. This conduction band splitting leads to part of the optical selection rules for the ground state transition. In the molybdenum based TMDs, the lowest conduction sub-band and the highest valence sub-band are both of the same spin and therefore lead to a bright, emitting transition. However, since

the conduction sub-bands are flipped in the W-based TMDs, the lowest energy conduction sub-band and the highest energy valence sub-band are of a different spin and therefore lead to a dark or non-emitting ground state [58]. This fact leads to the interesting observation that W-based TMD monolayers emit more light at room temperature than at liquid helium temperatures due to the fact that the added energy from the temperature allows the higher conduction sub-band to be populated more and lead to more bright recombinations. The opposite is true for the Mo-based TMDs as the higher temperatures would populate a higher energy dark state rather than lead to optically bright recombinations from the ground state.

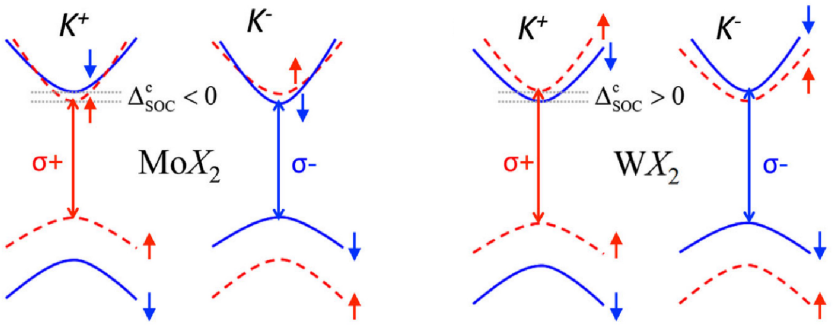

Fig. 2.3 Monolayer band structure close to the K and K$^-$ symmetry points for molybdenum based (left) and tungsten based TMDs (right). Adapted from reference [64].

The inversion symmetry in even layers of TMD crystals maintains the degeneracy of the spin projections in all K valleys along the outside of the Brillouin zone which as we have discussed above are split in both the conduction and valence band due to the spin-orbit interaction. However, the breaking of inversion symmetry in monolayers leads to the formation of two, inequivalent K^+ and K^- valleys which alternate when moving along the edge of the Brillouin zone. The inequivalency is manifested as a flipped spin in both the conduction and valence band edges when comparing the two [65]. Since the conduction band edge carries a quantum number $m_\pm = \pm 1$ and the valence band edge carries a quantum number of $m_\pm = 0$, angular momentum selection rules dictate $\Delta m_\pm = \pm 1$ corresponding to the absorption of left (σ^+) or right (σ^-) circularly polarized light in the K^+ and K^- valley respectively [59, 60]. This leads to a property called spin-valley locking which allows one to individually excite a valley through the choice of polarization of the incident light. The spin is said to be locked to one valley because the optical selection rules restrict excitations in the other valley due to an inefficient and slow spin-flip process, a slow, phonon-mediated inter-valley recombination, or an energetically unfavorable transition.

While excitation with circularly polarized light will selectively excite only one valley, emission does not necessarily follow the same rule. Valley de-polarization processes will allow a number of excited states to contribute to emission from the other valley due to a long

range coulomb exchange interaction. This creates an effective magnetic field which allows the valleys to couple at timescales shorter than or on the order of the recombination time [66]. Therefore, an excitation in one valley, instead of recombining radiatively, may induce an excitation in the other valley which will later emit light [67]. Since the exchange interaction acts on timescales shorter or on the order of the recombination time, valley de-polarization is seen in all TMDs. De-polarization times (valley polarization lifetimes) measured for WSe_2 range from 2 to 6 ps at 4K and are on the order of 1 ps for $MoSe_2$ [66, 68]. Comparing to the few picosecond recombination times for TMDs at low temperatures and especially the longer nanosecond times for room temperature, it can be concluded that valley de-polarization is a significant part of the valley properties of TMD monolayer emission [65, 68, 69].

A further implication of the spin-valley locking property is that when exciting with linearly polarized light, which consists of both right and left circularly polarized light, one can induce a coherent superposition of K^+ and K^- valley states (valley coherence) [70] which will emit light with the same polarization as long as the valley polarization lifetime is longer or on the order of the recombination time. Both of the previously mentioned properties have led to tremendous interest in valleytronics, or the manipulation of the valley pseudo-spin [71] with proposed applications in logic operations.

2.3 Excitonic properties of monolayer TMDs

Upon excitation of a semiconducting material, a negatively charged electron is elevated from the valence band to the conduction band leaving a positively charged hole behind. Both the hole and electron subsequently feel a Coulomb attractive force, not unlike a hydrgen atom, yet may move within the material due to a momentum given them by the excitation field. Similar to the hydrogen model, the dispersion of an exciton surrounding $k = 0$, meaning no momentum of one particle relative to the other, is quadratic with energy. This two-particle electron-hole pair is termed an exciton which may be of two varieties which are separated based on the extent of their wavefunctions within the semiconducting material. Frankel excitons are those with relatively small wavefunctions (smaller than the unit cell) due to low electric field screening stemming from a low dielectric constant with binding energies of 0.1 eV to 1 eV. Wannier-Mott excitons are those with a large wavefunctions relative to the unit cell and stronger electric field screening often exhibiting much smaller binding energies on the order of 0.01 eV. The lowest energy transition in a semiconductor is generally an exciton with a varying binding energy depending on the material properties. Transition metal dichalcogenides are no exception to this rule exhibiting a Wannier-Mott type exciton due to a large in-plane dielectric constant [72].

As the exciton is free to move in the semiconducting TMD crystal, there are several forces governing its properties which can be separated out as the direct and exchange Coulomb interactions with short-range and long-range coupling. The short-range direct Coulomb interaction is on the order of the unit cell and relates to the overlap of the electron and hole wave-functions while the long range direct interaction can be thought of as an electrostatic attraction between opposite charges which is weakly sensitive to spin and valley states of the individual particles. The direct interaction is mainly responsible for the binding energy of an exciton. The exchange interaction is a combination of Coulomb attraction and the Pauli exclusion principle which dictates that no two identical fermions can occupy the same state. Therefore, as the exciton travels through the semiconductor, there are many virtual electron hole recombinations which can be thought of simply as the travel of the hole, however, this recombination interacts with the spin properties of the charged particles and therefore can govern valley relaxation and depolarization as mentioned in the previous section [64].

So far, the discussion of excitons was a general one which can apply to many semiconducting materials including TMDs in their bulk form. We now move onto monolayer TMDs which host a strong out-of-plane quantum confinement. Interestingly, many comparisons can be made between monolayer TMD exciton properties and those of quasi-2D quantum wells formed in bulk semiconductors [73]. In both cases excitation reveals neutral excitons as well as charged excitons and bi-excitons which can freely travel within the 2D layer until they recombine. Fig. 2.4(a) shows the concept of a traveling exciton within a semiconducting crystal lattice while Fig. 2.4(b) displays a calculation of the electron wavefunction for MoS_2 assuming a fixed hole position at the origin with an extent over many unit cells. This provides us part of an answer as to which type of exciton TMD single layers host. The Wannier-Mott description in the effective mass approximation is often found to be the most successful at quantitative predictions of experiments [64]. An inset in Fig. 2.4(b) displays the momentum space of the exciton which shows confinement to the inequivalent $K^{\pm}$ valleys.

As discussed before, the strong quantum confinement in monolayers has profound effects on the electronic and optical properties of TMD materials. This is, therefore, also true for the exciton properties which are dominant in the optical spectrum of both absorption and emission. An optical absorption spectrum for an ideal two dimensional semiconductor is displayed in Fig. 2.4(c) where several exciton states, similar to a Rydberg series of a hydrogen atom, exist before the onset of the free particle regime where electrons are no longer bound to holes and are free to traverse the crystal alone [64]. An inset shows an energy level diagram for the quantized states displayed in the spectrum. The transition metal dichalcogenide excitons rely on the spin and valley indices as well as the magnetic quantum number instead of the usual hydrogenic quantum number n. The binding energy for each

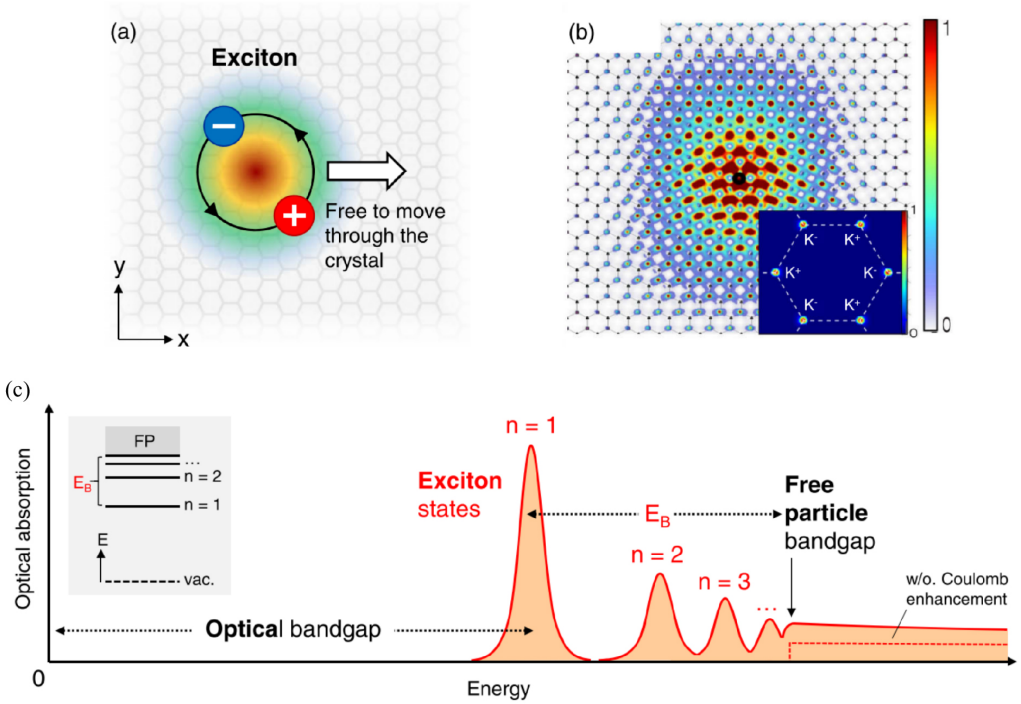

Fig. 2.4 **(a)** Schematic illustration of a free Wannier Mott exciton in the real space of the crystal lattice. **(b)** Simulation of the exciton wave function and its extent in monolayer MoS_2 for a hole fixed at the origin. Inset shows the wave function in momentum space across the Brillouin zone. **(c)** Illustration of the optical absorption of an ideal 2D semiconductor including several exciton states at lower energies than the free particle bandgap. Adapted from reference [64].

exciton can thus be defined as the energy from the optical transition of the state to the free particle band gap.

Upon thinning from bulk to monolayer, the optical band gap shifts to higher energies due to the change in electronic orbitals. However, the dielectric screening of the direct coulomb interaction is also reduced as shown in Fig. 2.5(a). This together with strong quantum confinement increases the binding energy of the excitonic states as illustrated by a dashed double red arrow in Fig. 2.5(b) [74]. Therefore, the free particle band gap is moved to even higher energies. The screening effect renders exciton binding energies in TMD monolayers extremely sensitive to the dielectric function of their environment. Studies of the binding energy for transferred monolayers of MoS_2 and $MoSe_2$ onto different substrates such as SiO_2 or hBN led to reductions of exciton binding energies due to the higher refractive indices of these materials relative to air [75].

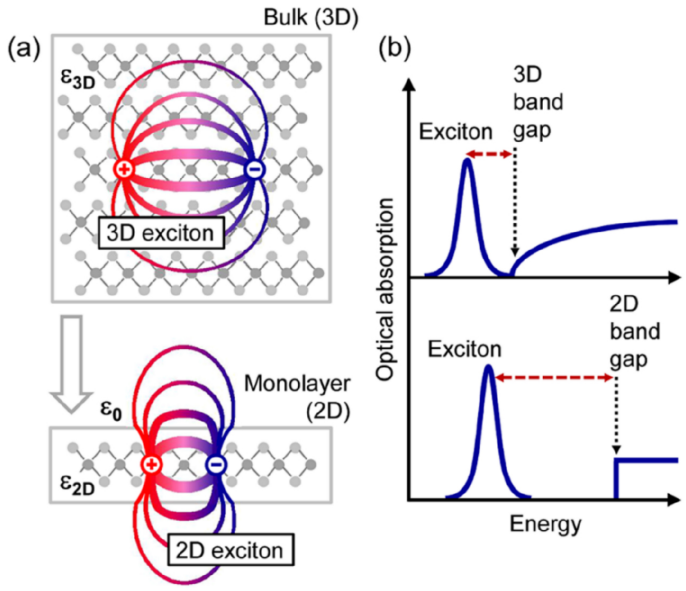

Fig. 2.5 **(a)** Real space representation of an exciton, consisting of an electron-hole pair, in a 3D bulk semiconductor and in a 2D monolayer. ε_{3D}, ε_{2D} and ε_0 represent the different permittivities. **(b)** Illustration of the impact of the transition from bulk to monolayer on the optical absorption. The exciton energy is reduced and its binding energy increased as the free particle band gap energy increases. Adapted from reference [74].

2.4 Dark excitons in tungsten based TMDs

Having discussed the excitonic foundation for the optical spectrum of TMD monolayers, it will be worthwhile to spend some time on the discussion of optically forbidden excitons in the W-based transition metal dichalcogenides. The strongly bound excitons and the spin-orbit splitting of the conduction and valence band in tungsten based TMDs leads to optical selection rules which leave the conduction and valence band edges to be of opposite spin. Since a light field can only couple to the orbital angular momentum and the selection rules require a change in the quantum number $\Delta m_{\pm} = \pm 1$ for an optically allowed transition, the spin cannot change across this transition. This leaves the lowest energy transition in W-based TMDs as an optically dark transition which can neither absorb nor emit light. It has been experimentally recorded at 40-50 meV below the neutral exciton with a pronounced fine structure splitting of 0.6 meV [76–78]. The fine structure splitting reveals two types of dark exciton. One is truly dark which means it cannot be detected by optical means, while the other is called a 'gray' exciton which allows one to optically detect it in Voigt geometry, shown in Fig. 2.6(c), or simply put detecting from the side of the sample [77, 78]. This is due to the fact that the 'gray' exciton has an out of plane dipole moment which emits latterly in the plane of the monolayer and exhibits a lifetime that is two orders of magnitude higher than for the bright exciton in a monolayer of WSe_2 [78]. Another approach to allow the

detection of these out-of-plane dipole moment excitons is to use very high NA objectives or utilize a magnetic field to couple part of the emission to a collection objective [78].

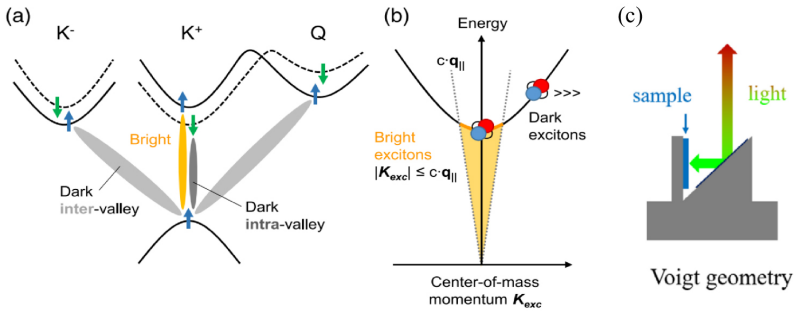

Fig. 2.6 **(a)** A schematic of the different allowed (bright) and forbidden (dark) electronic transitions in tungsten based monolayer TMDs with the respectively involved conduction band and valence band edges. **(b)** Illustration of the exciton ground state dispersion. The yellow area represents the light cone where bright transitions are allowed. Excitons outside of this area are essentially dark. Adapted from reference [64]. **(c)** Schematic illustration of the experimental arrangement called the Voigt configuration. Adapted from reference [77].

Additionally there are different varieties of optically dark excitons which are displayed in Fig. 2.6. Recombination from the opposite K valley or from the Q valley which is between the K symmetry point and the Γ point will also lead to dark excitons which are in reality inefficient due to the requirement of a phonon assisted process for the transition. Another way to achieve these momentum dark states is to utilize the quadratic dispersion at the K valley and excite an electron-hole pair with a large center of mass momentum which falls outside of the light cone (photon dispersion) thereby also requiring phonon-assisted recombination as shown in Fig. 2.6(b). The dark exciton is of interest in this thesis as we believe that it may be closely tied to filling of single photon emitting states and therefore recombining through 0-D states, a mechanism for which was recently predicted [79].

2.5 Conclusion

In this chapter we provided a basic overview of semiconducting transition metal dichalcogenides and their exciting properties which lead to visible light emission. We explored the crystal structure of TMDs noting the symmetries and stability of the crystal axes. We subsequently discussed the bulk and monolayer band structure which leads to a direct band gap in the monolayer limit. The spin orbit splitting in TMD monolayers and its consequences were briefly described. Further, we explored the formation of excitons in TMDs and noted the differences between molybdenum and tungsten based TMDs. The dark excitons formed

in tungsten based TMDs were briefly discussed as they are believed to be partly responsible for bright single photon emission in these materials.

Chapter 3

Single photon emission

This chapter will explore single photon emission with a specific emphasis on quantum emitters forming in transition metal dichalcogenides (TMDs) as this is a main focus of this thesis. I will begin by exploring different types of light sources and their photon statistics in order to clearly describe the unique nature of single photon emitters (SPEs). Next, I will discuss common properties of these emitters which are found in different material systems. However, most of the examples of these characteristics will be retrieved from work on TMD SPEs. Lastly, I will explore what is known of the origin of the emitters forming in 2D semiconductors and discuss the significance of strain in their formation process.

Single photon emitters were first discovered in 1973 [21] as emission of a radiative cascade from Mercury atoms followed closely by an observation of fluorescence from an attenuated beam of sodium atoms in 1977 [80]. The method of measuring their single photon nature, namely an HBT experiment which will be discussed in chapter 5, had already been developed in 1956 [81]. In general, a single photon emitter is a source of anti-bunched photons into a given spatio-temporal mode. A more intuitive explanation would state that such a source will yield exactly one photon at the same time from the same position after excitation. Many different material systems have been found to host point-like sources which yield single photons such as color centers in diamond [23], III-V quantum dots (QD) [82], as well as two-level emitters forming in 2D materials such as hexagonal boron nitride [18] or WSe_2 [11]. We will begin, however, with a theoretical description of different types of light sources in order to highlight the unique quantum nature of single photon emitters.

3.1 Theoretical basis of light sources

In order to understand single photon sources we must first understand why they are unique and how they are different from other light sources. These can be characterized based on

their photon statistics as single photon, coherent, or thermal (bunched). This is a measure of the number of photons that the source will emit per excitation. Fig. 3.1 illustrates the number of photons that can be emitted from different sources.

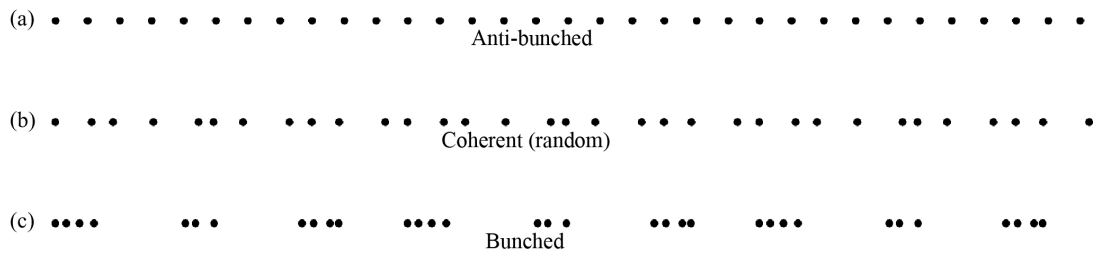

Fig. 3.1 Illustration of the number of photon emission events expected for **(a)** anti-bunched, **(b)** coherent/laser, **(c)** bunched/thermal light sources. Adapted from reference [83].

We will now discuss the derivation of the different types of light sources from quantum mechanics as well as from classical electrodynamics.

3.1.1 Single photon sources

Different material systems may host point-like sources which will yield single photons such as NV centers in diamond [23], III-V quantum dots [82] and two-level emitters forming in 2D materials [11, 18]. The phenomenological description is appropriate for a qualitative understanding of single photon emission, however, a more rigorous quantum mechanical derivation will provide a more in-depth understand of single photons. We first begin with a harmonic oscillator which is an approximation of the two-level system of a single photon source. The potential that describes this system is:

$$V(x) = \frac{1}{2} m\omega^2 x^2, \tag{3.1}$$

where m is the oscillator mass and ω is the angular frequency. Using the quantum mechanical momentum operator, the Hamiltonian of the system can be written as follows:

$$\hat{H} = \frac{\hat{p}_x^2}{2m} + \frac{1}{2} m\omega^2 \hat{x}^2, \tag{3.2}$$

where $\hat{p}_x$ is the momentum operator. In order to find a wavefunction $\psi(x)$ for this harmonic potential, one would subsequently solve the time-independent Schrödinger equation $\hat{H}\psi(x) = E_n\psi(x)$ and also obtain the eigen energies E_n. However, there is another formulation of the

Hamiltonian which is more insightful for studying the number state of a quantum harmonic oscillator. This uses the Hermitian conjugate annihilation ($\hat{a}$) and creation ($\hat{a}^\dagger$) operators defined below [83]:

$$\begin{aligned} \hat{a} &= \frac{1}{2m\hbar\omega^{1/2}}(m\omega\hat{x} + i\hat{p}_x), \\ \hat{a}^\dagger &= \frac{1}{2m\hbar\sqrt{\omega}}(m\omega\hat{x} - i\hat{p}_x), \end{aligned} \tag{3.3}$$

where $\hbar$ is the reduced Planck constant. The commutator of these operators $[\hat{a}, \hat{a}^\dagger] = 1$ Using these definitions, the Hamiltonian of the quantum mechanical harmonic oscillator is written as follows [83]:

$$\hat{H} = \hbar\omega(\hat{a}^\dagger\hat{a} + \frac{1}{2}). \tag{3.4}$$

Using the commutator of the creation and annihilation operators as well as their commutator with the harmonic oscillator Hamiltonian, we can understand the energy spectrum of the original potential. If we apply the $\hat{H}\hat{a}^\dagger$ or $\hat{H}\hat{a}$ operators to the eigenfunctions ψ_n using the time-independent Schrödinger equation, we can come to some conclusions [83]:

$$\begin{aligned} \hat{H}\hat{a}^\dagger\psi_n &= (\hbar\omega + E_n)\hat{a}^\dagger\psi_n, \\ \hat{H}\hat{a}\psi_n &= (\hbar\omega + E_n)\hat{a}\psi_n. \end{aligned} \tag{3.5}$$

One conclusion that we can make is that $\hat{a}^\dagger\psi_n$ and $\hat{a}\psi_n$ are also eigenfunctions of the Hamiltonian and yield energies of $(E_n \pm \hbar\omega)$. This means that the energy spectrum of the harmonic potential consists of equally spaced energy levels which explain the names of the creation and annihilation operators as these either raise the energy by one level or reduce it when applied to the system wavefunction. Since we also cannot accept a negative energy as a physical concept we apply the condition that there will be a lowest energy state or a ground state for which the application of the annihilation operator to the wavefunction will not reduce the energy further [83]:

$$\hat{a}\psi_0 = 0, \tag{3.6}$$

where ψ_0 is the ground state wavefunction. The final solution using all of the constraints of our quantum mechanical system will yield an energy of the nth level of the oscillator to be equal to:

$$E_n = \left(n + \frac{1}{2}\right)\hbar\omega. \tag{3.7}$$

Thus we can expand the formalism to include number states (also known as Fock states) $|n\rangle$ which describe a wavefunction $\psi_0(x)$ with an energy $(n+1/2)\hbar\omega$. Applying a creation or annihilation operator will either create or destroy a quanta of energy and either raise or lower the energy of the system by the same amount.

So far we have described a quantum mechanical harmonic oscillator which can be used to describe a two-level system in which the potential can only confine two energy levels. This is a good approximation for an exciton found in quantum dots, defect centers or 2D materials. However, the number state formalism we used here does not require the explicit inclusion of mass. Therefore, it can be easily carried over into a description of a massless harmonic oscillator or a quantized light field [83]. In this description, each number state $|n\rangle$ describes an electromagnetic wave packet with a number of photons (n). When we apply the creation and annihilation operators to the number state we raise or lower the energy of the system by adding or destroying a photon. The ground state in this description is simply known as the vacuum state where there are no photons in a wavepacket and therefore no propagation of light. The photon number statistics of the single photon Fock states is a discrete delta function yielding a single photon per excitation. An important note is that single photon sources cannot be described without the use of quantum mechanics.

3.1.2 Coherent light sources

We have explored a description of quantized light using the analogous case of quantized energy levels in a massive quantum mechanical harmonic oscillator in order to describe the emission of single photons. We can also use this formalism to describe coherent light sources such as lasers where an excitation creates many photons at once. The complex number state α can be used to describe these through a complex field amplitude in photon number units, written as [83]:

$$|\alpha\rangle = exp{-|\alpha|^2/2}\sum \frac{\alpha^n}{(n!)^{1/2}}\,|n\rangle\,. \tag{3.8}$$

Coherent states are not eigenstates of the harmonic oscillator Hamiltonian, however they are right eigenstates of the annihilation operator $\hat{a}$ and left eigenstates of the annihilation

operator $\hat{a}^{\dagger}$. Therefore, applying the annihilation operator to the above definition will yield the complex field amplitude α eigenvalue while applying the creation operator will yield a complex conjugate α^* eigenvalue. Using the formulation of the coherent state and the fact that it is an eigenstate of the annihilation and creation operator, it can be worked out that the probability that there are n photons in a coherent state propagating in free space ($P(n)$) is equal to [83]:

$$P(n) = \frac{\bar{n}^n}{n!} e^{-\bar{n}}, \tag{3.9}$$

where $\bar{n}$ is the mean photon number. The above formulation of the probability of finding n photons in a coherent number state describes a Poissonian distribution. Therefore, a coherent light source would yield a burst of photons with a mean number $\bar{n}$ with a standard deviation commonly known as $\Delta n = \sqrt{\bar{n}}$. The photon statistics of coherent light sources can also be shown to be Poissonian using an entirely classical approach which confirms this result [83].

3.1.3 Thermal light sources

Finally, we will shortly discuss thermal light sources which often yield bunched photons. Here we will not need a quantum mechanical definition as these can be classically described as black body radiation from an enclosed cavity with a temperature T. The radiation will consist of a continuous spectrum of oscillating modes with an energy density within the angular frequency range ω to $\omega + d\omega$ given by Planck's law:

$$\rho(\omega, T) d\omega = \frac{\hbar\omega^3}{\pi^2 c^3} \frac{1}{exp(\hbar\omega/k_B T) - 1} d\omega. \tag{3.10}$$

where k_B is the Boltzmann constant. This derivation of Planck's law requires a discrete energy spectrum for each oscillating mode similar to the one in the definition of the single photon energy packets (equation 3.7):

$$E_n = (n + \frac{1}{2})\hbar\omega, \tag{3.11}$$

where n is a positive integer and corresponds to the number of photons with angular frequency ω in the particular mode. Thus, equation 3.10 requires a definition of light which includes

discrete energy packets similar to the derivations of previous light sources discussed in this chapter. Furthermore, it can be shown that a single radiation mode within the enclosed cavity with an angular frequency of ω will yield a photon number statistics described by Bose-Einstein statistics:

$$P_{\omega}(n) = \frac{1}{\bar{n}+1}\left(\frac{\bar{n}}{\bar{n}+1}\right)^{n}, \tag{3.12}$$

where $\bar{n}$ is once again the mean photon number. The standard deviation, here defined by $\Delta n = \sqrt{(\bar{n}+\bar{n}^2)}$ is larger than that for coherent light thereby highlighting the broader photon number statistics of thermal light. Another name for thermal light source photon statistics is super-Poissonian. Fig. 3.2 shows the number distribution for thermal and coherent light for a mean number of $\bar{n}$ =10. This is very different from single photon emission where the number distribution would solely be a delta function at n = 1.

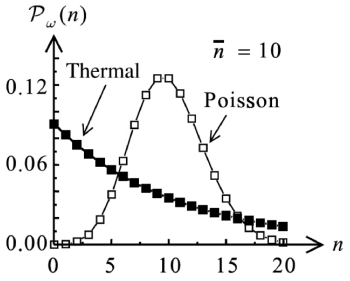

Fig. 3.2 Comparison of photon statistics for a coherent Poissonian and a thermal super-Poissonian light source. The average photon number for both is $\bar{n} = 10$. Adapted from reference [83].

Classical approaches can be used to describe both coherent and thermal sources of light. Single photon emission, however, is unique in that it is solely a quantum mechanical phenomenon and therefore has unique properties which are advantageous for a number of applications in quantum communication and research related to quantum mechanics. We have so far explored how single photon states can exist as propagating light. Now we will shift our focus to the systems designed to emit such light and their properties.

3.2 Single photon emitter optical properties

As discussed above a single photon emitter consists of a two-level system occupied by a single electron and a single hole state. Upon excitation, the electron is raised to the upper

level. The positively charged hole is left behind in the previous position of the electron. In most semiconducting materials the electron and hole are subsequently bound by a Coulomb force and an exchange force into a new quasi-particle called an exciton. For materials such as III-V semiconductors or TMDs, excitons are often free to move within the crystal, but, a single photon source in such materials is confined to a spatial position where the electron and hole energies fit inside the band gap of the material also leading to narrow linewidth emission. Since this electron-hole pair is spatially localized to this lower energy position, it must recombine and lose its energy either through a non-radiative process or in the case of ideal single photon sources recombine to generate one quanta of light. Therefore, spatial localization is a common property for single photon emitters. Fig. 3.3 shows the localization of TMD SPEs which are believed to be tied to strain [11].

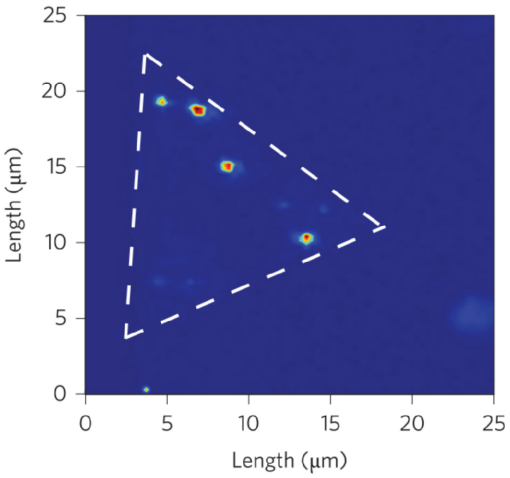

Fig. 3.3 Photoluminescence map of a monolayer of WSe_2 showing the spatial localization of quantum emitters. Adapted from reference [10].

In the case of quantum dots, the engineered design of less than 100 nm diameter III-V QDs or smaller than 10 nm collodial QDs provides the localization for the emitter. The designed artificial atom, which may host up to two excitons, is defined to be spatially localized during epitaxial growth or chemical preparation [84, 85]. As the material of the quantum dot is chosen to host a band gap with a conduction band below and a valence band above those of the surrounding material, the excitation of an electron in the two-level system is bound to it as there is no energetically favorable state in the spatial or spectral vicinity. For color centers in diamond, quantum emission occurs from a nitrogen vacancy center which is often formed during crystal growth or in subsequent annealing steps [28, 86]. Defects such as these are very tightly localized to a single atomic site. The localization of TMD single photon sources, however, is still heavily debated as it is not known whether nano-scale strain or defect emission is responsible for their formation. We will discuss the effects of strain

on TMD monolayer crystals later in the chapter, however, it has been found to be directly related to formation of SPEs. Whether, nano-scale strain pockets or strain activated defects are the localization centers for TMD SPEs is still unknown, however, it has been shown that emitters can be localized to areas smaller than 50 nm in WSe_2 [87] and with potentially greater precision for emitters defined in MoS_2 by helium ion irradiation [88].

Two more common properties can easily be extracted from the fact that a single photon source can only hold one or two excitons which will exhibit dipolar emission on recombination. The first conclusion that follows from this is that increasing the excitation power indefinitely will yield no further emission than what is maximally possible. The second is that the emission of the source will always be linearly polarized due to its dipolar nature. Fig. 3.4 shows exemplary power dependent and polarization dependent plots of single photon emission from WSe_2.

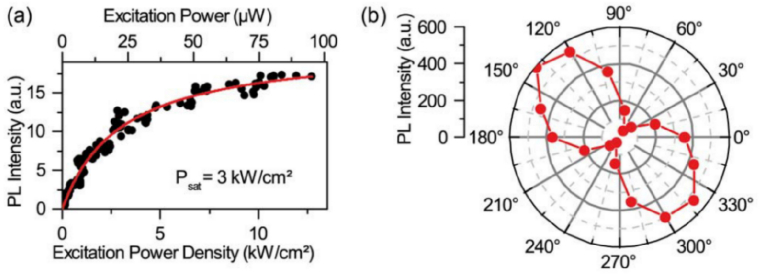

Fig. 3.4 Examples of **(a)** power saturation and **(b)** linear polarization of emission from a WSe_2 single photon source. Adapted from reference [11].

In Fig. 3.4(a) the emission saturates with increasing power as the emitter is maximally filled with the saturation power and intensity dependent on the non-radiative and radiative components of both the quantum state and the de-localized exciton state in the 2D material. The polarization dependence shown in Fig. 3.4(b) displays a characteristic pattern for linear polarization which confirms the dipolar nature of the emitter. TMD emitters have also been shown to exhibit a circular polarization dependence at high magnetic fields [10]. This is believed to be similar to excitons in III-V quantum dots where the left circularly polarized σ^- and right circularly polarized states σ^+ hybridize through the exchange interaction in the presence of in-plane anisotropy forming a linearly polarized, fine structure split doublet [89]. At high magnetic fields, this hybridization is thought to be broken and the circular polarization is regained leading to evidence that suggests that single photon emission may originate in trapped de-localized excitons by localized defects or strain pockets [10]. Another report suggests that the polarization of the single photon emitters is related to the strain topography at the position of the SPE [90].

The discussion has naturally lead to the fine structure splitting of emission in single photon emitters. This is evident in single photon emission through the observation of two energetically closely spaced emission lines with linearly polarized emission oriented in different directions. As discussed, in III-V quantum dots [89], and as seen in Fig 3.5, fine structure splitting arises due to anisotropy in the confining potential of the quantum emitter. In III-V quantum dots, this can arise due to an anisotropy in the shape of the artificial atom during its growth [89] which further yields cross-polarized emission fine structure split peaks. For SPEs forming in TMDs, the shape of the strain potential might play a large role in the fine structure splitting observed which may lead to similarly cross-polarized emission peaks [10, 12, 13, 91] but due to the difference in crystal symmetry of III-V materials and TMDs, linear polarization axes may not always be perpendicular.

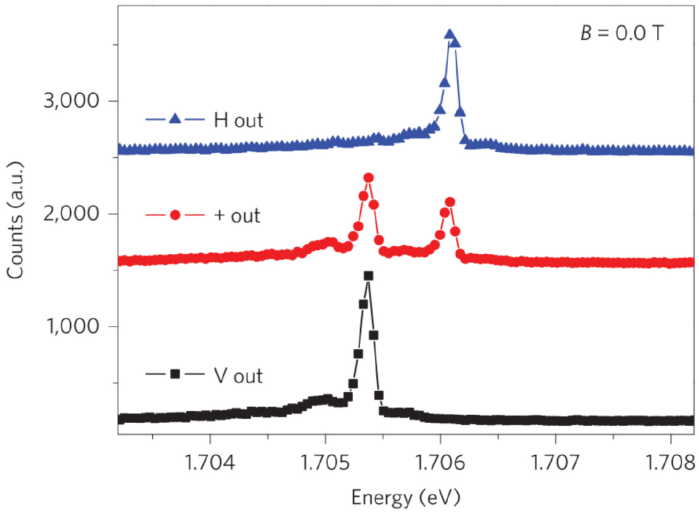

Fig. 3.5 Example of fine structure split emission from a WSe_2 single photon emitter. Adapted from reference [10].

Another consequence of the trapping of excitons into quantum states which emit single photons is the lengthening of the lifetime of emission. The lifetime of de-localized, neutral excitons in monolayer WSe_2 has been recorded to be $\approx$ 2 ps [69], while the lifetime of single photon sources found in the same material have been reported as 1-10 ns [10, 12, 91]. The lifetimes of III-V quantum dots also exhibit lengthened lifetimes in the range of several hundred picoseconds [92, 93]. An exemplary measurement of the lifetime is shown in Fig. 3.6.

As the quantum state is often excited above-band, higher energy states must relax down to the single photon emitting state which does not happen as quickly as the recombination time of de-localized excitons. This lifetime is often measured as a mixture of radiative and non-radiative lifetimes which can be used to define a quantum efficiency of the emitter:

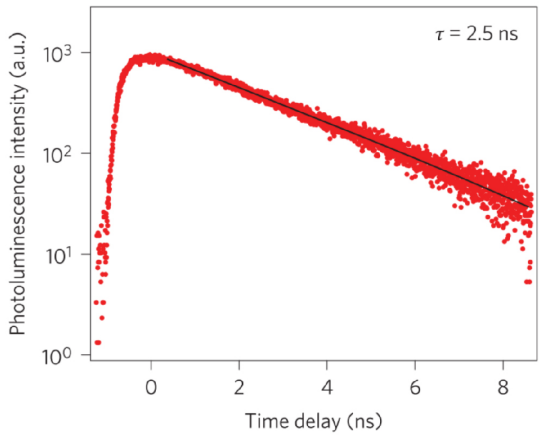

Fig. 3.6 Typical lifetime measurement of a localized single photon emitter in WSe_2 showing a lifetime of 2.5 ns. Adapted from reference [12].

$$\eta_{QE} = \frac{\tau_r}{\tau_r + \tau_{nr}}, \tag{3.13}$$

For quantum emitters in TMDs, this quantum efficiency is expected to be low with non-radiative processes dominating the emission decay as the quantum efficiency of monolayer TMDs is in the range of 0.06-5% [94–96]. In III-V quantum emitters, the quantum efficiency is near 100% [97], however, the extraction of the emitted photons is a difficult task as these single photon sources are often fabricated in a high refractive index environment. Another way to define the quantum efficiency is to measure the number of photons emitted from a source after exciting it with a single pulse. This definition leads to another figure of merit for all single photon sources, namely the brightness at the first lens. This value is defined as follows:

$$B_{lens} = \beta \eta_{lens} p_{state} \eta_{QE}, \tag{3.14}$$

where β is the probability of the source emitting light towards the collection optics which is often an objective lens, η_{lens} is the collection efficiency of this lens, p_{state} is the probability that the quantum state has been initialized after excitation which should be close to unity at the saturation power of the emitter [97]. For III-V quantum dots, β is often low as the emitter rests within a high refractive index substrate which redirects light away from any collection optics yet with placement inside a resonant structure a brightness of B_{lens} = 60-80% [97].

For TMD SPEs, this figure of merit has not been reported reliably yet the challenge for this material system rests in the low quantum efficiency of the emitter [98].

The last common property for single photon emitters which we will discuss is expressed in the single photon purity figure of merit. This is tested via a Hanbury-Brown-Twiss experiment which will be thoroughly discussed in Chapter 5. The measurement sends light from a source to a beamsplitter which separates the light into two paths ending in single photon counting detectors. Double detection events are then plotted vs the time between each detection. The probability of recording photons in both detectors simultaneously provides a robust measurement of the single photon purity as it should be zero for an ideal SPE. In reality, a value below 50% is judged as single photon in nature. Fig 3.7 displays an example of a second order correlation function ($g^{(2)}(t)$) for a WSe_2 SPE.

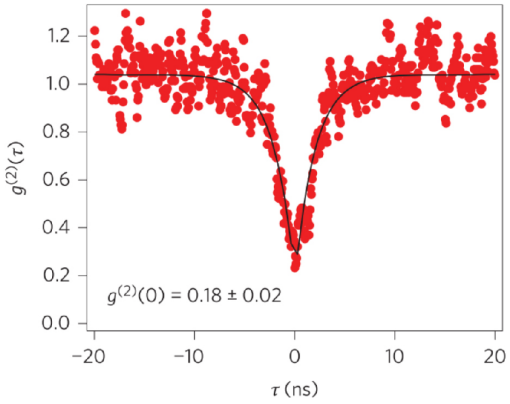

Fig. 3.7 Example of a $g^{(2)}(t)$ plot for a single photon emitter showing a $g^{(2)}(0) = 0.18 \pm 0.02$. Adapted from reference [12].

The values of $g^{(2)}(0)$ for SPEs in WSe_2 seen in experiment range from 0.022 to 0.30 [10, 12, 91, 99–101]. The emission often appears at the same wavelength as background emission which is not related to the single photon state, background correction yields $g^{(2)}(0)$ values as low as 0.002 to 0.03 [11, 100].

3.2.1 Coherence and dephasing

Applications such as quantum information processing will often require that the emitted single photons be indistinguishable from one excitation cycle to the next. This can be tested if two photons emitted by an SPE are passed through separate arms of a beamsplitter. If they are identical, they will produce full interference [102]. This quantum mechanical effect was first reported in 1987 and subsequently named after the physicists who discovered it in down-converted light, namely the Hong-ou-Mandel effect [103]. This experiment showed

that indistinguishable photons passing into a beamsplitter from two different paths at exactly the same time will exit through the same output path together. One property required for an indistinguishable single photon source is coherence. As a general wave phenomenon, two waves which occupy the same space, have the same wavelength and waveform as well as a constant phase difference are said to be coherent and will produce interference fringes. An ideal single photon source will always yield identical photons after each excitation cycle, however, in reality there are processes which will limit the coherence of consecutively emitted photons. These include mechanisms such as spectral diffusion, phonon sideband emission and pure dephasing.

Spectral diffusion is the change in emission wavelength of the SPE over timescales longer than the radiative lifetime [97]. This leads to different energies of consecutively emitted photons which will limit the coherence. As spectral diffusion is often caused by spin or charge fluctuations in the spatial vicinity of the SPE, crystal defects or surface states may result in random changes of the local charges over times longer than the decay time of the emitter and lead to Stark tuning of the emission wavelength [97]. Similarly fluctuations of randomly oriented nuclear spins in the surrounding material of some quantum dots lead to spectral diffusion of the emission of SPEs and therefore to a loss in coherence [104].

Alternately, if environmental effects such as charge and spin fluctuations happen on timescales shorter than the radiative lifetime or excited states interact with a phonon bath in that time (phonon absorption and emission at the same energy with different wavevectors), the reduction in coherence is called pure dephasing [97]. This will lead to a randomly time-varying phase difference for emitted photons and lead to a loss in coherence.

A phonon sideband is observed as a broad emission peak at slightly lower energies than that of the so-called zero-phonon line of the SPE. This occurs due to an interaction with the excited state and an acoustic phonon. As the SPE emits a photon, an acoustic phonon may be absorbed or, more likely, emitted in which case some of the energy of the excited state will be removed from the photon and therefore lead to a peak at lower energy. Since this recombination process involves a phonon, it will lead to incoherent emission which can be as much as 10% of the emitted light from InGaAs QDs [97]. This is also seen in many WSe_2 SPE emission spectra, often found at lower energies [31].

These are some of the dominant de-coherence mechanisms present in single photon emitters in different material systems including III-V and II-VI quantum dots, color centers in diamond or 2D materials. Some of the above-mentioned dephasing mechanisms such as phonon-induced processes may influence 2D materials differently than color centers or quantum dots due to the fact that the SPE will form along a surface instead of inside a bulk material. However, all of these common de-coherence mechanisms will be important for

every material system to some degree. The coherence time for SPEs in WSe_2 have previously only been reported once to be a very short value of 3.5±0.2 ps [98]. Compared to the coherence time of III-V quantum dots (430 - 770 ps [105, 106]), NV centers in diamond (as high as 15 ns [86]) or even SPEs in hexagonal boron nitride (81 ps [107]), TMD emitters offer far shorter values which may limit their potential use, however, this may be improved by protecting them from the environment via encapsulation or other means.

3.3 Transition metal dichalcogenide SPE origins

Having now discussed common single photon emitter properties, we will shift to the formation of these with a particular emphasis on TMD SPEs which is are large part of the completed work for this thesis. The formation of single photon sources in other material systems has long been studied and is generally agreed upon. For III-V or II-VI quantum dots, crystal growth of low bandgap islands inside a high bandgap material localizes the wavefunction of at least one exciton inside the structure. Therefore, molecular beam epitaxy is used to define the single photon source directly [108]. Colloidal quantum dots, on the other hand are defined by a chemical process which forms many semiconducting nano-particles of 2-10 nm radius which will subsequently emit single photons [85]. Color centers in diamond are also fairly well understood as crystal defects such as nitrogen substitutions in carbon vacancy sites [28, 86].

However, SPEs in 2D materials are often still under at least partial debate. Single photon sources in hexagonal boron nitride (hBN) emit quantum light at room temperature (RT) and exhibit smaller linewidths for few layer samples rather than monolayer [18], suggesting a deep level trap state originating in a crystal defect. The high annealing temperatures or electron beam irradiation required to activate the quantum states also point to a similar origin. One of the first reports of single photon emission in hBN suggest an anti-site complex N_BV_N [18], while other first principles calculations point to a carbon substitution and nitrogen vacancy C_BV_N. However, these works have not been able to explain the large range of emission energies of these emitters, which other reports believe to be a result of strain [20, 109]. Another explanation of this range of possible emission energies for hBN SPEs suggests coupling to a third higher energy state which indirectly couples to the two-level emitter and allows one to access low energy emitters with a higher energy excitation [110].

While hBN quantum emitters are generally believed to be a result of one or another type of deep level trap state with direct or indirect coupling to a third state, the formation of SPEs in TMDs is far less agreed upon. Different reports still suggest vastly different origins of the

quantum state. Many of these reports, however, agree on the requirement of strain for the formation of an SPE in monolayer TMDs [11, 13, 31, 111–114].

3.3.1 Strain Theory of TMDs and Exciton Funneling

Few layer TMDs, similar to graphene and other 2D materials, can withstand very large values of strain (6-11% [115] for monolayer) before failure of the crystal occurs. Such deformations, however, can induce large bandgap renormalizations and strain values of more than 3%, can lead to a transition from indirect to direct bandgap in bilayer WSe_2 [116]. Similarly strain of 2.5% or more will lead to a transition from direct to indirect bandgap in WS_2 [117]. Therefore, strain engineering can be a very useful tool for designing the bandgap of few layer TMDs.

TMDs consist of a crystal structure with a plane of transition metal atoms between two planes of chalcogen atoms. Under tensile strain, the three planes will shift closer to each other and under small compressive strains, these will shift further apart. This will change the overlap of the electron orbitals of the chalcogen and transition metal atoms and therefore lead to a change in the band structure of the material. For the selenium and sulfur TMDs, the conduction band at the K symmetry point of the Brillouin zone and the valence band at the Γ symmetry point depend on the out of plane d_{z^2} orbitals while the conduction band at the Q point and the valence band at the K point will depend on in-plane d_{xy} and $d_{x^2-y^2}$ orbitals [61] as shown in Fig. 3.8.

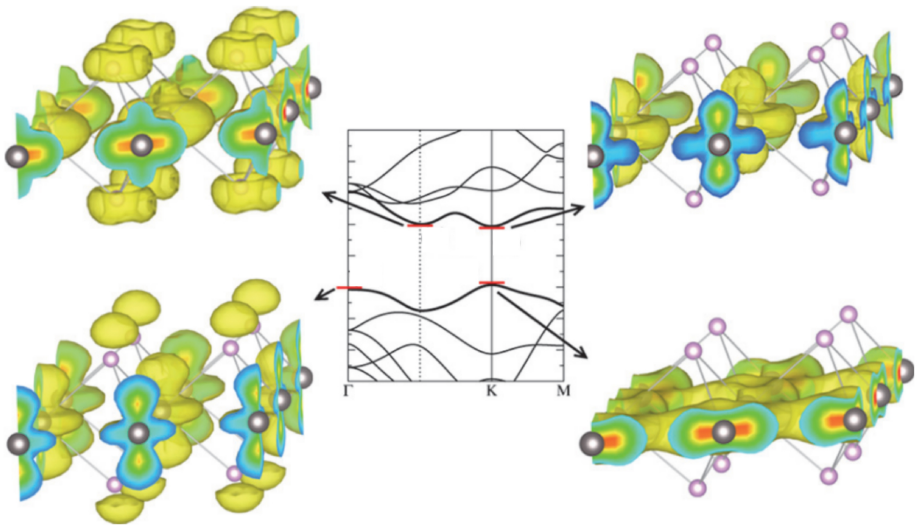

Fig. 3.8 Schematic illustration of electron orbitals surrounding TMD atoms and their influence on different points of the band structure. Adapted from reference [61].

Since strain will have a larger effect on the out-of-plane electron orbitals, the valence Γ and conduction K points in the Brillouin zone are strongly affected. In all of the previously mentioned TMDs, a small increase in tensile (compressive) strain leads to a reduction (increase) of the conduction band and an increase (reduction) of the valence band energy at the K symmetry point and therefore a reduction (increase) of the bandgap. Larger values of tensile strain lead to a transition to an indirect band gap with a shift of the valence band minimum to the Γ point. Conversely, with larger compressive strain values, the conduction band minimum will shift to the Q point and lead to a reduction of the band gap [61]. Strain in TMD monolayers has been reported using a polymer membrane bending apparatus [118–120], shown in Fig. 3.9(a), as well as flake transfer induced wrinkles [121], shown in Fig. 3.9(b), to study uni-axial deformations which are expected to lead to small changes in the band structure [61].

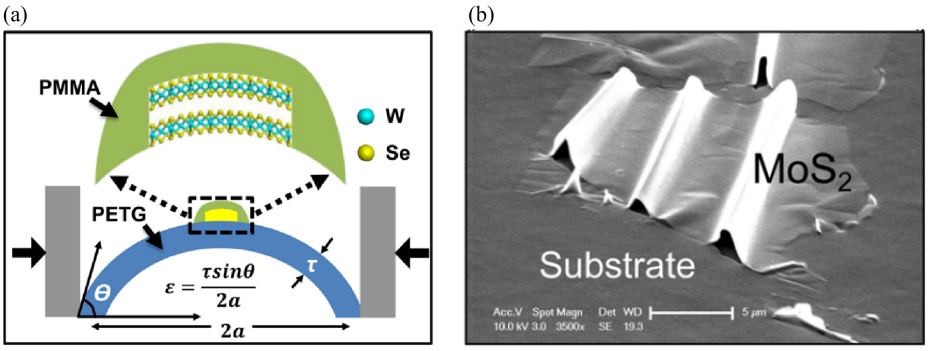

Fig. 3.9 **(a)** Schematic illustration of a bending apparatus used to strain a monolayer on a PETG membrane. Adapted from reference [118]. **(b)** SEM image of a wrinkled MoS_2 monolayer. Adapted from reference [121].

Alternately, bi-axial strain leads to a larger band gap renormalization [61] yet it is often induced in a smaller region than the size of a TMD flake. Localized bi-axial strain induced through a nano-indentation with the use of atomic force microscopy (AFM) cantilever tips [113, 122, 123] will form a region with an altered band structure which may appear in three types [124]. As shown in Fig. 3.10, type I corresponds to an increase of the valence band and a decrease in the conduction band with increasing strain, leading to a locally reduced bandgap which is true for TMDs [61]. Type II and III correspond to a decrease in both the valence band and the conduction band to varying degrees.

The difference in type II and type III band structure renormalizations with strain is contained in the concept of carrier funneling, which can be defined as the spatial diffusion of excited charge carriers toward regions which reduce the crystal energy. In type I renormalizations the electron and hole are both forced to diffuse toward the strain region as the valence band energy increases and the conduction band energy decreases thereby decreasing the total

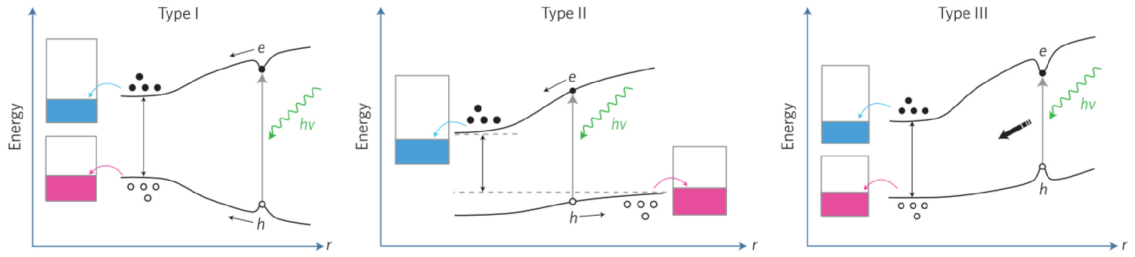

Fig. 3.10 Energy level diagram of three types of exciton funneling under strain from an AFM tip. The x-axis represents the radius of an AFM probe used to deform a suspended monolayer TMD. A decreasing tip radius results in higher values of strain. Adapted from reference [124].

energy of the exciton. The type III band structure change with increasing strain also leads to a diffusion of the entire exciton toward the strained region, however, in this case the hole is being forced away from this region due to the decreased valence band energy. The binding energy of the exciton, however, is stronger than the force in the opposite direction for the hole and therefore the entire exciton funnels toward the strained region. In type II, this exciton binding energy is overcome and the exciton can be dissociated into an electron and hole which are forced to spatially diffuse in opposite directions [124]. There is also a different case of a reduction in the valence energy and an increase in the conduction band energy at a strained position which leads to an inverse exciton funnel which has been predicted for black phosphorus [125]. Exciton funneling is only possible when the lifetime of the quasi-particle is longer than the diffusion time.

For TMDs, increased tensile strain leads to a type I funnel where excitons spatially diffuse toward strained regions within their lifetime. Since the lifetime of excitons in TMDs is typically on the order of 1 ns at room temperature [65], only excitons within 360 nm from the strained region will be funneled toward it [126]. At low temperatures, the lifetime of de-localized excitons is far shorter (1.8 ps for $MoSe_2$ and 2 ps for WSe_2 [69]), therefore, only those within an even smaller range will funnel toward a strained region. These reports have recorded the bright neutral exciton lifetime and diffusion length. However, in tungsten-based TMDs, there is a dark exciton formation as the ground state which cannot radiatively decay and will, therefore, be able to diffuse over larger distances (1.5 um for encapsulated WSe_2 at room temperature[126]). Evidence for exciton funneling can be found in a report of a bilayer of WSe_2 suspended over gallium phosphide dimer nano-antennas where strain is localized to the edges of the nano-antenna. The neutral exciton emission is brighter at the position of these edges and much brighter lower energy emission is also observed [116] as shown in Fig. 3.11(a). As the bilayer experiences tensile strain at the edges of the nano-antenna, the bandgap is reduced, however, the opposite happens at positions where the bilayer meets the substrate and compressive strain is applied. The bandgap renormalization can be seen in

Fig. 3.11(b). The strain regions funnel excitons formed on the nano-antenna but the barrier created by the compressive strain does not allow the funneling of excitons formed away from the nano-antenna [116].

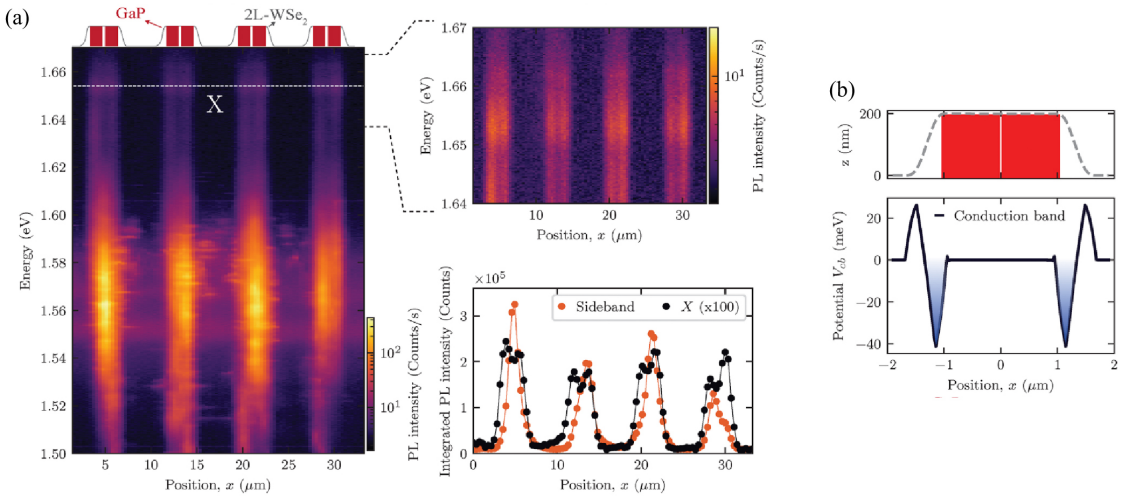

Fig. 3.11 **(a)** A linear photoluminescence scan of a WSe_2 bilayer transferred onto a row of GaP dimer nano-antennas shown schematically in the top inset. Top right panel shows photoluminescence only from the neutral exciton X. Bottom right panel shows integrated neutral exciton and low energy sideband portions of the spectrum at each position along the dimer row. **(b)** Calculated change of the bandgap for positions along the axis connecting the middle of the dimer nano-pillars. Top inset shows a schematic diagram of the bilayer transferred onto a dimer nano-antenna. Adapted from reference [116].

3.3.2 TMD SPE formation due to strain

As discussed in the previous section, strain can be used to locally decrease the bandgap in a TMD and funnel photo-induced excitons toward this region. Several reports of single photon emitters in WSe_2 have demonstrated the use of strain to form single photon emitters [13, 31, 111–114] with some suggesting that exciton funneling is an important mechanism for populating the quantum states [31, 116]. One of the first reports argues that nano-scale islands of strain induce the SPE state itself [11] similar to how quantum dots are a low bandgap material formed within a high bandgap material. This conclusion was reached because many TMD SPEs occur around the edges of the monolayer flakes and scanning tunneling microscopy has shown that nano-scale monolayer fragments occur at these edges [99]. Other reports demonstrate that the polarization of TMD SPEs may be influenced by the topography of the strained region at the position of the quantum emission [90, 127]. This would suggest another analogue between these emitters and molecular beam epitaxy grown quantum dots due to the similar polarization and fine structure splitting conditions arising from anisotropy in the shape of the dot.

A large part of the TMD SPE community also attributes the formation of the quantum state to vacancy or impurity defect centers [10, 12, 13, 113, 91, 112, 88, 114]. As the quantum emission is usually observed as a sharp emission line at energies slightly below the bandgap, it is natural to assume that shallow defect centers are hosting the single photon state. Some attribute this to Se vacancy centers [112, 128], while others have numerically (DFT) calculated that the most likely source of the emission is an anti-site complex Se_W [129]. Others go a step further and deterministically create crystal defects by irradiating a TMD monolayer with a beam of helium ions, after which narrow linewidth quantum dot-like emission is readily observed. There is no consensus over one type of defect or another. The community remains undecided about the exact origin of the single photon emission in TMDs, however, strain continues to play a large role in populating the quantum state in the defect-bound description [13, 112–114]. The evidence for the latter stems from the fact that the neutral exciton emission is quenched when sharp SPE features appear suggesting that the quantum emitter is populated by a funneling of the free neutral exciton [31]. Following this hypothesis, several groups have transferred WSe_2 monolayers onto pre-patterned substrates which induce strain in the middle of the flake [13, 31, 111, 112], while others use an AFM cantilever tip to induce the strain [113]. The transfer of monolayers onto pre-patterned SiO_2 or resist pillars yields at least one SPE formation at up to 96% of the predefined positions [31, 111] with a positioning accuracy of up to 120±32 nm [31]. Even higher positioning precision (<50 nm) has been achieved with plasmonic waveguides which also couple the emitted light to a waveguided mode [87]. Other methods of inducing strain in monolayer WSe_2 have also been found to yield single photon emission [114].

3.3.3 Recombination pathways and possible origins of SPE formation in TMDs

More work, however, has been carried out on carrier relaxation and population dynamics of the quantum states. One report asserts that the presence of a rise time in the dynamics of single photon emitters requires the introduction of a metastable third energy state which decays to the quantum emitter two-level system [130]. This work asserts that after excitation, hot carriers will relax to either a quantum state or a higher energy shallow supplying state which will subsequently relax to the emitter excited energy level. At increased temperatures, the carriers in the supplying states are no longer trapped and can relax down to the quantum emitter level much faster thereby shortening the rise time of the single photon emission [130]. In a more detailed approach, another work attempts to address which higher energy states are supplying the localized emitter states. In this report the precise definition of the

disorder leading to the SPE is not defined as the conclusions reached can apply to point defects, local strain or impurities [79]. The authors describe a system consisting of a bright and indirect dark neutral exciton level as well as direct and indirect localized states as shown in Fig. 3.12(a) [79]. The dark exciton in this study refers to the one discussed in the previous chapter of this thesis. The work ties features present in low temperature monolayer TMD photoluminescence spectra to different relaxation pathways. Direct localized single photon emission is connected to a direct transition from a bright neutral exciton level leading to sharp features close to the neutral exciton shown as X_{Loc} in Fig. 3.12(a) (b) [79]. Similarly an indirect transition from a localized state in the K' valley leads to lower energy sharp spectral features $X^{D}_{Loc,Phon}$ which are filled by a relaxation from the dark exciton level in that valley [79]. In all of the indirect transitions, phonons are required to yield emission within the light cone and lead to a spectral feature.

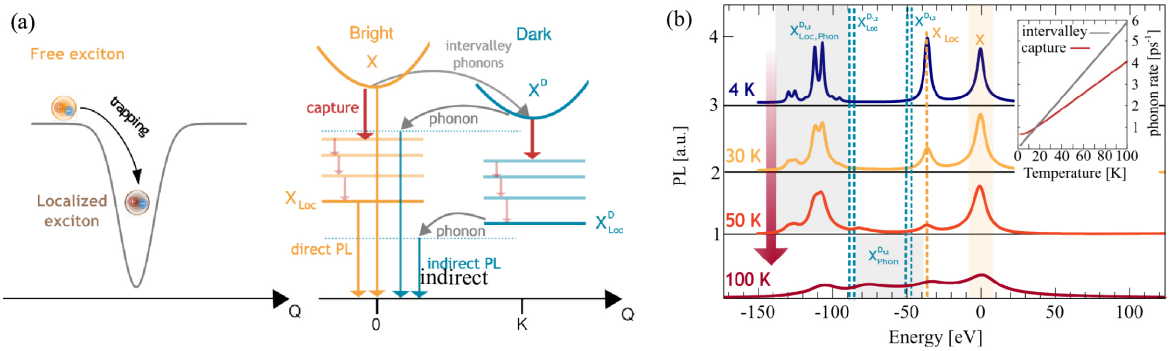

Fig. 3.12 **(a)** The left panel shows a schematic diagram of trapping free excitons by disorder in a monolayer TMD crystal. The right panel displays an illustration of the energy level diagram that is suggested to lead to the different types of single photon emission in TMDs. **(b)** Temperature dependent spectra expected for a 30 nm potential well with a depth of 40 meV. Inset shows temperature dependent bright exciton direct capture rate as well as intervalley phonon scattering rate. As the capture rate is dominant at low energies the spectral feature resulting from this will be more prominent at lower temperatures. Adapted from reference [79].

The theoretical study continues by discussing the evolution of the spectral features with increasing temperature (shown in Fig. 3.12(b)) or with an increasing trap state potential well width. Similar to many experimental reports, the increase in temperature leads to the disappearance of the X_{Loc} feature and the broadening and suppression of the $X^{D}_{Loc,Phon}$as well. The increase in the trap state potential leads to a redshift of all features, suggesting, that some single photon emitters originate from such wide potential wells [79].

Yet another report suggests an alternate mechanism for the radiative cascade leading to quantum emission. In this description, funneling leads free excitons to be trapped in a localized energy level resulting from a double selenium vacancy [128]. Since the crystal defect is localized in real space, it is not in momentum space thereby allowing inter-valley transitions through this localized emitter possible without the need for phonon interactions.

The strain at the position of the emitter also brings the conduction band edge in both valleys closer to this defect level and thereby increases the transition rate from the dark exciton in both valleys to the localized state [128]. The broken valley symmetry at the defect position allows the inter-valley mixing of the exciton trapped in the quantum state and therefore leads to fine structure splitting [128]. Under a magnetic field this splitting is increased as the free exciton valleys are brought relatively further away in energy, thereby agreeing with experimental observations of the Zeeman effect in TMD SPEs [10, 13, 12, 91, 99].

3.4 Conclusion

In this chapter we explored single photon emission by first discussing the theoretical basis of different light sources and their photon statistcs in order to be able to distinguish single photon emission as a quantum effect. Next we discussed some of the most common SPE properties including spatial localization, power saturation, linear polarization, fine structure splitting, long lifetimes, brightness, single photon purity and single photon coherence. We discussed examples in different material systems for each with an emphasis on TMD single photon emitters such as those found in WSe_2. Next, we explored what is known of the origin of single photon emitters with a particular emphasis on those found in TMDs. This included the discussion of strain as a necessary condition for observation of narrow linewidth emission and exciton funneling as a possible method of populating the quantum state. Later we discussed how these effects in few layer TMDs are believed to lead to SPE formation and while not much is known about the origin of the quantum state, the recombination pathways leading to single photon emission have also been discussed. The next chapter will shift to nano-photonics and engineering of the photonic environment as the main method of enhancing single photon emission in order to make it useful for a variety of applications.

Chapter 4

Mie resonators

We have so far discussed single photon sources in general as well as in the specific material system of 2-dimensional semiconducting materials. Next we will explore the enhancement of single photon emission via engineering of the photonic environment surrounding the light source. In order to discuss this we must first understand how the electromagnetic fields can be shaped by the presence of different materials. More specifically we will discuss how modify the environment with so-called Mie resonators, but before this can be accomplished, we must first understand how different materials react to electromagnetic fields and how they can change the propagation of light.

Since we mean to discuss the propagation of light through different materials as opposed to vacuum, the first concepts we must discuss are the relative permittivity (dielectric constant) and the refractive index. We can begin from one of Maxwell's equations also known as Gauss's law [131]:

$$\nabla \cdot D = 4\pi\rho_f, \tag{4.1}$$

where ρ_f is the free charge density and D is the displacement current defined as [132]:

$$D(r,t) = \varepsilon_0 E(r,t) + P(r,t), \tag{4.2}$$

where ε_0 is the free space or vacuum electric permittivity, $E(r,t)$ is the electric field and $P(r,t)$ is the polarization of a material through which an electric field is propagating. The polarization itself can further be defined using the electric field as follows [132]:

$$P(r,t) = \chi\varepsilon_0 E(r,t) + \chi^{(2)}\varepsilon_0 E^2(r,t) + \chi^{(3)}\varepsilon_0 E^3(r,t) + \cdots, \tag{4.3}$$

where χ, $\chi^{(2)}$ and $\chi^{(3)}$ are the first, second and third order electric susceptibilities. Our main interest in this chapter will be in linear media so we will ignore the non-linear, higher order terms for now. The higher order susceptibilities will be explored in the last section of this chapter. Using only the first term, we can define the first order susceptibility as $\chi = \varepsilon_r - 1$, where ε_r is the relative permittivity of a material, also called the dielectric constant of that material [132]. In most of this chapter we will assume that the materials we discuss are homogeneous, isotropic and, as we suggest earlier, linear except for some specifically mentioned cases. The dielectric constant is usually a complex quantity which depends on the wavelength of light passing through the material in question. The real part of ε_r concerns the movement of dipoles or free charges in the material with response to an incident electromagnetic wave. These may oscillate in phase with the wave or out of phase, thereby letting it pass through the material unhindered or refracting and slowing its propagation. The complex part of ε_r describes the absorption of the material. Throughout this chapter we will be focusing on non-magnetic dielectric materials, only briefly mentioning dispersive metals in which free charges play an important role in the dielectric constant. Therefore, we will mostly be concerned with the movement of bound dipoles in the material. We can now write the general complex definition of the refractive index as [133]:

$$n^* = \sqrt{\varepsilon_r \mu_r}, \tag{4.4}$$

where μ_r is the relative magnetic permeability. However, since we stipulated that the materials we will discuss are non-magnetic (μ_r = 1), the refractive index will be more simply written as $n^* = \sqrt{\varepsilon_r}$. We do know that the dielectric constant can consist of both a real and a complex part, so we can rewrite the complex refractive index as [133]:

$$n^* = \sqrt{n + i\kappa}, \tag{4.5}$$

where n is the real portion of the dielectric constant $Re(\varepsilon_r)$ and κ is the extinction coefficient or imaginary part of the permittivity $Im(\varepsilon_r)$. Using these definitions of the relative permittivity or dielectric constant as well as the refractive index we can begin to study how electromagnetic

fields pass through materials and how these materials can be used to control the propagation of light and confine it to small volumes.

4.1 Mie theory

In 1908, Gustav Mie wrote out the analytical solutions to Maxwell's equations for plane wave scattering from metallic nano-particles. We will explore them as the basis for the understanding of the photonic structures which we will discuss further. Mie theory was first formulated for a plane wave scattering from a metallic sphere of a radius on the order of the wavelength of the incident wave. At first Maxwell's equations are defined in a spherical coordinate system (r,θ,ϕ) defining all components of the electric and magnetic fields [40]:

$$\begin{aligned}
x^2\sin\theta E_r &= \frac{\partial(x\sin\theta M_\phi)}{\partial\theta} - \frac{\partial(xM_\theta)}{\partial\phi},\\
x\sin\theta E_{theta} &= \frac{\partial M_r}{\partial\phi} - \frac{\partial(x\sin\theta M_f)}{\partial x},\\
xE_{phi} &= \frac{\partial(xM_\theta)}{\partial x} - \frac{\partial M_r}{\partial\theta},\\
x^2\sin\theta M_r &= \frac{\partial(x\sin\theta E_\phi)}{\partial\theta} - \frac{\partial(xE_\theta)}{\partial\phi},\\
x\sin\theta M_\theta &= \frac{\partial E_r}{\partial\phi} - \frac{\partial(x\sin\theta E_\phi)}{\partial x},\\
xM_\phi &= \frac{\partial(xE_\theta)}{\partial x} - \frac{\partial E_r}{\partial\theta},
\end{aligned} \tag{4.6}$$

where E_r, E_θ, E_ϕ and M_r, M_θ, M_ϕ are the electric and magnetic field components in polar coordinates respectively. Also the variable $x = \frac{2\pi n^* r}{\lambda}$, where n^* is the complex refractive index of the material through which the plane wave is propagating and λ is the wavelength.

Next the geometry of a metallic sphere with radius R is defined upon which a plane wave will be incident. At the surface of the sphere the variable x will have a discontinuity because the refractive index changes at this position:

$$\begin{aligned}
x &= \frac{2\pi n_1^*}{\lambda_1} \qquad for \quad r < R,\\
x &= \frac{2\pi n_0^*}{\lambda_0} \qquad for \quad r > R,
\end{aligned} \tag{4.7}$$

where n_0^* and n_1^* are the complex refractive indices outside and inside the sphere respectively, while λ_0 and λ_1 are the wavelengths of the incident plane wave outside and inside the sphere

respectively. There are also boundary conditions for the electric and magnetic fields at the surface of the sphere which are defined as follows [133]:

$$\begin{aligned} E_{\theta in} &= E_{\theta out}, \\ E_{\phi in} &= E_{\phi out}, \\ (xM_{\theta})_{in} &= (xM_{\theta})_{out}, \\ (xM_{\phi})_{in} &= (xM_{\phi})_{out}, \end{aligned} \tag{4.8}$$

where the *in* and *out* subscripts denote components of x, the electric field and the magnetic field inside the sphere and outside the sphere respectively. Using these conditions we can solve equations 4.6 separately for the radial and angular components which further allows one to find solutions for only electrical resonances in the sphere ($E_r \neq 0$, $M_r = 0$) as well as only magnetic resonances ($E_r = 0$, $M_r \neq 0$). The electric resonance solutions ($M_r = 0$) yield the following [40]:

$$\begin{aligned} E_r &= \sum_{n=1}^{\infty} \frac{K_n(x)}{x^2} P_n(\theta,\phi), \\ E_{\theta} &= \sum_{n=1}^{\infty} \frac{1}{n(n+1)} \frac{K_n'(x)}{x} \frac{\partial P_n}{\partial \theta}, \\ E_{\phi} &= \sum_{n=1}^{\infty} \frac{1}{n(n+1)} \frac{K_n'(x)}{x\sin\theta} \frac{\partial P_n}{\partial \phi}, \\ M_r &= 0, \\ M_{\theta} &= \sum_{n=1}^{\infty} \frac{1}{n(n+1)} \frac{K_n(x)}{x\sin\theta} \frac{\partial P_n}{\partial \phi}, \\ M_{\phi} &= -\sum_{n=1}^{\infty} \frac{1}{n(n+1)} \frac{K_n(x)}{x} \frac{\partial P_n}{\partial \theta}, \end{aligned} \tag{4.9}$$

where n is the summation index, K_n is a cylindrical function and P_n is a spherical function of variables θ and ϕ. Similarly, the magnetic resonance solutions ($E_r = 0$) are as follows [40]:

$$
\begin{aligned}
E_r &= 0, \\
E_\theta &= \sum_{n=1}^{\infty} \frac{1}{n(n+1)} \frac{K_n(x)}{x \sin\theta} \frac{\partial B_n}{\partial \phi}, \\
E_\phi &= -\sum_{n=1}^{\infty} \frac{1}{n(n+1)} \frac{K_n(x)}{x} \frac{\partial B_n}{\partial \theta}, \\
M_r &= \sum_{n=1}^{\infty} \frac{K_n(x)}{x^2} B_n(\theta, \phi), \\
M_\theta &= \sum_{n=1}^{\infty} \frac{1}{n(n+1)} \frac{K_n'(x)}{x} \frac{\partial B_n}{\partial \theta}, \\
M_\phi &= \sum_{n=1}^{\infty} \frac{1}{n(n+1)} \frac{K_n'(x)}{x \sin\theta} \frac{\partial B_n}{\partial \phi},
\end{aligned}
\tag{4.10}
$$

where B_n is another spherical function of variables θ and ϕ.

There are also further bounds on these solutions at the origin ($r = 0$) forcing the internal fields to have a radial component involving spherical Bessel functions. Similarly, the scattered fields must tend towards a diverging spherical wave at infinity ($r = \infty$) therefore forcing the radial scattered field solutions to involve a spherical Hankel function. We can also rewrite the incident, internal (inside the sphere) and scattered waves (away from the sphere) separately due to the boundary conditions mentioned above and define the internal and scattered solutions as bounded by the conditions at $r = 0$ and $r = \infty$. Here we will also rewrite the magnetic field in terms of H, thereby including the magnetization of the material and also relax the conditions for a non-dispersive material makeup of the sphere. This leads to the following general solutions for the internal fields [131]:

$$
\begin{aligned}
E_{int} &= \sum_{n=1}^{\infty} \frac{i^n E_0 (2n+1)}{n(n+1)} \left(-i d_n N_{e1n}^{(1)}(k_1, r) + c_n M_{o1n}^{(1)}(k_1, r) \right), \\
H_{int} &= \frac{-k_1}{\omega \mu_1} \sum_{n=1}^{\infty} \frac{i^n E_0 (2n+1)}{n(n+1)} \left(d_n M_{e1n}^{(1)}(k_1, r) + i c_n N_{o1n}^{(1)}(k_1, r) \right),
\end{aligned}
\tag{4.11}
$$

where E_0 is the incident plane wave electric field intensity, $k = \frac{\omega}{c} n$ is the wave vector outside of the sphere, $k_1 = \frac{\omega}{c} n_1$ is the wave vector inside the sphere, ω is the angular frequency, μ_1 is the permeability inside the sphere and d_n and c_n are coefficients dependent on Bessel and Hankel functions as well as the angular frequency. M and N are spherical harmonic functions including Legendre polynomials and spherical Bessel functions as defined below [131]:

$$
\begin{aligned}
M_{emn} &= \nabla \times (r\psi_{emn}), \\
M_{omn} &= \nabla \times (r\psi_{omn}), \\
N_{emn} &= \frac{\nabla \times M_{emn}}{k}, \\
N_{omn} &= \frac{\nabla \times M_{omn}}{k},
\end{aligned}
\tag{4.12}
$$

where

$$
\begin{aligned}
\psi_{emn} &= \cos m\phi P_n^m(\cos\theta) z_n(kr), \\
\psi_{omn} &= \sin m\phi P_n^m(\cos\theta) z_n(kr),
\end{aligned}
\tag{4.13}
$$

where P_n^m are the associated Legendre polynomials and $z_n(kr)$ are spherical Bessel functions. The solutions presented here are sums because the internal fields, as well as the scattered fields, will consist of a sum of partial waves (resonances). It is interesting to note the internal field lines for some of these partial waves. Since the original Mie solutions were written for a metallic sphere, we know that charge currents on the surface of the sphere will yield the resonances of the structure. The magnetic and electric field lines are orthogonal on this surface [40] so knowledge of only the electric field lines is necessary to describe all internal field lines. For electric solutions, the first four partial waves are displayed in Fig. 4.1. The electric field line pattern shown here very closely resembles those seen for an electric dipole, quadrupole, etc. That is why these resonances are later named the electric dipole, quadrupole, etc. resonances.

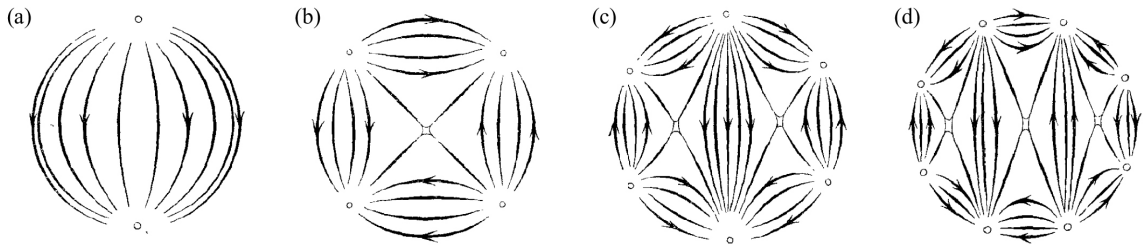

Fig. 4.1 First four electric partial oscillations or resonances which form Mie solutions to Maxwell's equations. Adapted from reference [40].

For the magnetic solutions, the radial component of the electric field is zero ($E_r = 0$), therefore the electric field lines form closed spherical curves. The first four partial waves are shown in Fig. 4.2. Similar to the electric resonances, the magnetic partial waves resemble the field lines for a magnetic dipole, quadrupole etc., thereby, giving these resonances their names as well.

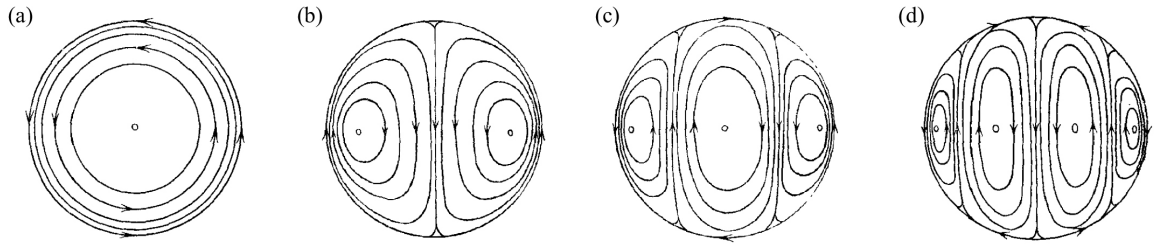

Fig. 4.2 First four magnetic partial oscillations or resonances which form Mie solutions to Maxwell's equations. Adapted from reference [40].

Next we define the general solutions for the scattered fields which will be more interesting for this thesis [131]:

$$\begin{aligned} E_s &= \sum_{n=1}^{\infty} \frac{i^n E_0 (2n+1)}{n(n+1)} \left(i a_n N_{e1n}^{(3)}(k,r) - b_n M_{o1n}^{(3)}(k,r) \right), \\ H_s &= \frac{k}{\omega \mu} \sum_{n=1}^{\infty} \frac{i^n E_0 (2n+1)}{n(n+1)} \left(a_n M_{e1n}^{(3)}(k_1,r) + i b_n N_{o1n}^{(3)}(k_1,r) \right), \end{aligned} \tag{4.14}$$

where a_n and b_n are other coefficients dependent on Bessel and Hankel functions as well as the angular frequency. Here the superscript of (3) denotes spherical Hankel functions in the definitions of ψ_{emn} and ψ_{omn} in equations 4.13.

Experimental characterization of Mie resonators involves illuminating visible light from nano-scale structures and therefore researchers are often focused on the intensity of scattered light often defined as a cross section $\sigma = P/I$, where P is the scattered power from the nano-structure under study and I is the incident light intensity in units of power over area. The scattering cross section is therefore measured in units of area but it is used to loosely define a spectrum of scattered light from a structure under study. The general Mie solutions for the scattered fields in equation 4.14 can be used to solve for the scattering cross section from a sphere with an arbitrary material makeup. The scattered cross section can thus be defined as the following [131]:

$$\sigma_s = \frac{2\pi}{k^2} \sum (2n+1)(|a_n|^2 + |b_n|^2), \tag{4.15}$$

where a_n and b_n are the same coefficients as used in equation 4.14.

4.2 High-refractive-index nano-antennas

So far, we have discussed the Mie solutions to Maxwell's equations which can only describe spherical particles or infinite cylinders. Many structures of interest in experiment are often not ideal shapes and therefore no analytical solution exists to model their internal or external fields. However, numerical simulations can be used to approximate the expected fields as well as the scattering cross section for an illuminated structure as described at the end of the last section. In this section, we will discuss an alternate method of calculating the multi-pole expansion of the scattering cross section. The resonances of monomer and dimer nano-antennas and their multi-polar contributions will be explored in the context of scattering cross sections and near-field electric and magnetic field profiles. Examples in previously reported gallium phosphide (GaP) dimer nano-antennas will also be discussed.

4.2.1 Multi-polar expansion of scattered plane wave

In order to find an expression for the multi-pole expansion of the scattering cross section, we begin with a general example of a Mie resonator in vacuum illuminated by a plane wave with electric field amplitude $|\mathbf{E}_{inc}| = E_0$ at a frequency f. As the incident wave excites the resonator the current density distribution **J(r)** can be defined by the electric field distribution in the resonator **E(r)** in the following way [134]:

$$\mathbf{J(r)} = -i\omega\varepsilon_0(n^2-1)\mathbf{E(r)} \tag{4.16}$$

where **r** is a position vector in cartesion coordinates, ω is the angular frequency, ε_0 is the permittivity of free space and n is the refractive index of the resonator. For plasmonic resonators, **J(r)** is the current density distribution close to and on the surface of the resonator, while for dielectric resonators, this corresponds to a displacement current distribution in the resonator. For the case of dielectrics, the fluctuation of bound dipoles inside the material will carry these pseudo-currents.

The multi-pole moments, mentioned as partial waves in Mie's solutions discussed in the previous section, can be derived from this current density distribution as follows [134, 135]:

$$
\begin{aligned}
p_\alpha &= -\frac{1}{i\omega}\left[\int J_\alpha j_0(kr)d^3\mathbf{r} + \frac{k^2}{2}\int \frac{j_2(kr)}{(kr)^2}(3r_\alpha(\mathbf{r}\cdot\mathbf{J}) - r^2 z_\alpha)d^3\mathbf{r}\right], \\
m_\alpha &= \frac{3}{2}\int (r\times J)_\alpha \frac{j_1(kr)}{kr}d^3\mathbf{r}, \\
\hat{Q}^e_{\alpha\beta} &= -\frac{3}{i\omega}\left[\int (3(r_\beta z_\alpha + r_\alpha z_\beta) - 2(\mathbf{r}\cdot\mathbf{J})\delta_{\alpha\beta})\frac{j_1(kr)}{kr}d^3\mathbf{r}\right. \\
&\left. +2k^2\int \left(5r_\alpha r_\beta(\mathbf{r}\cdot\mathbf{J}) - r^2(r_\alpha z_\beta + r_\beta z_\alpha) - r^2(\mathbf{r}\cdot\mathbf{J})\delta_{\alpha\beta}\right)\frac{j_r(kr)}{(kr)^3}d^3\mathbf{r}\right], \\
\hat{Q}^m_{\alpha\beta} &= 15\int \left[r_\alpha(\mathbf{r}\times\mathbf{J})_\beta + r_\beta(\mathbf{r}\times\mathbf{J})_\alpha\right]\frac{j_2(kr)}{(kr)^2}d^3\mathbf{r},
\end{aligned}
\tag{4.17}
$$

where $\alpha,\beta = x,y,z$, k is the wave number, $j_n(\rho) = (\sqrt{\pi/2\rho})z_{n+1/2}(kr)$ is the spherical Bessel function with $z_n(kr)$ as the Bessel function of the first kind. Equations 4.17 define the first four multi-pole moments which correspond to the first two electric and magnetic partial waves in the notation used by Mie, namely the electric dipole (**p**), the magnetic dipole (**m**), the electric quadrupole ($\hat{Q}^e$) and the magnetic quadrupole ($\hat{Q}^m$). These contribute to the total scattering cross section (C_{total}) of the resonator incoherently, therefore a simple sum of the partial scattering cross sections resulting from the multi-poles can be used to define it [134, 136]:

$$
\sigma_{scat} = C_{total} = \frac{k^4}{6\pi\varepsilon_0^2|E_0|}\left[\sum(|\mathbf{p}|^2 + |\frac{\mathbf{m}}{c}|^2) + \frac{1}{120}\sum(|\hat{Q}^e|^2 + |\frac{k\hat{Q}^m}{c}|^2) + \cdots\right], \tag{4.18}
$$

where c is the speed of light. As this is quite difficult to solve, a long wavelength approximation must be made to the spherical Bessel functions leading to the following multi-pole moment definitions [134]:

$$
\begin{aligned}
p_\alpha &\approx -\frac{1}{i\omega}\left[\int z_\alpha d^3\mathbf{r} + \frac{k^2}{10}\int (r_\alpha(\mathbf{r}\cdot\mathbf{J}) - 2r^2 z_\alpha)d^3\mathbf{r}\right], \\
m_\alpha &\approx \frac{1}{2}\int (r\times J)_\alpha d^3\mathbf{r}, \\
\hat{Q}^e_{\alpha\beta} &\approx -\frac{1}{i\omega}\left[\int (3(r_\beta z_\alpha + r_\alpha z_\beta) - 2(\mathbf{r}\cdot\mathbf{J})\delta_{\alpha\beta})d^3\mathbf{r}\right. \\
&\left. +\frac{k^2}{14}\int \left(4r_\alpha r_\beta(\mathbf{r}\cdot\mathbf{J}) - 5r^2(r_\alpha z_\beta + r_\beta z_\alpha) + 2r^2(\mathbf{r}\cdot\mathbf{J})\delta_{\alpha\beta}\right)d^3\mathbf{r}\right], \\
\hat{Q}^m_{\alpha\beta} &\approx \int \left[r_\alpha(\mathbf{r}\times\mathbf{J})_\beta + r_\beta(\mathbf{r}\times\mathbf{J})_\alpha\right]d^3\mathbf{r}.
\end{aligned}
\tag{4.19}
$$

The definition of a toroidal dipole moment (**T**) is also pertinent for discussions of the anapole and higher order anapole mode in the last section of the chapter. This can be thought of as the higher order term of the electric dipole moment and both of these can now be written, in the long wavelength approximation, as [134]:

$$\begin{aligned} p_\alpha &\approx -\frac{1}{i\omega}\int z_\alpha d^3\mathbf{r}, \\ T_\alpha &\approx \frac{1}{10c}\int \left(r_\alpha(\mathbf{r}\cdot\mathbf{J}) - 2r^2 z_\alpha\right) d^3\mathbf{r}, \end{aligned} \tag{4.20}$$

where the total scattering cross section is now calculated as follows:

$$C_{scat}^{total} = \frac{k^4}{6\pi\varepsilon_0^2|E_0|}\left[\sum(|\mathbf{p}+ik\mathbf{T}|^2 + |\frac{\mathbf{m}}{c}|^2) + \frac{1}{120}\sum(|\hat{Q}^e|^2 + |\frac{k\hat{Q}^m}{c}|^2) + \cdots\right]. \tag{4.21}$$

Using a numerical simulation method, such as finite-difference time-domain simulations (FDTD), to compute the electric fields inside the resonator (**E(r)**), the current density distribution can be calculated using equation 4.16. Next, equations 4.19 and 4.20 can be used to compute the multi-pole moment contributions to the total scattering cross section, which can subsequently itself be calculated using equation 4.21. This allows us to not only model the total scattering cross section, but understand the multi-pole origin of the modes inside a resonator with any geometry, such as the nano-antennas studied later in the thesis.

4.2.2 Monomer nano-antennas

To begin with, the example of a dielectric sphere can be used to understand the total scattering cross section and all of the relevant contributions. From this, one can easily transition to a cylindrical nano-antenna structure also called a monomer nano-antenna. The first geometry can be described as a lossless dielectric sphere in vacuum with a radius of 90 nm and a refractive index of $n = 4$, which is similar to the real part of the refractive index of silicon (Si). As we stipulate that the nano-particle is lossless, this sets $\kappa = 0$. A plane wave with a broad spectrum is propogating in free space and scatters from the nano-sphere. The resulting scattering cross section is shown in Fig. 4.3(a).
Four clear peaks can be identified in this spectrum, but in order to understand the resonant contributions from different dipole moments or partial waves, we must use the mult-pole expansion described previously. This yields four contributions from the electric dipole (ED), the magnetic dipole (MD), the electric quadrupole (EQ) and the magnetic quadrupole (MQ). The scattering cross section of each of these resonances is displayed in Fig. 4.3(b). It is

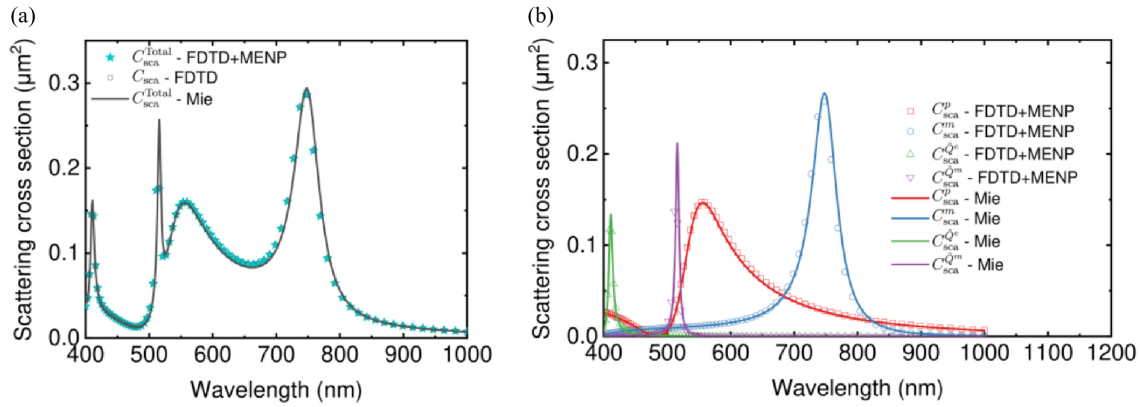

Fig. 4.3 **(a)** Total scattering cross section for a sphere (r = 90 nm) with refractive index $n = 4$ in free space. Solid black line corresponds to analytical Mie theory result. Empty circles correspond to FDTD simulations. Blue stars correspond to FDTD simulations and decomposition using an open source Matlab implementation of multi-pole expansion. **(b)** Multi-pole contributions to the total scattering cross section from the same geometry. Solid lines correspond to Mie solutions. Empty squares, circles and triangles correspond to the multi-pole contributions calculated using FDTD simulations and the Matlab implementation of the multi-pole expansion. Adapted from reference [134].

clear to see that adding each contribution from this figure to the total scattering cross section yields the spectrum shown in Fig. 4.3(a). If this sphere were to be metallic instead of dielectric, then its refractive index (n) would become negative and have similar resonances with one exception. As the fields cannot penetrate deep inside the nano-particle, no magnetic response can be expected so any contribution from a magnetic dipole or quadrupole would vanish [45]. This in fact is one of the advantages of using dielectric materials for fabricating nano-resonators.

Realistic nano-resonators, however, are not lossless ($\kappa \neq 0$) and are often positioned on a substrate as it is difficult to completely isolate them in free space. In this case the scattering cross section is approximated by performing a dark field spectroscopy experiment, the setup of which will be described in chapter 5. The bottom row of Fig. 4.4 shows dark field scattering spectra from silicon nano-particles, dark field images and SEM of which are shown in the top row of the same figure, with a varying radius placed onto a silicon substrate. The peaks shown in this figure are much broader than in Fig. 4.3 due to the presence of underlying silicon and non-zero absorption in both nano-particles and substrate. It is still possible, however, to identify peaks corresponding to different contributions from the magnetic and electric dipole as well as from the magnetic quadrupole.

While spherical nano-particles are used for some applications, such as plasmonic nano-cavities [137] and yagi-uda nano-antennas [138], cylindrical structures, often referred to as nano-antennas, are easier to fabricate with great positioning precision and so can be much more useful. Single nanometer-scale cylindrical antennas, sometimes referred to as nano-disk

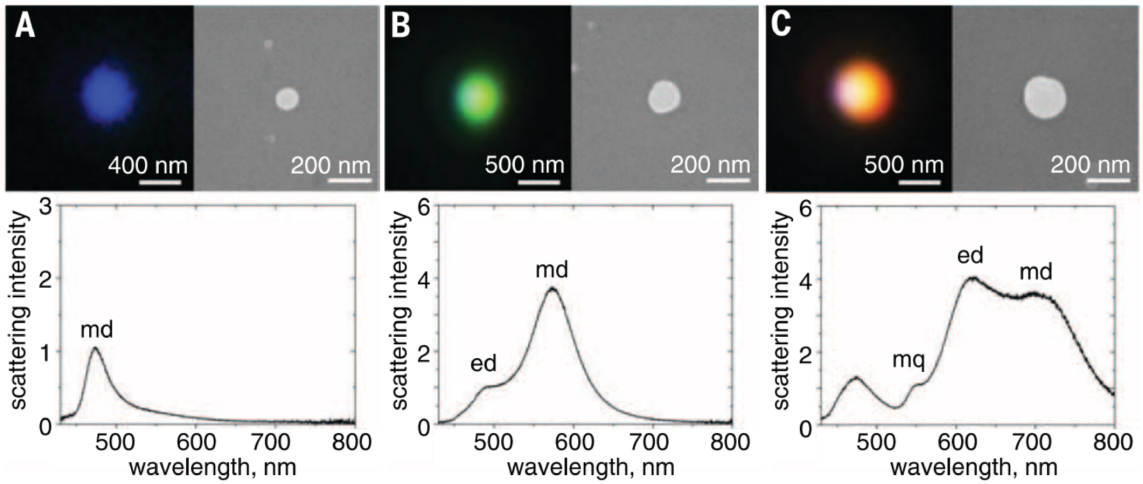

Fig. 4.4 **(a)-(c)** Dark field microscope images (upper left) and SEM images (upper right) of Si nano-particles on a silicon substrate. Bottom row shows dark field scattering spectra from each nano-particle. Particle radius: **(a)** r = 50 nm, **(b)** r = 70 nm, **(c)** r = 90 nm. Adapted from reference [45].

or nano-pillar antennas, have been fabricated from silicon [42], gallium phosphide (GaP) [43], germanium [139], GaAs/AlGaAs [140] and WS_2 [46, 47]. Due to their somewhat similar geometry to spherical nano-particles, magnetic dipole and electric dipole resonances are observed in their scattering cross sections as shown in Fig. 4.5, while higher order modes are not as easily resolvable.

The lower and higher wavelength peaks seen in Fig. 4.5(a) represent the magnetic and electric dipole resonance respectively. They result from a mainly magnetic or electric dipole moment contribution respectively as shown by the electric field lines in the insets above each peak. Fig 4.5(b) on the other hand shows the simulated evolution of the dark field spectra as the radius of the nano-disk is increased. The two resonances, seen as bright lines in this figure, redshift with increasing radius which is expected from a Mie resonator which increases in size. The radius is the most easily tunable parameter in the fabrication which will lead to a shift of the resonances.

The nano-disk antenna, also referred to as the monomer nano-antenna, is a fairly simple structure which is individually used for realization of strong coupling with an exciton resonance in WS_2 [46] as well as enhancing non-linear processes such as second or third harmonic generation through coupling to an anapole resonance [47] which will be discussed in the last section of this chapter. Other more complex structures as oligomers for realization of Fano resonances have been fabricated [141] as well as large arrays of monomers for holography [142] or the realization of a bound-state-in-continuum (BIC) through a surface lattice resonance [143]. However, we will focus on dimer nano-antennas as this is heavily featured in the experimental work presented later in this thesis.

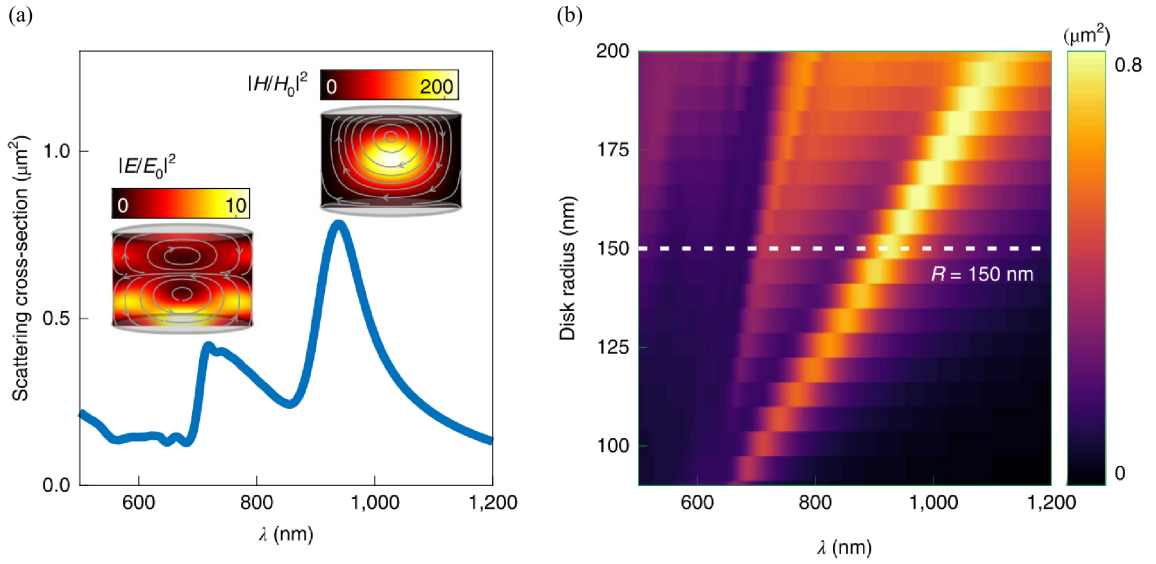

Fig. 4.5 **(a)** Simulated total scattering cross-section of a WS_2 nano-disk in vacuum with a height h = 200 nm and a radius of r = 150 nm. Insets above two peaks show the electric ($|E/E_0|^2$) and magnetic ($|H/H_0|^2$) field intensities for resonances with mainly electric dipole moment (wavelength = 715 nm) and magnetic dipole moment (wavelength = 940 nm) contributions respectively. **(b)** Simulated scattering cross sections for the same geometry over a range of radii. The scattering cross section shown in **(a)** is highlighted with a dashed white line. Adapted from reference [46].

4.2.3 Dimer nano-antennas

The dimer nano-antenna consists of two closely-spaced (less than or on the order of the wavelength of light) single-pillar (monomer) nano-antennas. As these are placed in very near proximity, the individual nano-antenna resonances will interact and therefore can no longer be identified as individual. This leads to hybridization of each monomer resonance into two dimer modes [144] which are cross-polarized, where one mode is polarized along the axis connecting the centers of the individual nano-pillars (commonly referred to as dimer axis) and another polarized perpendicular to the first. For both modes, there is a localization of the fields outside the nano-antenna geometry [145]. For an incident plane wave with electric field polarization along the dimer axis this yields highly localized electric fields in the distance between the monomers, commonly referred to as the dimer gap. For a perpendicular polarization, the magnetic field is highly confined in the dimer gap [145]. The magnetic response, however, only appears in dielectric dimer nano-antennas as plasmonic structures do not allow fields to penetrate deep inside the nano-particle [45, 145, 146]. Simulations of the electric field intensity for the two polarizations are shown for silicon and gallium phosphide dimers in Fig. 4.6(a) and (b) with an experimental imaging of the near-fields in silicon dimers displayed in the top row of Fig. 4.6(c).

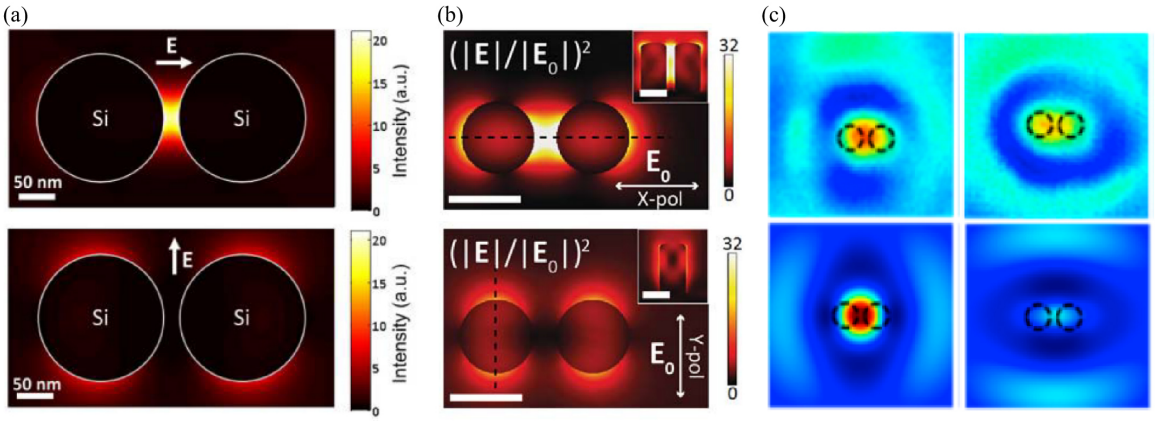

Fig. 4.6 **(a)** Spatial distribution of the electric field intensity surrounding a Si dimer nano-antenna as a cross-sectional surface through the middle of the structure height. Adapted from reference [147]. **(b)** Spatial distribution of the electric field intensity surrounding a GaP dimer nano-antenna as a cross-sectional surface through the middle of the structure height. Insets show cross-sectional view from the side of the nano-antenna as shown by the dashed lines in the main figure. Adapted from reference [43]. **(c)** Experimental (top row) and simulated (bottom row) near-field maps of Si nano-dimers collected using a SNOM. The wavelength of collection is 640 nm. The left column corresponds to excitation polarization along the dimer axis and the right column corresponds to a polarization perpendicular to the first. Adapted from reference [146].

The experiments shown in the top row of Fig. 4.6(c) were performed with a scanning near field optical microscope (SNOM) which alters the electric field confinement due to the close proximity of a metallic tip. In fact, the simulations shown in the bottom row of Fig. 4.6(c) do not resemble those seen in the (a) or (b) due to the presence of the SNOM tip. However, it is possible to see a reduction of the near field hotspot in the dimer gap for an excitation perpendicular to the dimer axis when compared to an excitation parallel to the dimer axis which is consistent with the electric field confinement expected for these modes without the presence of the SNOM tip.

Dielectric dimer nano-antennas have been employed in many different applications. The highly confined electric fields of silicon dimer nano-antennas with gaps as small as 20 nm have been used for fluorescence enhancement of crystal violet fluorescent molecules [147], surface enhanced Raman scattering as well as fluorescence enhancement of trans-β-Apo-8'-carotenal emission [44] and optical trapping of polystyrene nano-particles [148] as well as CdSe/ZnS core-shell colloidal quantum dots [149]. Similarly GaP dimer nano-antennas have yielded fluorescence enhancement in Star 635P fluorescent dyes [43]. Another report of dimer nano-antennas fabricated in this material, which unlike silicon yields no absorption in a large range of visible wavelengths, demonstrated enhancement of the fluorescence and Raman signal of a WSe_2 monolayer due to a dimer mode which confined electric fields in the gap as well as close to the top surface of the nano-antenna [150].

Plasmonic dimer nano-antennas have mostly been fabricated in a triangular shape earning the name of bowtie nano-antennas. Noble metal bowtie nano-antennas (often fabricated from gold or silver) have been shown to host similar resonances which are polarized along the dimer axis (coupled mode) or perpendicular (uncoupled mode) [151]. Gold bowtie nano-antennas have been employed to enhance the fluorescence of TPQDI dye through radiative rate and quantum efficiency enhancement [152]. An advantage that these structures have to previously used dielectric dimer nano-antennas is their shape. The double vertex geometry, similar to a tip cavity structure, with a small separation enhances the confinement of electric field and leads to exponentially increasing intensities with a decreasing gap [153]. This is due to a reduction of the mode volume through an increase of the maximum electric field intensity induced by the boundary conditions on the parallel and perpendicular electric field components. This tip-cavity structure can be modeled as consecutive, progressively smaller introductions of low refractive index (ε_l) slots and high refractive index (ε_h) bridges. Each induces an increase of either the perpendicular component of the electric field ($E_\perp$) across the slots or the parallel component ($E_{||}$) across the introduced bridges by a factor of $\varepsilon_h/\varepsilon_l$. The cumulative effect leads to very large enhancements of the electric field intensity in a high refractive index tip-cavity structure with a very small low refractive index gap for a polarization orientation along this separation [153]. Positioning of nano-antenna structures which resemble the tip-cavity geometry has also been shown through the use of an atomic force microscopy cantilever tip to translate one nano-triangle with respect to the other and thereby reduce the dimer gap [154] in order to increase the local electric field intensity of the hotspots.

Nano-antenna structures involving two particles have been shown to be advantageous for many different applications. One of these is the Purcell enhancement of single photon emitters which is a major theme in this thesis. The next section in this chapter will explore how the photonic environment can be engineered to provide an increased radiative rate of spontaneous emission which will be the basis for the design of previously discussed, as well as novel, dimer nano-antennas for Purcell enhancement of single photon emission presented in chapters 6 and 8.

4.3 Purcell effect

The Purcell effect was first discovered by Edward Purcell in 1946 where he showed the radiative rate enhancement of radio-frequency waves from nuclear spin relaxation in paraffin due to the presence of a coaxial cable cavity with a quality factor of 670 [48]. In his first work, he was not aware why the nuclear spins relaxed over much shorter times ($\approx$ 1 min) than

expected ($\approx$ several hours). Later, however, an effect that was named after him provided an answer. The spontaneous emission rate of any emitter depends on its photonic environment. There are different methods of describing this behavior in different systems. As Purcell's early work was on nuclear magnetic resonance studies involving cavities, the first formalism used to describe this effect included the notation of cavities including the quality factor and the mode volume.

4.3.1 Photonic cavity formalism

Any resonant cavity can be said to have a quality factor for each resonance which is proportional to the energy stored over the energy dissipated per round trip of the wave at a specific wavelength inside the structure [155]. Another definition involves the frequency of the resonance and its linewidth or full-width at half maximum ($Q = \frac{f_r}{\Delta f}$) [155]. In most cases, these two definitions lead to the same result. This quality factor can be defined for a variety of electromagnetic cavities including LC circuits, Fabry-Perot cavities, photonic crystal cavities or as seen in Purcell's work a length of coaxial cable. As a cavity confines electromagnetic waves inside a certain volume, this will change the photonic environment for an emitter should it be placed inside the cavity mode. An important note here is that there is an assumption on the size of the emitter. In order for this cavity formalism to be accurate, the emitter must be point-like in comparison to the cavity. Single photon emitters are often formed due to crystal defects, which by definition are on the scale of an atom, or are grown into artificial atoms, which are several nano-meters in size. In either case, the source is much smaller than the photonic structure which modifies the photonic environment surrounding it, thereby confirming that this assumption is realistic. We now continue with the next definition required for this formalism. That is the mode volume defined as follows [153]:

$$V_{eff} = \frac{\int \varepsilon(\mathbf{r})|E(\mathbf{r})|^2 dV}{max(\varepsilon(\mathbf{r})|E(\mathbf{r})|^2)}, \tag{4.22}$$

where $\varepsilon(\mathbf{r})$ is the electric permittivity of the material in which the resonance is formed and $|E(\mathbf{r})|^2$ is the electric field intensity. This defines how tightly the resonance is confined. These two properties, namely quality factor and mode volume, are the most important for determining a Purcell factor or a radiative rate enhancement as defined by Edward Purcell himself. There are two more conditions on the Purcell effect if the radiative rate enhancement for a light source is to be calculated. The emission energy or wavelength of the source must match the resonant energy or wavelength of the cavity. Also, the emitter, which is assumed

to be point-like, must be placed in the mode volume of the cavity. Once these two conditions are met, the final form of the Purcell factor (F_P) can be calculated from the following [156]:

$$F_P = \frac{3}{4\pi^2}\left(\frac{\lambda_{free}}{n}\right)^3 \frac{Q}{V_{eff}}, \tag{4.23}$$

where λ_{free} is the resonant wavelength in free space and n is the refractive index of the cavity material. As seen from equation 4.23, the radiative rate enhancement of an emitter placed in a cavity will increase if the quality factor of a cavity increases or if the mode volume decreases.

Much work has focused on increasing the quality factor or decreasing the mode volume of cavity systems. Some of the simplest systems achieving high quality factors are known as micro-cavities, which consist of two distributed bragg reflector (DBR) mirrors forming a Fabry-Perot type cavity as shown in Fig. 4.7(a). The DBR mirrors themselves consist of alternating layers of high and low refractive index material which induce destructive interference in transmitted waves and constructive interference in reflective waves, thereby functioning as a mirror over a range of wavelengths. Some of these cavities use one concave mirror which forms a cavity with a mode volume much smaller than possible for two planar DBR mirrors. The quality factors of such micro-cavities reach values higher than $Q = 10,000$ [157].

Another example of a cavity which can induce a Purcell enhancement and be described using this formalism is the photonic crystal cavity (PHC) which consists of a suspended 2 dimensional slab of high refractive index material through which holes, arranged in a periodic lattice, have been patterned as displayed in Fig. 4.7(b). This forms a cavity in the 2D plane through use of interference similar to the DBR mirrors and employs total internal reflection for confinement of electric fields in the out of plane direction [158]. In these cavity systems, quality factors of up to 2 million and mode volumes on the order of $(\lambda/n)^3$ have been achieved [158].

An alternative version of PHCs, named nano-beams [159], have also been confirmed to exhibit high quality factors while maintaining mode volumes as low as $10^{-2}(\lambda/n)^3$ with the addition of a low refractive index slot in the middle of the cavity [153, 160]. An example of a nano-beam cavity is shown in Fig. 4.7(c). Photonic crystal cavities have been used experimentally for the Purcell enhancement of single photon emitters [157, 159, 158, 161, 162] with a Purcell factor as high as ≈ 40 reached in a InGaAs quantum dot coupled to an H1-PHC [161]. Strong coupling [34, 163] and optical trapping of nano-particles [164] have also been demonstrated.

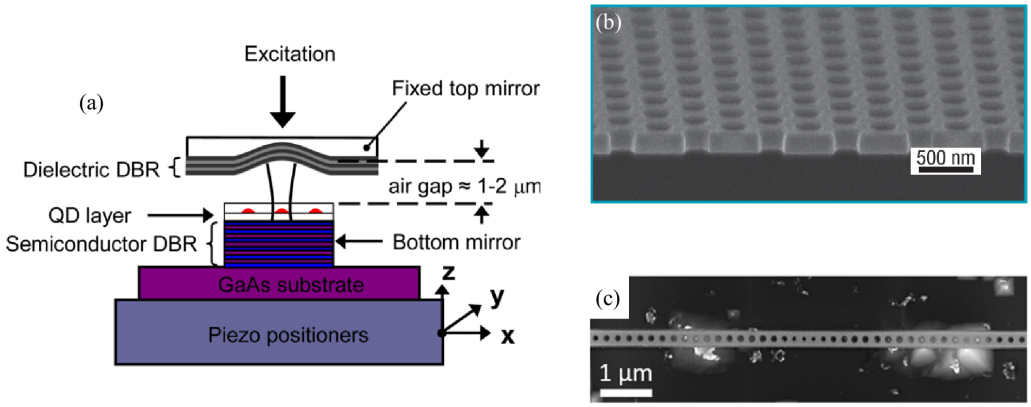

Fig. 4.7 **(a)** Schematic representation of a 0D microcavitiy including a concave top DBR mirror and a planar bottom DBR mirror with a layer of III-V quantum dots in the mode volume of the cavity. Adapted from reference [157]. **(b)** Side view SEM image of a cross-sectional cut of a photonic crystal cavity membrane with circular air holes. The cavity lattice is hexagonal. The omission of one or a few holes allows resonances to exist inside this region while being reflected from the surrounding air holes. Adapted from reference [158]. **(c)** Top view SEM image of a suspended nano-beam cavity with circular air holes. The cavity is formed by the smaller radius of the middle two air holes which allows some resonances to be confined to this region. Adapted from reference [159].

4.3.2 Fermi's golden rule

As the quality factor of a cavity or photonic structure is reduced, such as in the case of Mie resonators, the two definitions of Q mentioned above are no longer equal. The cavity formalism used to describe the Purcell factor breaks down and is no longer applicable to descriptions of the radiative rate enhancement of spontaneous emission for point-like emitters in the near field of structures such as nano-antennas. This is why a more general form of the radiative emission rate enhancement must be written. This can be derived from Fermi's Golden Rule which describes the spontaneous emission rate (γ) of a transition from an excited to a ground state of a two-level quantum system [165]:

$$\gamma = \frac{2\pi}{\hbar^2} \sum_f |\langle f|\hat{H}_I|i\rangle|^2 \delta(\omega_i - \omega_f), \tag{4.24}$$

where $|f\rangle$ describes the final (ground) state, $|i\rangle$ is the initial (excited) state, $\delta(\omega_i - \omega_f)$ is a delta function at an angular frequency which is the difference in those of the initial and final state and $\hat{H}_I = -\hat{\mu} \cdot \hat{E}$ is the interaction Hamiltonian of the transition dipole ($\hat{\mu}$) with the electric field ($\hat{E}$). This formulation can be simplified to the following expression [165]:

$$\gamma = \frac{2\omega}{3\hbar\varepsilon_0}|\mu|^2\rho_\mu(\mathbf{r}_0,\omega_0), \tag{4.25}$$

where μ is the dipole moment of the transition and $\rho_\mu(\mathbf{r}_0,\omega_0)$ is the partial local density of optical states written as [165]:

$$\rho_\mu(\mathbf{r}_0,\omega_0) = 3\sum_k \left[\mathbf{n}_\mu \cdot (\mathbf{u}_k\mathbf{u}_k^*)\cdot \mathbf{n}_{mu}\right]\delta(\omega_\mathbf{k}-\omega_0), \tag{4.26}$$

where $\mathbf{n}_\mu$ is a unit vector in the direction of μ while $\mathbf{u}_k$ and $\mathbf{u}_k^*$ are normal modes describing the complex electric fields as a result of an interaction of the dipole with the electric fields surrounding it. These normal modes are the optical states, described as photon number states in chapter 3, which will result from the transition from excited to ground state.

While this formulation is correct it is easier to compute the radiative rate using Green's function formalism. Therefore, we must first explore the dyadic Green's function tensor (**G(r,r')**) which can simply be described as the fields at point **r** due to a point source located at point **r'**. This is a tensor because it includes elements for each orientation of the dipole moment of the point source. The Green's function can be written as follows [165]:

$$\mathbf{G(r,r')} = \left[\mathbf{I} + \frac{1}{k^2}\nabla\nabla\right] G_0\mathbf{(r,r')}, \tag{4.27}$$

where **I** is the unit tensor and G_0**(r,r')** is the scalar Green's function which is a solution to the Helmholtz equation for the vector potential in free space corresponding to a radiating spherical wave, defined below as[165]:

$$G_0\mathbf{(r,r')} = \frac{e^{ik|\mathbf{r}-\mathbf{r'}|}}{4\pi|\mathbf{r}-\mathbf{r'}|}. \tag{4.28}$$

Using equations 4.27 and 4.28 we can rewrite the partial local density of optical states from Fermi's golden rule in equation 4.24 as [165]:

$$\rho_\mu(\mathbf{r}_0,\omega_0) = \frac{6\omega_0}{\pi c^2}\left[\mathbf{n}_\mu \cdot Im(\mathbf{G}(\mathbf{r}_0,\mathbf{r}_0;\omega_0))\cdot \mathbf{n}_\mu\right], \tag{4.29}$$

where ω_0 is the frequency of the transition. The imaginary part of the Green's function is used in this formulation of the partial local density of optical states. Therefore, disregarding constants, a qualitative description of the partial local density of optical states is the imaginary part of the electric field at the position of the transition dipole due to the same dipole's emission at the orientation and angular frequency of the dipole transition. As the change in photonic environment will often not change the dipole moment of a two-level quantum state transition (μ), the Purcell enhancement of the emission rate will only depend on a change in the partial local density of optical states or on the electric fields emitted by the dipole at its own position effectively driving it. This is a more general description of the Purcell effect, however, it can be expressed in a Q/V form when the conditions of high Q factor cavities are met. Simulations of the Purcell factor may use this approach, however, due to technical reasons another approach, derived from this formulation of the partial local density of optical states, may be advantageous as discussed in chapter 5.

Examples of employing nano-antenna structures for Purcell enhancement include previously mentioned reports of dielectric dimer nano-antennas in silicon [44, 147] and gallium phosphide [43, 150] as well as the careful nano-scale design of a monomer nano-antenna using an iterative approach expected to yield radiative rate enhancement factors of up to more than 800 [166]. Plasmonic structures hosting Mie resonances have also exhibited high Purcell factors ranging from 2.4 to 551 [42, 98]. The use of GaP and WS_2 dimer nano-antennas for Purcell enhancement of single photon emission is also a large part of the research presented in chapters 6 and 8.

4.4 Anapole modes and second harmonic generation

While Mie resonances in fabricated nano-antenna structures often include a major contribution from either a dipole or quadrupole moment, there are some mixed modes which include equal contributions from two different multi-pole moments. One such resonance, called an anapole mode, confines incident electromagnetic radiation due to the destructive interference of the far-field emission of the two multi-pole moment contributions and results in a minimum in the total scattering cross section. This confinement effect opens interesting research opportunities in non-linear light applications such as second or third harmonic generation. In order to discuss this anapole resonance, we must first return to equation 4.19 where the electric dipole includes a higher order term which can be described as a toroidal moment with a similar far-field radiation pattern [134]. For the electric dipole definition, the higher order contribution now defined as a toroidal moment is shown in equation 4.20. Since their far-field radiation patterns are almost identical, it is possible for these two contributions

to cancel out if the phases are at π radians from each other [134, 167]. This guarantees that the resulting mode will be completely non-radiative, therefore, light trapped in the structure at this resonance will not be able to radiate away. In realistic nano-disk or nano-antenna structures this mode is never absolutely non-radiative as there is a small contribution from a magnetic quadrupole moment which couples some of the energy in this resonance to far-field radiation [167]. Fig. 4.8(e) shows the geometry of a silicon nano-disk which hosts an anapole resonance.

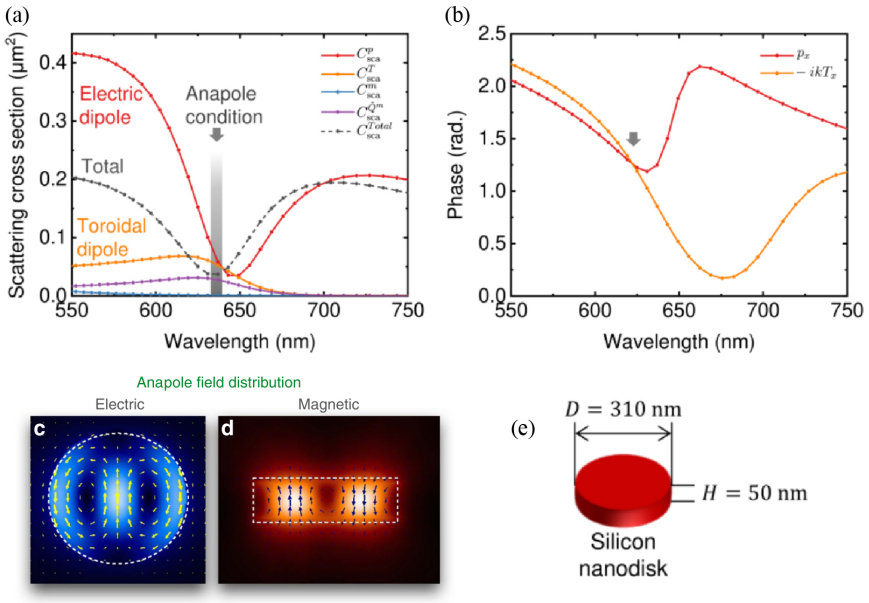

Fig. 4.8 **(a)** Scattering cross section contributions of different multi-pole moments from a Si nano-disk antenna. The anapole condition is highlighted. The main contributions at this condition include the electric dipole moment, the toroidal moment and the magnetic quadrupole moment. Adapted from reference [134]. **(b)** Phases of the electric dipole moment and toroidal moment contributions to the total scattering cross section. The crossing point between the phase of the electric dipole moment and the negative of the phase of the toroidal moment defines the anapole condition where far-field radiation cancels out. Adapted from reference [134]. **(c)** Spatial distribution of the electric field intensity at the anapole condition as a cross-sectional cut through the middle of the height of a Si nano-disk antenna. Yellow arrows show the direction of the electric field lines at different positions within the nano-disk geometry. Adapted from reference [167]. **(d)** Spatial distribution of the magnetic field intensity at the anapole condition as a cross-sectional cut through a diameter of the Si nano-disk antenna. Yellow arrows show the direction of the magnetic field lines at different positions in the nano-disk geometry. Adapted from reference [167]. **(e)** Illustration of the geometry of a Si nano-disk which results in the scattering cross section shown in **(a)** and phase in **(b)** with a diameter of 310 nm and a height of 50 nm. Adapted from reference [134].

In Fig. 4.8(a), the multi-pole moment contributions to the total scattering cross section are plotted showing the electric dipole, toroidal and magnetic quadrupole moments as contributing to the scattering at the spectral position of the anapole condition. The phase of the electric dipole moment and the negative of the phase of the toroidal moment contribution are displayed in Fig. 4.8(b) showing a crossing point at the position previously defined as

meeting the anapole condition ($\mathbf{p} = -ik\mathbf{T}$) [134]. This cancellation due to opposite phases can also be seen in the formulation of the total scattering cross section from equation 4.21 where the electric dipole and toroidal moment will cancel and yield zero for this term.The electric and magnetic fields inside a nano-disk at this anapole condition display a characteristic pattern which is closely associated to the anapole mode throughout the literature. It shows the field lines of the electric dipole and magnetic toroidal moment contributions which are responsible for the destructive interference, as shown in Fig. 4.8(c) and (d).

After describing this non-radiating anapole resonance, we move on to an application which will benefit from it. Multiple harmonic generation can be enhanced or suppressed by coupling to a light-confining resonance. In order to understand higher harmonics generation we must first go back to the description of the polarization of a material written in equation 4.3. Earlier, we were only interested in the first term of this equation which allowed us to define the dielectric constant and discuss Mie resonances. However, now we will look at higher order terms in the polarization which account for the higher order harmonics. Focusing on the second and third terms in the formulation of material polarization, $\chi^{(2)}$ and $\chi^{(3)}$ are the second and third order susceptibilities which simply quantify a material's ability to generating second or third harmonics at a given wavelength [168]. Another interesting point to remember is that the second and third terms of the polarization depend on $E^2(r,t)$ and $E^3(r,t)$ respectively, therefore the confinement and increase of electric fields will affect these terms much more than the first.

Next we must define second and third harmonic generation. Also known as frequency doubling or tripling, these effects yield light at twice or three times the energy of an incident plane wave on a material under illumination. As an example, if two photons of wavelength 800 nm are incident on a material, surface or nano-structure structure with a non-zero second order susceptibility ($\chi^{(2)}$), such as the gallium phosphide (GaP) nano-disk shown in Fig. 4.9 [43], then second harmonic generation will yield a single photon at a wavelength of 400 nm. An energy diagram describing this process is shown in Fig. 4.9(b).

The excitation pathway raises the energy from the ground state to a virtual energy state and subsequently raises this to another virtual energy state from which emission is produced by a transition down to the ground state. These virtual energy states can be real energy levels in a material such as exciton resonances or higher energy states or they can be entirely virtual. This means that second, third, etc. harmonic generation will be produced for a $\chi^{(2,3,\cdots)} \neq 0$ material, surface or structure even if there are no real states at the energy of the excitation or at multiples of this energy. However, since this process is coherent, the intensity of this non-linear signal will depend on the relative phase of the electric fields at the excitation and the higher order harmonic energy. This is known as phase-matching which is a vital

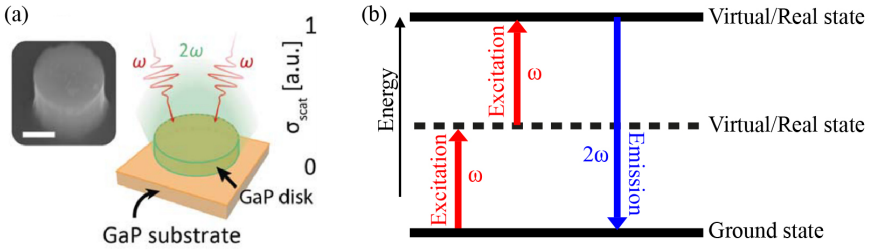

Fig. 4.9 **(a)** Schematic of a GaP monomer nano-antenna on a GaP substrate showing excitation at a frequency ω and collection of second harmonic generated light at double the frequency 2ω. Inset shows a tilted view SEM image of a fabricated GaP monomer nano-antenna. Scale bar = 200 nm. Adapted from reference [43]. **(b)** Energy level diagram illustrating the second harmonic generation process. This includes excitation from a ground state to two consecutive virtual or real states, depending on the system under study, due to absorption of two photons at angular frequency ω. The emission process from the second virtual or real state to the ground state subsequently yields one photon with an angular frequency of 2ω.

requirement for efficient emission of higher order harmonic generation. Since the phase of the electric fields at the two energies depends heavily on the dielectric constant of the material, the intensity of the SHG signal will be maximized when the dielectric constant of the material under illumination is the same at the excitation and higher harmonic energies [168].

Another condition that must be met is that the material used for higher order harmonics must exhibit some symmetry. For instance, second as well as even order harmonic generation is largely suppressed for crystals with centro-symmetry or inversion symmetry. This condition is relaxed for odd order harmonic generation. The restrictions on the even order harmonics can be explained by the multi-pole expansion of the respective terms in the polarization definition of equation 4.3. For instance, the second harmonic generation term ($P_{2\omega}$), seen as the second term in equation 4.3, can be expanded as follows [168–170]:

$$P_{2\omega} = \chi_d^{(2)} : E(\omega)E(\omega) + \chi_q^{(2)} : E(\omega)\nabla E(\omega) + \cdots, \tag{4.30}$$

where $\chi_d^{(2)}$ and $\chi_q^{(2)}$ are the second order dipole and quadrupole susceptibilities respectively. For centro-symmetric crystals or those which exhibit inversion symmetry, the dipole moment contributions will cancel therefore leaving the term depending on the square of the electric field to be equal to zero [169]. The higher order terms such as the quadrupole moment term, however, are much more negligible since they depend on the divergence of the electric field which for most experimental setups is close to zero therefore also not contributing much to the overall second harmonic generation. Since this condition is based on symmetry, all even order harmonics will be subject to it as well.

Judging from the electric field dependence of the higher order harmonics, it can be concluded that the intensity of emitted light expected from these effects will be dependent on the incident illumination intensity as well as on any resonances which locally increase the electric field intensity in the material being studied. For second harmonic generation, the emitted signal will be quadratic with the increase in confined electric energy provided by an anapole or higher order anapole resonance. Reported research involving the enhancement of second harmonic generation through a cylindrical monomer nano-antenna anapole resonance includes structures fabricated in gallium phosphide [43], WS_2 [47] and GaAs/AlGaAs [140]. There are also reports of anapole resonances in germanium nano-disks showing third harmonic generation enhancement through the use of a higher order anapole mode which exhibits an internal electric field pattern similar to that seen in Fig. 4.10(a) with a much higher enhancement due to the sharp confinement of the incident radiation as shown in Fig. 4.10(b) [139].

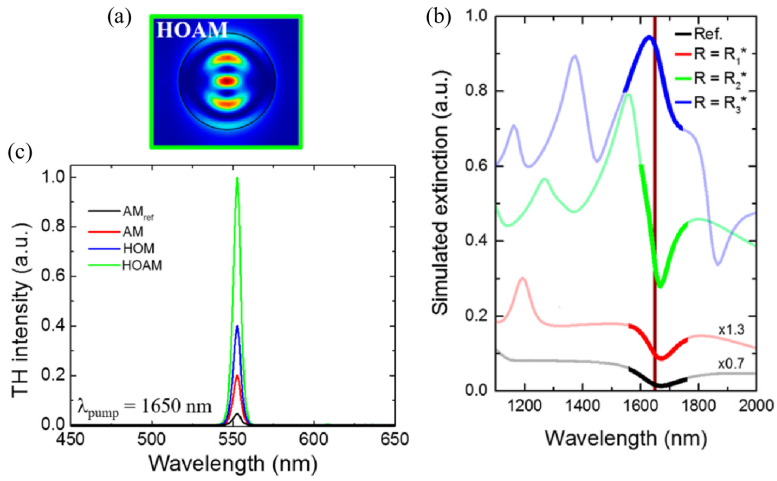

Fig. 4.10 **(a)** Simulated spatial distribution of the electric field intensity inside a Ge nano-disk antenna at a higher order anapole mode. **(b)** Simulated extinction cross sections for nano-disks with different sizes. The anapole mode (shown in red) for a radius of 350 nm, the higher order anapole mode (shown in green) for a radius of 635 nm and a higher order mode (shown in blue) for a radius of 700 nm is highlighted. The higher order anapole mode shows a sharper minimum in the extinction cross-section than the anapole mode. **(c)** Experimental third harmonic generation spectra from three nano-disks with an anapole, higher order anapole, and higher order mode resonant with an excitation at 1650 nm yielding third harmonic generation signal at 550 nm. The higher order anapole mode exhibiting the sharp confinement in **(b)** yields the brightest third harmonic generation signal. Adapted from reference [139].

4.5 Conclusion

In this chapter, I explored Mie resonators and the applications which their modes can enable and enhance. The discussion began with a brief description of the dielectric constant and

refractive index which are a fundamental part of understanding how materials react to incident electromagnetic radiation. Using this definition, I explored the Mie solutions to Maxwell's equations for a spherical metallic nano-particle ending with a general solution which can be applied to dielectric particles as well. Next, the discussion moved to high refractive index nano-antennas as this is a large part of the experimental work I have completed for this thesis. This began with a description of the scattering cross section and its multi-pole contributions which lead to the Mie resonances observed in realistic nano-particles and nano-antennas. Next, a description of monomer and dimer nano-antennas was given to introduce the structures which will be discussed in the experiments and simulations presented in chapter 7 and 8. After this, a description of the Purcell effect was provided as its use in enhancing the rate of single photon emission due to coupling with nano-antenna structures is central to this thesis. A formalism for photonic cavities was introduced along with a definition of the partial local density of optical states using Green's functions as a general description of the effect for all resonant structures. Lastly, this chapter focused on non-radiative anapole modes which result from the far-field destructive interference of radiation from electric dipole and magnetic toroidal moment contributions to the scattering cross section. Their reported use in non-linear light generation such as second and third harmonic generation was discussed for different material systems. The next chapter will describe a number of experimental and simulation setups used for the research presented in the experimental chapters 6, 7 and 8.

Chapter 5

Experimental Methods

5.1 Introduction

This chapter will explore all experimental methods of fabrication, measurement and simulation utilized in the next three chapters of this thesis. The first section will focus on 2D material fabrication beginning with exfoliation of various transition metal dichalcogenide (TMD) monolayers and multi-layers onto either a polymer stamp for further transfer or onto a substrate of SiO_2/Si. There will also be a short section on nano-fabrication of SiO_2 nano-pillars, gallium phosphide (GaP) dimer nano-antennas and WS_2 monomer and dimer nano-antennas. Next the discussion will shift to experimental setups used to measure μ-PL, time-resolved PL, anti-bunching, coherence time, dark field scattering and second harmonic generation. Lastly, a discussion of numerical finite-difference time-domain simulations will focus on methods of calculating scattering cross sections, electric field distributions, confined electric energies as well as a Purcell factor and collection efficiency enhancement for a dipole positioned on nano-antennas.

5.2 2D material fabrication

Two-dimensional materials such as TMDs consist of layers which are vertically stacked and held together by weak van-der-Waals forces which allow for simple methods of delaminating individual layers through mechanical exfoliation. This so-called "Scotch tape method" was first used in isolating single layers (monolayers) of metallic graphene [171] yet it has now been employed in the preparation of single sheets of semiconducting as well as insulating crystals. While there have been attempts to grow these monolayers with chemical vapor deposition [172] or separate them with liquid exfoliation techniques [51], the optical quality

of mechanically exfoliated crystals is still higher than for other methods of isolating few-layer 2D semiconductors and is also experimentally easily attainable. In the work completed and presented in chapters 6 and 7, the exfoliation of single or mult-layers of TMD crystals was performed mechanically and for the work shown in chapter 6, the transfer of the exfoliated monolayers was performed via a poly-dimethylsiloxane (PDMS) stamp.

5.2.1 Mechanical exfoliation

The mechanical exfoliation process requires the use of a low residue adhesive tape (Nitto® BT-150E-CM) which is used to peal few layer crystals from a bulk crystal and transfer them onto a target substrate. The process is shown in Fig. 5.1, where a bulk crystal is placed onto a clean portion of tape. Subsequently a protective film is placed on top so that the surface of the bulk crystal as well as the tape remains clean from dust or any other contaminants. Slight pressure is applied to the crystal with a cotton bud. The pressure used here depends on the bulk crystal roughness. The more rough the crystal appears, the more pressure that will be required to allow crystals to peal off of onto the tape. Subsequently, the protective film is removed and the bulk crystal is pealed off slowly using tweezers. This process is repeated until a good coverage of the tape with small crystals is achieved. This portion of tape is then brought into contact with another clean tape and re-pealed at least twice to allow the multitude of small crystals to cleave and become thinner. A clean tape can also be used for each re-peal so that after this process, there are several portions of tape with useful areas of thin crystals which can be used for exfoliation onto a target substrate. Once the re-pealing process is complete, the tape with thin crystals is brought into contact with the target substrate and pealed off in a fast or slow manner as to leave as many flakes onto the surface. The speed with which the tape is pealed off from the target surface depends on which substrate is used.

In the work presented in chapter 6, the crystals are exfoliated onto a PDMS stamp which is used for further transfer onto a desired substrate. In this case the tape is pealed off with a medium speed from the stamp to achieve two competing effects. First, the tape is not pealed slowly as the visco-elastic properties of the PDMS would not allow it to adhere to the crystals well and therefore leave very few flakes on the stamp. Secondly, the tape is not pealed too fast as this would force the visco-elastic PDMS to behave as a hard substrate which would break the crystals and yield small area crystals. For the work presented in chapter 7, the mechanical exfoliation is performed onto a SiO_2/Si substrate. For this, the tape is brought in contact with the substrate, trimmed with scissors to the area of the substrate and heated to 105°C using a hotplate, which forces the tape to adhere uniformly to the SiO_2 surface. After one minute, the substrate is removed from the hotplate and the tape is very slowly pealed

from the substrate. The speed used here is slow so that the crystals are not broken up in the pealing process and as many large area flakes are left on the SiO_2/Si substrate.

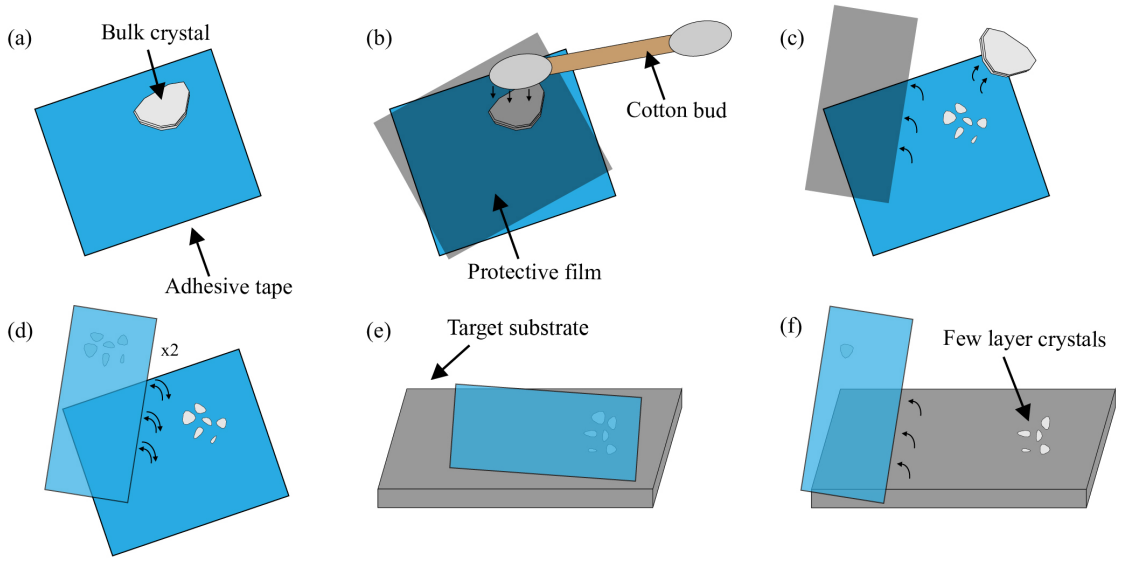

Fig. 5.1 Mechanical exfoliation procedure. **(a)** A bulk crystal is attached to clean tape. **(b)** A protective film is placed over the bulk crystal and a cotton bud is used to gently apply pressure to the crystal. **(c)** The protective film is carefully removed and the bulk crystal is pealed off. A large density of small crystals should be left on the crystal. If not, repeat (a)-(c) until this is achieved. **(d)** A clean portion of tape is attached to this tape and re-pealed at least two times. More peals may be required. **(e)** The tape is attached to the target substrate. **(f)** The tape is slowly or quickly pealed off depending on whether the target substrate has a hard surface (SiO_2) or visco-elastic properties (PDMS) respectively.

5.2.2 Photoluminescence imaging

Once exfoliation onto a desired substrate is complete, a crystal with the desired thickness must be identified. For the work completed in chapter 7, the desired bulk crystal thickness is on the order of 50 to 200 nm. This is identified through atomic force microscopy. For the identification of monolayer TMDs, the use of Photoluminescence (PL) imaging allows one to characterize whether a certain crystal is single layer. This is completed in a microscope set up to perform PL with a CCD camera used to record images introduced in reference [173]. An illustration of the microscope setup also is shown in Fig. 5.2(a). The microscope light source yields white light which is passed through a 550 nm short-pass filter, allowing excitation of the crystals believed to be single layer with the higher energy part of the spectrum and exclude any near-infrared and infrared light. The collection path includes a 600 nm long-pass filter which does not allow the excitation to be collected while permitting emitted light from a monolayer to pass through and be detected onto the camera. A bright field and PL image of a WSe_2 monolayer used in the work presented in the next chapter are shown in Figs. 5.2(b)

and (c). The position of the monolayer is identified by the bright yellow color. The intensity of light is used to discern whether the crystal under the illumination is monolayer, bilayer or even trilayer, with thicker crystals being indistinguishable from each other in PL. The color is an artifact of the filters placed before the pixels of the CCD camera however it is very useful as it can help identify which crystal has been exfoliated to the monolayer limit.

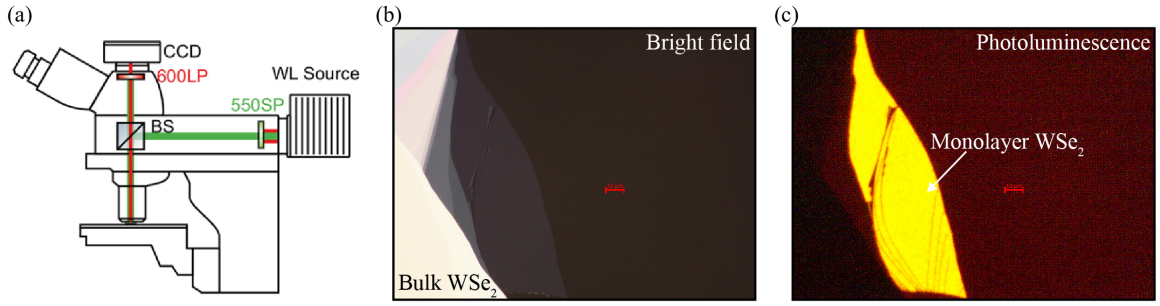

Fig. 5.2 **(a)** Schematic illustration of the microscope setup used to record PL images. Adapted from reference [173]. **(b)** Bright field image of a WSe_2 monolayer attached to bulk crystals. **(c)** Photoluminescence image of the monolayer of WSe_2 emitting bright light seen in yellow color due to filters on the pixels of the CCD camera used to record the image.

5.2.3 Transfer procedure

There are a variety of deterministic methods of depositing single layers of 2D materials onto arbitrary substrates including the polycarbonate (PC) method, the wet transfer method, the polymethyl methacrylate (PMMA) method and the PDMS method [174]. The polycarbonate method utilizes a PC layer which is used to pickup monolayer crystals before being melted onto a target substrate trapping the crystal between itself and the substrate. The PC layer can subsequently be dissolved through the use of chloroform. This method is advantageous for hetero-structure fabrication yet it does involve a risk of washing away the transferred crystals when the PC is being dissolved. The wet transfer method requires the exfoliation of crystals onto a hydrophilic substrate such as SiO_2/Si. Subsequently a polymer is deposited onto the desired crystal and the sample is placed in water when intercalation of water molecules can separate the crystal from the SiO_2/Si substrate and allow the crystal and polymer to float on the surface of the water. Subsequently the target substrate is placed in the water below the desired crystal. The water is pumped down and the crystal is transferred onto the target substrate before finally dissolving the polymer left on top. The placement of the monolayer may not be as deterministic using this transfer method and hetero-structures may be difficult to fabricate [174]. The PMMA method requires exfoliation onto a PMMA layer which has been spun onto a water-soluble or other dissoluble polymer. The PMMA layer is broken

surrounding the desired crystal and the layer underneath is dissolved. The PMMA layer with the desired flake is then floated on the surface of water and picked up with an annular holder which adheres to the PMMA layer without touching the crystal. The PMMA layer and crystal are then mechanically deposited onto the target substrate and the PMMA layer is slowly pealed away to leave the crystal in the desired location [174]. This method is also often used for hetero-structure fabrication, yet it is disadvantageous for transfer onto low adhesion substrates such as DBR mirrors.

Here, the all-dry PDMS transfer technique will be discussed. The setup used to deposit the desired crystal onto the target substrate is shown in Fig. 5.3(a). Once the desired monolayers or multi-layered crystals are identified, the PDMS stamp which is usually attached to a glass slide is secured to a holder arm upside down by means of a vacuum pump. The target substrate is also held to a micro-manipulator stage by means of the same vacuum. The vacuum controls box in Fig. 5.3(a) allows the user to choose where to guide the vacuum. As the arm is positioned above the target substrate the identified crystal on the PDMS is aligned to the desired location on the target substrate via a bright field microscope with long distance objectives. Slowly the arm attached to the PDMS stamp and the crystal are lowered using a piezo-scanner stage while the crystal is repositioned above the desired location after each step. Once the crystal approaches the desired substrate, the flake is slowly brought into contact with the desired location of the target surface. After a short wait for the PDMS stamp and crystal to adhere to the target substrate, the piezo-scanner is moved in the reverse direction so that the PDMS stamp is very slowly retracted. As as shown in Fig. 5.3(b) the interface between contacted and not-contacted PDMS moves across the target surface while the vacuum holder arm is slowly moved away from the target substrate. As this process is very slow, the visco-elastic properties of the PDMS will separate it from the crystal leaving it onto the desired substrate without breaking the crystal into smaller area flakes. In many transfers of monolayer crystals, the flake may break, however, the aim is to minimize the occurrence of this and to leave a flake with as large an area as possible onto the target surface. A schematic of the PDMS transfer method is shown in Fig. 5.3(c).

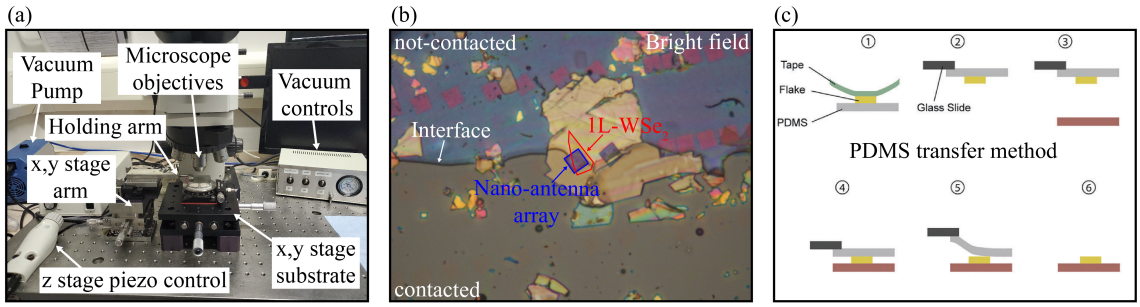

Fig. 5.3 **(a)** Photograph of the transfer setup with labeled components used for 2D material transfer procedures. **(b)** Bright field image of an ongoing transfer procedure. The interface between the uncontacted and contacted PDMS layer is seen in the middle of the image. The monolayer of WSe_2 is close to the substrate and is slowly being attached to the nano-antenna array. **(c)** Schematic illustration of the PDMS transfer method. The steps require the exofilation of 2D materials on PDMS stamp which is attached to a glass slide. The glass slide is aligned to the area of the target substrate and slowly contacted. The PDMS is then even more slowly retracted leaving the 2D material onto the target substrate. Adapted from reference [174].

5.3 Clean room fabrication of nano-structures

In order to fabricate the target substrate of SiO_2 nano-pillars and GaP dimer nano-antennas required for the results presented in chapter 6 or to fabricate the WS_2 monomer and dimer nano-antennas for the results shown in chapter 7, nano-fabrication techniques such as electron beam lithography (EBL) and reactive ion etching (RIE) were used to define resist patterns into the desired material. As most of this work was performed by collaborators, the fabrication techniques will not be discussed in detail but only a brief overview of the fabrication process for each type of nano-structure will be given.

5.3.1 SiO_2 nano-pillar fabrication

The SiO_2 nano-pillar fabrication process (performed in Sheffield) begins with thermally grown 290 nm SiO_2 on a silicon wafer. The substrate is diced and cleaned in acetone and IPA baths for 5 minutes each followed by a 5 minute O_2 plasma ash. After the substrate was baked at 180°C for 1 minute on a hotplate to remove residual moisture, an adhesion promoter (HMDS) was spin coated on top at 5000 rpm for 30s. Next, a negative-tone resist (ma-N 2403 from Microresist) was spun onto the adhesion promoter at 3000 rpm for 1 minute and baked at 100°C for 1 minute. Finally, a conductive polymer (Electra92) is spun on top of the resist at 4000 rpm for 30s before baking once more at 100°C for 1 minute. The last polymer layer is used to reduce the buildup of charges on the insulating SiO_2 substrate when the sample is exposed to an electron beam, reducing the error in the next step.

The sample is placed inside a 50 kV electron beam lithography system (Raith Voyager) where an array of disks with a varying radius (50-250 nm) are patterned into the resist using a 20 μm aperture, yielding a beam current of $\approx$ 50 pA. Development of the resist followed in ma-D 525 (Microresist) for 2 minutes after which the substrate was rinsed in DI water for 30s and baked at 100°C for 15 minutes to harden the remaining negative resist for the etching step. Inductively coupled plasma reactive ion etching (Oxford Instruments PlasmaPro 100 Cobra) is employed to transfer the resist pattern into the SiO_2 layer stopping after an etch depth of 100 nm. The recipe used, including 25 mTorr pressure with 5 sccm of CHF_3 and 30 sccm of Ar, is a standard SiO_2 etching recipe. The fabricated sample was then washed in acetone and IPA for 5 minutes each after which a 3 minute O_2 plasma ash was employed to remove all remaining organic residues and leave SiO_2 nano-pillars with vertical sidewalls used to induce single photon emitters (SPEs) as discussed in chapter 6. The fabrication steps are shown in Fig. 5.4.

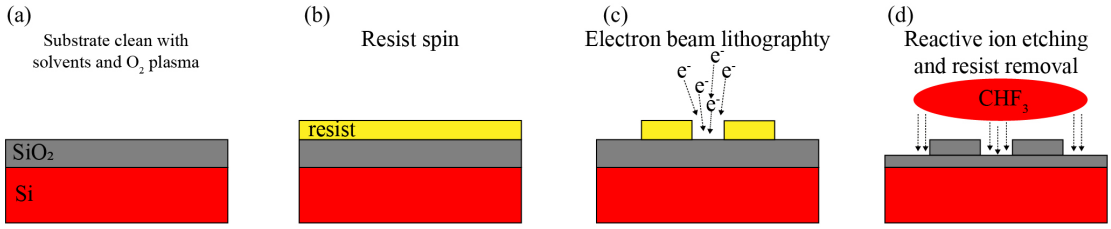

Fig. 5.4 Fabrication procedure for SiO_2 nano-pillars. **(a)** The thermally grown SiO_2/Si substrate is cleaned with acetone and IPA and ashed with an O_2 plasma. **(b)** A layer of resist is spin coated on top. **(c)** Electron beam lithography and development is used to define a pattern in the resist layer. **(d)** Reactive ion etching using CHF_3 transfers the pattern into the SiO_2 and the resist is removed with acetone.

5.3.2 GaP dimer nano-antenna fabrication

The GaP dimer nano-antennas, fabricated by a collaborator, are defined in a wafer of gallium phosphide purchased from UniversityWafers Inc. A similar cleaning procedure used as a first step for the fabrication of SiO_2 nano-pillars was repeated for this process as well. As the next step, a layer of 80 nm of SiO_2 was sputtered onto a diced and cleaned piece of the GaP wafer. Next, a chromium layer of 80 nm was evaporated on top of the SiO_2. Subsequently, a 50 nm thick negative tone resist (ma-N 2400.50) was spin coated onto the substrate. This was patterned into an array of GaP dimer nano-antennas with radii ranging from 150 nm to 300 nm using a 20 kV electron beam lithography system witha a 10 μm aperture. The unexposed resist was removed using the same developer as for the SiO_2 nano-pillar fabrication (ma-D 525), after which the substrate was rinsed in IPA and water. The chromium layer is then etched into a mask by immersing the substrate in a bath of Cr wet etchant (Sigma Aldrich)

for 30s. The SiO_2 is also patterned into a mask through the use of reactive ion etching with CHF_3 gas. The final step transfers the pattern into the GaP wafer with 12 sccm of Cl_2 gas and 30 sccm of Ar. The height of the resulting dimer nano-antennas was nominally 200 nm. The resist, chromium and SiO_2 masks were removed after a bath of buffered oxide etch for 5 minutes, which is a mixture of a buffering agent and hydrofluoric acid. The recipe used in reference [43] is the same as for the gallium phosphide dimer nano-antennas used in the work presented in chapter 6. A schematic illustration of the fabrication procedure is displayed in Fig. 5.5.

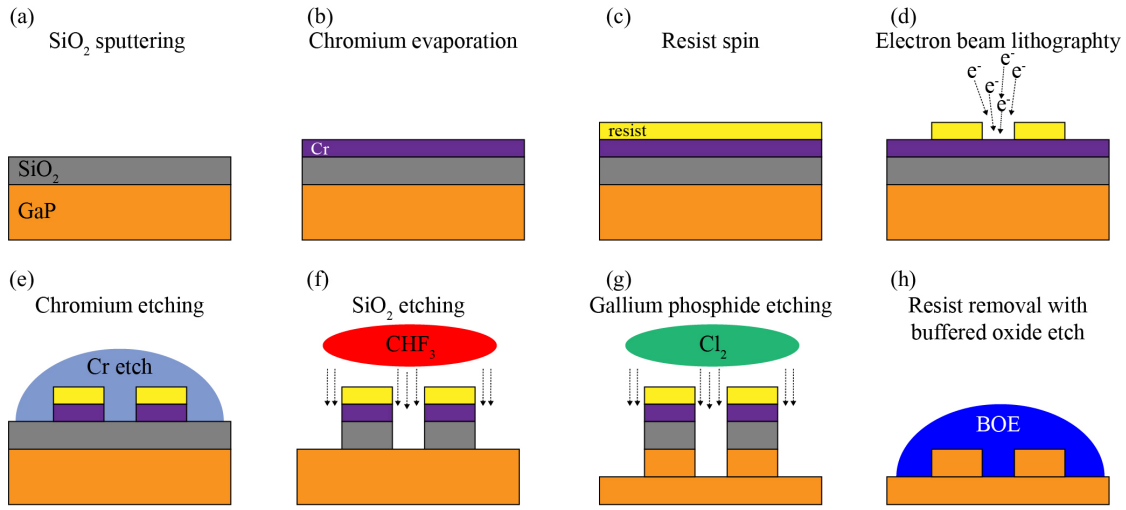

Fig. 5.5 Fabrication procedure for GaP dimer nano-antennas **(a)** An SiO_2 layer is sputtered onto a clean GaP wafer. **(b)** A Cr layer is evaporated onto the SiO_2. **(c)** A negative-tone resist is spin coated on top. **(d)** Electron beam lithography and development defines a pattern into the resist. **(e)** The chromium layer is etched into a mask using a Cr etchant. **(f)** Reactive ion etching transfers the pattern into the SiO_2 layer using CHF_3 gas. **(g)** RIE transfers the pattern into the GaP wafer using Cl_2 gas. **(h)** The masks of resist, Cr and SiO_2 were removed using a buffered oxide etch. Adapted from reference [43].

5.3.3 WS_2 nano-antenna fabrication

The fabrication procedure for WS_2 monomer and dimer nano-antennas, carried out by a collaborator, is performed after an exfoliation of WS_2 crystals onto a 290 nm SiO_2/Si substrate as described earlier in the section on mechanical exfoliation. Large flakes with recognizable crystal edges at 120° to each other were identified for the fabrication of the nano-structures and their thicknesses were measured with AFM. After a cleaning procedure in acetone and IPA baths for 5 minutes each, the samples were spin coated with positive ARP-9 resist (AllResist GmbH) at 3500 rpm for 60 s and baked at 180°C for 5 min yielding a thickness of 200 nm. Next, electron beam lithography with a 50 kV system yielding a beam current of 560 pA was employed to pattern the resist into circular and square patterns.

During the patterning stage of dimer nano-antenna fabrications, care was taken to align the axis connecting the two nano-pillars (dimer axis) either along the edge of the flake, i.e. along the zigzag or armchair axis, and at different angles with respect to these. Reactive ion etching was employed to transfer the resist patterns into the large area WS_2 flakes which were identified earlier based on their crystal axes. The etch was stopped when the etch depth matched the original thickness of the flake. The last step, carried out to remove the remaining resist after etching, included a bath in 1165 resist remover for 1 hour followed by a bath of acetone for 1 hour and a 5 minute rinse in IPA. The final step to remove organic residues and yet not etch the WS_2 crystal, was a 1 hour UV ozone treatment. The fabrication steps are shown schematically in Fig. 5.6(a)-(d).

Three different nano-pillar geometries were fabricated into both monomer and dimer nano-antennas by employing two different etching recipes to the two types of resist pattern mentioned above. Firstly, an anisotropic (physical) etch recipe with a gas mixture of CHF_3 (14.5 sccm) and SF_6 (12.5 sccm), a pressure of 0.039 mbar and a DC bias of 180 V was used to define circularly shaped nano-antennas with vertical sidewalls using the previously circular resist patterns, schematically illustrated in Fig. 5.6(e). The second type of recipe yielded a more isotropic (chemical) etch with a gas mixture of solely SF_6 (20 sccm), a pressure of 0.13 mbar and a DC bias of 50 V. Etching previously circular resist patterns yielded hexagonal nano-antennas due to the faster removal of WS_2 in the armchair crystal axis leaving a zigzag edge terminated structure which follows the symmetry of the WS_2 crystal. A schematic representation of this structure is shown in Fig. 5.6(f). The final geometry for the WS_2 monomer and dimer nano-antennas is square. This is a result of etching the square resist pattern with the isotropic recipe. This chemical etching recipe is initially expected to result in a diamond geometry with two 120° vertices and two 60° vertices as it will etch in the direction of exposed armchair axes. However, due to the faster etching of the sharp 60° angles which are oriented in the armchair axis, this ultimately led to 90° angles describing a square shaped nano-antenna, as shown schematically in Fig. 5.6(g). The hexagonal geometry and, in part, the square nano-antenna geometry are formed due to the relative stability of the zigzag axis and can therefore lead to atomically sharp vertices.

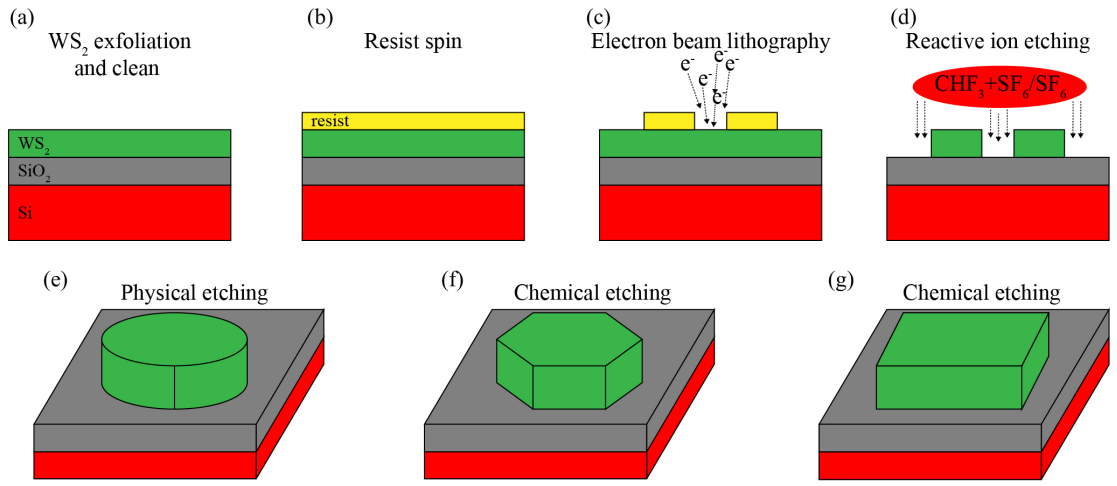

Fig. 5.6 Fabrication procedure for WS_2 nano-antennas. **(a)** Exfoliation of WS_2 thick crystals onto a SiO_2/Si substrate. **(b)** Resist is spun onto the substrate with exfoliated WS_2. **(c)** Electron beam lithography and development define a pattern into the resist layer. **(d)** Reactive ion etching using a mixture of CHF_3 and SF_6 gasses (physical etch) or solely SF_6 (chemical etch) to etch the resist pattern into the WS_2 crystals. The resist is subsequently removed. The different types of nano-antenna geometries available for fabrication using this procedure are shown in **(e)**:circular, **(f)**:hexagonal, **(g)**:square.

5.4 Photoluminescence measurements

The photoluminescence spectroscopy performed for the work presented in chapter 6 is carried out in home-built setups in several Sheffield laboratories. The first of these setups is central to all other measurements involving PL as this setup includes a Helium bath cryostat which holds the samples as well as the excitation and collection paths. For each subsequent measurement, the emitted light is fiber coupled to a setup which is either in a different portion of the lab or in a different lab altogether. The discussion of these setups will begin with this central setup and PL spectroscopy measurements. Subsequently, time resolved photoluminescence will be explored after which anti-bunching and coherence time measurement setups will be described.

5.4.1 μ-PL spectroscopy

The samples under study, yielding the results presented in chapter 6, were placed in a liquid helium bath cryostat (CRYO ANLAGENBAU GMBH) designed to contain samples at a temperature of 4.2K for prolonged periods of time. The liquid helium is periodically refilled as it evaporates through a return line which brings the helium gas to a compressor that can recycle it. An attocube basic measurement insert with a window for optical access and a cage system contains the samples under study and is inserted directly into the liquid helium from

the top of the bath cryostat. This insert is pumped to vacuum (<10^{-5} mbar) with an oil free pump and a low pressure helium exchange gas is added from a bladder before insertion into the cryostat. The samples are attached to a stack of three (x,y,z) attocube piezo positioners (ANP101) via silver paint to ensure heat transfer between the environment and the sample. As the sample is being inserted into the liquid helium bath, the positioners are grounded to avoid charge accumulation and discharge which may damage the piezo crystals. The cage also includes two lenses passing the excitation to an aspheric lens (NA = 0.64) which focuses the light onto the sample. The collected signal is returned through this same path. A schematic illustration of the sample insert is shown in Fig. 5.7(a). An optical breadboard containing the μ-PL setup shown in Fig. 5.7(b) is placed on top of the liquid helium bath cryostat using in-house fabricated pins to hold the beamsplitter of the setup shown in Fig. 5.7(b) above the sample insert window with a drilled hole to allow optical access between the breadboard and the insert and sample. The beampsplitters shown in Fig. 5.7(a) and (b) represent the same element.

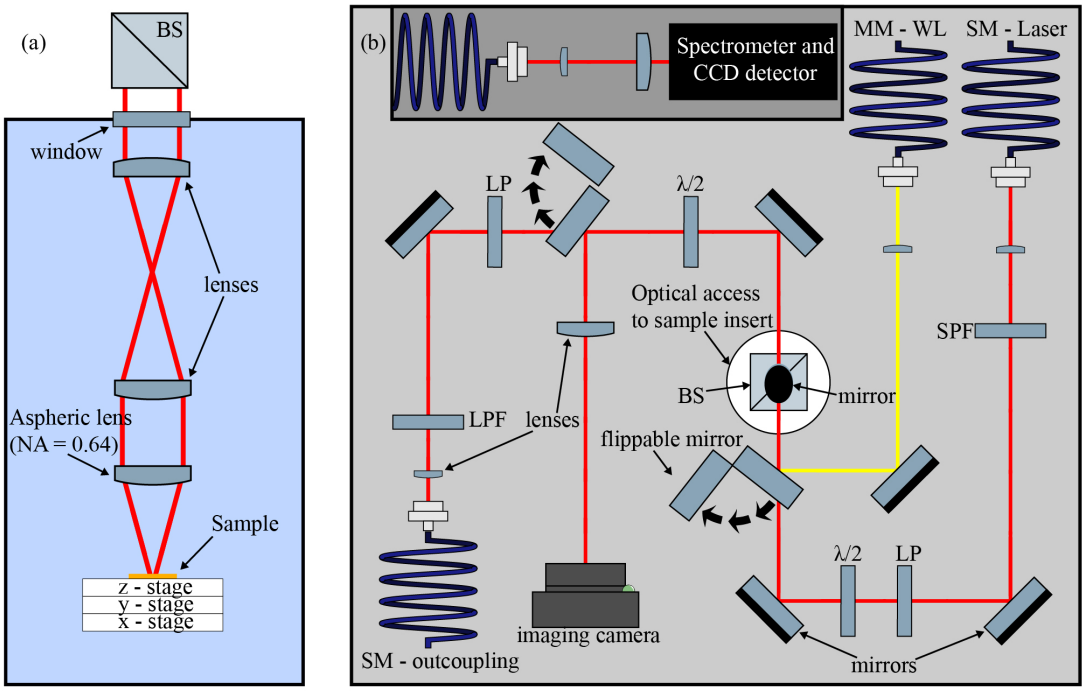

Fig. 5.7 **(a)** Schematic illustration of the attocube measurement insert in a liquid helium bath cryostat. **(b)** Schematic of the home-built setup placed on the bath cryostat and used for μ-Photoluminescence measurements. The inset shows an unattached portion of the setup where the outcoupled light from the μ-PL setup is coupled to a spectrometer and CCD.

Laser light is coupled through a single mode fiber (SM-Laser) and collimated before passing through a short pass filter (700 nm SPF) which cleans the excitation source. The

light is then passed through a thin film linear polarizer (LP) and half wave plate ($\lambda/2$). The half wave plate is mounted on a motorized rotation stage allowing the control of the linear polarization orientation of the excitation. The 50:50 beamsplitter (BS) directs light down into the insert to excite the sample. The emitted light from the sample is guided through the cage system in the sample insert and then passes straight through the beampslitter reflecting from a mirror placed above. This guides the light through another half wave plate and linear polarizer before being filtered by a long pass filter (700 nm/750 nm LPF). The second half wave plate is also mounted on a motorized rotation stage allowing the measurement of the polarization dependence of the emitted light. The long pass filter rejects the excitation laser and only allows the emitted light from the sample to be coupled to a single mode fiber for measurement. Another excitation path shown in yellow begins with a multi-mode fiber coupled white light source (MM-WL,Thorlabs SLS201L) and is sent to the BS using a mirror on a flip mount. This path is used to illuminate the sample so that it can be positioned to the area of interest during measurements. The image of the sample surface illuminated with white light is recorded via a CMOS camera (Thorlabs) through a flip mounted mirror in the detection path. This excitation and collection setup placed atop the liquid helium bath cryostat fiber couples light to be measured using other setups. For the spectroscopic analysis shown in chapter 6, the single mode fiber is coupled to a spectrometer and charge coupled device (CCD) from Priceton Instruments (Spectrometer: SP2750, CCD: PyLoN BR-eXcelon), as shown in the top inset in Fig. 5.7(b). The PL emitted from monolayer WSe_2, presented in the next chapter, was recorded with two spectrometer gratings (300 gr/mm and 1800 gr/mm) at a blaze wavelength of 750 nm. The fiber-coupled excitation lasers used for PL spectroscopy were two continuous wave (CW) diode lasers at 633 nm and 725 nm (Thorlabs) as well as a pulsed diode laser (PicoQuant) at 638 nm with a variable repetition rate from 5 to 80 MHz and a minimum pulse width of 90 ps. All experiments performed for WSe_2 single photon emitters were carried out at liquid helium temperatures unless otherwise stated. The only PL not recorded using this setup (Fig. 6.4(c) in chapter 6) used an analogous optical table mounted setup with stepper motors instead of piezo stages.

5.4.2 Time-correlated single photon counting

Time-correlated single photon counting (TCSPC) is one of the first techniques which provides information about the dynamics of the excitation and recombination process in a variety of emission sources including SPEs, Poissonian light sources or super-Poissonian sources. As the measured processes occur very quickly, the use of this technique has pushed the limits of the resolution of all components employed in these measurements. The final timing resolution is named the instrument response function (IRF) which is often measured as

a Gaussian peak appearing very soon after time zero. The width of this peak defines the overall timing resolution of the setup corresponding to the that of the component with the worst resolution. The time-correlated single photon counting electronics (Becker and Hickl) exhibit resolutions below 30 ps. The detectors used often show lower resolution, such as for avalanche photo-diodes (APDs) (below 50 ps), although there are some superconducting nano-wire single photon detectors with resolutions (less than 20 ps) which outpace even the electronics. The last element of any dynamics measurement which may limit the resolution is the pulse width of the excitation source. Pulsed diode lasers yield pulse widths below 100 ps which are often the largest source of limitation in the timing resolution. Femtosecond pulse widths are also available for mode locked Ti:Sapphire lasers which find some use in TCSPC, however, they are limited by their often set repetition rate which cannot be easily changed. The setup discussed below is limited by the use of a pulsed diode laser for excitation with pulse widths of no less than 90 ps.

Measuring the dynamics of a quantum transition, as will be described in chapter 6, requires an understanding of its excited state population and the rate of decay to the ground state. If a quantum emitter is modeled as a two-level system, then the decay rate or change in the population of the excited state can be written as the following rate equation:

$$\frac{dn_1}{dt} = n_1(t)(\gamma_r + \gamma_{nr}), \tag{5.1}$$

where $n_1(t)$ is the population of the excited state, γ_r is the radiative decay rate and γ_{nr} is the non-radiative decay rate, which takes into account all non-radiative processes. The solution to this differential equation is as follows:

$$n_1(t) = Ae^{-t/\tau}, \tag{5.2}$$

where A is the population at time zero after the excitation pulse and $\tau = (\gamma_r + \gamma_{nr})^{-1}$ is the measured lifetime which is a combination of the radiative and non-radiative decay time. The measured dynamics curve can thus be fit with this exponential decay solution to extract a lifetime value. However, in practice the decay of the PL from the two-level system will yield results which can be fit with a convolution of an exponential decay function and a gaussian function which corresponds to the measurement setup IRF. Another possibility is that the dynamics exhibits two exponential decay components which force the use of a solution as follows:

$$n_1(t) = Ae^{-t/\tau_1} + Be^{-t/\tau_2}, \tag{5.3}$$

where the new values to be extracted from fitting (τ_1 and τ_2) correspond to the lifetimes of two separate processes which may each exhibit a radiative and non-radiative component. An example of this is the room temperature decay of the neutral exciton resonance in monolayer WSe_2 at high excitation power densities. A long decay component corresponds to the lifetime of the free exciton before recombining either radiatively or non-radiatively. A fast decay component corresponds to exciton-exciton annihilation (Auger recombination) processes which are entirely non-radiative [175].

In order to measure the dynamics of single photon emission in WSe_2 as shown in chapter 6, the signal collected from the setup in Fig. 5.7(b) is guided through the spectrometer shown in the inset and an exit slit is used to spectrally filter the PL signal. As the light is passing through the spectrometer, the grating disperses the incident light in space. A mirror inside the spectrometer can send the dispersed light to an exit slit in the side of the spectrometer where the width of the slit allows only a portion of the spectrum to pass and leave the spectrometer, as schematically depicted in Fig. 5.8(a). As the spectrum can be spread far wider than the width of the slit, one can select a very small spectral window (1-2 nm) to leave the spectrometer. This method of spectral filtering was used for the measurement of the single photon emission dynamics shown in chapter 6. The light leaving the spectrometer is directed to a collimating lens and is subsequently coupled to a multi-mode fiber which is attached to an avalanche photo-diode (IDQuantique, id100). This APD creates a voltage pulse every time a photon is detected. The collection path used for the measurement of the dynamics in the next chapter after spectrally filtering the light through the spectrometer is shown in Fig. 5.8(b). The laser excitation used for the dynamics results in chapter 6 is the pulsed diode laser mentioned in the discussion of the μ-PL spectroscopy setup.

A brief description of the time-correlated single photon counting electronics will give a brief idea as to how the dynamics results are gathered and plotted. A schematic representation of the TCSPC electronics are shown in Fig. 5.8(c). Starting from the left side, a square wave reference signal from the excitation laser is sent to one constant fraction discriminator (CFD), often named the SYNC, and a signal from the APD is sent to the other once a photon has been detected. These discriminators use a unique method of interfering the signal with itself to yield a sinusoidally shaped signal which crosses zero at a constant time from the beginning of the pulse. The pulse is recognized as measured by the CFD only once this zero-point is crossed thereby eliminating a large source of timing jitter induced by the detectors before this method was implemented. For better operation of the electronics, the threshold of acceptable

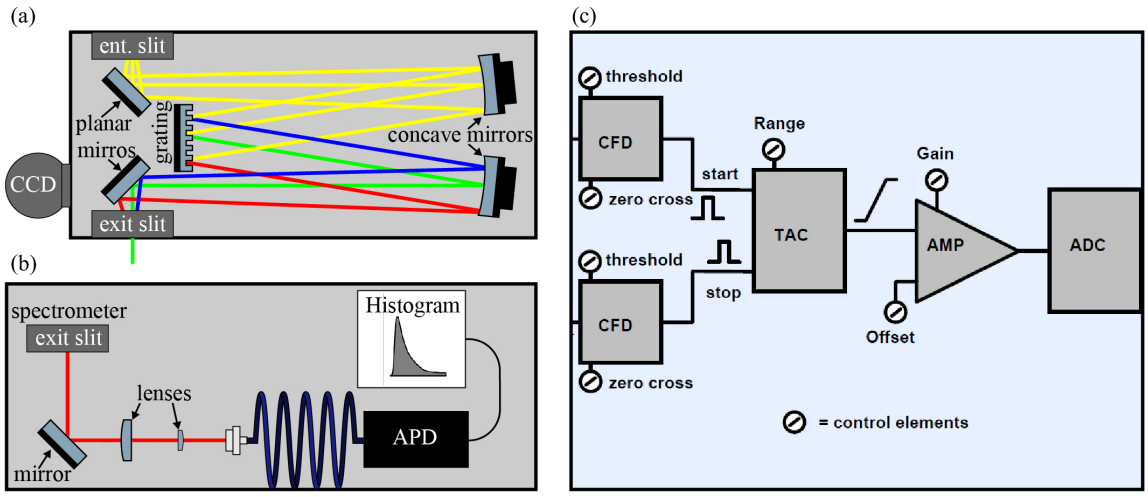

Fig. 5.8 **(a)** Schematic representation of the spectrometer used to spectrally filter single photon emission so that its dynamics can be measured **(b)** Schematic illustration of the coupling of the spectrally filtered light from the spectrometer to an APD which is attached to a TCSPC card and records the PL dynamics. Inset adapted from reference [176] shows an example of the time-resolved trace of the photoluminescence which can be used to extract the rise and decay time of single photon emission. **(c)** Schematic of the TCSPC card electronics components. Adapted from reference [176].

pulse amplitudes and the zero-crossing level can be adjusted in the CFD. Next, the two discriminators pass their signals to the time to amplitude converter (TAC). This resembles a capacitor which begins to accumulate a voltage upon receiving a start pulse from the detector after passing the CFD. The accumulation is stopped once a reference pulse from the SYNC is received. The resulting voltage corresponds to a time interval between the detection of a photon and the reference pulse after the one which has excited the emitter. This arrangement of start and stop pulses is used to reduce the deadtime of the TCSPC electronics which for most measured emission sources would yield many start pulses but very few stop pulses. In the reverse configuration, the start pulse from the detection of a photon will almost always be quickly followed by a stop pulse. Since the repetition rate of the laser does not vary over the time of the measurement, the measured time interval can be subtracted from the time between excitation pulses. Before this, however, the measured time interval leaves the TAC as a voltage which passes through a gain amplifier (AMP) which can select a portion of the range set in the TAC in order to provide more resolution across a smaller time scale. Once this process is complete, the voltage is passed to an analog to digital converter (ADC) and recorded into a time channel after subtracting from the time interval between excitation puleses yielding a time of emission after excitation. The results are recorded in a number of channels yielding a histogram of the statistics of many excitation and emission cycles which collectively yield a function which can be fit and a lifetime value extracted.

5.4.3 Hanbury Brown-Twiss setup

As discussed in chapter 3, ideal single photon sources can only be described by a quantum mechanic approach which yields only one photon per excitation cycle. No realistic system will be ideal, however, so a hope for quantum computing and quantum communication applications is that at least no more than one photon will be emitted, i.e. a high single photon purity. In order to test a new light source believed to be single photon in nature, a Hanbury Brown and Twiss (HBT) experiment was set up in 1956 [81]. A schematic illustration of the setup used for the results shown in chapter 6 is displayed in Fig. 5.9(a). Once the emission is spectrally filtered as before, the light is coupled to a 50:50 beamsplitter fiber (BS fiber) which splits the incoming emission into two pathways leading to two single photon detectors. For these measurements, superconducting nano-wire single photon detectors (SNSPDs, Single Quantum) were used due to their low noise and the lack of any afterglow effect which was observed with silicon APDs. The time of arrival of photons was correlated and each pair of detection events in the SNSPDs were placed into a channel based on the difference in their detection time. The time between detection events was measured using a start and stop pulse from the two single photon detectors together with the TCSPC electronics described above. For the measurements shown in chapter 6, the single photon source in WSe_2 was excited with a 725 nm CW diode (Thorlabs).

As discussed in chapter 3, single photon emitters cannot produce two photons simultaneously and therefore the single photon can only be recorded at one detector. This suggests that the number of double detection events for a time difference of zero (simultaneous detection) will be zero for an ideal SPE or as close to it as possible for a realistic one. The middle figure in the inset of Fig. 5.9(a) represents the expected coincidence counts trace after many detection events to provide enough statistics for reliable data. If the source was ideally coherent, then a the left plot in the inset of Fig. 5.9(a) would be expected. Finally if the light source is bunched, as in thermal light sources, the expected trace would resemble the right figure of the inset in Fig. 5.9(a).

Using different excitation sources for single photon emission may yield different results. If the excitation is pulsed, an anti-bunched result may resemble Fig. 5.9(b), yielding peaks at regular intervals corresponding to the time interval set by the repetition rate of the laser. In this case, the peak at zero time between start and stop pulses should not be present for an ideal SPE. For a continuous wave excitation, the anti-bunching measurement should yield a plot resembling Fig. 5.9(c) after sufficient time for accumulation of statistics. The minimum at delay time $\tau = 0$ must be below a value of 0.5 after correcting the double coincidence counts for dark counts, as described in reference [23], for the emitter to be judged single photon in nature.

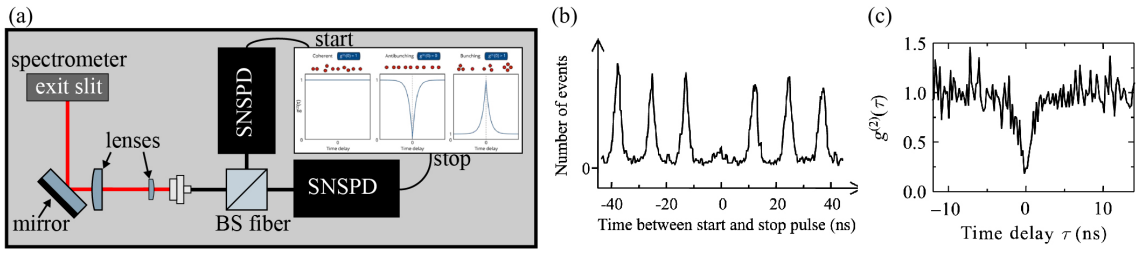

Fig. 5.9 **(a)** Schematic illustration of the coupling of the spectrally filtered light from the spectrometer to an HBT setup consisting of a beamsplitting fiber which splits the light into two paths which are coupled to SNSPDs. The correlation of the detection events in the two detectors will lead to either coherent light, anti-bunched light or bunched light as shown in the inset. Inset adapted from reference [177]. **(b)** Exemplary representation of the $g^{(2)}(\tau)$ function for a single photon source excited by a pulsed laser. Adapted from reference [83]. **(c)** Example of the $g^{(2)}(\tau)$ function for a single photon source excited by a continuous wave laser. Adapted from reference [83].

This HBT experiment provides a measurement of the second order correlation function $g^{(2)}(\tau)$, often used as the name of the measurement, which can defined as:

$$g^{(2)}(\tau) = \frac{E^*(t)E^*(t+\tau)E(t)E(t+\tau)}{\langle|E(t)|^2\rangle\langle|E(t+\tau)|^2\rangle} \tag{5.4}$$

where $E(t)$ is the electric fields describing the detected photons and τ is the delay between their arrival time. For classical electric fields this is simply a correlation of the intensities:

$$g^{(2)}(\tau) = \frac{\langle I(t)I(t+\tau)\rangle}{\langle I(t)\rangle^2} \tag{5.5}$$

where $I(t)$ is the intensity of the detected light. For quantum mechanical fields as in the case of single photon sources, the limit at $g^{(2)}(0)$ can be analytically computed to be:

$$g^{(2)}(0) = \frac{\langle n(n-1)\rangle}{\langle n\rangle^2} \tag{5.6}$$

where n is the observable photon number.

5.4.4 Coherence time interferometry

A long coherence time of single photon emitters guaratees that consecutive photons will be in phase and coherent for a long time. This is very important for applications which require single photon emission at a singular wavelength or similar phases. Coherent single photons

may also be indistinguishable which is a requirement for some applications such as quantum key distribution. An indistinguishability measurement takes into account all properties of a single photons including energy, phase, position and polarization state. This is tested through a Hong-ou-Mandel experiment which interferes single photons at different time delays and measures the double coincidence counts on two detectors similar to the HBT measurement. In this case, two indistinguishable single photons incident on two separate sides of a 50:50 beamsplitter would exit together, therefore, leading to zero simultaneous coincidence counts when the two photons are overlapped in time.

However, for these measurements, only the coherence time of WSe_2 SPEs was recorded using a Mach-Zehnder interferometer as shown in Fig. 5.10. Once the single photon emission is spectrally filtered as discussed above it is fiber coupled (SM Fiber) and sent to the left side of the setup shown in Fig. 5.10. The emission passes a 50:50 beamsplitter (BS) and is sent down two paths. The first path allows the light to propagate in free space passing a retro-reflector mounted on a motorized delay stage. This stage is used to change the length of the path and therefore the time for the light to traverse it. After the retro-reflector, the single photons are interfered with those passing down the other arm onto another 50:50 beampslitter. The other path includes a fiber phase shifter (PS). As a voltage is applied across a length of fiber, the phase of the single photons passing through is quickly shifted before interfering with the delayed photons in the other arm of the interferometer. The single photon emission passing through the entire interferometer is fiber coupled to an APD (Excelitas) where interference fringes are visible due to the varying phase of one arm. As the delay stage brings the two paths to equal lengths, the interference fringes become larger with higher maxima (I_{max}) and lower minima (I_{min}). Therefore the fringe contrast (v) yields a measure of the level of coherence. The fringe contrast is calculated as follows:

$$v = \frac{I_{max} - I_{min}}{I_{max} + I_{min}} \tag{5.7}$$

This value was computed at different positions of the delay stage yielding smaller interference fringes as the path lenght difference between the two arms was increased. The fringe contrast can be shown to be proportional to a time-averaged, coarse grained first order correlation function ($g^{(1)}(\tau)$). This can be written as follows [178]:

$$v = (1-\varepsilon)\frac{|g^{(1)}(\tau)|}{g^{(1)}(0)} \tag{5.8}$$

where $(1-\varepsilon)$ is the maximum resolvable fringe contrast of the interferometer at the energy of the emitter. The time resolution (≈0.1 ps) here is defined by the steps of the delay stage. The shape of the decay of the coherence with time can provide insight into de-phasing processes. This is one method used in chapter 6 to provide insight into the dominant decoherence mechanism in WSe_2 SPEs. The laser excitation used for the power dependent measurements in chapter 6 is a CW diode laser (Thorlabs) at 633 nm. For the quasi-resonant measurement presented in the same chapter a CW diode laser (Thorlabs) at 725 nm was used.

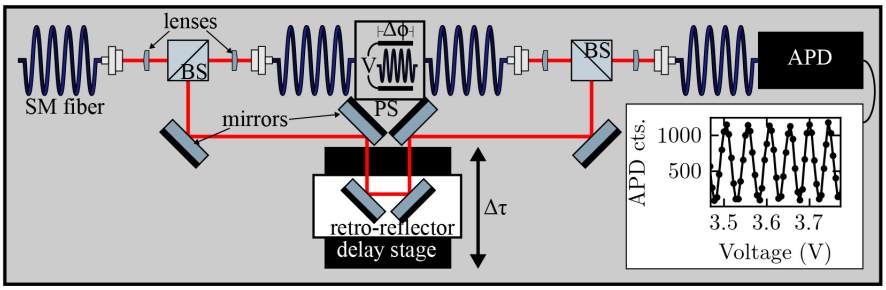

Fig. 5.10 Schematic illustration of the Mach-Zehnder interferometer used for measurement of the coherence of WSe_2 single photon emitters. The resulting interference fringes, shown in the inset, are used to extract a first order correlation function ($g^{(1)}(\tau)$) and measure the coherence time.

5.5 Dark field spectroscopy

Dark field spectroscopy is a powerful tool to characterize nano-scale resonators such as monomer and dimer nano-antennas. The scattering cross section which, as discussed in chapter 4, results from an incoherent sum of contributions from electric and magnetic dipole and quadrupole moment resonances among other higher order contributions. Therefore, the measurement of the scattering cross section from such nano-resonators allows one to extract information about the Mie resonances inside the structures. The dark field configuration illuminates the sample at large angles to the normal and only collects light which is scattered at small angles. This is often performed in transmission, as shown in Fig. 5.11(a), where a light stop spatially filters the illumination beam profile to an annulus which is subsequently focused onto the sample using a condenser lens. This illuminates the sample at high angles to the normal. Scattered light collected at these large angles is guided to an iris diaphragm and blocked inside the objective. The light scatterd at low angles to the normal is guided through the detection path.

In the work shown in chapter 7, a Nikon LV150N commercial microscope with a home-built fiber coupled output, shown schematically in Fig. 5.11(b) was utilized to perform dark field spectroscopy. Incident illumination from a tungsten halogen lamp is guided to a circular

beam blocker with a diameter smaller than that of the beam. This forces the beam profile to to be of an annular shape once again. The illumination is guided through a 50:50 beamsplitter cube down to a dark field objective (50x Nikon, 0.8 NA) and subsequently the sample plane. The annular beam profile only illuminates the sample at very high angles to the normal. Reflected light passes through the objective and beamsplitter once more. The high angle scattered light is blocked by an aperture while the light scattered at small angles to the normal is then focused onto a fiber coupler. Due to the small diameter of the multi-mode fiber core (60 μm) used to couple light to a Princeton Instruments spectrometer and CCD (the same as those used for PL measurements), only light reflected from the sample at very small angles to the normal is collected. Another reason for the choice of a small fiber core diameter was the ability to collect scattered light from only one nano-structure. The measurements of dark field scattering spectra for WS_2 monomer and dimer nano-antennas presented in chapter 7 were all carried out in room temperature and ambient conditions.

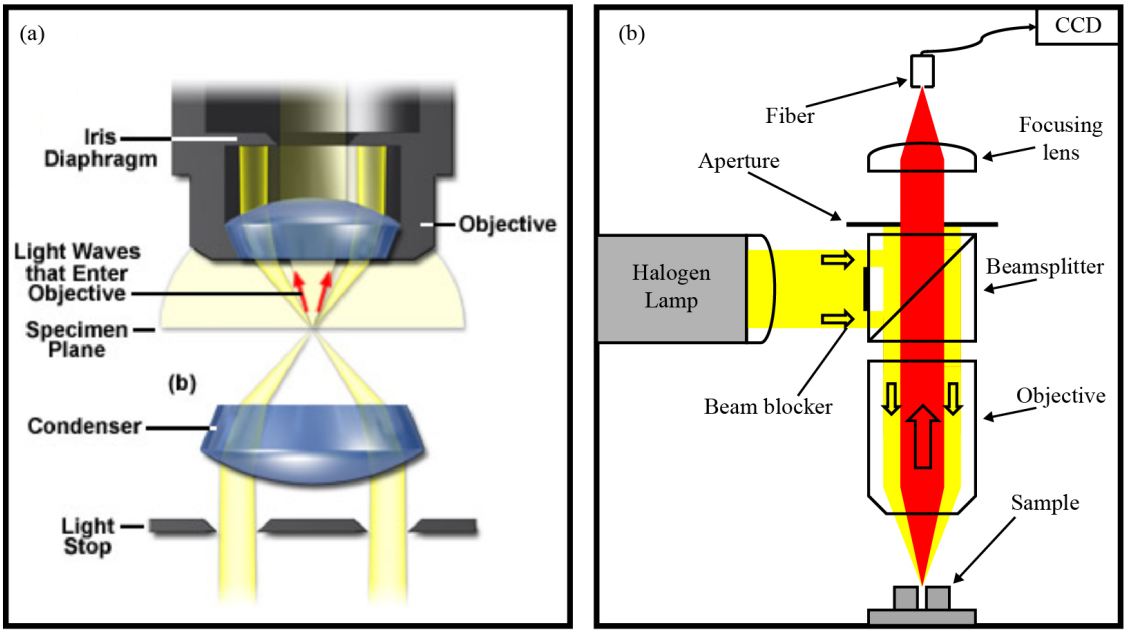

Fig. 5.11 **(a)** Schematic illustration of a transmission dark field spectroscopy setup with a separate condenser lens and objective. Adapted from Zeiss education in microscopy and digital imaging website. **(b)** Schematic illustration of the commercial microscope with a dark field objective and a fiber outcoupling used in the dark field spectroscopy experiments.

5.6 Second harmonic generation

As discussed in chapter 4, second harmonic generation (SHG) is an interesting non-linear light application which can benefit from coupling to anapole and higher order anapole resonances in Mie resonators. The work presented in chapter 7 tests this approach and identifies interesting properties of SHG signal from WS_2 dimer nano-antennas. The schematic representation of the home-built setup used for these measurements is shown in Fig. 5.12. The nano-antenna samples were excited with a Ti:Sapphire fs-pulsed laser (Spectra-Physics) tuned to the anapole resonance of each structure under study. The collimated laser light was guided to the measurement setup via a free space path. A manually rotating neutral density filter wheel (ND) was used to attenuate the laser power so as not to burn the nano-antenna structures. A 750 nm long pass filter (LPF) was used to clean the laser wavelength which was tuned from 800 nm to 850 nm. Next, the excitation was linearly polarized (LP) and guided to a dichroic mirror (DM) and, after passing a half wave plate ($\lambda/2$) mounted on a motorized stage, was focused onto the sample by a 100x Mitutoyo objective lens (0.7 NA) exciting a single nano-structure.

The second harmonic generated signal emitted from the sample was then reflected by the dichroic mirror towards the collection path which includes three short pass filters (SPF, 450 nm, 550 nm, 750 nm) to clean the collected light so that only SHG signal passes through to be coupled to a multi-mode fiber. The fiber was briefly coupled to a Princeton Instruments spectrometer and CCD to check the spectrum of the SHG signal and then attached to an APD (IDQuantique, id100). A few spectra of the SHG signal were also recorded with the CCD. The APD was used to record integrated SHG signal from different nano-antenna structures and compare monomers to dimers as well as perform excitation power dependent measurements and polarization dependent measurements. Excitation powers of no more than 3 mW average power were used as higher intensities damaged some nano-structures.

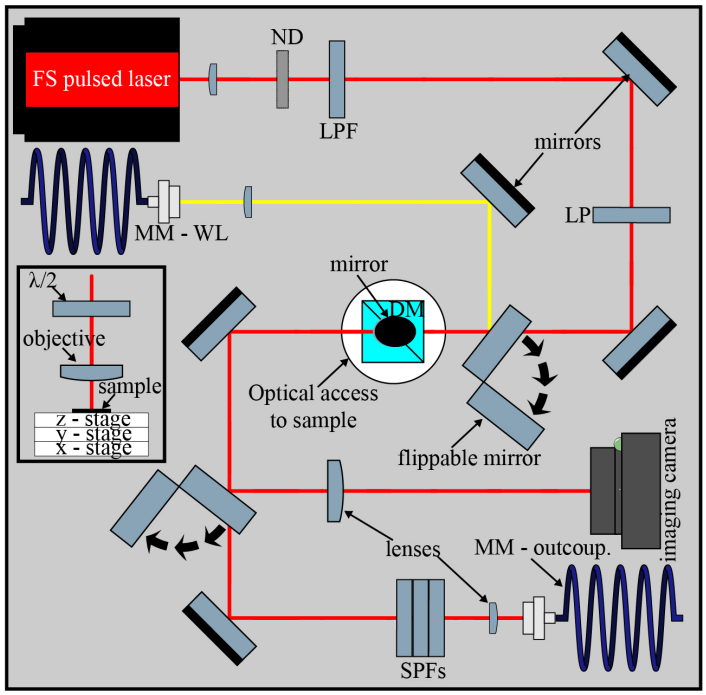

Fig. 5.12 Schematic illustration of the home-built setup used to perform second harmonic generation experiments. It is very similar to the μ-PL setup, however, it includes a dichroic mirror instead of a 50:50 beamsplitter. Also this setup was placed on an optical bench instead of onto a bath cryostat as the measurements were carried out in ambient conditions.

5.7 Finite-difference time-domain simulations

Finite-difference time-domain simulations (FDTD), also known as Yee's method, were performed in order to simulate different parameters of SiO_2 nano-pillars, GaP dimer nano-antennas and WS_2 monomer and dimer nano-antennas in the work presented in chapters 6, 7 and 8. The software used for the simulations in these chapters is from Lumerical Inc.

This method of numerically solving differential equations allows one to solve Maxwell's equations for an arbitrary geometry with arbitrary refractive indices and model the photonic action of nano-resonators. As a finite-difference method, a 3D spatial grid is defined inside the volume of the geometry of each simulation. A so-called Yee lattice is employed to discretize Maxwell's equations in space. The electric and magnetic fields inside the volume of any Yee cell, shown in Fig. 5.13 are calculated at staggered positions to each other with a difference in position of half of the cell length. The time dependence of Maxwell's equations are also discretized using the central difference approximations. At the beginning of the simulation, light is usually injected from a source and time is allowed to evolve, often limited to 1000 fs. At each half step of time the electric or magnetic field is evaluated at every point within the Yee lattice. In the next half step in time, the other field is computed. As this

numerical simulation method is in the time-domain, light is collected as an amplitude of a wave with time and subsequently Fourier transformed to give spectral information.

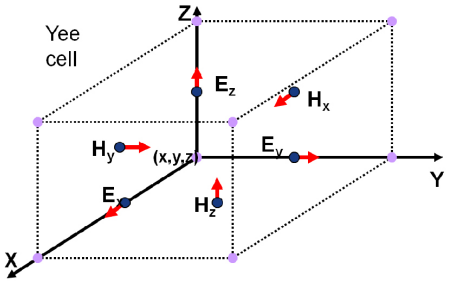

Fig. 5.13 Representation of the Yee cell used to discretize space in order to perform finite-difference time-domain simulations with staggered electric and field calculation points. These are also staggered in time which is also discretized. Adapted from Lumerical webpage.

In the work shown in chapters 6 through 8, FDTD simulations of the scattering cross section, the spatial distribution of the electric field intensity, the confined electric energy, the Purcell factor and the collection efficiency were performed for different geometries. The refractive index of SiO_2 was retrieved from a library of materials in the simulation software. The refractive index of WS_2 was extracted from reference [46] and that of GaP was taken from reference [179].

5.7.1 Scattering cross section

The first and most basic simulations of the scattering cross section (σ_{scat}) were performed to be compared with dark field spectra from fabricated monomer and dimer nano-antennas or to model whether a structure may host photonic resonances. The geometry of a structure under study, for example a WS_2 dimer nano-antenna, is shown in Fig. 5.14(a) and (b). Two hexagonal monomer nano-antennas in close proximity are defined with a height and radius on a substrate of SiO_2. The simulation region is defined surrounding this structure yet it is wide enough to allow the fields both surrounding the dimer and into the SiO_2 to propagate without being truncated unrealistically. The light source used to illuminate the structure is a total-field scattered-field (TFSF) source which introduces a plane wave in the near field of the nano-antenna structure and also simulates the far-field scattered light outside of the region defined by the white rectangle in Fig. 5.14(a). The excitation is polarized along the blue double arrow and propagates in the direction of the pink arrow. As the incident plane wave scatters from the structure, it leaves the near field region scattering to the far-field where there is a monitor placed above the structure used to collect the intensity of the light scattered in this direction. The choice of TFSF source and scattering monitor position is used

to emulate dark field spectroscopy. As the scattering monitor is placed above the injected wave, it does not collect any of the incident illumination as this is contained to the near field region inside the white rectangle in Fig. 5.14(a). The scattering monitor therefore only collects the scattered light which propagates upward similar to reflected light collected in the dark field spectroscopy setup described in the previous section. The polarization of the incident wave was set depending on the comparative experiment performed with dark field spectroscopy. If unpolarized light was simulated, then an incoherent sum of the results for perpendicular excitation polarizations was used to emulate this.

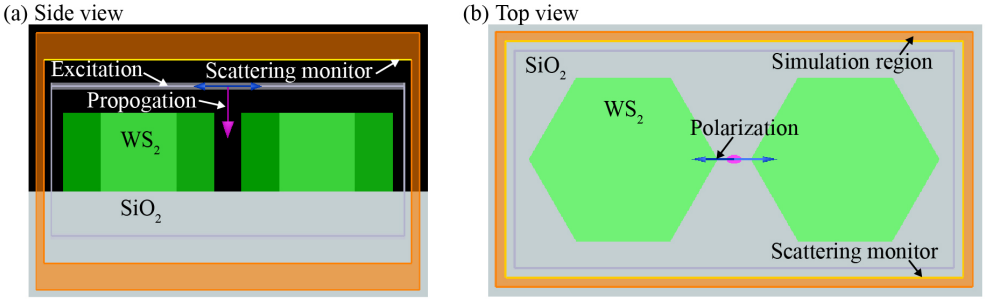

Fig. 5.14 Top **(a)** and side **(b)** view of a schematic illustration of the geometry of a hexagonal WS_2 dimer nano-antenna for the simulation of the scattering cross section. The scattering cross section is recorded by collecting scattered light in the far-field above the excitation source.

5.7.2 Spatial distribution of electric and magnetic field intensities

The results from the second type of simulation performed specifically for the spatial distribution of the electric field intensity are presented in chapter 6 and 8. Spatial distributions of the magnetic field intensity are presented in chapter 7. The geometry of an exemplary WS_2 dimer nano-antenna with a very small gap placed on a SiO_2 substrate is defined in the geometry shown in Fig. 5.15(a) and (b). GaP dimers and SiO_2 nano-antennas were simulated similarly with a change of substrate to GaP for those dimers. The light from the same TFSF source is injected from above the structure propagating parallel to the normal towards the nano-antennas. The polarization is set parallel to the dimer axis to illuminate the dimer mode or perpendicular to it for the study of a dimer anapole mode. For this simulation the scattered fields are not interesting, therefore, all results are recorded within the near-field region. This is where the monitors used to record the electric or magnetic field distributions are positioned. One monitor is set as a vertical cross section through the middle of the structure along the dimer axis. Another is set as a plane 0.5 nm above the top surface of the nano-antenna in order to understand the electric field intensity at a position where single photon emitters might be placed. The electric field intensities are calculated as the square of the electric field

in the positions where the monitors collect data divided by the fields due to a plane wave propagating in free space ($E_{int} = (|E|/|E_0|)^2$). For some of the figures presented in chapter 6 and 8, only the electric field at a single point near the inner vertex of the dimer is recorded. In this case, the monitor is reduced to a single point in the dimer mode hotspot.

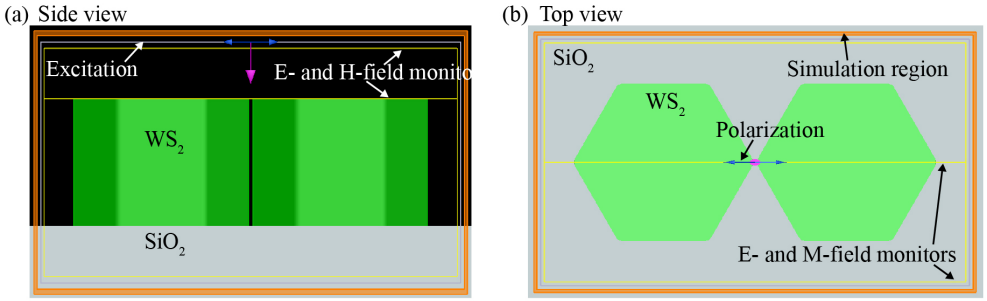

Fig. 5.15 Top **(a)** and side **(b)** view of a schematic illustration of the geometry of a hexagonal WS_2 dimer nano-antenna for simulations of the spatial distribution of the electric and magnetic field intensities. The electric and magnetic fields are recorded in a plane 0.5 nm from the top surface of the nano-antenna and as a vertical cross-sectional cut through the middle of the dimer.

5.7.3 Confined electric energy

Another simulation performed on monomer and dimer nano-antennas is the calculation of the confined electric energy inside the structure. For this a similar geometry, displayed in Fig. 5.16(a) and (b), to the previously shown is employed with the only difference being in the monitors collecting the light and the polarization of the incident illumination. The monitor recording the electric and magnetic field values is placed at the midpoint of the nano-antenna height. Firstly, the spatial distribution of the electric and magnetic field intensities were used to identify the characteristic pattern of an anapole mode as discussed in chapter 4. Next, the electric energy ($W_E^{(S)}$) was calculated by integrating the electric field intensity over the monitor surface on the inside of the nano-antenna geometry [43]:

$$W_E^{(S)} = \frac{n^2}{2} \int \int ||E(\mathbf{r}, \lambda)||^2 dS, \tag{5.9}$$

where n is the refractive index of the resonator and S is the surface defined by the plane of the simulated monitor inside the nano-antenna geometry. The integration was carried out by applying a filter to the electric field intensities which set all values outside of the nano-antenna geometry to zero and integrated over the entire monitor surface. As discussed in chapter 4, an anapole resonance confines the incident energy and therefore yields a minimum in scattering.

This simulation, however, yields a peak for the electric energy at the anapole resonance. This provides another method of identifying an anapole resonance.

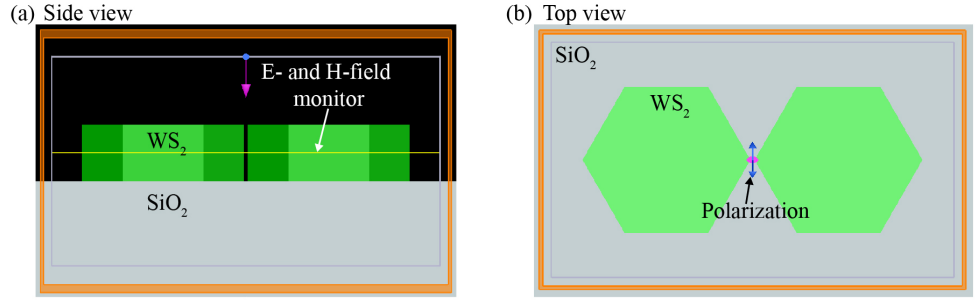

Fig. 5.16 Top **(a)** and side **(b)** view of a schematic illustration of the geometry of a hexagonal WS_2 dimer nano-antenna for simulations of the confined electric energy inside the structure. The electric field intensity is simulated at a cross-sectional surface at the midpoint of the nano-antenna height and subsequently integrated only over the inside of the dimer structure to obtain the confined electric energy.

Next, a simulation of the second harmonic generation enhancement can be extracted from the electric energy. As SHG is a second-order non-linear process, it is proportional to the electric energy squared ($|W_E^{(S)}|^2$), therefore, a square of the confined energy will be proportional to the SHG signal. As the anapole resonance enhances the SHG signal, confirmed by previous reports [47], the SHG enhancement factor can be calculated when comparing the signals from two structures or when comparing a nano-antenna to a bulk crystal. For dimer nano-antennas, a polarization dependence of the enhancement is demonstrated, therefore, changing the incident polarization in the simulation can model this dependence. This can be achieved by integrating the simulated electric energy squared ($|W_E^{(S)}|^2$) over the wavelength range of the excitation laser used in experiments to provide a comparison to measured results.

5.7.4 Purcell enhancement

As this thesis heavily focuses on single photon emission, the Purcell factor for an ideal dipole placed at different positions along the top surface of a WS_2 or GaP dimer nano-antenna as well as a SiO_2 nano-pillar was simulated. An example geometry including a WS_2 dimer nano-antenna is shown in Fig. 5.17(a) and (b). The excitation source for this simulation is an electric dipole positioned 0.5 nm from the top surface of the structure with a polarization along the dimer axis at different positions on the same axis. The maximum Purcell factor found for most dimer nano-antennas was calculated in to be in the electric field hotspots identified using the simulation of the spatial distribution of the electric field. The precise

position of the dipole with respect to the nano-structure and the discretized spacial mesh is shown in the side and top view of Fig. 5.17(c).

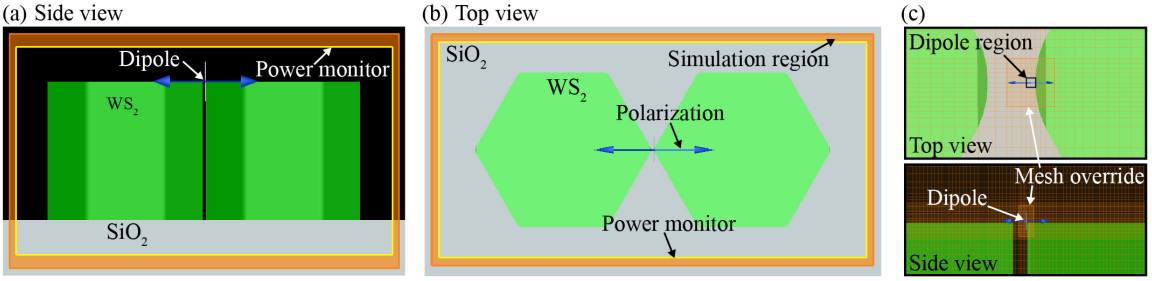

Fig. 5.17 Top **(a)** and side **(b)** view of a schematic illustration of the geometry of a hexagonal WS_2 dimer nano-antenna used in simulations of the Purcell factor for a dipole placed 0.5 nm above the top inside vertex. The position of the dipole source is better defined in the close-up views in **(c)**. The use of a vertex radius of curvature is also shown in this figure. The radiated power away from the structure is recorded for a dipole placed onto the dimer nano-antenna and divided by the power radiated from the dipole placed at a surface of SiO_2 to yield the Purcell factor.

The dipole source emits light from a small dipole region shown in the top view of Fig. 5.17(c). As this dipole region is not a single point, the simulations may not precisely simulate a point source. Also, the simulated emission energy of the dipole may induce large errors in calculations with very fine spatial discretization (Mesh override). The correct approach to simulate the Purcell factor is usually to compute the Green's function at the position of the dipole and divide the imaginary part for a dipole placed on the nano-antenna structure by the results from a simulation with the dipole placed in vacuum or onto a substrate such as SiO_2 or GaP. However, as the mesh required for these simulations is particularly fine (0.25 nm Yee cells), this approach yields large errors due to the inability of the simulation software to properly simulate the ideal dipole source. Therefore, another approach is used to find the Purcell factor. This requires the calculation of the radiated power from the dipole and comparing this quantity for a dipole placed onto the nano-antenna structure to a dipole in free space or onto a substrate as mentioned above.

Beginning from an undriven harmonic oscillator, used to model spontaneous decay in a two-level system, the radiative rate enhancement due to an inhomogeneous photonic environment can be written as follows [165]:

$$\frac{\gamma}{\gamma_0} = 1 + q_i \frac{6\pi\varepsilon_0}{|\mu_0|^2} \frac{1}{k^3} Im[\mu_0^* \cdot \mathbf{E}_s(\mathbf{r}_0)], \tag{5.10}$$

where q_i is the quantum efficiency of the emitter, μ_0 is the intrinsic dipole moment of the two-level system and $\mathbf{E}_s$ is the secondary field emitted from the dipole and acting as a driving

force on the same emitter. This very closely resembles the equation derived from Fermi's golden rule using Green's functions. Alternatively, one can calculate the energy dissipation as a result of radiation from the system due to the dipole emitter using Poynting's theorem in both a free space environment as well as an inhomogeneous photonic environment, such as a nano-antenna. The relative change in the rate of energy dissapation between these two environments (P/P_0) can be written as follows [165]:

$$\frac{P}{P_0} = 1 + \frac{6\pi\varepsilon_0\varepsilon}{|\mu|^2}\frac{1}{k^3}Im[\mu^* \cdot \mathbf{E}_s(\mathbf{r}_0)]. \tag{5.11}$$

The resemblance between the two solution to the undriven harmonic oscillator problem in different environments suggests that they may be very closely related. In fact it turns out that if $q_i = 1$, these equations would be identical ($\gamma/\gamma_0 = P/P_0$) [165]. Therefore, if the quantum efficiency of the two-level emitter is unity, the Purcell factor (change in radiative recombination rate) can be extracted simply from the change in the rate of energy dissipation from the system for the two different environments. Since the simulation software can only emulate an ideal dipole emitter ($q_i = 1$), the Purcell factor is very simply calculated by measuring the change in the radiated power away from the system. These results are collected by the power monitor defined in Fig. 5.17(a) and (b) as a yellow rectangular box. All simulations of the Purcell factor in chapter 6 and 8 were carried out using this method.

5.7.5 Collection efficiency enhancement

The last simulation involves the collection efficiency (η_{NA}) enhancement of placing a single photon source on either a SiO_2 nano-pillar or on a GaP dimer nano-antenna. In order to attempt this, a dipole source was placed in the gap of a dimer nano-antenna as well as above the outside corner of the SiO_2 nano-pillar and the far-field emission pattern was computed by using a scattering monitor which recorded the power emitted upwards in the direction of the objective in the experimental setup discussed in a previous section of this chapter. The fraction of light collected by the numerical aperture (NA) of the objective corresponds to the fraction of power emitted in an upward cone defined by the collection angle of the objective.

This was simply calculated by placing a monitor at a sufficient distance away from the dipole source and top of the nano-structure to record the transmitted power. After this a circular filter was applied to the data, representing a cross section of the objective collection cone (defined by the NA) at the predefined height. The collected power through this spatial filter was then divided by the power emitted into the upper half-space to yield the collection

efficiency for a dipole placed atop the nano-structure. The power emitted into the upper half-space was computed by placing a power monitor very close to the dipole source.

5.8 Conclusion

This chapter has provided an overview of all experimental methods of fabrication, optical measurements and numerical simulations utilized to produce the results presented in the next three chapters of this thesis. The discussion began with an explanation of mechanical exfoliation, PL imaging for identification of monolayer regions and all-dry PDMS transfer of mono- or multi-layer stacks onto a target substrate. A brief discussion of the nano-fabrication techniques used to produce pre-patterned substrates with SiO_2 nano-pillars, GaP dimer nano-antennas as well as WS_2 monomer and dimer nano-antennas.

The home-built μ-Photoluminescence setup used for the work presented in chapter 6 was explored including outcoupling and spectral filtering for time-resolved PL dynamics, anti-bunching and coherence time measurements. The commercial dark field spectroscopy and home-built second harmonic generation setup used to produce results presented in chapter 7 were also described.

Finally, the discussion of this chapter focused on numerical simulations of the scattering cross section from monomer and dimer nano-antennas for identification of Mie resonances. Spatial distributions of the electric and magnetic field intensities presented in chapter 6, 7 and 8 were discussed. The confined electric energy in nano-antennna anapole resonances used to model the SHG enhancement was explored. The method for simulation of the Purcell factor of dipole emitters placed onto SiO_2 nano-pillars, GaP dimer nano-antennas and WS_2 nano-antennas was presented. Finally the method for calculation of the collection efficiency for a dipole placed on SiO_2 nano-pillars and GaP dimer nano-antennas was described. In the next chapter, work on WSe_2 single photon emitters forming on the previously discussed SiO_2 and GaP substrates will be presented.

Chapter 6

Single photon emitters in WSe_2 on GaP dimer nano-antennas

6.1 Introduction

Single photon emitters (SPE) in WSe_2 have drawn tremendous research interest as the first discovery of quantum sources of light in 2D materials [10–13, 91, 99] and also due to the host crystal which exhibits favorable excitonic properties [64] as well as the possibility for integration with various substrates, including nano-structured surfaces [31, 98, 111, 116, 150]. The nature of the SPEs is still under debate with various theories suggesting strain-induced potential exciton traps [79], momentum-dark states [180], or even various types of defects [128, 129]. However, this has not hindered the development of integrated WSe_2 SPE devices including electroluminescent structures [101], waveguides [87] and tunable high-Q micro-cavities [162]. Moreover, the evidence of bi-exciton cascade emission was also reported [181].

Strain engineering has also proven to be a scalable and reliable method of forming SPEs in WSe_2 as discussed in chapter 3 allowing very precise positioning [87]. Arrays of SPEs, have also been fabricated using strain induced in a monolayer of WSe_2 by a pre-patterned substrate of silicon dioxide (SiO_2) [111] or polymer nano-pillars [31]. Similarly, metallic nano-structures were also employed to not only form emitters but also to enhance their spontaneous emission rate via coupling to plasmonic resonances [42, 98]. However, plasmonics are known to suffer from non-radiative losses and lead to quenching of closely placed emitters which might require the use of dielectric spacers, thereby increasing the fabrication complexity [42]. High refractive index dielectric resonators, hosting both electric and magnetic modes as opposed to plasmonic structures [146], offer a solution to these

problems while maintaining tightly confined resonances that can be used for emission enhancement of dye molecules [43] and excitons in 2D semiconductors [150].

In this chapter, I will present the use of gallium phosphide (GaP) nano-antennas and SiO_2 nano-pillars for the formation of SPEs in monolayer WSe_2. This will begin with a brief description of the resonant properties of the two nano-structures and shift to the optical properties of the single photon sources formed on each pre-patterned substrate. Subsequently, I will explore and compare the brightness, power saturation and lifetimes of the emitters on SiO_2 nano-pillars and GaP nano-antennas in order to demonstrate quantum efficiency (QE) enhancement for those SPEs forming on the latter nano-structures. The improved QE observed then allows a more in-depth study of the excitation and emission dynamics of the SPEs with insight into their recombination pathways. Finally, the chapter will end with a systematic study of the coherence properties of these 2D quantum emitters leading to more precise conclusions concerning the dephasing mechanisms in this system. This work has also been reported in the following reference [182].

6.2 Comparison of resonances in SiO_2 and GaP nano-structures

The discussion will begin with examining the nano-structures used to induce strain in monolayer WSe_2 in order to form single photon emitters. As previously reported, arrays of pre-patterned SiO_2 nano-pillars induce strain in a monolayer of WSe_2 leading to single photon emission [111]. These structures, however, are not expected to yield any photonic enhancement to SPEs forming near them due to the low refractive index of the material, while gallium phosphide dimer nano-antennas (consisting of two closely spaced nano-pillars), as previously reported, have been shown to enhance the photoluminescence (PL) of WSe_2 neutral exciton emission [150] while simultaneously inducing exciton funneling through strain [116]. In order to compare the resonant properties of the two materials and configurations, finite-difference time-domain (FDTD) simulations of the scattering cross section of both monomer and dimer nano-structures were carried out in gallium phosphide and silicon dioxide for a range of radii (r = 150, 200, 250, 300 nm) as shown in Fig. 6.1. In the case of the dimers, the radius corresponds to that of each individual nano-pillar.

The scattering cross section of the gallium phosphide nano-antennas in Fig. 6.1(a) and (c) yield broad Mie resonances, which can be characterized as various dipole and anapole modes, due to the high refractive index of the material ($n_{GaP} \approx 3.2$). The scattering cross section of the SiO_2 nano-pillars in Fig. 6.1(b) and (d), however, do not yield any resonances due to the low refractive index of this material ($n_{SiO_2} \approx 1.5$) which leads to low confinements of the fields. Therefore, gallium phosphide is expected to lead to highly confined resonances

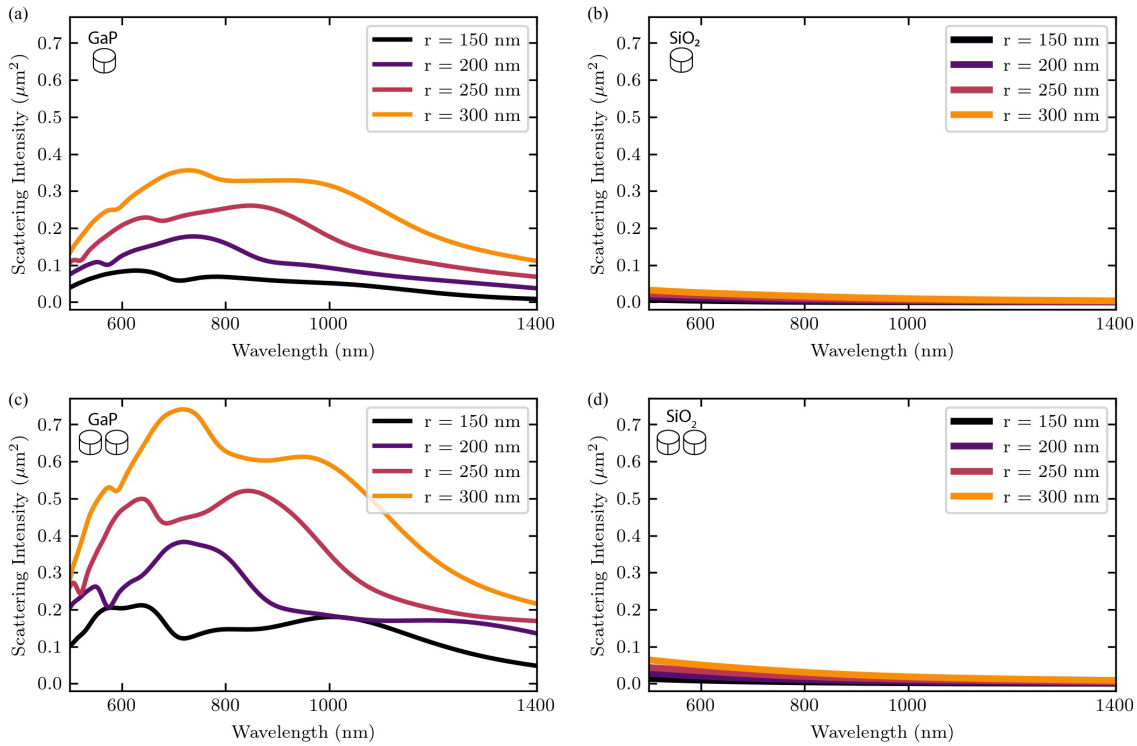

Fig. 6.1 **(a)** Simulated scattering cross section for GaP dimer nano-antennas with varying radius r = 150, 200, 250, 300 nm, height h = 200 nm and gap width g = 50 nm. **(b)** Simulated scattering cross section for SiO_2 nano-pillars with varying radius r = 150, 200, 250, 300 nm and height h = 100 nm.

which will confine the electric fields close to the nano-antennas. Comparing monomer to dimer in each material results in higher scattering cross sections for the dimer. As the configuration is expected to highly confine the electric fields between the two monomer structures, as discussed in chapter 4, the dimer will scatter more light therefore, higher fluorescence enhancements of emitters surrounding the nano-antenna are expected. The conclusion from this numerical study is that all structures are able to induce SPE formation in monolayer WSe_2 through strain, yet the GaP dimer nano-antenna may lead to the highest photoluminescence enhancement while the SiO_2 monomer may yield the lowest. The reason these two structures were chosen for the experiments demonstrated in this chapter was in order to make a comparison between WSe_2 single photon emitters which have not experienced photonic enhancement and those that have.

To provide evidence for fluorescence enhancement, the factors which influence the SPE photoluminescence must be understood. The emission intensity collected from a single photon emitter coupled to a nano-antenna resonance is dependent on its position **r** with respect to the anti-nodes of the resonance as well as on both emitter and photonic mode

wavelength (λ_{em} and λ_{exc} respectively). The measured photoluminescence intensity $I(\mathbf{r}, \lambda_{em})$ depends on three factors [150, 183]:

$$I(\mathbf{r}, \lambda_{em}) \propto \gamma_{exc}(\mathbf{r}, \lambda_{exc}) \cdot QE(\mathbf{r}, \lambda_{em}) \cdot \eta_{NA}(\mathbf{r}, \lambda_{em}) \tag{6.1}$$

where $\gamma_{exc}(\mathbf{r}, \lambda_{exc})$ is the excitation rate, $QE(\mathbf{r}, \lambda_{em})$ is the quantum efficiency of the emitter and η_{NA} is the efficiency of the collection optics. The excitation rate is a function of the wavelength of the pump and the electric field intensity at the position of the dipole emitter which is itself dependent on the resonances of the photonic structure. The quantum efficiency can be defined as follows:

$$QE(\mathbf{r}, \lambda_{em}) = \frac{\gamma_r(\mathbf{r}, \lambda_{em})}{\gamma_r(\mathbf{r}, \lambda_{em}) + \gamma_{nr}(\mathbf{r}, \lambda_{em})} \tag{6.2}$$

where $\gamma_r(\mathbf{r}, \lambda_{em})$ is the radiative recombination rate of the emitter and $\gamma_{nr}(\mathbf{r}, \lambda_{em})$ is the non-radiative recombination rate. These both depend on the intrinsic properties of the quantum emitter as well as on the environment including charge and spin states surrounding the position of the SPE as well as the properties of the substrate material, such as refractive index or bandgap alignment, which is in close proximity to the emitter. The radiative recombination rate also depends upon the photonic environment or, as discussed in chapter 4, the local density of optical states which may provide a Purcell enhancement that will increase γ_r for a proper position and orientation of the emitter [166]. The last factor influencing the photoluminescence of an emitter coupled to a resonant mode is the collection efficiency which can be influenced by a nano-antenna's ability to redirect emitted or scattered light. This is a function of the refractive index and geometry of the structure.

Numerical simulations, using FDTD software as discussed in the previous chapter, were performed to find expected values of each of the three factors for an in-plane dipole placed onto either a SiO_2 nano-pillar or a GaP dimer nano-antenna. The dipole wavelength (λ_{em} = 750 nm) was chosen to closely emulate a single photon emitter in WSe_2 forming at a strained region in a monolayer induced by its transfer on either structure as shown in the schematic representations at the top of Fig. 6.2(a) and (b).

The excitation rate, also described as the absorption cross section, as the first factor in equation 6.1 ($\gamma_{exc}(\mathbf{r}, \lambda_{exc})$), is proportional to the electric field intensity ($|E|^2$) at the position of the quantum emitter. As the simulations attempt to find a value for the enhancement of the electric field intensity, the values are normalized by the intensity of the normally incident plane wave ($|E_0|^2$) with linear polarization along the axis connecting the centers of

the nano-pillars. Subsequently, when a comparison of GaP and SiO_2 substrates is performed, the $|E|/|E_0|^2$ values can be divided to find the relative enhancement. The spatial distributions of the electric field intensity displayed in the bottom portion of Fig. 6.2(a) and (b) were simulated for a plane at the top surface of a GaP dimer nano-antenna (r = 150 nm, h = 200 nm, gap = 50 nm) and a SiO_2 nano-pillar (r = 150 nm, h = 100 nm) respectively. This plane was chosen as it is the most likely place for a single photon emitter in a transferred WSe_2 monolayer to form and it is also the position with the highest electric field confinement. The hotspots forming at the top surface of the GaP dimer nano-antennas and the SiO_2 nano-pillars are expected to extend several nanometers in the vertical direction therefore requiring the monolayer to be in direct contact with the structure in order to form SPEs with enhanced emission rates. As a side note, this is not possible with plasmonic structures as this leads to quenching of the emission due to charge transfer to the metallic structure. The incident plane wave was set to the dipole wavelength (750 nm). The enhancement of the electric field intensity of the GaP nano-antennas ($|E|/|E_0|^2$) exceeds a factor of 10 and is particularly pronounced in the gap between the two nano-pillars (dimer gap). Under the same excitation conditions, the enhancement of the electric field intensity at the top surface of the SiO_2 nano-pillars is an order of magnitude lower with a maximum surrounding the edges of the structure. This lower confinement of the electric fields is expected from the lack of resonances seen in Fig. 6.1 as well as from the much lower refractive index of SiO_2.

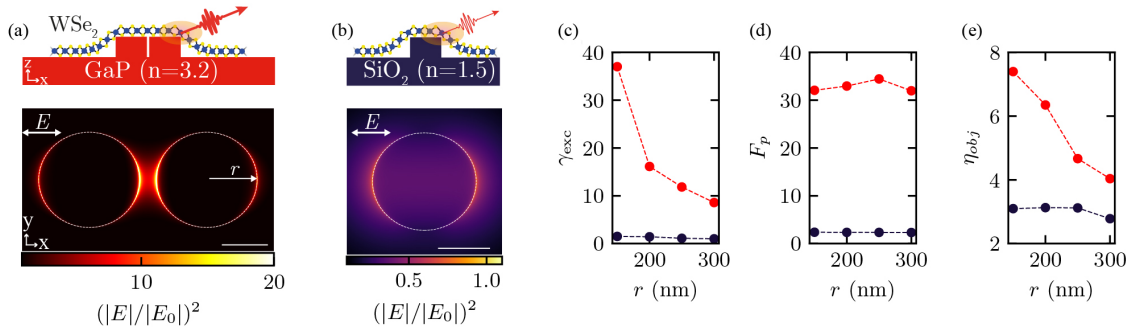

Fig. 6.2 **(a)** Top panel: schematic illustration of a monolayer of WSe_2 deposited on top of a GaP dimer nano-antenna. Bottom panel: Simulated spatial distribution of the electric field intensity surrounding a GaP dimer nano-antenna (r = 150 nm, h = 200 nm, gap = 50 nm) at the top surface of the structure compared to vacuum. Hotspots extend several nanometers in the vertical direction, exponentially decreasing in intensity. **(b)** Top panel: schematic illustration of a monolayer of WSe_2 deposited on top of a SiO_2 nano-pillar. Bottom panel: Simulated spatial distribution of the electric field intensity surrounding a SiO_2 nano-pillar (r = 150 nm, h = 100 nm) at the top surface of the structure compared to vacuum. **(c)-(e)** Simulations of the excitation rate **(c)**, Purcell enhancement factor **(d)** and light collection efficiency **(e)** for a dipole emitter placed in the position of highest electric field intensity for a GaP dimer nano-anatenna (red) and a SiO_2 nano-pillar (blue) with a range of radii. Adapted from reference [182].

The position of the single photon emitter is expected to be at the edges of the structure geometry within this plane where the maximum field enhancement is expected. Fig. 6.2(c) displays the maximum values of the electric field intensity for a GaP dimer nano-antenna (red dots) and a SiO_2 nano-pillar, (blue dots) for an incident plane wave at a wavelength of 638 nm (laser excitation wavelength used in subsequent experiments shown in next sections). The maximum excitation rate ($\gamma_{exc}(\mathbf{r}, \lambda_{exc})$) is highest for the smallest dimer nano-antenna (r = 150) decreasing exponentially for larger values of the radius. This is due to the Mie origin of the resonance inducing the electric field intensity enhancement. As discussed in chapter 4, as the size of the nano-antenna increases, all resonances redshift and therefore the electric field enhancement at the excitation wavelength is reduced as the resonance of the structure redshifts away. For the SiO_2 nano-pillar the excitation rate is fairly constant for the range of radii yet it is much lower due to the weak confinement of the structure.

The next factor to be simulated is the quantum efficiency ($QE(\mathbf{r}, \lambda_{em})$). In these simulations the approximation of low intrinsic quantum yield [98, 150] can be applied. In this case, the enhancement of the quantum efficiency can be safely approximated as the radiative decay rate enhancement through the Purcell factor $F_P = \gamma_r/\gamma_r^0$. As discussed in the previous chapter, the Purcell factor for a dipole positioned within a certain geometry as normalized to one in vacuum is equal to the enhancement of the rate of energy dissipation P/P_0 [165]. For the Purcell simulations, the GaP dimer nano-antennas or SiO_2 nano-pillars were excited with a dipole of wavelength ($\lambda_{em} = 750nm$) placed at 0.5 nm above the top surface of the structure. The dipole was positioned within the hotspot with maximum electric field intensity of each structure, namely above the inner GaP dimer edge close to the gap or above the outer edge of the SiO_2 nano-pillar. Fig. 6.2(d) displays the Purcell factors (F_P) calculated for the GaP dimer (red dots) and the SiO_2 nano-pillar (blue dots) at each radius. For both structures, the radiative rate enhancement does not change much over the range of radii, however, it is an order of magnitude higher for a dipole positioned onto a GaP dimer nano-antenna.

The final factor in equation 6.1 is the collection efficiency (η_{NA}), depending on the amount of light in the detection optics, which is most often an objective with a numerical aperture (*NA*). A dipole emitter placed in free space would emit light in all directions equally, however, its placement onto a substrate will change the far-field emission pattern. Simulations of the radiation pattern for a dipole placed either in the middle of a GaP dimer gap close to the top surface of the structure or at the top edge of a SiO_2 nano-pillar are shown in Fig. 6.3. The precise position of the dipole in the simulation of the two structures is shown in Fig. 6.3(a). The far-field radiation pattern for a dipole on a GaP dimer nano-antenna (red) and SiO_2 nano-pillar (gray) are shown in Figs. 6.3(b) and (c). These display two cross-sectional views along the dimer axis and perpendicular to it respectively for Fig. 6.3(b) and (c). As

expected, the higher index of GaP will direct most of the emitted light towards the substrate. The collection efficiency (η_{NA}), however, is calculated as the percentage of light which is emitted upwards, away from the substrate, into a cone defined by the numerical aperture of the objective. As shown in Fig. 6.2(e), the collected light by the objective (NA = 0.64) is calculated to be from 4% (r = 300 nm) to nearly 8% (r = 150 nm) for a dipole positioned onto a GaP dimer nano-antenna. For a dipole placed at the top edge of a SiO_2 nano-pillar, the collection efficiency is expected to be between 2.7% (r = 300 nm) and 3.1% (r = 150 nm) depending on the radius of the structure. Thus, the collection efficiency for both structures is of the same order of magnitude.

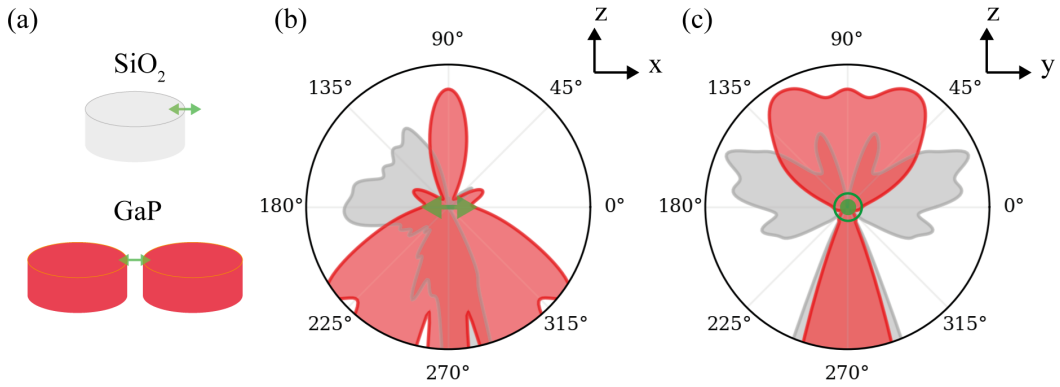

Fig. 6.3 **(a)** Representation of the position of a dipole (green) in the collection efficiency simulations. **(b),(c)** far-field radiation patterns for a plane parallel to the dipole orientation **(b)** and perpendicular to it **(c)** for a GaP dimer nano-antenna (red) and a SiO_2 nano-pillar (gray). Adapted from reference [182].

When the three factors described in equation 6.1 are all taken into account, the GaP dimer nano-antennas are expected to induce an enhancement of the PL intensity of a dipole emitter by at least two orders of magnitude [43, 150] compared to SiO_2 nano-pillars. This results from the increase in the excitation rateγ_{exc} and the spontaneous emission rate through the Purcell factor F_P as well as a modest improvement of the collection efficiency η_{NA}.

6.3 Optical properties of WSe_2 SPEs on SiO_2 nano-pillars

Having explored the photonic resonances of the GaP dimer nano-antennas and the SiO_2 nano-pillars as well as their expected effects on the photoluminescence of a WSe_2 single photon source, the discussion will shift to the observed properties of the SPEs forming on the SiO_2 nano-pillars and comparing them to previous reports. In order to form SPEs in a monolayer of WSe_2 using SiO_2 nano-pillar as strain sites, a pre-patterned substrate was fabricated as discussed in the previous chapter.

A scanning electron microscopy (SEM) image of a single nano-pillar of the completed substrate is shown in Fig. 6.4(a). Next, a monolayer of WSe_2 was mechanically exfoliated and transferred onto the fabricated SiO_2 nano-pillars with an all-dry technique. A bright field microscope image of the deposited monolayer is shown in Fig. 6.4(b). The monolayer seen in a yellow color is outlined by a dashed black line. Fig. 6.4(c) displays a room temperature PL map of the monolayer of WSe_2 deposited onto the SiO_2 nano-pillar array. The emission from the monolayer is uniform everywhere even though the monolayer is strained by its transfer onto the nano-pillars.

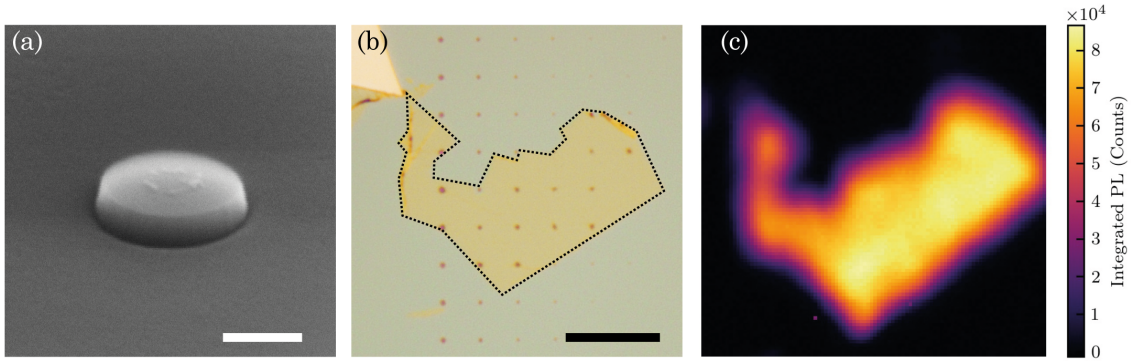

Fig. 6.4 **(a)** Tilted SEM image of a fabricated SiO_2 nano-pillar of height 100 nm. Scale bar = 200 nm. **(b)** Bright field microscope image of a monolayer of WSe_2 (yellow area outlined in black dashed line) deposited onto an array of SiO_2 nano-pillars. Scale bar = 10 μm. **(c)** Room temperature PL map of the transferred monolayer WSe_2. Adapted from reference [182].

Once the fabricated sample was cooled to the temperature of liquid helium in a cryostat, used for PL measurements as discussed in chapter 5, it was excited with a 638 nm pulsed laser (90 ps pulse width and variable repetition rate). The photoluminescence emitted from the positions of the nano-pillars exhibits narrow-linewidth peaks with a broad background emission, previously reported as a band of localized states [11–13, 99], at the position of some of the higher energy lines. Fig. 6.5(a) shows an exemplary PL spectrum from one of these sites where the monolayer has been strained by its transfer onto the nano-pillar geometry. The inset of this figure displays a polarization dependent measurement of the intensity of the brightest peak in the spectrum at this position which is highlighted in gray and exhibits a linear polarization. This is to be expected for an in-plane dipole single photon emitter observed in previous reports [10, 11]. The emitter also exhibits intensity saturation under increased excitation powers, photoluminescence decay with a lifetime of $\tau = 5.8$ ns and a spectral stability of 1 meV over 150s as shown in Fig. 6.5(b), (c) and (d) respectively. These properties all agree with previous reports of strain-induced WSe_2 single photon emitters [10–13, 99]. Therefore, these experiments provide evidence, short of an anti-bunching measurement, to the fact that the narrow-linewidth emission observed in

the cryogenic PL spectrum at strained cites of a monolayer of WSe_2 is indeed a two-level in-plane dipole quantum emitter such as those previously observed.

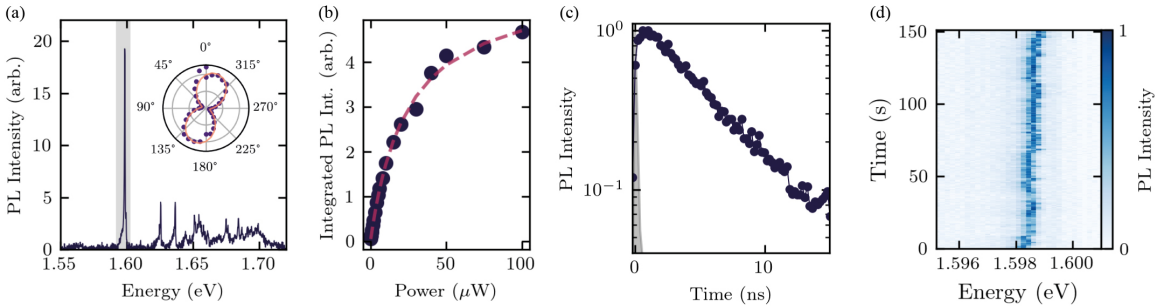

Fig. 6.5 **(a)** Low temperature PL spectrum of monolayer WSe_2 from the position of a SiO_2 nano-pillar showing narrow-linewidth emitters. Inset presents a polar plot of the linear polarization dependence of the emitter highlighted in gray in the spectrum. **(b)** Power dependent measurement of the PL intensity of the emitter highlighted in **(a)** under 638 nm and 80 MHz pulsed excitation. **(c)** Time-resolved PL of the SPE highlighted in **(a)**. **(d)** Stability of the PL emission highlighted in **(a)**. Adapted from reference [182].

6.4 Optical properties of WSe_2 SPEs on GaP nano-antennas

The previous section, provided evidence that the fabrication procedures have formed strain-induced SPEs in monolayer WSe_2 on SiO_2 nano-pillars. In this section, the properties of similar emitters formed by transferring monolayer WSe_2 onto GaP dimer nano-antennas will be explored. The fabrication of an array of the gallium phosphide structures, performed by a collaborator from Imperial College London, is very similar to the above mentioned fabrication of SiO_2 nano-pillars with a few extra steps as discussed in the previous chapter.

Subsequently, as for the SiO_2 substrate, a monolayer of WSe_2 mechanically exfoliated from bulk was transferred onto the GaP array using an all-dry transfer technique. A bright field microscope image of the transferred monolayer is shown in Fig. 6.6(a). The edges of the monolayer are not clearly visible on this substrate as on the SiO_2 due to the reduced contrast for the single layer at the top of the GaP wafer. Only portions of the monolayer which have been stretched atop the dimer nano-antennas are visible as they have been elevated and stretched over the substrate geometry. A room temperature PL image was also recorded using a Nikon microscope with a 550 nm short pass filter and a 600 nm long pass filter in the excitation and collection path respectively. This was subsequently overlaid onto the bright field microscopy image as shown in Fig. 6.6(b). Bright emission is observed surrounding all GaP dimer nano-antenna positions suggesting a strain-induced funneling of WSe_2 excitons before recombination as well as emission from monolayer which is elevated above the substrate as it is stretched atop the nano-antenna geometry.

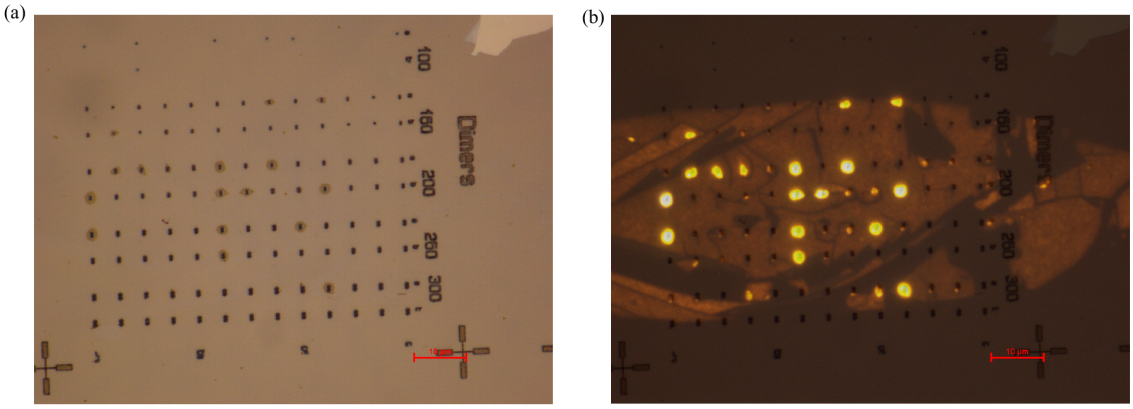

Fig. 6.6 **(a)** Bright field image of a monolayer of WSe_2 deposited on an array of GaP dimer nano-antennas. Only visible portions of the monolayer are surrounding several nano-antenna positions. **(b)** Room temperature PL image of monolayer WSe_2 deposited on an array of GaP dimer nano-antennas overlaid on the bright field image. The bright portions indicate monolayer WSe_2 PL emission with the brightest regions at several nano-antenna positions.

The samples were similarly cooled to $T = 4K$ as for the monolayer transferred onto the SiO_2 substrate and excited using the same pulsed laser. The laser wavelength was chosen to be below the GaP band gap so that it can only be absorbed by the WSe_2 monolayer. The inset in Fig. 6.7(a) shows a map of integrated PL intensity centered at the position of a dimer nano-antenna of radius r = 250 nm. The PL signal is strongly localized to the nano-antenna position where the monolayer is strained, as opposed to the negligible emission from the surrounding area where WSe_2 is not strained. The PL spectrum from nano-antenna positions (shown in Fig. 6.7(a)) exhibit spectrally isolated, narrow linewidth emission with a negligible background contrary to what was observed in PL from WSe_2 on the SiO_2 substrate as demonstrated in the previous section.

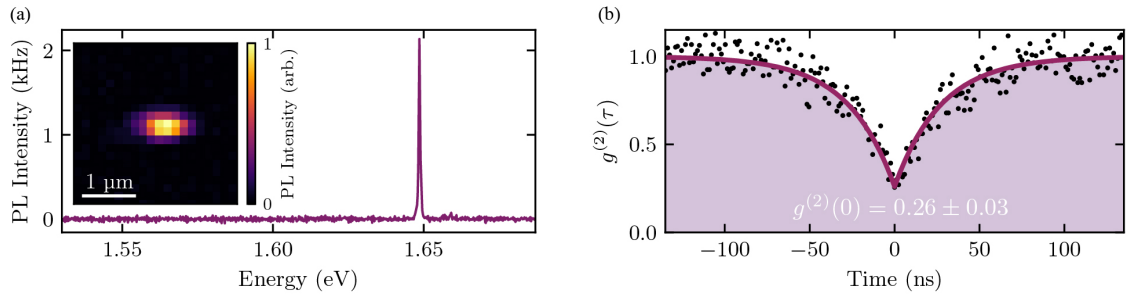

Fig. 6.7 **(a)** PL spectrum of monolayer WSe_2 from the position of a GaP dimer nano-antenna (r = 250 nm) under 638 nm, 20 MHz pulsed excitation at a power of 15 nW. Inset shows low-temperature integrated PL intensity map from the monolayer. Bright spot in the center corresponds to the nano-antenna position. **(b)** Second order photon correlation curve for the emitter in **(a)** showing single photon emission under 725 nm continuous wave excitation. Adapted from reference [182].

Next, an anti-bunching measurement was performed using a Hanbury Brown-Twiss setup as described in the previous chapter. The excitation source used was a 725 nm continuous-wave laser which is below the delocalized neutral A-exciton resonance in WSe_2, therefore, it can only be absorbed by the state responsible for the narrow-linewidth emission. Fig. 6.7(b) shows the background-corrected second order correlation function $g^{(2)}(\tau)$ [23] for the emission displayed in Fig. 6.7(a). The pronounced dip in the measurement indicates single photon emission with a $g^{(2)}(0)$ value of 0.26 ± 0.03 which is consistent with the range of previous reports (0.022 to 0.30 [10, 12, 91, 99–101]).

Further properties of the single photon emission lines forming on GaP dimer nano-antennas are shown in Fig. 6.8. The cryogenic PL spectrum from the WSe_2 monolayer at the position of a GaP dimer nano-antenna with radius r = 250 nm excited with a linear polarization at 638 nm and collected under two orthogonal polarization directions is shown in Fig. 6.8(a) with blue and red colors respectively. The high energy (blue trace) peak is cross linearly polarized with the multitude of peaks at lower energy (red trace). The linear polarization properties of each is shown in Fig. 6.8(b) where integrated PL is recorded for the blue and red highlighted regions in Fig. 6.8(a) using the same respective colors. This energy structure exhibiting a few high energy peaks and many low energy peaks at different polarizations is repeated over a number of nano-antennas as shown in Fig. 6.9(d)-(f). The SPEs forming on the GaP dimer nano-antennas exhibit lower spectral wandering, shown in Fig. 6.8(c) (<300 μeV), than those on the SiO_2 nano-pillars. This stability of single photon emission is also observed in highly strained WSe_2 monolayers [111].

The PL lifetime of high energy emitters are often observed to be longer than those of the multitude of low energy peaks. For the SPEs shown in Fig. 6.8(a), the emission line highlighted in blue exhibits a PL lifetime of τ = 42 ns, while for the emitter highlighted in red, the decay time si τ = 7 ns. This pattern of high energy long-lived emitters and low energy short-lived emitters was again observed to repeat for different nano-antenna sites. The two types of single photon emission yielded a similar saturation behavior with a difference in saturation intensity, shown in Fig. 6.8(e), where the blue and red traces again correspond to the emitters highlighted in blue and red in Fig. 6.8(a) respectively. The linewidth (FWHM) of the peak highlighted in blue exhibits a homogeneous broadening with increased excitation power density as shown in Fig. 6.8(f).

Fine structure splitting (FSS) is also seen for some emitters forming on GaP dimer nano-antennas. The presence or absence of an FSS at zero magnetic field has previously been reported to be linked to the varying anisotropy of the confining potential of SPEs in WSe_2 [100]. The emitters shown in Fig. 6.8(a) were subsequently studied using a higher-resolution grating in order to clearly observe which peaks exhibit an FSS. The high energy emission

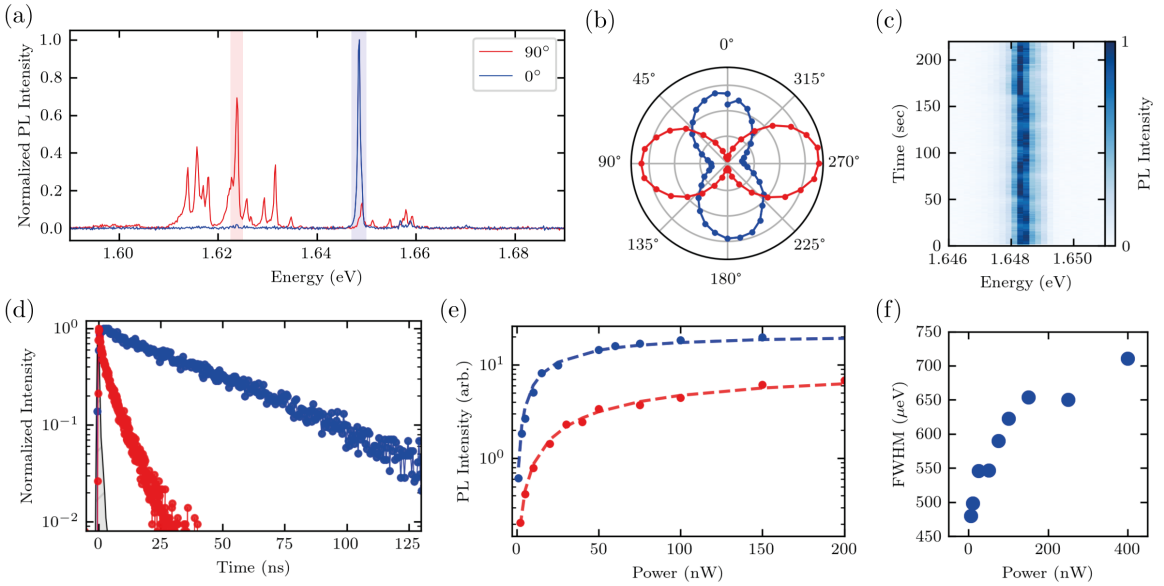

Fig. 6.8 **(a)** Low temperature PL spectrum of monolayer WSe_2 from the position of a GaP dimer nano-antenna. Blue spectrum represents linearly polarized collection oriented parallel to the excitation polarization. Red spectrum represents a linear polarization oriented perpendicular to the excitation. **(b)** Polar plot of the intensity of peaks highlighted in blue and red from **(a)** respectively. **(c)** Spectral stability of PL emission from peak highlighted in blue in **(a)**. **(d)** Time-resolved PL from the peaks highlighted with matching colors in **(a)**. **(e)** Power dependent measurement of the PL intensity under 638 nm, 80 MHz pulsed excitation for peaks highlighted with matching colors in **(a)**. Saturation power is similar for both emitters. **(f)** Linewidth of blue highlighted peak in **(a)** with increasing excitation power. Adapted from reference [182].

line is shown to be composed of two cross linearly polarized peaks indicating a fine structure splitting in Fig. 6.9(a). The low energy emitters, however, do not exhibit any FSS as shown in Fig. 6.9(b) yet the degree of linear polarization of these SPEs is near unity. Statistics of the recorded zero magnetic field FSS splitting energies, displayed in Fig. 6.9(c), shows a range from 600 to 800 μeV which agrees with previous reports [10, 12, 13].

The repeated pattern of high and low energy peaks with different polarization properties for GaP dimer nano-antennas with different radii is displayed in Fig. 6.9(d)-(f). In each polarization dependent spectrum, a high energy emitter exhibiting a FSS is followed by many lower energy peaks all exhibiting the same polarization which is not the same as that of the high energy line nor do they show any fine structure splitting. This suggests that the two types of emission originate from two different types of strain-induced SPEs in monolayer WSe_2 with a different confinement potential well with regards to energy and width [79] which could be a result of various nano-scale strain profiles or crystal defects.

The last property discussed in this section concerns strain in the monolayer of WSe_2 induced by the varying radius of the GaP dimer nano-antennas. A reduction in the radius of the structure leads to increased strain [116] and therefore a larger renormalization of the

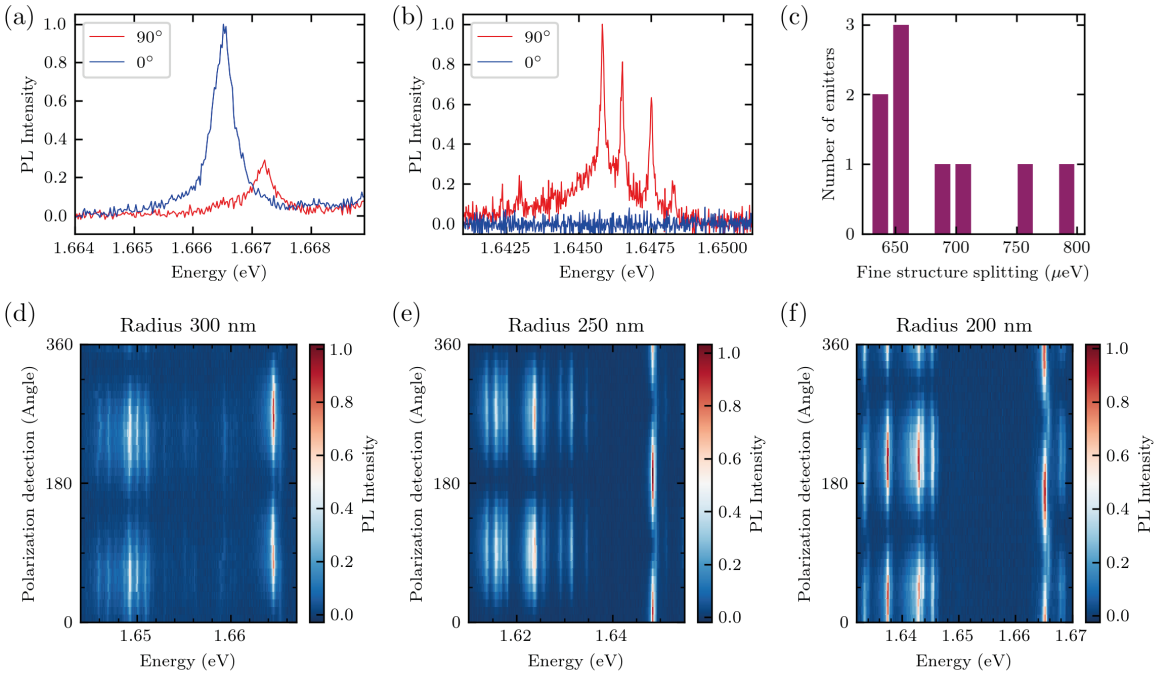

Fig. 6.9 High resolution PL spectra at co- and cross-polarized detection centered on the blue **(a)** and red **(b)** highlighted peaks in Fig. 6.8(a). **(a)** Fine structure split doublet seen for the high energy peak. **(b)** No fine structure splitting observed in low energy peaks, however, they do exhibit near unity degree of linear polarization. **(c)** Statistics of fine structure splitting values observed for high energy peaks measured at different nano-antenna positions. **(d)-(f)** Polarization dependent PL emission for SPEs observed at the positions of GaP dimer nano-antennas with a radius of **(d)** 300 nm, **(e)** 250 nm, **(f)** 200 nm. Adapted from reference [182].

band structure as discussed in chapter 3. The spectral position of the neutral A-exciton of monolayer WSe_2 (X) is shown as a dashed line in Fig. 6.10. The energy of the exciton resonance is red-shifted with decreasing nano-antenna radius. This X emission energy is calculated from the un-strained value by interpolating the theoretical curve described in reference [116] with the experimental gauge of -49 meV/% for tensile strain of the WSe_2 monolayer at room temperature [184].

All recorded emission energies of WSe_2 SPEs forming on GaP dimer nano-antennas are plotted as a function of the radius of the structure on which they are observed (yellow dots) in Fig. 6.10. Since the quantum emitters are very much dependent on their local environment, they span a large range of energies, however, this range clearly redshifts with decreasing nano-antenna radius similar to the neutral exciton resonance (X). This observation confirms the impact of strain on the confinement potential and emission energy of the WSe_2 SPEs forming on GaP dimer nano-antennas.

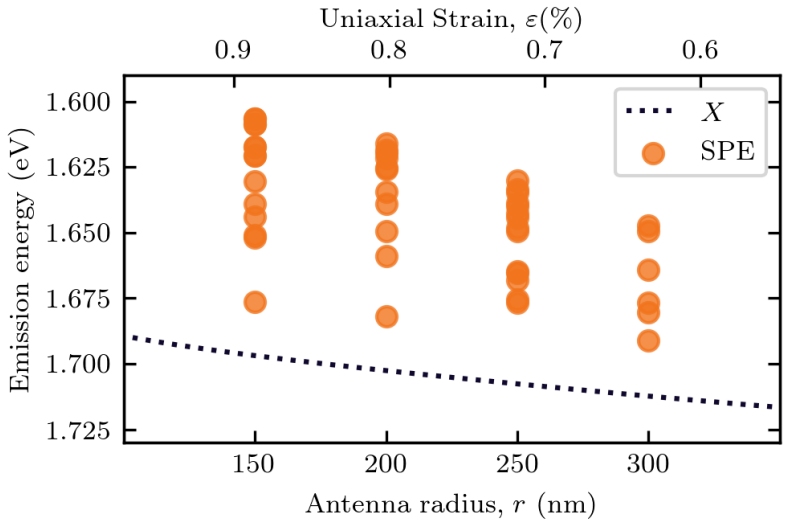

Fig. 6.10 Emission energies of WSe_2 SPEs observed at the positions of GaP dimer nano-antennas with different radii (yellow dots). The calculated spectral position of the de-localized neutral exciton emission (X) for the strain induced in the monolayer by nano-antennas with different radii is plotted as a dashed line. Adapted from reference [182].

6.5 Quantum efficiency enhancement of WSe_2 SPEs on GaP nano-antennas

As shown in the previous sections, both GaP dimer nano-antennas and SiO_2 nano-pillars strain monolayer WSe_2 and form single photon emitters, however, the photonic properties of the two structures are vastly different and thus lead to SPEs with different properties. After the analysis of more than 50 SPEs on GaP dimer nano-antennas and 20 SPEs forming on SiO_2 nano-pillars, the PL intensity, lifetime and excitation power saturation behavior will be compared in this section.

Fig. 6.11(a) displays the PL intensity (at saturation) of each SPE on GaP dimer nano-antennas (red dots) and on SiO_2 nano-pillars (blue dots), as a function of their emission energy. The intensity values are normalized to the average excitation power in the saturation regime. No correlation can be extracted between the intensity and spectral position of the SPEs, however, a clear increase in intensity of 2 to 4 orders of magnitude is seen for all emitters forming on the GaP nano-antennas when comparing to those on SiO_2 nano-pillars.

Further insight into this enhancement is provided by the SPE PL saturation behavior, shown in Fig. 6.11(b). As these experiments were carried out with a pulsed laser excitation using different repetition rates due to large variations in individual PL lifetimes, Fig. 6.11(b) presents a histogram of saturation powers as an energy per pulse value (average power

divided by laser repetition rate) with red bars representing SPEs on GaP nano-antennas and blue bars indicate emitters on SiO_2 nano-pillars. For the setup used in these experiments 1 fJ of pulse energy corresponds to an energy density of 30 nJ/cm^2. The SPEs forming on the GaP nano-antennas exhibit more than 3 orders of magnitude lower saturation pulse energies than those on SiO_2 nano-pillars. The reasons for this striking observation will be explored further.

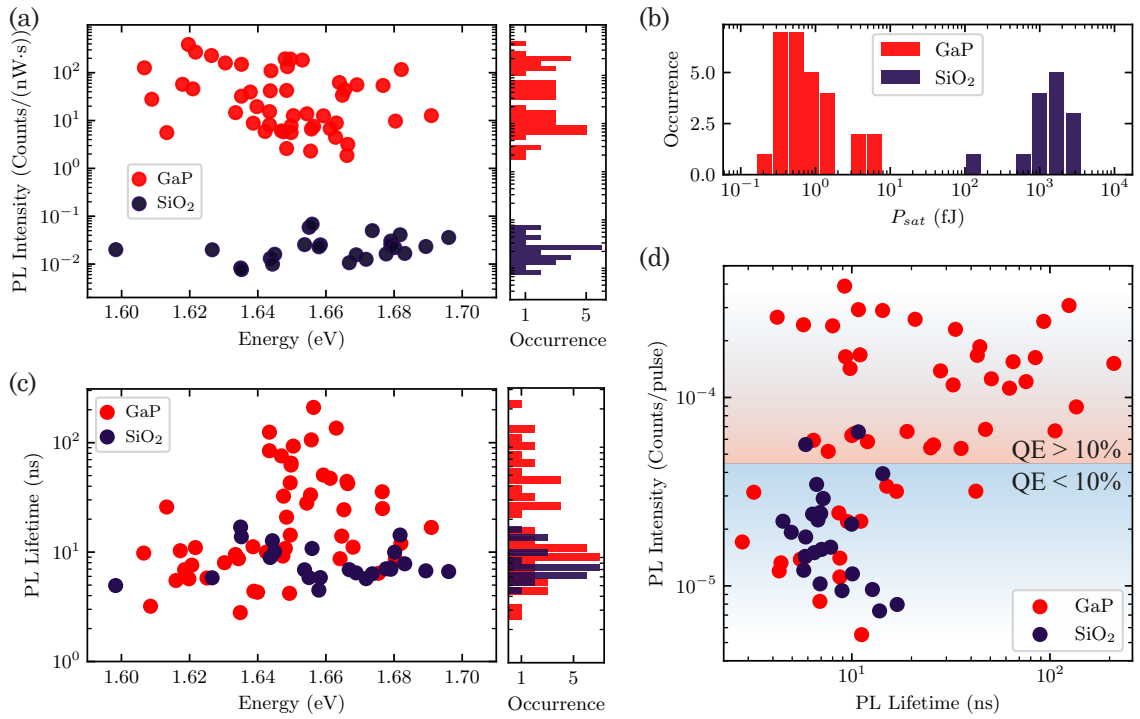

Fig. 6.11 **(a)** PL intensity of SPEs normalized by the average laser excitation power at saturation of the emitter. Right histogram shows the number of occurrences observed for each range of PL intensities. **(b)** Histogram of the energy per excitation pulse required to saturate an SPE. **(c)** PL decay times of SPEs. Right histogram shows the number of occurrences observed for each range of lifetimes. **(d)** PL peak intensity of SPEs per excitation pulse plotted as a function of the emitter decay time. Red and blue regions of the plot represent emitters with quantum efficiency of more than and less than 10% respectively. The data collected from SPEs on GaP dimer nano-antennas is shown in red. The data from SPEs on SiO_2 nano-pillars is shown in blue. Adapted from reference [182].

An enhancement of the first term in equation 6.1, the excitation rate, is one of the factors which will contribute to the reduced saturation values P_{sat} and increased intensity. However, as shown in Fig. 6.2(c), this can only account for a reduction in P_{sat} and increase in PL intensity by at most a factor of 40. Therefore, additional contributions linked to the dynamics and quantum efficiency of the monolayer-WSe_2/SPE system must be considered.

Fig. 6.11(c) plots the PL lifetimes of SPEs on GaP dimer nano-antennas (red dots) and SiO_2 nano-pillars (blue dots) as a function of their emission energies. The decay times of SPEs forming on the SiO_2 substrate are similar to previously observed lifetimes on the order of 10 ns or less [10–12, 31, 111]. The emitters forming on GaP nano-antennas, however, exhibit a broad distribution of lifetimes ranging from 2 ns up to more than 200 ns. The only correlation between lifetime and emission energies that can be observed is the abundance of long-lived emitters in a relatively small range of emission energies (1.64 eV - 1.68 eV). This can be described by understanding the origin of different portions of the PL decay dynamics. While the lifetime experiments reveal a relationship between radiative and non radiative rates of the emitters ($1/\tau_{decay} = 1/\tau_r + 1/\tau_{nr}$), the radiative component is more directly dependent on the width and confinement energy of the potential well forming the SPE. The non-radiative component, however, may also be affected by interaction with phonons or coupling to the local environment with a change in the confinement potential due to strain. If either the radiative or non-radiative rate is much shorter than the other, then it will define the entire PL decay time. This suggests that the PL decay time of the long-lived emitters exhibiting a relatively small range of emission energies may be defined by the radiative component which as stated above may be more dependent on the confinement potential energy than the non-radiative decay time. This may seem counter-intuitive as the emitters within the small range of emission energies exhibit longer, not shorter, lifetimes. Thus, the radiative component has not shortened but this result suggest a lengthening of the non-radiative rate.

In order to shed more light on the PL decay dynamics, the SPE PL counts per excitation pulse are plotted as a function of their lifetime in Fig. 6.11(d). The emitters forming on GaP nano-antennas (red dots) exhibit higher overall PL counts per excitation pulse than those forming on SiO_2 nano-pillars (blue dots). The emitters on the GaP substrate also yield comparable or longer lifetimes than SPEs on SiO_2. Taken together, these two facts suggest an enhancement of the quantum efficiency QE. This can be estimated for SPEs under pulsed excitation by normalizing the detected photons at saturation from each emitter by the laser repetition rate [98] as a $QE = 1$ would be expected if a photon is detected for each excitation pulse. In order to provide an accurate number of detection photons, the collection efficiency of the experimental setup was calculated by measuring the losses of a 725 nm laser passing through. The values obtained from this calibration are listed in table 6.1 [182].

The values for the transmission efficiency of the linear polarizer and spectrometer as well as the CCD efficiency are taken from the relevant datasheets. The total collection efficiency of the experimental setup was calculated to be 0.56%. From the simulations of the far-field radiation pattern, the collection efficiency resulting from the directivity enhancement of the GaP and SiO_2 nano-structures was also taken into account in the calculation of the detected

Component	*Transmission*
Optical breadboard	50%
Linear polarizer	78%
Single Mode fibre coupling	2%
Spectrometer in-coupling	90%
Spectrometer mirrors (x3)	$97\%^3$=91%
Grating Efficiency	90%
CCD Quantum Efficiency	98%
TOTAL COLLECTION EFFICIENCY	**0.56%**

Table 6.1 Collection efficiency of the μ-PL setup used for the spectroscopy of WSe_2 SPEs forming on SiO_2 nano-pillars and GaP dimer nano-antennas. Adapted from reference [182].

photons. The final estimation of quantum efficiency of the WSe_2 SPEs forming on GaP dimer nano-antennas (red bars) and SiO_2 nano-pillars (blue bars), corrected for the total collection efficiency of the optical setup and resonator, is shown in Fig. 6.12.

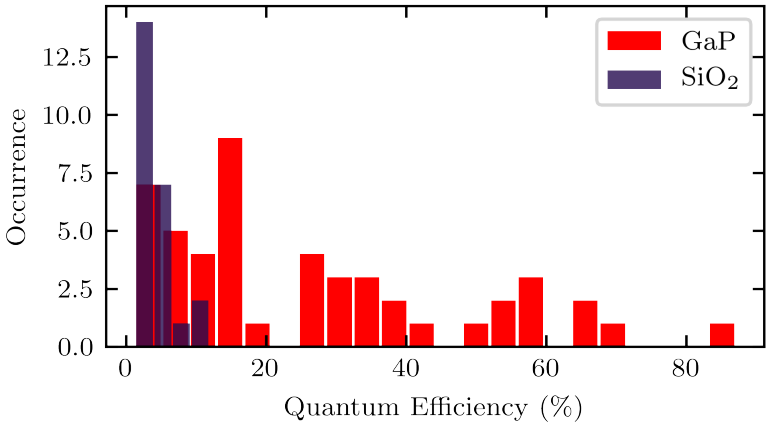

Fig. 6.12 Calculated quantum efficiency of SPEs in WSe_2 forming on GaP dimer nano-antennas (red) and on SiO_2 nano-pillars (blue). Adapted from reference [182].

The average quantum efficiency *QE* of the SPEs forming on the SiO_2 substrate is 4±2% consistent with previous reports [98]. Thus the quantum emitters forming on SiO_2 nano-pillars, shown in the bottom left portion of Fig. 6.11, are mainly defined by short non-radiative processes. For emitters on GaP the average *QE* is higher at 21±3% with some SPEs reaching values as high as 86%, corresponding to a single photon emission rate of 69 MHz and a brightness at the first lens of 0.06 [97]. This suggests that the lifetimes of many SPEs forming on the GaP substrate are largely defined by the radiative component. A red and blue area highlighting emitters with quantum efficiency of more or less than 10% is added to Fig. 6.11(d). The high *QE* emitters forming on GaP dimer nano-antennas exhibit

a large range of lifetimes (4 - 200 ns). The long-lived (>10 ns) high *QE* SPEs shown in the top right portion of Fig. 6.11(d) suggest long radiative and longer non-radiative decay times as previously suggested by the abundance of long-lived emitters at a relatively small range of emission energies. Such long emitter lifetimes were previously observed only in hexagonal boron nitride encapsulated WSe_2 monolayers [129] where non-radiative processes are known to be suppressed. In the case of emitters forming on GaP dimer nano-antennas, reduced non-radiative channels could be a result of the high surface quality of crystalline GaP structures as opposed to thermally grown SiO_2 or due to a non-negligible probability that some SPEs are formed in a suspended portion of the monolayer as it is stretched either across the dimer gap or between a nano-pillar and the planar substrate [116]. In either case, this suggests that the intrinsic radiative lifetimes of WSe_2 single photon emitters may greatly exceed previously measured times on the order of 10 ns or less. The upper left portion of Fig. 6.11(d), displaying high *QE* short-lived emitters may be a result of a wide confinement potential well which would result in short radiative decay times. However, the short lifetimes of these high *QE* SPEs are more likely to be a result of Purcell enhanced radiative decay which increases the quantum efficiency. This can occur if the quantum emitters form in close proximity to a near-field hotspot where there is a higher local density of optical states. The Purcell enhancement factor in either short or long-lived emitters forming on GaP dimer nano-antennas cannot be precisely determined as the intrinsic radiative decay of WSe_2 emitters is not known and the lifetimes of the more than 50 SPEs recorded in these experiments exceeds one order of magnitude. The enhanced quantum efficiency observed is a second factor, from equation 6.2, which can contribute to the increase in PL intensity and decrease in saturation powers of SPEs on GaP dimer nano-antennas when compared to SiO_2 nano-pillars. The maximum contribution expected from the quantum efficiency enhancement is an order of magnitude as shown in Fig. 6.2.

6.6 Dynamics of exciton formation in strain-induced SPEs

The enhanced quantum efficiency in emitters forming on GaP dimer nano-antennas allows further insights into the dynamics of the WSe_2 2D/SPE system. As described in chapter 3, highly strained portions of the WSe_2 monolayer result in a reduced band gap at the K symmetry point in momentum space due to a reduction of the conduction band and an increase of the valence band energies. The transfer of a WSe_2 monolayer onto GaP nano-antennas induces such strain leading to the band structure spatial profile shown in Fig. 6.13(a). As free excitons are funneled into the strained region, a fraction of these may be captured into a

0D state, formed either by a defect state or a nano-scale strain island, and lead to quantum emission at energies below the bright and dark exciton resonances in un-strained WSe_2.

Due to the increased brightness and quantum efficiency *QE* of the SPEs forming on GaP dimer nano-antennas, the exciton relaxation and recombination dynamics can be closely studied. Fig. 6.13(b) shows the PL spectrum of an SPE exhibiting a quantum efficiency of 86%, therefore, non-radiative decay channels are suppressed for this emitter. The time-resolved PL decay trace for this same emitter under various 20 MHz pulsed excitation powers, shown in Fig. 6.13(c), consists of a short rise time and long lifetime. The different average excitation powers of 1, 100 and 1000 nW correspond to below, close to and far greater than the saturation power for this SPE respectively. The inset focuses on the rise times of the traces immediately after the laser excitation pulse which is shown as a dotted line in the larger figure. The rise time clearly shortens with increasing excitation power while the PL decay exhibits only a relatively small shortening.
This data is then fit with a simple empirical model assuming a non-radiative exciton reservoir (funneled free excitons) which feeds into an SPE two-level emitter. This results in the following system of two differential equations:

$$\begin{aligned} \frac{dn_1}{dt} &= -\frac{n_1}{\tau_1} + \frac{n_X}{\tau_2}, \\ \frac{dn_X}{dt} &= -\frac{n_X}{\tau_2} \end{aligned} \tag{6.3}$$

where n_1 is the population of the excited state of the two-level emitter and n_X is the population of the exciton reservoir. Thus, $\tau_1 = (\gamma_r + \gamma_{nr})^{-1}$ is the recombination time of the quantum emission defined by the radiative γ_r and non-radiative γ_{nr} decay rate, while $\tau_2 = (\Gamma_t + \Gamma_{nr})$ is the exciton reservoir decay defined by the trapping rate into the strain-induced SPE state and non-radiative decay channels of the free excitons. This model excludes Auger recombination and saturation processes as these will be discussed later. The analytical solution to these differential equations has the following form:

$$n_1 = e^{-\frac{t}{\tau_1}} \left[n_1(0) + A(e^{\frac{t}{\tau_1} - \frac{t}{\tau_2}} - 1) \right] \tag{6.4}$$

where $A = n_X(0)\frac{\tau_1}{\tau_2 - \tau_1}$. The initial conditions for each relative rate equation are $n_X(0)$ and $n_1(0)$. Equation 6.4 is subsequently used to fit the experimental PL dynamics to reveal the decay ($\tau_{decay} = \tau_1$) and rise time $\tau_{rise} = \tau_2$). The decay times, plotted in Fig. 6.13(e), decrease from 8.5 to 7.4 ns as the excitation power is increased from 1 to 1000 nW and persists at this value for even higher powers at 3000 nW. The rise times, plotted in Fig.

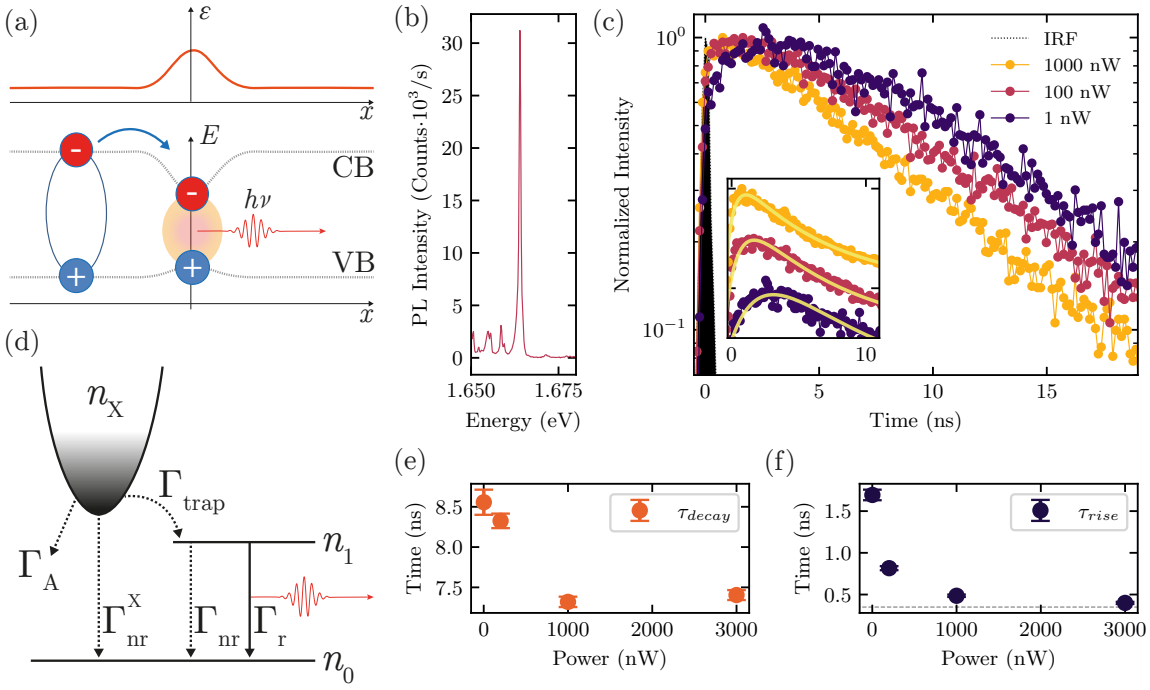

Fig. 6.13 **(a)** Bottom panel: Energy diagram representation of an exciton as an electron hole pair with the electron in the conduction band (CB) and the hole in the valence band (VB) funneling towards a strained region at the origin. The dashed lines representing the energy of the CB and VB are plotted as a function of position. Top panel: Plot of strain with position related to the bottom panel. **(b)** PL spectrum of a strain-induced WSe_2 SPE with a quantum efficiency of 86% and saturation power of 57 nW under 638 nm, 80 MHz pulsed excitation. **(c)** Time-resolved PL for the emitter highlighted in **(b)**. IRF is shown in gray. Inset represents a portion of the PL decay traces fitted with the analytical model discussed in equation 6.3 highlighting the change in rise time. Plots in the inset are offset vertically for display purposes. **(d)** Schematic illustration of the three level system presented by the model for which rate equations are shown in equation 6.5. This includes a dark exciton reservoir (n_X), an excited state in the quantum emitter (n_1) and a ground state for the emitter (n_0). It also displays the processes involving the radiative and non-radiative decay of the dark exciton and excited quantum state. **(e)** PL decay times of the emitter shown in **(b)** with increasing excitation power extracted from the fits shown in the inset of **(c)**. **(f)** PL rise times of the emitter shown in **(b)** with increasing excitation power extracted from the fits shown in the inset of **(c)**. The instrument response function is represented by a gray dashed line in **(f)**. Adapted from reference [182].

6.13(f), decreases from 1.7 ns to a time approaching the experimental resolution for the same increase in power. Additional PL dynamics traces at different excitation powers from other SPEs forming on GaP nano-antennas are shown in Fig. 6.14(a) and (b) with their respective PL spectrum in the insets. These results are also fit with the same analytical solution. In these cases, as the excitation power is increased, the rise time reduces to below the experimental resolution and only a single exponential decay is observed.

In order to understand the behavior of the rise and decay times with increasing power, several processes which influence both the populations of the free exciton reservoir and the

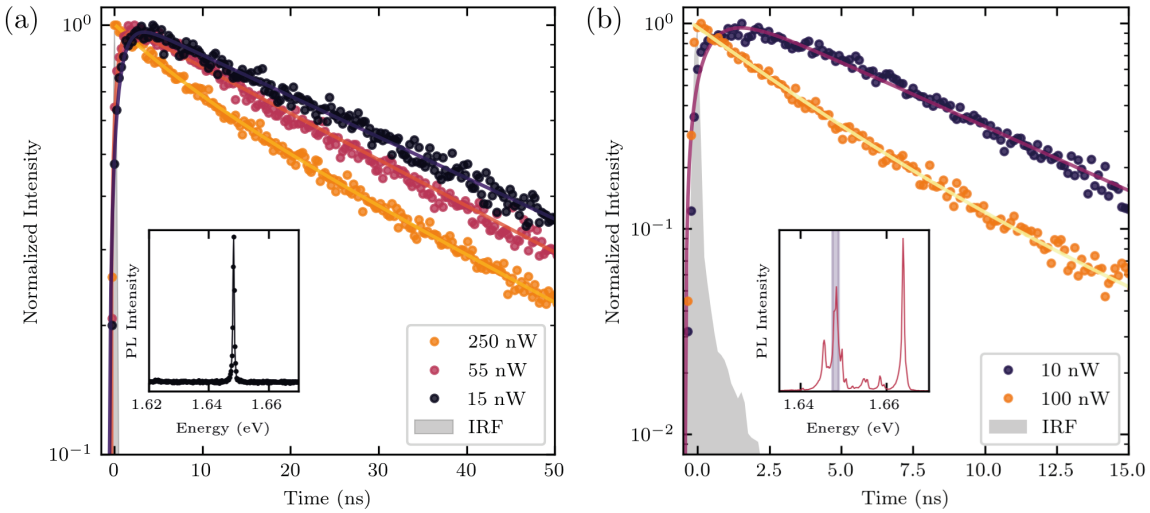

Fig. 6.14 **(a)** Power dependent PL lifetimes for the emitter shown in Fig. 6.7(a). Inset shows the spectrum of the emitter. **(b)** Power dependent PL lifetimes for the low energy emitters forming on the GaP nano-antenna where the emitter in Fig. 6.13(b) is observed. Inset shows the entire spectrum at this position with the emitter studied highlighted in gray. IRFs are shown in gray. Adapted from reference [182].

SPE state must be considered. As the lowest energy state hosting free excitons in the 2D WSe_2 monolayer, the dark exciton discussed in chapter 2 is an ideal candidate for the exciton reservoir in the empirical model used to fit the PL dynamics results. This is also inferred due to the much shorter timescale of the bright exciton recombination at cryogenic temperatures (a few picoseconds [69, 185]). The WSe_2 dark exciton, which is initially populated by relaxation of hot carriers, can decay via sample-dependent non-radiative recombination with a rate Γ_{nr}^{X} and through exciton-exciton annihilation (Auger recombination) with a rate (Γ_A) [175, 186] which grows with increasing excitation power ($\propto n_X^2$). The last decay channel for this dark exciton, as discussed above, is trapping in the SPE state (Γ_t) which leads to a small reduction of the reservoir population (n_X) as this state can only host one exciton per excitation cycle. Once the quantum state is filled, such as at saturation, the trapping rate reduces to nothing. On the other hand, the 0D state is filled by the trapping of free excitons until saturation occurs, therefore the condition $0 \leq n_1 \leq 1$ applies to the this population. The decay of the SPE state, as stated before, is either through a radiative recombination leading to photoluminescence or through sample-dependent non-radiative channels. The conditions defined above yield a model which is schematically illustrated in Fig. 6.13(d) and also defined by the following rate equations:

$$\begin{aligned}\frac{dn_X}{dt} &= -[\Gamma_{nr}^X + \Gamma_t(1-n_1)]n_X - \Gamma_A n_X^2, \\ \frac{dn_1}{dt} &= -(\Gamma_r + \Gamma_{nr})n_1 + \Gamma_t(1-n_1)n_X\end{aligned} \tag{6.5}$$

The factors of $(1-n_1)$ are included in these differential equations in order to take into account the conditions imposed on the two populations by saturation of the SPE state. The 0D state is modeled as a single excited and ground state in this model. The internal energy level structure of the SPE is further revealed in the next section. At the low excitation limit (1 nW of laser excitation power at 20 MHz repetition rate and 5% absorption in the WSe_2 monolayer), the density of created dark excitons is approximated to be $n_X \approx 3 \cdot 10^8$ cm^{-2}. As the GaP dimer nano-antenna near-field hotspots may increase the absorption of the monolayer by an order of magnitude, this estimate is a lower bound. At this low power, a dark exciton population of $n_X \approx 10^9$ cm^{-2} is not expected to lead to any noticeable Auger recombination [175]. Similarly, this low excitation power yields unsaturated PL intensity from the SPE ($n_1 \ll 1$). Thus, the Auger and saturation effects can be neglected and the rate equations describing the model illustrated in Fig. 6.13(d) will reduce to those in equation 6.3 and result in a solution similar to equation 6.4 where the second decay time will include both a non-radiative and trapping component as before ($\tau_2 = (\Gamma_t + \Gamma_{nr})$). For the emitter shown in Figs. 6.13(b) and (c), the non-radiative component can be neglected as the quantum efficiency for this SPE was calculated to be $QE = 86\%$. Therefore, an estimate of the trapping rate (Γ_t) of this emitter is taken to be the inverse of the rise time of the PL dynamics trace at an excitation of 1 nW. This indicates that the average dwelling time of the dark exciton before being captured into the SPE state is $1/\Gamma_t = \tau_t \approx 1.7ns$ at low excitation powers below the onset of saturation or exciton-exciton annihilation.

At increased excitation powers, the dark exciton population (n_X) and the SPE state population (n_1) will grow and the Auger and saturation terms become non-negligible. Therefore, they must be included into any conclusions about rates from the PL dynamics as they will change both rise and decay times. The population of the dark exciton state immediately after excitation is estimated to be on the order of $n_X(t=0) \approx 10^{10}$ cm^{-2} for a power of 100 nW and $n_X(t=0) \approx 10^{11}$ cm^{-2} for a power of 1000 nW, both shown in Fig. 6.13(c). For such carrier concentrations, the exciton-exciton annihilation process was found to be very efficient [175, 186].

A more detailed study at low powers could help identify the individual contributions of Auger recombination and SPE saturation. However, it is possible that at higher powers, the SPE PL intensity saturates not due to filling of the quantum state but due to very fast non-radiative depletion of the dark exciton population. The deposition of a monolayer of WSe_2

onto GaP dimer nano-antennas results in the formation of bright and high *QE* SPEs which do not require high excitation powers to yield many photon counts. The emitters forming in WSe_2 on SiO_2 nano-pillars, however, are dim due to a lower quantum efficiency and excitation rate, therefore, they require larger excitation powers for proper study which leads to exciton-exciton annihilation processes which further reduce the dark exciton population and brightness. This negative feedback mechanism through ever increasing excitation power can thus lead to a reduction of the quantum efficiency. Taking all of these effects together, GaP dimer nano-antennas induce higher excitation efficiency, higher quantum efficiency, a reduced Auger contribution and a slightly increased collection efficiency in the hybrid WSe_2 2D/SPE system when compared to SiO_2 nano-pillars which can account for the three orders of magnitude increase in the saturation powers and the intensity presented in Fig. 6.11. The variation of 2 to 4 orders of magnitude observed in the intensity and saturation powers is attributed to the uncertainty in the position and polarization of the formed WSe_2 single photon emitters as both are tied to the enhanced excitation and quantum efficiency which results in the reduced Auger contribution.

6.7 Coherence of WSe_2 SPEs on GaP dimer nano-antennas

The last study performed on WSe_2 single photon emitters forming on GaP dimer nano-antennas involves the coherence time of these emitters and attempts to ascertain the dominant dephasing mechanisms. A systematic measurement of the coherence time has so far not been reported, likely due to the low brightness of WSe_2 SPEs and the close spectral proximity of emission energies both of which are improved through coupling to gallium phosphide dimer nano-antenna resonances. Previous reports only investigated the coherence properties of these emitters under non resonant excitation and high power densities [98], concluding that power broadening is the dominant dephasing mechanism. In this study, the first-order correlation function ($g^{(1)}(\tau)$) is extracted from interference fringes measured on an APD after passing filtered single photon emission under continuous wave laser excitation through a Mach-Zender interferometer as described in the previous chapter [178].

The conclusion of the previous report was tested by performing a power dependent measurement using an above-band excitation (633 nm), shown in Fig. 6.15. The excitation powers were chosen below, close to and above the saturation power of the emitter. A single exponential decay fit of the fringe contrast values measured at different delay times ($g^{(1)}(\tau) \approx \exp(-|\tau|/T_2)$) yielded a coherence time range of T_2 = 1.8 - 2.8 ps which agrees with previous reports [98]. These results indicate that power broadening is not the dominant decoherence mechanism, however, it does lead to a reduction in the zero-time fringe contrast

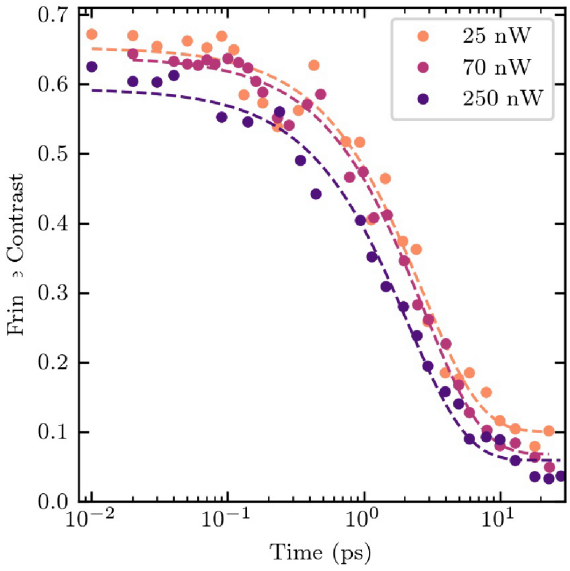

Fig. 6.15 Power dependent fringe contrast ($v(\tau)$) of a SPE in WSe_2 under above-band excitation (633 nm). Dashed lines represent single exponential decay fits to the experimental results. Small changes in the coherence time are observed with a reduction of the zero-time fringe contrast at high power. The recorded coherence times are as follows, 25 nW: 2.88 ps, 70nW: 2.68 ps, 250nW: 1.76 ps. Adapted from reference [182].

suggesting background contribution from processes such as Auger recombination which, as discussed in the previous section, is non-negligible for higher excitation powers.

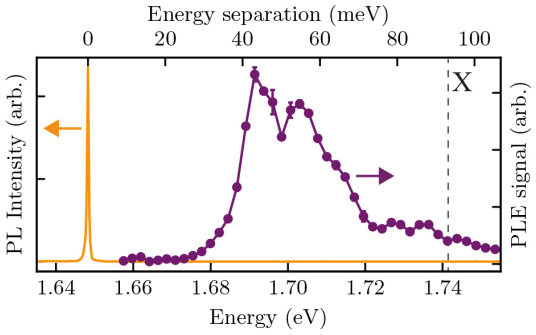

Fig. 6.16 Photoluminescence excitation experiment of the SPE shown in Fig. 6.7 with PL emission from the SPE shown in yellow and the intensity of this emission under different excitation wavelengths shown in purple.The PLE signal exhibits a series of peaks below the neutral exciton (X) attributed to higher energy confined excitations in the quantum emitter. Adapted from reference [182].

Next, a photoluminescence excitation experiment was performed to gain insight into the internal energy level structure of the single photon emission, the spectrum of which is shown in orange on the left side of Fig 6.16. This is accomplished by scanning the excitation energy of a continuous wave M Squared SOLSTIS laser and recording the intensity of the single

photon emitter peak. This measurement identified at least two higher energy states in the 0D potential well defining the SPE as shown in in Fig. 6.16 [11].

In order to determine if the creation of free excitons surrounding the SPE position influenced the coherence time, the fringe contrast was measured for an excitation below saturation at an above-band energy of 1.96 eV (633 nm) and quasi-resonantly at an energy of 1.71 eV (725 nm). Above-band excitation creates high energy free excitons which can introduce dephasing in the SPE emission either by locally changing the charge state or via scattering with phonons. Quasi-resonant excitation, however, should only create localized excitons in the SPE state. The recorded fringe contrast is shown in Fig. 6.17. By fitting the observed decay with a single exponential as for the previous measurement, the coherence time under above-band and quasi-resonant excitation yielded a T_2 value of 2.83 ± 0.2 ps and 3.12 ± 0.4 ps respectively. This slightly improved value of the coherence time under quasi-resonant excitation suggests that the presence of free excitons in the monolayer surrounding the SPE position is not the dominant dephasing mechanism although the zero-time fringe contrast is improved. The full-width at half maximum of the PL spectrum of the emitter, shown in the inset of Fig. 6.17, (450 μeV) corresponds to the observed value of T_2 = 2.9 ps via the well known relation, FWHM = $2\Gamma = 2\hbar/T_2$. This is an indication of very low spectral wandering and together with the single exponential decay of the fringe contrast suggests that WSe_2 SPE coherence is limited by pure dephasing, which is attributed to phonon interactions during recombination or relaxation from higher energy states internal to the potential well of the quantum state. A similar measurement of $g^{(1)}(\tau)$ under resonant excitation of the observed optical transition may yield information on the intrinsic coherence time of the strain-induced SPEs. The measurement of coherence is an average over many consecutive photon pairs which interfere as the phase is varied in one arm of the setup. The measurement of the indistinguishability of emitted photons, however, may be a more informative experiment as each photon pair is individually interfered on a beamsplitter and may leave together from one side of a beamsplitter. This may yield much larger indistinguishabilities than expected from these results.

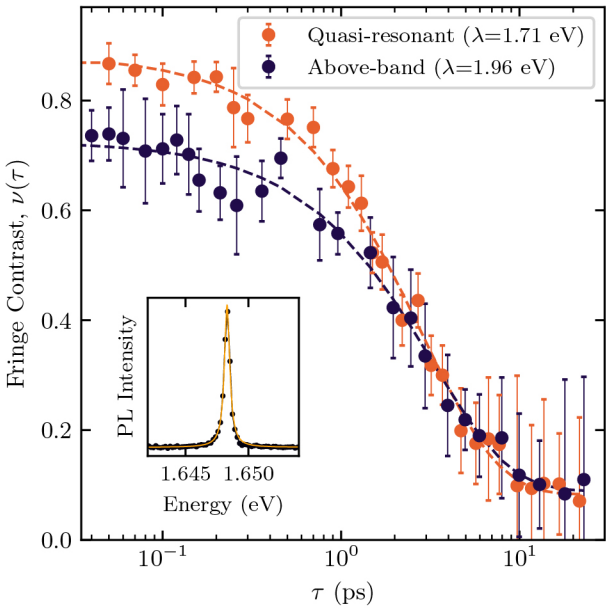

Fig. 6.17 Fringe contrast for two different excitation wavelengths. The above band excitation (blue dots) is at 638 nm (1.96 eV) and yields a coherence time of $T_2 = 2.83 \pm 0.2$ ps The quasi-resonant excitation (orange dots) is at 725 nm (1.71 eV) which is lower than the unstrained monolayer WSe_2 neutral exciton and it yields a coherence time of $T_2 = 3.12 \pm 0.4$ ps. The inset shows the PL spectrum of the SPE under study (black dots) fitted with a Lorentzian peak (yellow line). The linewidth of this emission is 450 μeV, corresponding to a coherence time of $T_2 = 2.9$ ps in close agreement to the measured value from the interferometric measurements. Adapted from reference [182].

6.8 Conclusion

In this chapter, I have discussed the potential use of high refractive index GaP dimer nano-antennas in order to position and enhance the properties of WSe_2 single photon emitters as opposed to previously used SiO_2 nano-pillars. The photonic properties of both structures were explored. Three factors, namely excitation enhancement, quantum efficiency and collection efficiency, leading to the photoluminescence enhancement of SPEs were discussed for both structures and simulated with FDTD simulations. The enhancement of these factors provided by the GaP dimer nano-antennas compared to SiO_2 nano-pillars was shown with a cumulative value of up to 800. In order to provide a comparison to emitters forming on GaP nano-antennas, a substrate of thermally grown SiO_2 was patterned with EBL and etched with RIE in order to fabricate an array of nano-pillars after which a monolayer of WSe_2 was transferred on top. The cryogenic spectral, polarization, power dependent, lifetime, and stability properties of SPEs forming on SiO_2 nano-pillars recorded agreed with previous reports therefore providing an ideal platform for comparison. Next, a monolayer of WSe_2 was similarly deposited onto an array of GaP nano-antennas with varying radius. The room temperature PL of the layer showed enhancement of emission surrounding the nano-antenna

positions suggesting exciton funneling. The cryogenic PL of the monolayer exhibited very bright (>30 kHz), localized, often spectrally isolated, narrow-linewidth emission centered at the position of nano-antennas. An HBT measurement confirmed the single photon nature of the emission with a $g^{(2)}(0)$ value of 0.26 ± 0.03 which is consistent with the previously reported range of 0.022 to 0.30 [10, 12, 91, 99–101]. The emission was also linearly polarized and more stable than for SPEs forming on SiO_2 nano-pillars. The spectra at many nano-antenna sites yielded a structure of few high energy, long lived emitters together with a multitude of low energy, short-lived emitters and negligible background emission from the band of localized states which can be observed in the emission from the WSe_2 on SiO_2 nano-pillars. The high energy peaks also exhibited power saturation at higher intensities than the multidude of peaks. A highly-resolved spectrum of these emitters showed a fine structure splitting for the high energy emitters with values of 600-800 μeV which agrees with previous reports [10]. The low energy emitters did not show any FSS, however, they showed near unity degree of linear polarization. These properties suggest that the high and low energy emitters originate from different confinement potential wells and may be a result of various nano-scale strain islands or defects. Lastly, strain was confirmed to influence the emission energies of the SPEs forming on GaP dimer nano-antennas. The smaller structures, inducing higher strains in the monolayer, yielded more red-shifted emitters.

Next, a comparison of emitters forming on GaP dimer nano-antennas and SiO_2 nano-pillars yielded a 10^2 to 10^4 PL intensity enhancement as well as similar in magnitude reduction of the saturation power for the same structures respectively. PL decay times of 4 to 200 ns were recorded for the SPEs forming on GaP nano-antennas, while emitters on SiO_2 nano-pillars yielded lifetimes below 10 ns as previously reported. This indicated enhanced quantum efficiency of the 2D/0D WSe_2 system and was confirmed by comparing the photon detection rate per excitation cycle under pulsed excitation for each emitter after a calibration of the collection efficiency. This yielded an average quantum efficiency of 4% and 21% for emitters on SiO_2 and GaP respectively with a maximal QE of 86% for an emitter on the gallium phosphide dimers. The maximally achieved quantum efficiencies on GaP dimers is higher than previously reported (65% [98]) while the average is slightly lower (44% [98]). The long-lived emitters forming on the GaP nano-antennas were attributed to reduced non-radiative decay channels, revealing a possibly much longer radiative decay time than previously reported. Short-lived emitters on the same structures appear to have also experienced Purcell enhancement.

A systematic power dependent study of the PL dynamics enabled by the enhanced quantum efficiency on GaP dimer nano-antennas provided insight into the relaxation and recombination mechanisms of the 2D/0D WSe_2 system. An energy level model involving the

capture of de-localized dark excitons into the SPE state was suggested to describe the system with the addition of non-radiative decay processes in both the SPE and higher energy exciton state as well as exciton-exciton annihilation which is relevant at high excitation powers. The high quantum efficiency of emitters on GaP dimer nano-antennas allowed the first report of an average dwelling time of a dark exciton before being trapped into the 0D state ($\tau_t \approx 1.7$ ns) at powers below saturation. The 2 to 4 orders of magnitude PL enhancement of emitters forming on GaP nano-antennas when compared to SiO_2 nano-pillars is accounted for by an enhanced excitation, quantum and collection efficiency as well as a reduced Auger contribution at the low excitation powers enabled by the high *QE* after careful study of the provided model using the power dependent PL dynamics. The saturation behavior observed for emitters forming on both structures were understood to not only depend on the filling of the quantum state but also on Auger processes which deplete the higher energy dark exciton reservoir.

The enhanced quantum efficiency, however, does not lead to a long single photon coherence time (3.12$\pm$0.4 ps) as measured using an interferometry setup. This value is much lower than that measured for III-V quantum dots (400-770 ps) [105, 106] or even single photon emitters in hexagonal boron nitride (hBN) (81 ps) [107]. An attempt to attribute the dominant dephasing mechanism to power broadening or dephasing induced by above-band excitation failed, however, this provided the insight that the coherence time may be largely limited by pure dephasing through phonon interactions with the SPE state. An option available to improve the coherence time of these emitters could be the encapsulation of the WSe_2 monolayer by hBN which reduces incoherent non-radiative processes due to the proximity of the substrate and also does not permit the adsorption of molecules onto the emissive layer. The encapsulating hBN layers will also dampen any phonon emission and may reduce the pure dephasing rate as well.

These results assert that high refractive index dielectric nano-antennas exhibiting photonic resonances provide many advantages for producing and studying bright SPEs in monolayer WSe_2 while also illuminating the limitations of previously used low-refractive-index SiO_2 or polymer nano-pillars. Emitters formed on such structures require excitation powers resulting in a negative feedback loop due to increased exciton-exciton annihilation which further requires more power to observe WSe_2 single photon emitters.

Chapter 7

WS_2 nano-antennas

7.1 Introduction

As we discussed in previous chapters TMDs have drawn a large scientific interest in the past decade mainly due to their unique optical and excitonic properties in the monolayer limit [8, 64]. They have also been integrated with nano-photonic structures such as plasmonic and dielectric cavities to achieve weak and strong coupling [34, 150, 187–189], low-threshold lasing [36], coupling to collective resonances in periodic structures [190, 191] and Purcell enhancement of WSe_2 (SPEs) [42, 98]. In the previous chapter of this thesis, I also discussed the quantum efficiency enhancement of these SPEs [182]. This has been limited to single and few-layer TMD samples integrated with photonic structures in different material systems [192].

Nano-photonic structures fabricated from 2D materials, however, have recently been demonstrated, expanding very quickly in the use of hexagonal boron nitride (hBN). Recent reports utilize electron beam induced and reactive ion etching to fabricate suspended one and two-dimensional photonic crystal cavities as well as ring resonators, circular bragg gratings and waveguides from this material [193, 194]. Simply exfoliated flakes of hBN have also been shown to control the spontaneous emission rate of excitons in MoS_2 monolayers [195] while micro-rotator structures etched into carefully selected flakes and manipulated with atomic force microscopy (AFM) has yielded modulation of second harmonic generation (SHG) enhancement.

Photonic resonators fabricated in TMDs, however, have only recently been demonstrated even though this material system offers a number of advantages such as a large refractive index (n>4) and transparency window in the visible [46]. Similar to other 2D materials the weak van-der-Waals attractive forces allow simple exfoliation of crystals for the fabrication process as well as a compatibility with a variety of substrates. Another noteworthy advantage

is the large optical anisotropy due to the layered nature of the crystal [196]. Previous reports have demonstrated strong coupling in WS_2 photonic crystals [163], gratings [197], nano-antenna resonators [46] and bulk flakes of different TMDs [198]. Waveguiding has also been achieved in monolayer WS_2 photonic crystals [199] and bulk TMD flakes [196]. Separate works involving TMD nano-disk Mie resonator anapole resonances have also been shown to provide second and third harmonic generation enhancement [47] and Raman scattering enhancement [200]. Numerical studies have also considered the possibility of entire optical circuits using TMD materials [201] as well as MoS_2 nano-resonator modes [202] and WS_2 nano-antenna metasurface resonances [203].

In this chapter, I will present experimental dark field spectroscopy results of WS_2 monomer and dimer nano-antennas fabricated in mechanically exfoliated (25-500 nm thick) flakes onto SiO_2/Si sbstrates using electron beam lithography (EBL) and reactive ion etching (RIE). The dark field spectroscopy experimental results will be compared to numerical finite-difference time-domain (FDTD) simulations of the same geometries. I will also explore the identification of resonant Mie modes using further numerical analysis of the scattered and internal fields from these structures. Next, I will discuss second harmonic generation experiments which result in enhanced signal due to coupling with an anapole resonance as well as polarization dependent signal from the dimer nano-antennas. Lastly, I will discuss the results of dark field spectroscopy after employing a novel method of translating and rotating constituent nano-pillars in dimer nano-antennas using post-fabrication atomic force microscopy (AFM). This work has also been reported in the following reference [53].

7.2 Fabrication of nano-antennas

Bulk crystals of WS_2 consist of covalently bonded monolayers, displayed in Fig. 7.1, with a hexagonal crystal structure stacked vertically and held together by van-der-Waals forces. WS_2 flakes were exfoliated onto a 290 nm SiO_2/Si substrate yielding various thicknesses up to 500 nm. Fabrication included spinning of a positive resist onto the exfoliated flakes, patterning circular or square disks with varying radii using EBL, and RIE to transfer the pattern into the WS_2 crystal until the etch depth matched the original flake height thereby defining the nano-antenna height. The subsequent fabrication procedure (carried out by collaborators at the University of York [53]) can be seen in Fig. 7.1(b). The choice of etching recipe allowed the fabrication of three different nano-pillar geometries with potentially atomically sharp vertices. An anisotropic etch using a mixture of CHF_3 and SF_6 gases, a high DC bias and low chamber pressure resulted in circular nano-pillars with vertical sidewalls due to the physical

process. An atomic force microscopy scan and a scanning electron microscopy (SEM) image are shown in the upper row of Fig. 7.1(c).

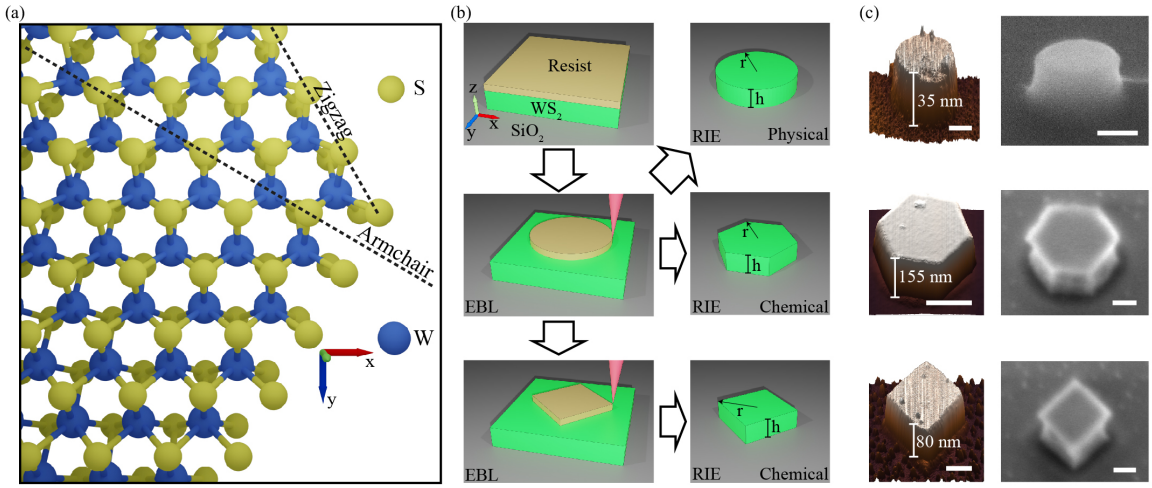

Fig. 7.1 **(a)** Schematic of a top view of monolayer WS_2 at the position of a hexagonal nano-antenna vertex. The edge of the monolayer is along the zigzag axis as this is the more stable of the crystal axes. **(b)** Fabrication procedure of different geometries of WS_2 nano-antennas. The radius is defined as usual for the circular geometry. For the hexagonal and square geometries the radius is the distance from the center of the structure to an outside vertex. **(c)** AFM scans (left column) and SEM images (right column) of the three different types of fabricated nano-antennas. Scale bars in AFM = 200 nm. Scale bars in SEM = 100 nm. Adapted from reference [53].

The second, more isotropic etch, resulted from only SF_6 gas, a reduced DC bias and increased chamber pressure. This chemical process yielded a hexagonal geometry with vertical sidewalls and a radius defined from the center of the structure to one of the outside vertices as shown in Fig. 7.1(b). This definition corresponds to the radius of the previously circular resist pattern. This etching recipe preferentially removed the WS_2 crystal in the direction of the armchair crystal axis (defined in Fig. 7.1(a)) leading to zigzag terminated sidewalls of a hexagonal geometry following the crystal symmetry. DFT results of previous reports also predict the higher stability of the zigzag axis in TMD crystals [54, 55]. An AFM scan and SEM image of the hexagonal geometry are shown in the middle row of Fig. 7.1(c).

The last geometry that was achieved using a combination of resist patterning and chemical etching of the WS_2 crystal yielded a square geometry nano-pillar. The EBL patterning was first used to define a square pattern with sides oriented parallel to the zigzag axis of the crystal. The subsequent chemical etching recipe similarly removed the crystal in the armchair axis ultimately leading to 90° angles, thereby describing a square nano-antenna geometry. An AFM scan and SEM image of fabricated nano-pillars is displayed in the lower row of Fig. 7.1(c). The latter two geometries achieved may yield atomically sharp vertices, however, the

measurement procedure of the radius of curvature was resolution limited due to a finite AFM cantilever tip radius (5 nm).

7.3 Photonic resonances of WS_2 monomer nano-antennas

Once fabricated, the single nano-pillar (monomer) nano-antennas with a hexagonal geometry were probed with a dark field spectroscopy setup described in chapter 5. This study included monomer nano-antennas of three different heights (170 nm, 60 nm and 25 nm) over a range of radii (100 - 370 nm). These spectra are displayed in Figs. 7.2(a)-(c). After measurement of the radius and height of the nano-antennas using SEM and AFM analysis, numerical (FDTD) simulations of identical geometries were carried out. These can be seen in Figs. 7.2(d)-(f) with close agreement to experiment. As expected from Mie theory, the experiments and simulations show a red-shift of all resonances with increasing radius. However, the height of the nano-antennas also plays a large role in tuning the spectral positions of the resonances. A comparison of the experiment and simulation at each height for a single radius, highlighted by a dashed white line in the upper panels, is displayed in Figs. 7.2(g)-(i). A decrease in height from 170 nm to 25 nm, blue-shifts all resonances despite the increase in radius from 150 to 290 respectively, suggesting that the nano-antenna height is an even more powerful tool for engineering of nano-antenna resonances.

The comparison between simulation and experiment allowed the identification of an electric dipole resonance with small contributions from higher order modes as well as anapole and higher order anapole mode (HOAM) present in the fabricated structures. In order to discern the contribution of different multi-pole moments to the observed resonances, the total scattering cross section must be calculated as described in chapter 4. FDTD simulations and a Matlab open source script used to calculate the multi-pole expansion of the scattered fields was employed to study geometries identical to those of the the monomer nano-antennas which yield the results shown in Figs. 7.2(g)-(i) with the exception of placing them in vacuum [134]. The latter was set so that the broadening from the substrate was absent and the identification of individual resonances is simpler. The total scattering spectra extracted from these simulations will also not match that seen in Fig. 7.2 as this calculation takes into account scattering in all directions whereas dark field spectroscopy only records light scattered toward the collection optics. The scattering cross sections and their dipole, toroidal and quadrupole moment components are shown in Fig. 7.3(a), (b) and (c) for the geometries of (r = 150 nm, h = 170 nm), (r = 200 nm, h = 60 nm) and (r = 290 nm, h = 25 nm) respectively.

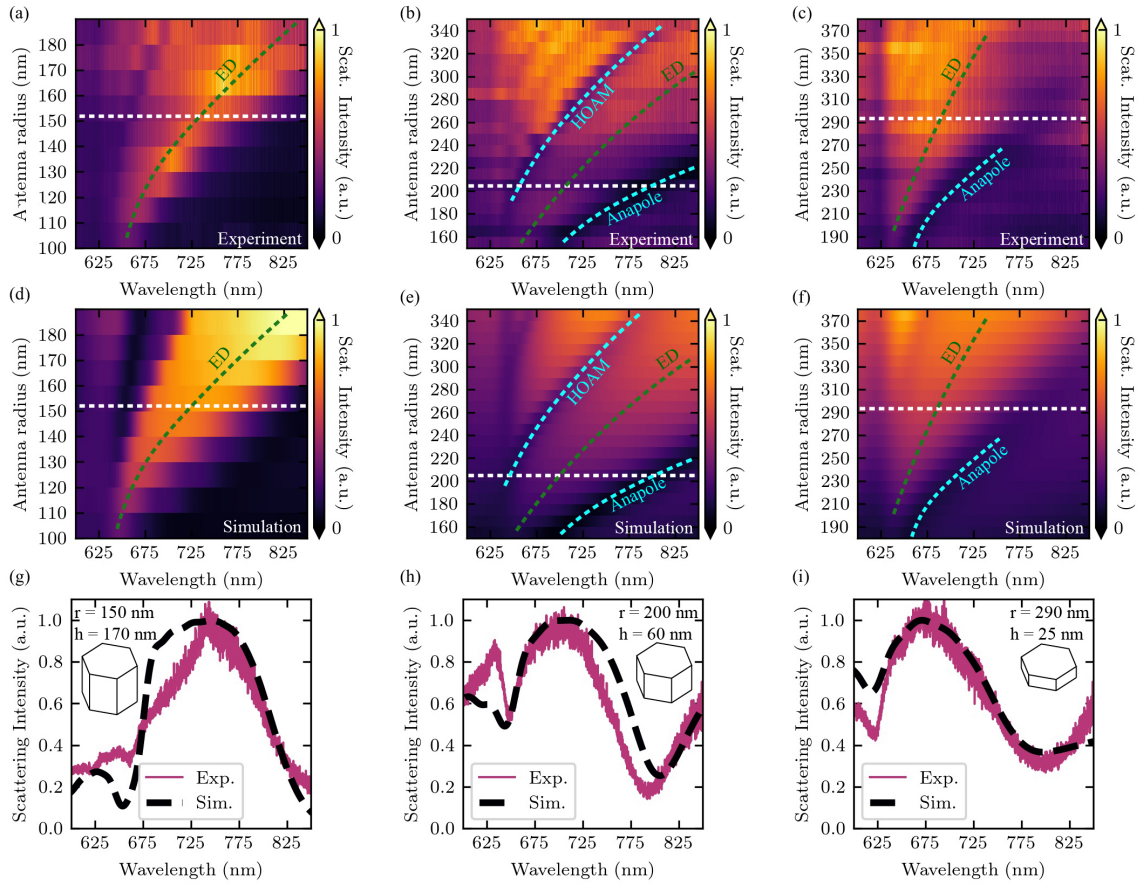

Fig. 7.2 **(a)-(c)** Experimental dark field spectra for nano-antennas with a range of radii and heights of **(a)** 170 nm, **(b)** 60 nm,**(c)** 25 nm. Electric dipole (ED), anapole, and higher order anapole modes (HOAM) are identified. **(d)-(f)** Simulated scattering cross sections for the geometries of the nano-antennas of the experimentally measured structures. The identification of the resonances is confirmed by the numerical results. **(g)-(i)** Comparison of experimental dark field spectra and simulated scattering cross sections for three nano-antennas with the following radii and heights: **(g)** r = 150 nm, h = 170 nm, **(h)** r = 200 nm, h = 60 nm, **(i)** r = 290 nm, h = 25 nm. White dashed lines in the upper panels identify the spectra and cross sections plotted. Adapted from reference [53].

As displayed in Fig. 7.3, the electric dipole moment contribution is dominant for all three geometries with much smaller contributions from the higher order components, thereby allowing the identification of the resonance labeled as ED in Fig. 7.2. For the largest geometry, there is a contribution from the magnetic dipole moment which becomes more important at lower energy and therefore has an overall small effect on the ED resonance. In the smaller heights shown in Fig. 7.3(b) and (c) there is an additional non-negligible contribution of the toroidal moment which destructively interferes with the electric dipole moment in the far-field and defines the anapole and higher order anapole modes also labeled in Fig. 7.2. An even smaller, yet non-negligible, contribution from the quadrupole magnetic

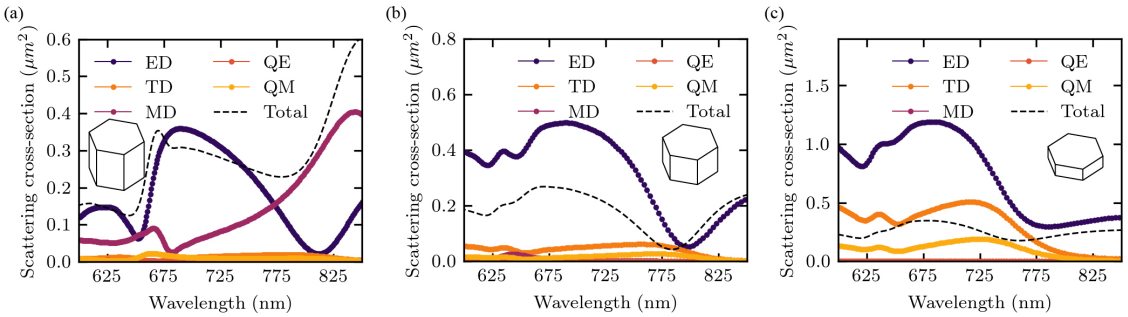

Fig. 7.3 Scattering cross section and its decomposition into multi-pole components for a hexagonal nano-antenna with **(a)** r = 150 nm and h = 170 nm, **(b)** r = 200 nm and h = 60 nm, **(c)** r = 290 nm and h = 60 nm. The electric dipole moment contribution is dominant for each size with a non-negligible magnetic dipole moment contribution for **(a)**, a magnetic quadrupole moment for **(c)** and a toroidal moment for **(b)** and **(c)**. All simulations have been performed in vacuum.

moment is also seen. This component allows the confined energy in the anapole mode to radiate away and therefore leads to the non-zero scattering intensity at this wavelength.

The condition for the formation of an anapole mode in Mie resonators, as was discussed in Chapter 4, dictates that the contributions from the electric dipole moment and the toroidal moment must match and their phases must cancel ($p = -ikT$) [134, 167]. Therefore, the phase of the electric dipole and the negative of the phase of the toroidal contribution with respect to wavelength is plotted in Fig. 7.4(a) to identify points at which these two curves intersect and define anapole and higher order anapole modes. For a hexagonal monomer, nano-antenna with r = 250 nm and h = 60 nm, there are three crossings of the phase contributions at 666 nm, 705 nm and 856 nm. The total scattering cross section (dashed line in Fig. 7.4(a)), which takes into account higher order modes as well, also exhibits minima in intensity at similar wavelengths providing further proof that these resonances confine the incident plane wave.

The magnetic $(|H|/|H_0|)^2$ and electric field $(|E|/|E_0|)^2$ intensities compared to vacuum levels at the anapole (891 nm) and higher order anapole (677.5 nm) minima in scattering are shown in figure 7.4(b) and (c) for a hexagonal nano-antenna with a radius of 250 nm and a height of 60 nm. The exciting plane wave is incident from the top of the structure (z-axis) with the images being a horizontal cross sectional cut through the middle of the antenna height. The polarization of the excitation wave is shown by the double white arrow in the top left of the panels. The colors show the field intensities while the gray field lines represent the electric charge currents inside and surrounding the structure clearly identifying this as an anapole mode induced by the interference of a magnetic toroidal mode and an electric dipole mode [46, 47, 167].

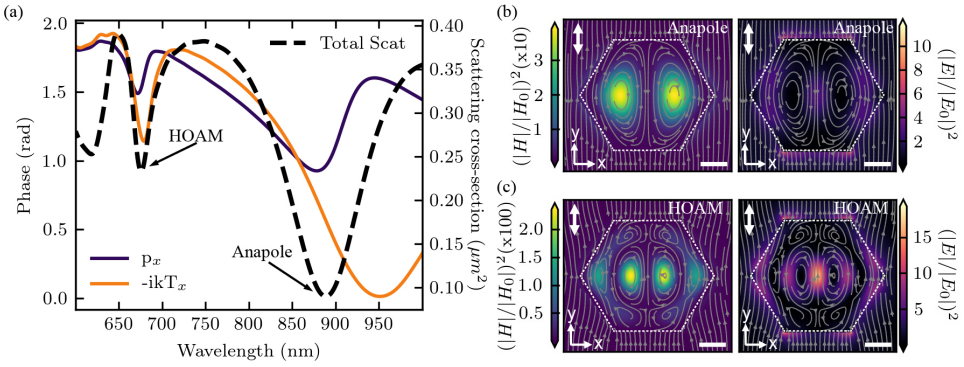

Fig. 7.4 **(a)** Simulation of the phases of the electric dipole (purple line) and toroidal moment (yellow line) contributions to the total scattering cross section (black dashed line). Crossing points of the phases of the two contributions identify the formation of anapole and higher order anapole modes which are seen as minima in the total scattering cross section. **(b),(c)** A cross sectional top view of the magnetic and electric field intensities is taken through the middle of the nano-antenna height (h = 30 nm). The gray field lines indicate the electric charge currents responsible for the anapole modes. Polarization of the incident plane wave to excite the resonance is shown by the white double arrow in the upper left of each panel. Dashed white outlines represent the physical edges of the structure. The field intensities in **(b)** are recorded at the anapole resonance (891 nm) and those in **(c)** are recorded at the HOAM (677.5 nm). Radius = 250 nm, Height = 60 nm. Scale bar = 100 nm.

The measurement of monomer nano-antennas was limited to the hexagonal geometry as large changes in the scattering spectra were not expected for the different geometries. In order to prove this, the problem was studied numerically. The definition of the radius of the structures leaves the possibility of a change in volume when there is a change in geometry even if the radius remains the same. Since the modes inside the nano-antenna structures are Mie resonances, they are heavily dependent on the geometry and the volume of the high refractive index nano-antenna [40]. The radius of the nano-antennas is defined as the distance from the center of the structure to an outside vertex for the hexagonal and square nano-antennas. This convention was used as this is the value that is closest to the nominally defined radius in the resist pattern before etching thereby allowing the possibility to set a radius and subsequently define the desired geometry using only the etching method.

The simulated scattering cross section expected from the three different WS_2 nano-antenna geometries available for fabrication are displayed in Fig. 7.5. These calculations are performed in vacuum in order to allow simple identification of modes which broaden with the addition of a substrate. The same height (150 nm) and range of radii (80-250 nm) was used for the different geometries. A magnetic resonance denoted as MD, an electric dipole resonance denoted as ED and the more complex anapole and HOAM were all identified. It is interesting to note that all resonances blue-shift when moving from circular to hexagonal and square nano-antennas for the same radius as expected from the geometrical argument. Therefore, the choice of nano-antenna geometry provides more precise tuning of the nano-antenna modes.

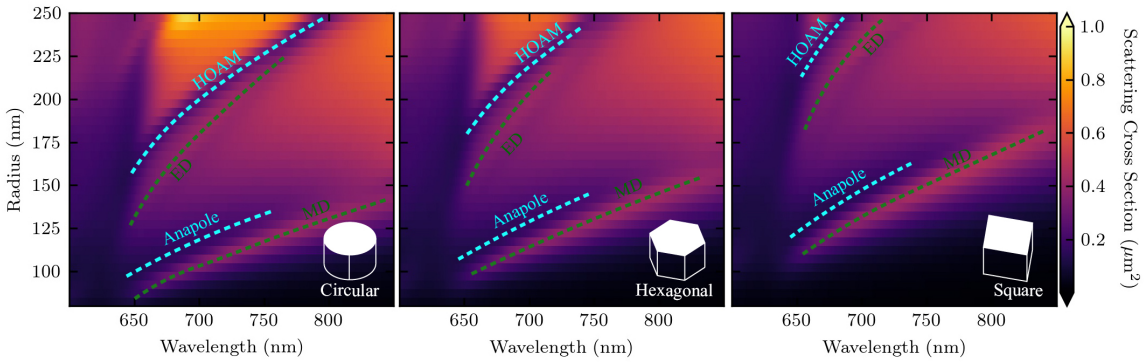

Fig. 7.5 A comparison of the scattering cross sections of monomer nano-antennas with different geometries yet the same height and radii. A magnetic dipole (MD), electric dipole (ED), anapole, and higher order anapole (HOAM) are identified. Adapted from reference [53].

7.4 Photonic resonances of WS_2 dimer nano-antennas

Next, a more complex architecture is considered by positioning two of the hexagonal monomer nano-antennas in close proximity, forming a dimer nano-antenna shown schematically in the left panel of Fig. 7.6(a). The right panel of the same figure displays an SEM image of a fabricated structure.

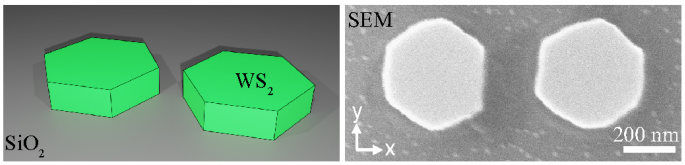

Fig. 7.6 Left panel: Schematic illustration of a hexagonal dimer nano-antenna. Right panel: Top view SEM image of a fabricated hexagonal dimer nano-antenna. Adapted from reference [53].

Unpolarized dark field spectroscopy was performed on an array of fabricated dimer nano-antennas with a height of h = 60 nm, a range of radii (168 nm to 216 nm) and nano-pillar separation gap of g = 130 nm. These are compared to FDTD simulated scattering cross sections with good agreement as shown in Fig. 7.7. The resonances in these spectra also red-shift with with increasing radius which asserts that the tuning mechanisms for dimers are the same as those for monomers. While a dipole resonance is observed, a major feature of these spectra is a minimum which redshifts from 730 nm to 840 nm with the above-mentioned change in radius resembling an anapole mode.

Three more dimer nano-antennas are selecting with the same height and radii within the previous range (r = 165 nm, 185 nm, 200 nm). The experimental and calculated scattering spectra are plotted together with a simulation of the confined electric energy at a cross-section

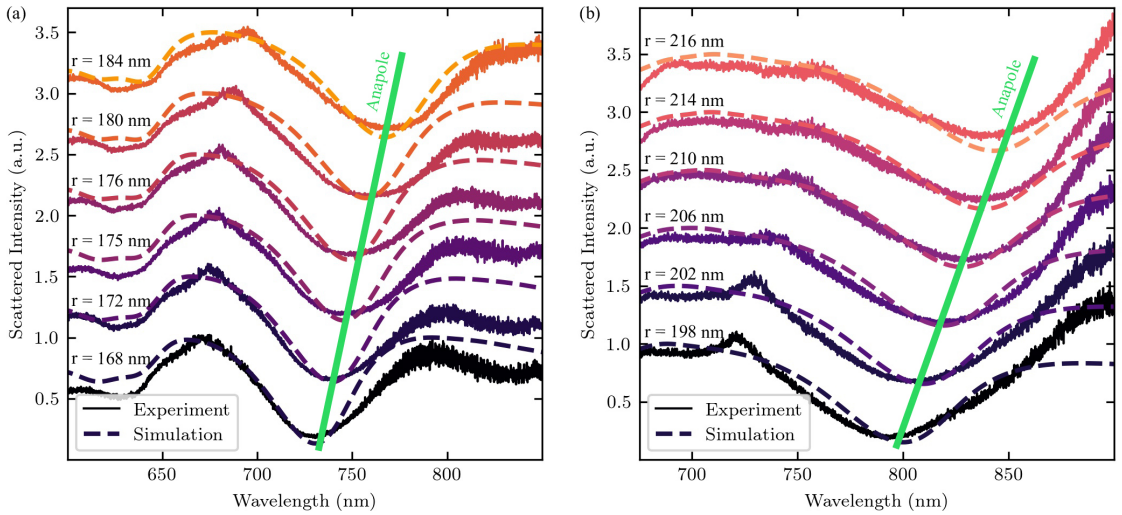

Fig. 7.7 **(a)** Vertically offset dark field spectra compared to simulations for a range of radii (168 nm to 184 nm) with a height of 60 nm. **(b)** Same as **(a)** for a different range of radii (198 nm to 216 nm) with the same height. The solid green line highlights the position of a resonance which closely resembles an anapole mode in these structures. Adapted from reference [53].

surface at the middle of the dimer height (h = 30 nm). This was simulated by integrating the electric field intensity distribution inside the boundaries of the nano-antenna geometry as described in chapter 5. As previously discussed in chapter 4, the anapole resonance corresponds to the destructive interference of an electric dipole resonance and a magnetic toroidal mode. This leads to the conclusion that far-field scattering as that measured in dark field spectroscopy would exhibit a minimum at the wavelength of this resonance. The energy injected by the incident plane wave cannot radiate away and therefore the confined electric energy must exhibit a maximum at this resonance position. As seen in Fig 7.8(a), the dashed red curves corresponding to the confined electric energy in the dimer nano-antenna peaks at a position for which the scattering exhibits a minimum. This is very strong evidence of a dimer anapole mode.

In order to provide further evidence of the identification of this resonance, the electric and magnetic field intensity spatial distribution for the mid-height cross-sectional surface used for the electric energy calculation is plotted in Fig. 7.8(b) with excitation polarization set perpendicular to the axis connecting the midpoints of the individual nano-pillars (dimer axis). The three anti-nodes seen in the electric field intensity distribution together with the two seen in the magnetic field intensity distribution confirm the presence of an anapole mode similar to that seen in monomer nano-antennas in the previous section.

Since this anapole resonance appears in a dimer nano-antenna instead of a single nano-particle such as the monomer nano-antenna, it is worth to compare the two. As discussed in

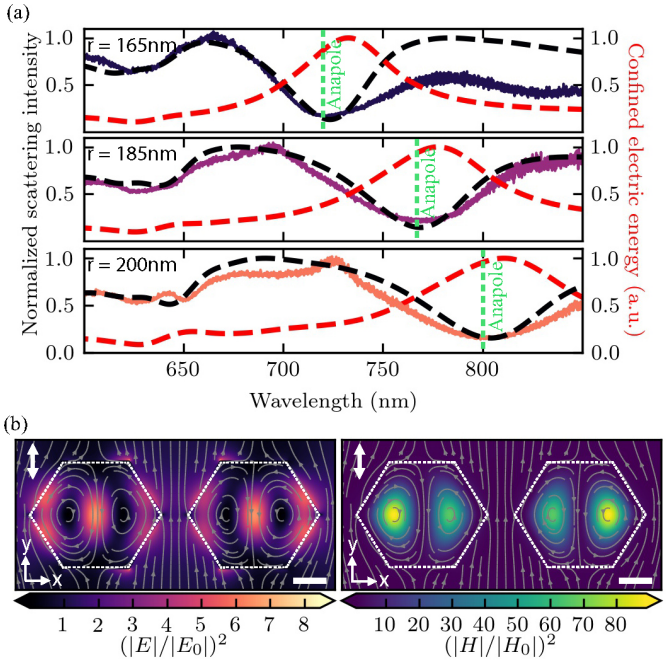

Fig. 7.8 **(a)** Dark field spectra from three hexagonal nano-antennas with a height of 60 nm, a gap distance of 130 nm and radii of 165 nm, 185 nm and 200 nm under unpolarized illumination. Dashed black lines represent simulated scattering cross sections of the nano-antenna geometries. Dashed red lines represent simulated electric energy confined within the dimer nano-antenna calculated for a cross-sectional surface at the midpoint of its height. The dashed green line highlights the position of the anapole resonance. **(b)** Top view of the spatial distribution of the electric (left panel) and magnetic (right panel) field intensities in and surrounding a dimer nano-antenna (r = 200 nm, h = 60 nm, g = 70 nm) for a cross-sectional surface at the midpoint of its height at the anapole resonance. The polarization of the excitation is depicted by the white double arrow. Gray field lines show the electric charge currents in and surrounding the nano-antenna. White outlines represent the extent of the nano-antenna geometry. Scale bars = 100 nm. Adapted from reference [53].

chapter 4, when two monomer nano-antennas are separated by a distance smaller or on the order of the wavelength of the resonances in the individual structures, these modes hybridize and split energetically. Two new cross-polarized modes emerge with a polarization along the dimer axis (X-pol) and perpendicular to it (Y-pol). In order to confirm this hybridization process in the WS_2 hexagonal dimer nano-antennas, the scattering cross section of two hexagonal nano-pillars for excitation polarizations X-pol and Y-pol with a varying radius is compared to that expected from two individual monomer nano-antennas in Fig. 7.9.

The scattering cross section of a dimer with three different gap separations (g = 50 nm, 500 nm, 2 μm) was simulated and compared to the same quantity for two isolated nano-pillars at the two polarizations (X-pol and Y-pol) as shown in Fig. 7.9. The scattering cross section results for the dimer with gap g = 2 μm correspond quite well to the doubled monomer results and also do not show a splitting for the two different excitation polarizations. As the gap is reduced to 500 nm and further to 50 nm, an energy splitting at the anapole mode minimum

(750-770 nm) and at the dipole resonance (670-700 nm) is observed for the two excitation polarizations clearly showing the expected hybridization of the monomer resonances.

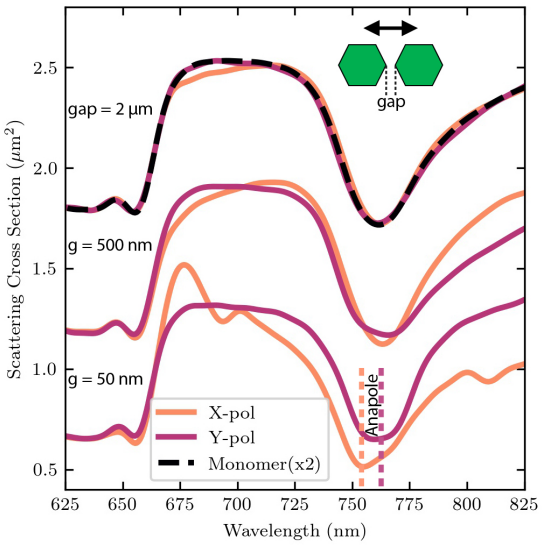

Fig. 7.9 Scattering cross sections simulated for a dimer nano-antenna (r = 250 nm, h = 150 nm.) with different gaps. The yellow lines repesent excitation polarization along the dimer axis and the red lines represent polarization perpendicular to it. The splitting of the anapole resonance into two cross-polarized modes is evident for smaller gap distances indicating hybridization of their individual modes. The spectra are vertically offset for display purposes. Adapted from reference [53].

To confirm whether this behavior is consistently observed in the fabricated dimer nano-antennas, dark field spectroscopy with polarization along the dimer axis and perpendicular to it is performed on the three geometries of hexagonal WS_2 dimer nano-antennas shown previously in Fig. 7.8(a). Fig. 7.10 displays the cross-polarized experimental results for structures with a height of 60 nm, radii of 165, 185 and 200 nm and gap of g = 130 nm. The black curves represent the results for a polarization along the dimer axis and the colored curves (purple, red and yellow) represent the perpendicular polarization. The energy splitting is clear for the smaller radii, but not as clear in the larger structure due to an unrelated low energy peak obscuring the anapole mode position.

A comparison of monomer and dimer anapole modes may yield interesting possibilities for applications in second harmonic generation. In order to do this, a numerical study of the nano-antennas with similar dimensions is performed. Firstly, an electric field intensity distribution for the monomer (r = 200 nm, h = 60 nm) and dimer (r = 200 nm, h = 60 nm, g = 70 nm) is calculated for a cross-sectional surface at mid-height and Y-pol excitation polarization, as shown in Fig. 7.11(a) and (b) respectively. Both structures exhibit the three electric field intensity anti-nodes expected for an anapole resonance with a difference that the dimer pattern is not symmetric with respect to a single nano-pillar but rather with respect

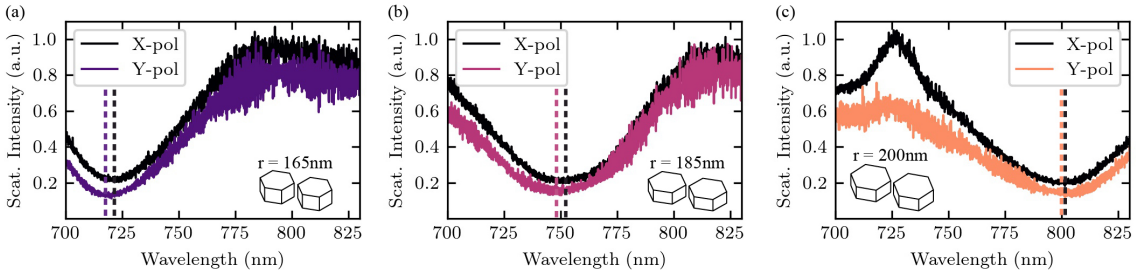

Fig. 7.10 Dark field scattering spectra for excitation polarization along the dimer axis (color plots) and perpendicular to it (black plots) for the dimers yielding the dark field spectra shown in Fig. 7.8(a) with a height of 60 nm, a gap of 130 nm and a radius of **(a)** 165 nm, **(b)** 185 nm and **(c)** 200 nm. Dashed lines corresponding to the position of the anapole resonance in each plot show the energy splitting due to hybridization of individual modes. Adapted from reference [53].

to the entire structure. The electric field intensity anti-nodes in the dimer nano-antenna also yield larger values over a smaller area indicating a more tightly confined electric energy.

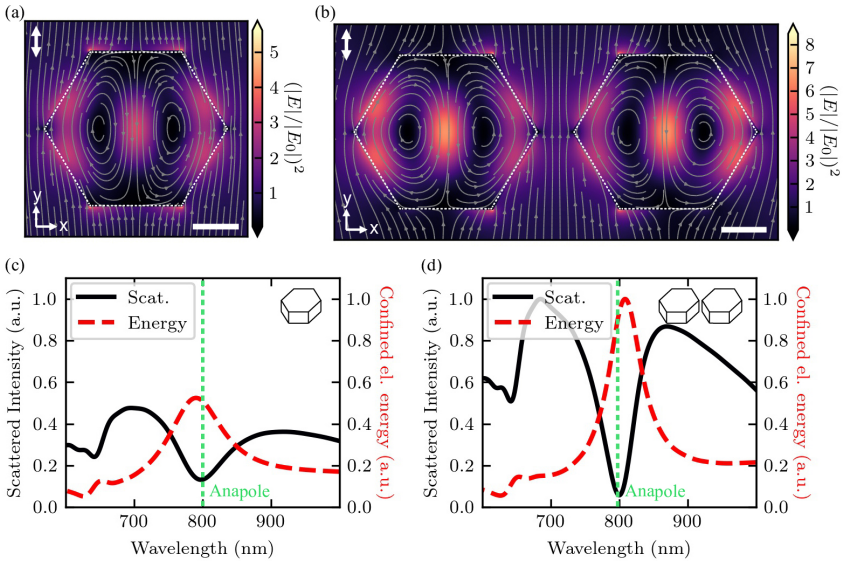

Fig. 7.11 **(a),(b)** Spatial distributions of the electric field intensity for a monomer (**(a)**, r = 200 nm, h = 60 nm) and dimer (**(b)**, r = 200 nm, h = 60 nm, g = 70 nm) in a cross-sectional surface at the midpoint of the structure's height. White double arrows show the polarization of the illumination. Gray field lines represent the electric charge currents in and surrounding the nano-antenna. Dashed white outlines show the outer edges of each structure. Scale bars = 100 nm. **(c),(d)** Scattering cross sections and confined electric energy in the surface at the midpoint of the antenna height simulated for the monomer **(c)** and dimer **(d)** shown in **(a)** and **(b)** respectively. The plots are normalized to the maximum of the dimer response for comparison. The vertical green dashed line shows the position of the anapole mode for each. Adapted from reference [53].

The confined electric energy obtained from an integration over the cross-section defined in Figs. 7.11(a) and (b) for a Y-pol excitation polarization is shown together with the scattering cross sections simulated for these structures in Fig. 7.11(c) and (d). The dimer resonance exhibits a deeper scattering minimum and an electric energy which is higher by a factor of

1.9 when compared to the monomer mode. Two un-coupled monomers would yield slightly higher electric energy than the dimer structure. This confined energy in both structures due to the non-radiative anapole mode is very advantageous for SHG enhancement as shown in the next section.

7.5 Second harmonic generation enhancement

As discussed in chapter 4, second harmonic generation is a second order process which, to a dipole approximation, scales with the electric energy at the excitation wavelength squared, $|W_E^S|^2$ [43]. Therefore, the electric energy confined to the inside of the nano-antennas described for Fig. 7.11 is expected to lead to second harmonic generation enhancement for excitation wavelengths at the spectral position of the anapole resonance.

In order to experimentally probe this expected SHG enhancement, a monomer (r = 215 nm, h = 50 nm) and dimer (r = 205 nm, h = 60 nm, g = 130 nm) nano-antenna, which both host anapole resonances near 800 nm, were probed with a fs-pulsed Ti-sapphire laser at 804 nm and the resulting second harmonic signal was detected using a spectrometer and CCD. For comparison, the SHG signal from a bulk flake of thickness 60 nm was also measured. The polarization of the excitation was set perpendicular to the dimer axis (Y-pol). Fig. 7.12(a) shows the second harmonic generated spectrum at 402 nm which has been normalized to the excited area in each measurement. For the signal recorded from the bulk flake, the spectrum was normalized to the area of the laser spot ($A = \pi r^2$ for r = 700 nm), whereas, for the nano-antenna measurements, the intensities were normalized to the area of each ($A_{di} = 3r^2\sqrt{3}$ for the dimer with r = 205 nm and $A_{mono} = 3r^2\sqrt{3}/2$ for the monomer with r = 215 nm) as the SiO_2/Si substrate is not expected to nor did yielded any SHG signal. As seen in the figure, the signal recorded for the nano-antennas are comparable and much higher than the bulk measurement. The SHG enhancement as a result of the nano-antenna resonance was extracted by integrating the spectra from Fig. 7.12(a) and dividing the nano-antenna results by those emitted from bulk. For the dimer nano-antenna, the SHG signal was higher by a factor of 7.2 and for the monomer the signal was higher by a factor of 4.5.

For the next experiments, the use of an APD, which integrates all collected wavelengths of light, was required to record the SHG signal. In order to make sure the experiments would indeed still measure second harmonic signal, the collected light emitted from a WS_2 bulk crystal (h = 60 nm) under 850 nm laser excitation was fiber-coupled and recorded with a spectrometer and CCD (shown in Fig. 7.13(a)) before reconnecting the fiber to the APD. At this point a power dependent experiment was performed on the same bulk crystal which exhibited a quadratic intensity increase as shown in Fig. 7.13(b). This is expected for

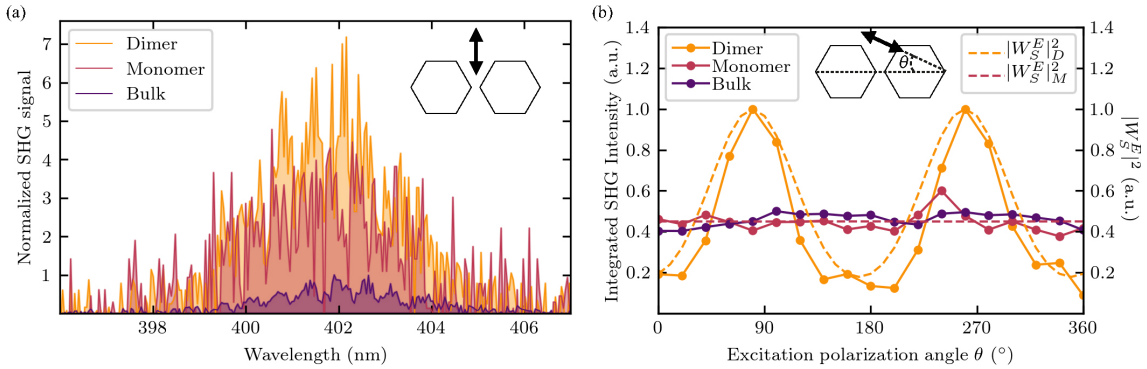

Fig. 7.12 **(a)** Second harmonic generation spectrum emitted from a dimer nano-antenna (yellow, r = 205 nm, h = 60 nm, g = 130 nm), a monomer nano-antenna (red, r = 215 nm, h = 50 nm) and a bulk crystal (purple, h = 60 nm) normalized to the area of each structure. The excitation polarization is set perpendicular to the dimer axis as shown by the black double arrow in the inset. The spectrally sharp features seen in the SHG signal were also observed in the spectrum of the laser, thereby originating from the excitation. **(b)** Normalized and integrated excitation polarization resolved SHG signal emitted from a monomer nano-antenna (red, r = 240 nm, h = 50 nm), a dimer nano-antenna (yellow, r = 200 nm, h = 60 nm, g = 130 nm) and a bulk crystal (purple, h = 60 nm). Inset illustrates the angle of the excitation polarization axis with the dimer axis. Dashed lines represent simulations of the confined electric energy inside the nano-antenna geometry squared ($|W_E^S|^2$). Adapted from reference [53].

second harmonic generated light as discussed in chapter 4 and therefore confirms that the measurement records only this signal.

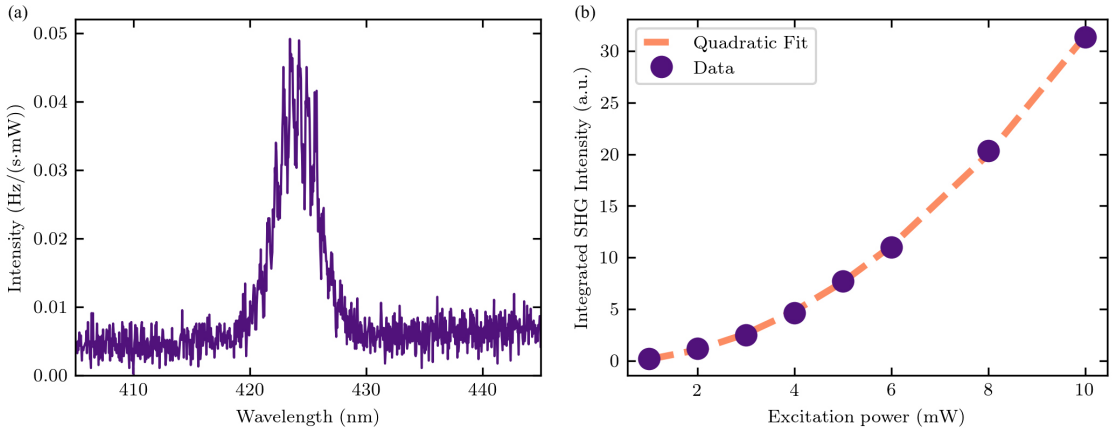

Fig. 7.13 **(a)** Spectrum of second harmonic generated light from a 60 nm bulk WS_2 crystal at an excitation wavelength of 850 nm. **(b)** Power dependent, integrated second harmonic signal from the bulk crystal compared to a quadratic fit of the data.

Using this experimental setup, the normalized polarization dependence of the SHG signal from a monomer (r = 240 nm, h = 50 nm), a dimer (r = 200 nm, h = 60 nm, g = 130 nm) and a bulk flake (h = 60 nm) at an excitation wavelength of 850 nm were recorded as shown in Fig. 7.12(b). The signal recorded for the dimer nano-antenna exhibits a clear linear polarization

dependence while the same is not evident for the bulk or monomer measurements. The reason for this lies in the confinement of the electric field which further influences the enhancement of second harmonic generation. For the X-pol mode, the electric field is highly confined to the outside vertices of the dimer nano-antenna, so it does not contribute to the SHG enhancement inside the structure. For the Y-pol mode, however, the confinement of the electric field is mostly to the inside of the structure thereby leading to strong enhancement of SHG. For the monomer and bulk measurements, the position of electric field confinement does not change as in the dimer, thereby not leading to any polarization dependence of the SHG enhancement. As described in chapter 5, the electric energy confined to a cross-sectional surface inside the nano-antenna can be simulated for any excitation polarization. As discussed in chapter 4, the square of the confined electric energy is expected to be proportional to the enhancement of the second harmonic signal. Comparing the square of the electric energy to the recorded SHG results in Fig. 7.12(b) would provide an answer to whether the second harmonic signal enhancement observed in experiment is due to coupling of the excitation to the anapole modes in the photonic structures. The simulations of the electric energy squared are shown in Fig. 7.12(b) as dashed lines (yellow for the dimer and red for the monomer) which correspond very well to the relative change in the intensity of recorded SHG signal with rotation of the excitation polarization. These experiments show that a dimer and monomer nano-antenna can be used to enhance second harmonic generated light, however, only the dimer nano-antenna may be used for polarization dependent SHG signal.

7.6 AFM repositioning

Photonic structures with very small gaps are highly desirable in both research and applications due to the possibility of a very strong confinement of the electric and magnetic fields. As discussed in chapter 4, resonators containing a closely spaced double-vertex structure lead to strongly confined electromagnetic fields far below the wavelength of light due to boundary conditions on the normal and parallel components of the field at sharp refractive index contrasting boundaries [153]. The confined fields also increase as the spacing between the two vertices is decreased [153]. This leads to the conclusion that very small low-index (such as air) gaps positioned between two high-index vertex structures will result in very large field intensities which can be advantageous for different applications as will be discussed in chapter 8.

The smallest lateral, low refractive index gap between two vertex-shaped structures (5 nm) has only been achieved in plasmonic nano-triangles manipulated with an AFM cantilever tip [154]. In high-index dielectrics, the smallest gaps (on the order of 10 nm) have been

achieved with focused ion beam (FIB) milling [204] but this is an irreversible process that often damages the crystals. Therefore, it is disadvantageous for some applications.

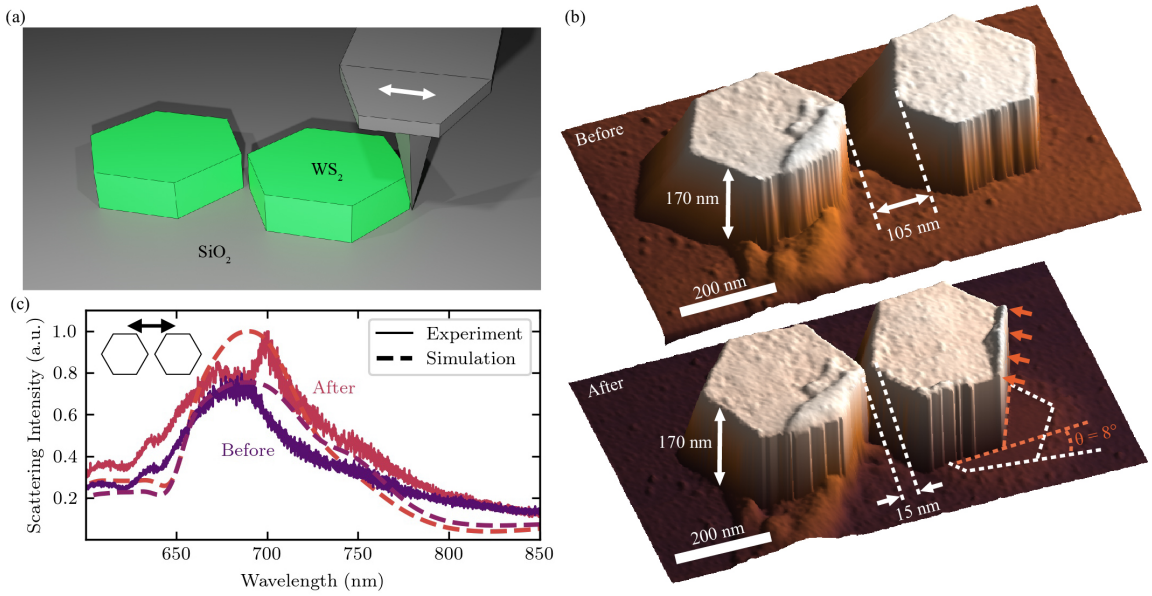

Fig. 7.14 **(a)** Illustration of the AFM technique used to translate or rotate a single nano-pillar of a dimer nano-antenna. **(b)** AFM scans of a dimer nano-antenna (r = 140 nm, h = 170 nm) before and after being repositioned. The gap reduces from 105 nm to 15 nm and one nano-pillar is rotated by 8° placing the inside vertices closer to each other. **(c)** Dark field spectra of the dimer nano-antenna with excitation polarization parallel to the dimer axis, as shown in the inset, before (purple) and after (red) the repositioning procedure. Dashed lines represent simulated scattering cross sections for the same geometries before and after the reduction in the gap. Adapted from reference [53].

The EBL and RIE fabrication procedure illustrated in Fig. 7.1(b) results in dimer nano-antennas with a minimum gap of 50 nm. In order to improve this, the weak van-der-Waals attractive forces of the WS_2 crystal can be utilized in mechanical translation and rotation by an AFM cantilever tip. This post-fabrication procedure, performed by a collaborator at the University of Sheffield, consists of scanning a contact mode AFM cantilever tip parallel to the dimer axis on the outside edge of the dimer nano-antenna [53]. The choice of a low set-point forces the tip to collide with one of the constituent nano-pillars in the dimer and displace it. A schematic illustration of this procedure is shown in Fig. 7.14(a). As the tip is scanned to collide with the nano-pillar towards the center of the dimer, it is translated closer to the other constituent nano-pillar and reduces the dimer gap. As shown in Fig. 7.14(b), this can be used to reduce the dimer gap from 105 nm to 15 nm. Another possibility is to scan the AFM tip along a tangent of the nano-pillar thereby rotating it. A rotation of 8° can be seen in the manipulation performed in Fig. 7.14(b). This can be used to position the inside vertices closer or farther apart from each other.

Dark field spectroscopy was also performed before and after the AFM repositioning of this dimer nano-antenna as shown in Fig. 7.14(c). The excitation polarization was set to the X-pol configuration as this is more sensitive to changes in gap separation. The dipole resonance seen as a broad peak at $\approx$ 680 nm is brighter after the manipulation as expected for a reduced dimer gap in this geometry. Simulations of the scattering cross section of the geometries before and after AFM repositioning are shown as dashed lines in Fig. 7.14(c). The simulations and experiment are in good agreement, indicating that the photonic response of the nano-antenna has indeed been modified by the reduction of the dimer gap to 15 nm.

Further atomic force microscopy scans of repositioning manipulations performed on other dimer nano-antennas are shown in Fig. 7.15. For these manipulation, the minimum separation gap achieved in these experiments (10 nm) is seen in Fig. 7.15(a). The largest rotation (57°) is recorded in Fig. 7.15(b). Smaller separation distances may be achievable, however, the accurate measurement of the gap width is a considerable challenge due to the finite size of the AFM cantilever tip which is estimated to be 5 nm, thereby setting the minimum gap achieved in these experiments to be 10$\pm$5 nm.

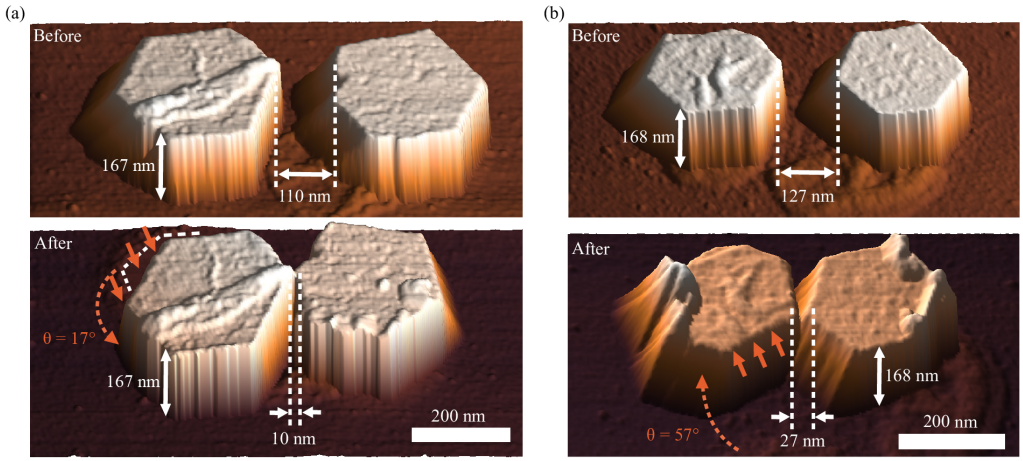

Fig. 7.15 **(a)** AFM scans of a dimer nano-antenna (r = 163 nm, h = 167 nm) before and after repositioning yielding a reduced gap from 110 nm to 10 nm and a rotation of 17°. **(b)** AFM scans of another dimer nano-antenna (r = 140 nm, h = 168 nm) before and after repositioning yielding a reduced gap from 127 nm to 27 nm and a rotation of 57°. Adapted from reference [53].

7.7 Conclusion

In this chapter, I have discussed the fabrication of monomer and dimer WS_2 nano-antennas in three different geometries, namely circular, hexagonal and square. Dark field characterization of hexagonal monomer nano-antennas were subsequently compared to simulations of their

scattering cross sections. The resonances of these antennas were tuned using both the radius and height of the nano-antennas as expected from the Mie theory discussed in chapter 4. The origin of the resonances were identified using the multi-pole expansion of the total scattering cross section which was calculated for three different monomer geometries. This yielded a dominant electric dipole mode with contributions from higher order resonances as well as a toroidal moment contribution which together with the electric dipole moment form an anapole resonance. The characterization of the anapole resonance as well as a higher order anapole mode was performed by identifying destructive interference resulting from equal contributions yet opposite phases of the electric dipole component and magnetic toroidal component. The characteristic electric and magnetic field patterns at the anapole and HOAM resonance were also identified. Subsequently the need for studying only a single nano-antenna geometry was shown to be due to the subtle redshift or blueshift of the resonances from the choice of etching mechanism and therefore shape of the nano-antenna. This also identified a more precise method of tuning the resonances of nano-antennas through the etching recipe.

The discussion shifted to dark field characterization of dimer nano-antennas which also showed close agreement to simulations of the scattering cross section. A dimer anapole mode was identified through a similar wavelength of a scattering minimum and a maximum in the simulation of the electric energy confined to the inside of the structure as well as through the characteristic electric and magnetic field patterns in the nano-antenna. The hybridization of resonances in dimers was discussed and studied numerically to apply to both the dipole and anapole resonance which was also observed in dark field spectroscopy of three dimer nano-antennas. The hybridization of the modes led to the splitting of each resonance found in monomers to two cross-polarized modes. Comparison of the electric field intensity distribution and confined electric energy was performed for the monomer and dimer anapole resonances with the conclusion that the dimer anapole resonance leads to nearly two times larger electric energy confinement. Second harmonic generation experiments were subsequently performed with the result of enhanced SHG signal from both monomer and dimer nano-antennas. Polarization dependent SHG enhancement was also observed for dimer nano-antennas. The SHG conversion efficiency of the WS_2 nano-antennas studied in this chapter was severely limited compared to previous reports [47] due to the choice of excitation wavelength and the highly reduced phase matching from the difference in refractive index at the excitation (800 nm: $n \approx 4$) and emission wavelengths (400 nm: $n \approx 2.5$). A careful redesign of the monomer and dimer nano-antennas to shift the anapole resonance to longer wavelengths, may allow for phase matched and highly efficiency second harmonic generation. Post-fabrication AFM repositioning was also introduced for dielectric dimer nano-antennas

for the first time. This procedure allowed the reduction of the dimer gap and rotation of constituent nano-pillars which is expected to increase the confinement of fields in the dimer gap. The maximum rotation angle achieved in different AFM repositioning trials was 57° showing the possibility for large rotations. The minimum dimer gap attained was recorded as 10±5 nm which corresponds to the limit defined by FIB milling [204] in dielectrics and is very close to the that set by AFM manipulation of plasmonic nano-triangles [154].

This AFM repositioning procedure is possible due to the weak van-der-Waals attractive forces attaching the WS_2 crystal to the substrate. In the next chapter, I will discuss the implications of polarization dependent SHG enhancement in WS_2 dimer nano-antennas as well as those of the ultra-small dimer gaps (10±5 nm) achieved with the post-fabrication technique on different applications.

Chapter 8

Simulation of WS_2 dimer nano-antennas

8.1 Introduction

As seen in the last chapter, WS_2 nano-antennas host widely tunable Mie resonances which can be adapted to many applications with a variety of methods. Second harmonic generation (SHG) experiments led to an opportunity to produce polarization dependent enhancement which will further be explored in this chapter. Also, a post-fabrication method of reducing the dimer gap was introduced which may provide a regime of high electric field intensities due to ultra-small spacings of dielectric nano-resonators which will be investigated numerically, with regards to their viability for applications, in this chapter.

Photonic structures containing an ultra-small low refractive index gap between two vertex-shaped high refractive index structures are highly desirable for the strong electric and magnetic field confinement possible inside these geometries. As briefly discussed in the previous chapter and explored in the section on dimer modes in chapter 4, the sharp refractive index contrasting boundary leads to enhancements of the confinement with factors of $\varepsilon_h/\varepsilon_l$. One of the applications which would benefit from such small low-index gaps between high-index vertices is the enhancement of single photon emission (SPE) through the Purcell effect as discussed in chapter 4. The large electric field intensities expected to be present in the middle of a WS_2 dimer nano-antenna gap suggests that the study of the Purcell effect for an SPE placed in this position, which increases with the partial local density of optical states as stated in chapter 4, is a worthwhile endeavor.

Another application which would also greatly benefit from high electric field confinement is optical trapping of nano-particles, which consists of an attractive force in the direction of an electromagnetic hotspot under optical excitation. The expected force is dependent on the particle size and refractive index, input pump power and the energy confinement provided by the photonic environment [164]. Previous reports of nano-antenna optical trapping utilize

plasmonic nano-resonators which induce large trapping forces in dielectric particles [205], yet they suffer from large temperature increases which leads to a loss in stability and may be detrimental to biological nano-particles. Similarly, their plasmonic nature leads to quenching of emission due to increased optical absorption processes [148, 206]. Alternatively, dielectric resonators, such as silicon dimer nano-antennas [148, 149], can be very advantageous as they do not risk degrading biological samples and do not lead to quenching of optical emission.

In this chapter, I will discuss further simulations of the WS_2 dimer nano-antennas which may yield interesting research avenues for further experiments enabling exciting applications. Firstly, the linear polarization dependence of the second harmonic generation enhancement will be revisited and more of its polarization properties will be explored enabling interesting applications such as non-linear logic gates [207] or second harmonic generating optical elements. Next, the electric field intensity spatial distributions for three optimized WS_2 dimer nano-antenna geometries all with a gap of the minimum achieved separation in the last chapter (10 nm) will be simulated. The optimization process will be presented with a description of how changes in geometrical parameters lead to increased electric field intensities. A short discussion of the radius of curvature used in these simulations will follow including the measurement of fabricated structures using atomic force microscopy (AFM) as well as the simulated impact on the electric field intensity. Further the Purcell effect expected for optimized designs of all three geometries will be explored numerically along the dimer axis at the top surface of the nano-antenna for dimer gaps of g = 10 nm and g = 50 nm. This will subsequently lead into a discussion of tuning mechanisms for modulation of the electric field intensity and the Purcell effect. One mechanism that will be discussed is the separation of the constituent nano-pillars of the dimer nano-antenna and the other involves the rotation of nano-pillars with respect to the dimer axis. The last, brief discussion will consist of simulations of the optical trapping forces that can be expected in such dimer structures for different nano-particles as well as the modulation of this force with increased dimer gaps. This work has also been reported in the following reference [53].

8.2 Polarization dependent second harmonic generation simulations

As discussed in chapter 5 and 7, the simulation of the confined electric energy inside the geometry of a nano-antenna at an anapole resonance can be used to calculate the relative enhancement of the second harmonic generation signal. Therefore, the expected SHG signal enhancement due to the anapole resonance at different incident polarizations and wavelengths

can easily be calculated . When this effect is combined with the fact that all resonances, including the anapole and higher order anapole mode (HOAM), hybridize with decreasing gap separation, as presented in the last chapter, and therefore energetically split, some interesting properties can be extracted with a variety of possible applications.

To understand this the confined electric energy ($W_E^{(S)}$) in a dimer nano-antenna (r = 200 nm, h = 60 nm, gap = 100 nm) anapole mode is simulated for polarizations along the axis connecting the centers of the nano-pillars (dimer axis), defined here as X-pol, and perpendicular to it, defined as the Y-pol. The electric energy confined in the two hybridized resonances and scattering cross sections for each polarization are plotted in Figs. 8.1(a) and (b). The confined electric energy is calculated by integrating over the electric field intensity for a cross-sectional surface at the midpoint of the nano-antenna height. The green line in these plots corresponds to the anapole mode for un-polarized excitation. This clearly distinguishes the X-pol and Y-pol anapole resonances in both scattering cross section as well as in confined electric energy. This hybridized splitting leads to very interesting results when a degree of linear polarization is defined for the SHG signal enhancement. In order to compute this quantity, the electric energy is first squared to yield the SHG signal enhancement ($|W_E^{(S)}|^2$). Then the degree of linear polarization (D_{SHG}) is defined as follows:

$$D_{SHG} = \frac{|W_E^{(S)}|_Y^2 - |W_E^{(S)}|_X^2}{|W_E^{(S)}|_Y^2 + |W_E^{(S)}|_X^2} \tag{8.1}$$

where $|W_E^{(S)}|_Y^2$ and $|W_E^{(S)}|_X^2$ correspond to the SHG signal enhancement for a Y-pol and X-pol excitation respectively. Fig. 8.1(c) displays this degree of linear polarization of the SHG signal enhancement where the red area corresponds to a linear polarization perpendicular to the dimer axis (Y-pol) and the blue are represents linear polarization parallel to the dimer axis (X-pol). An interesting point to note is that near unity degree of linear polarization of the enhancement can be achieved for SHG signal excited at a wavelength of $\approx$ 830 nm. Similarly, the polarization of the SHG enhancement due to the anapole resonance can be rotated with a change in wavelength opening the opportunity for very fast rotation of the polarization of second harmonic generated light.

This degree of linear polarization, can also be tuned and modulated with a change in the dimer gap. An increase in the separation between WS_2 nano-pillars yields less SHG enhancement in both incident polarizations, therefore, the degree of linear polarization is also reduced. Conversely, reducing the dimer gap is expected to lead to increased SHG enhancement in a range of wavelengths due to the anapole resonance with increased degree of linear polarization of the SHG enhancement. Due to the fact that SHG signal from bulk WS_2

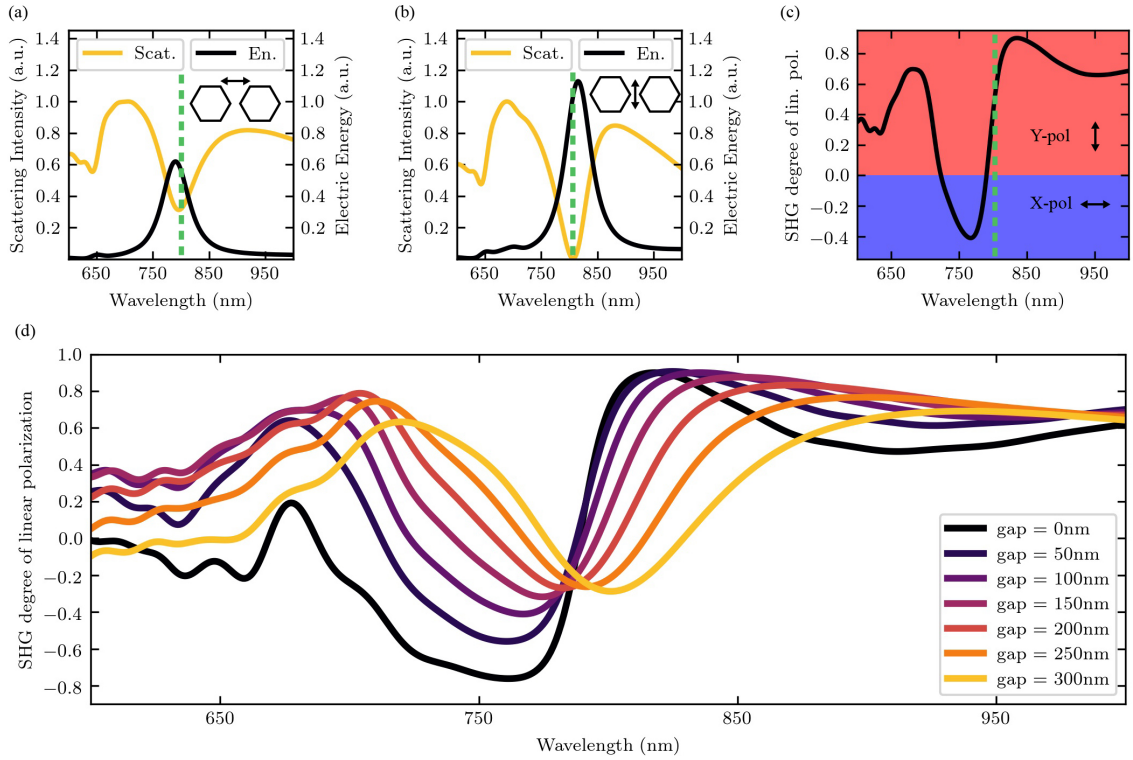

Fig. 8.1 **(a)** and **(b)** Simulated scattering cross sections (yellow) and confined electric energies (black) for a hexagonal WS_2 dimer nano-antenna (r = 200 nm, h = 60 nm, gap = 100 nm) under X-pol and Y-pol excitation respectively. Electric energy is calculated as an integral over the electric field intensity for a cross-sectional surface of the dimer nano-antenna at the midpoint of its height. **(c)** Simulated degree of linear polarization of the SHG enhancement due to coupling with the anapole mode for the same nano-antenna. **(d)** Simulated degree of linear polarization of the SHG enhancement for nano-antennas with a range of dimer gaps.

is relatively weak as shown in the last chapter, this enhancement degree of linear polarization will dominate the SHG signal and therefore induce a degree of linear polarization very similar to what is plotted in Fig. 8.1.

8.3 Electric field intensity and Purcell enhancement of emission simulations

The logical next step from achieving ultra-small dimer gaps using atomic force microscopy (AFM) repositioning, as discussed in the previous chapter, is to study the electric field confinement induced by this novel structure. In order to do this, numerical simulations were employed to study dimer nano-antennas with different geometries which can be achieved with nano-fabrication, namely circular, hexagonal and square. Optimized designs were calculated by a series of simulations which attempted to change the radius and height of

the dimer nano-antennas in order to achieve maximum electric field intensities at the upper inside vertex of each dimer nano-antenna geometry. The gaps for each simulation were kept at the minimum achieved in experiment (10 nm). Fig. 8.2(a) shows the electric field intensity spectrum at the inner top vertex of the hexagonal WS_2 dimer nano-antenna (r = 240). As the height is increased from 170 nm to 200 nm, a peak in $(|E|/|E_0|)^2$ narrows in linewidth and slightly increases in maximum intensity. From 200 nm to 230 nm this peak once again broadens and reduces in intensity. The optimal height was found to be 200 nm.

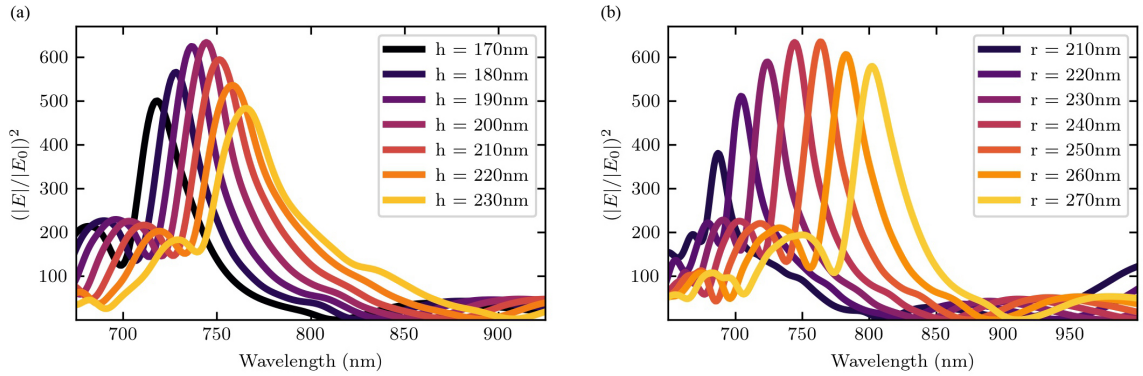

Fig. 8.2 **(a)** Simulated electric field intensity spectrum for a position at the inner top vertex of a hexagonal WS_2 dimer nano-antenna (r = 240 nm, gap = 10 nm) for a range of heights. **(b)** Simulated electric field intensity spectrum for a position at the inner top vertex of a hexagonal WS_2 dimer nano-antenna (h = 200 nm, gap = 10 nm) for a range of radii.

A change in radius from 210 nm to 270 nm at a height of 200 nm and dimer gap of 10 nm is shown in Fig. 8.2(b). This yields a larger tuning of the resonance observed as a peak in the electric field intensity $(|E|/|E_0|^2)$. Variation from the optimal radius (r = 240 nm) will result in a large decrease in maximal intensity and a slight broadening. This suggests that variation of radius and height independently can optimize different parameters of the resonance. A variation of the height would yield a small peak position tuning and a small change in the maximum electric field intensity, however, it will induce large changes in the linewidth of this peak. A variation of the radius can be used to change the maximum intensity and tune the resonance while maintaining a similar linewidth. This optimization procedure attempted to find the maximum electric field intensity that can be achieved within the dimer hotspots for any resonance spectral position or linewidth. However, if some application adds constraints to the range of wavelengths or the linewidth available, a variation of the individual parameters can still be used to find the optimum geometry within the set requirements.

A similar procedure was applied to all three geometries of nano-antennas which are available for fabrication and the final optimized design geometries with a gap of 10 nm are as follows: circular design: r = 225 nm, h = 200 nm; hexagonal design: r = 240 nm, h = 200

nm; square design: r = 260 nm, h = 150 nm. As these simulations were excited with a broad energy spectrum, the electric field intensities are lower than they would be if only excited with a narrow range of wavelengths at the specific resonance.

Simulating with a narrow pulse excitation, the electric field intensity spatial distribution of each optimized design is plotted for a plane 0.5 nm from the top surface of the dimer nano-antenna in the top panel of Fig. 8.3(a)-(c). The bottom panel of each figure shows the electric field intensity spatial distribution for a vertical cross-sectional cut through the middle of the nano-antennas. Each distribution was calculated at the wavelength of the maximum electric field intensity (751.5 nm, 749.5 nm, 697 nm for the circular, hexagonal and square geometries respectively). Electric field hotspots are observed forming at the vertices in the dimer gap as well as at the vertices on the outside of the structure for an incident plane wave polarized along the dimer axis (X-pol). The maximal intensities inside the gap reach values of more than 10^3 compared to vacuum. When comparing the three different geometries, the circular design yields the smallest maximum electric field intensities of 900, while the hexagonal and square geometries induce even higher electric field intensities up to 1410 and 1260 respectively.

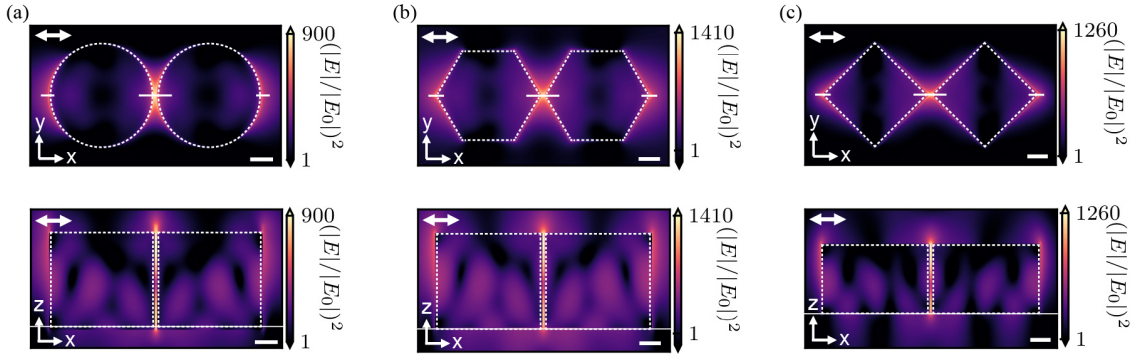

Fig. 8.3 Top-view (top panel) and side-view (bottom panel) spatial distributions of the electric field intensity in and surrounding optimized designs of each geometry of WS_2 dimer nano-antennas at a gap separation of 10 nm. **(a)** Circular design: r = 225 nm, h = 200 nm, wavelength = 751.5. **(b)** Hexagonal design: r = 240 nm, h = 200 nm, radius of curvature of vertices = 22 nm, wavelength = 749.5. **(c)** Square design: r = 260 nm, h = 150 nm, radius of curvature of vertices = 10 nm, wavelength = 697.5. Hotspots of electric field confinement form at inner and outer edges of the dimer nano-antenna. Excitation polarization is parallel to the double white arrow in the top left corner of the panels. Axes (x,y) indicate results from a surface 0.5 nm above the top of the dimer. Axes (x,z) indicate a vertical cross-sectional cut through the dimer axis. Dashed white outlines represent the spatial extent of the nano-antennas. Scale bars = 100 nm. Adapted from reference [53].

In order to simulate structures which are as realistic as possible, the radius of curvature of the vertices of the hexagonal and square designs were set to the smallest measured for fabricated structures, namely 22 nm and 10 nm respectively. This was calculated from atomic force microscopy scans of different hexagonal and square dimer nano-antennas. As

the measured structures yield radii of curvature which are often below or on the order of the AFM resolution, set by the cantilever tip, a geometric approach was employed for this measurement.

Exemplary AFM scans of a square (r = 265 nm, h = 84 nm, g = 220 nm) and hexagonal (r = 240 nm, h = 135 nm, g = 90 nm) dimer nano-antenna used in this measurement are shown in Figs. 8.4(a) and (b). The calculation used only the portions of the AFM scans in which the bottom of the cantilever tip oscillated directly above the structure underneath in order to reduce the error as much as possible. Figs. 8.4(c) and (d) show a portion of the upper AFM scans which include the dimer gap where the value extracted from the scan is denoted as x, which is the shortest resolvable distance between two edges which are at 90° or 120° from each other for the square and hexagonal geometries respectively. This can be considered as the base of a triangle formed also by two radii of curvature which perpendicularly intersect the edges of the respective structure. The angle between these two radii can easily be calculated to be 90° and 60° for the square and hexagonal geometries respectively. The radius of curvature can then be simply calculated using the Pythagorean theorem.

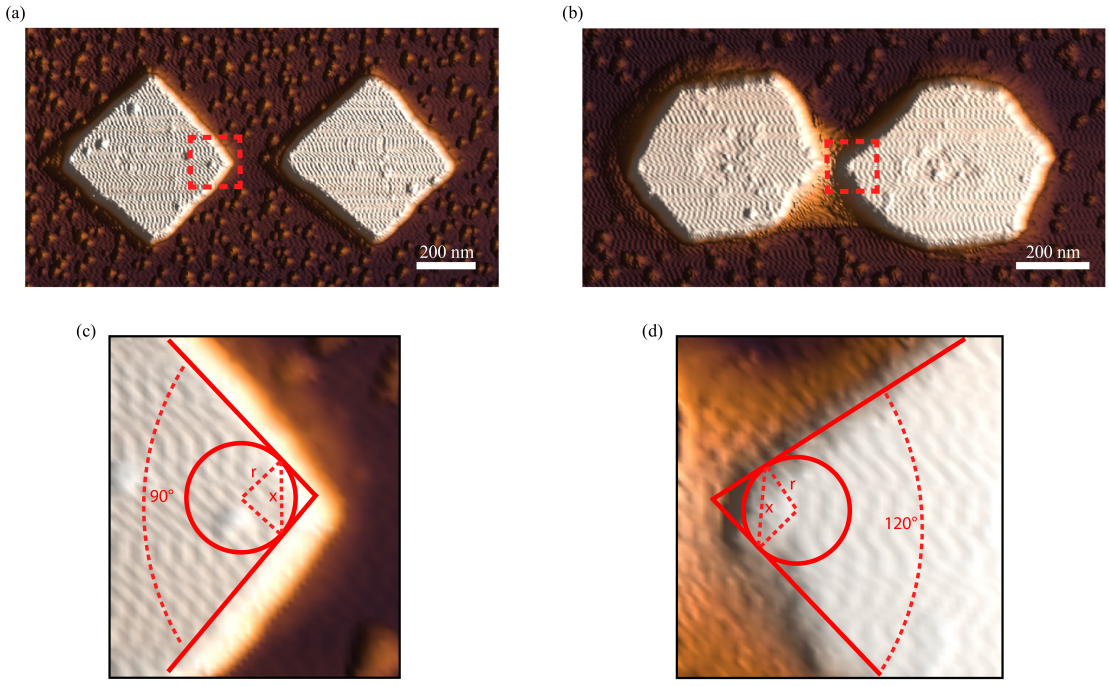

Fig. 8.4 **(a),(b)** AFM scan of a square (r = 265 nm, h = 84 nm, gap = 220 nm) and hexagonal (r = 240 nm, h = 135 nm, gap = 90 nm) dimer nano-antenna with small curvature radii at their vertices. **(c),(d)** Close-up portions of the AFM scans shown as dashed red squares in **(a)** and **(b)**. Overlapped sold red lines represent the edges of the structure. Inscribed circles used to calculate the radius of curvature (r) in each after a measurement of the shortest distance from one edge of the structure to the other (x). Adapted from reference [53].

This measurement provided the minimum radius of curvature of the vertices in the fabricated WS_2 hexagonal and square dimer nano-antennas for more realistic simulations of the electric field intensity and other subsequent numerical studies. One question which might be pertinent at this point is what influence this radius of curvature may have on the electric field intensity within the gap hotspots. In order to study this, simulations of the optimized hexagonal and square designs were performed with different radii of curvature but the same overall radius, height and gap. The electric field intensity spectrum at a point within the gap hotspots is shown in Fig. 8.5.

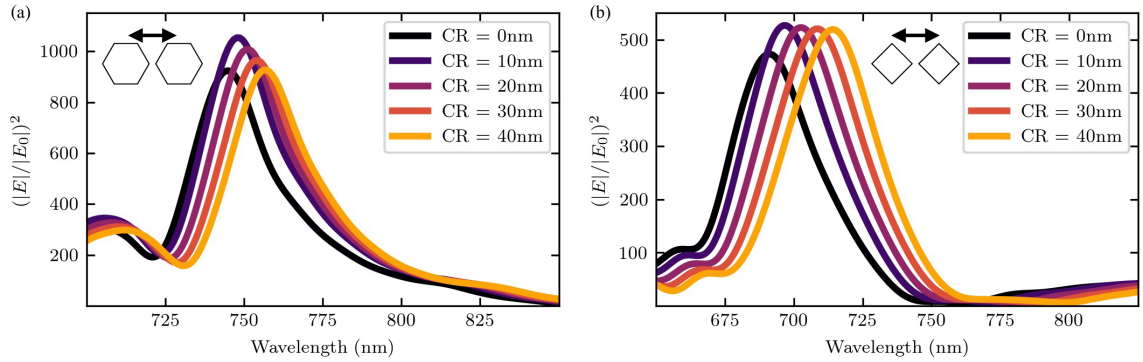

Fig. 8.5 **(a)** Simulated electric field intensity spectra for different curvature radii at a point within the dimer gap hotspot for a WS_2 hexagonal dimer nano-antenna with radius r = 240 nm, height h = 200 nm and gap g = 10 nm. **(b)** Simulated electric field intensity spectra for different curvature radii at a point within the dimer gap hotspot for a WS_2 square dimer nano-antenna with radius r = 260 nm, height h = 150 nm and gap g = 10 nm.

For both structures, the maximum electric field intensity grows with an increase in the radius for small r, however, this pattern is reversed above r = 10 nm for both at which point the maximum electric field intensity decreases with growing r. The initial increase is related to how the fields resonate inside the structure. As the overall radius of the structure does not change, an increase in radius of curvature will lead to an increase in the volume of the entire structure which forms a more gradual confinement potential for the electromagnetic fields in the resonator thereby yielding less coupling of the incident light to leaky resonances and therefore more intense electric field hotspots. A similar approach is used in the design of photonic crystal cavities where the lattice spacing of holes surrounding the position of the cavity is shifted from the periodic structure of the rest of the photonic crystal. This step is carried out to provide a gradual, quadratic confinement potential for the resonance [208]. After this point, the increase in curvature radius only leads to a de-localization of the hotspot and confinement therefore leading to lower maximum electric field intensities. As shown by the simulation results in Fig. 8.5, the increase of the curvature radius plays a small role in reducing the electric field intensity in the gap hotspot. This suggests that fabrication imperfections in terms of the radius of curvature of the vertices will not detrimentally affect

any application which relies on the large electric field intensities. As the curvature radius is increased while the other parameters of the structure are kept constant, the volume of the structure, as stated above, is slightly increased which then leads to a redshift of the dimer X-pol resonance as expected for Mie resonances and as discussed in chapter 4.

After understand that the impact of the radius of curvature on the maximum electric field intensity is not large and recording the minimum values extracted from AFM scans of fabricated structures, the Purcell factor for a single photon emitter positioned on top of each optimized geometry is simulated. This simulation is carried out by positioning an ideal dipole emitter 0.5 nm from the top surface of each structure at different points along the dimer axis. The positions used are shown as solid white lines in Fig. 8.3. The simulated Purcell factors for two different gap separations, namely 10 nm and 50 nm, of the circular, hexagonal and square optimized designs are shown in Fig. 8.6 as solid or dashed lines respectively. The observed maxima at the inner vertices of the nano-antennas yield the largest results for all geometries as expected from the maximum electric field intensities observed at the same position. Weakly confined hotspots are also observed at the outside edges of the structures which also lead to local maxima in the Purcell factor with values as high as 20. For a gap of 10 nm, the circular, hexagonal and square geometries exhibit Purcell factors of 105, 157 and 153 respectively. For a gap of 50 nm, the Purcell factors are all much lower, reaching values no higher than 46.

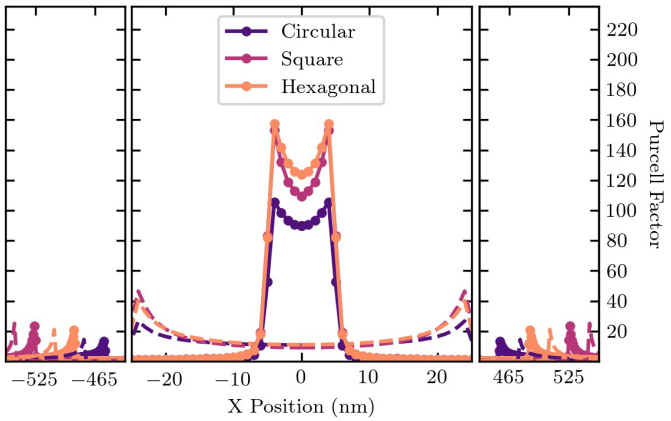

Fig. 8.6 Purcell factors simulated for a dipole positioned 0.5 nm above the top surface of dimer nano-antennas along the dimer axis in the three different geometries. Solid dots and lines represent a gap of 10 nm while dashed lines represent a gap of 50 nm. The simulated positions of the dipole are represented as solid white lines in Fig. 8.3. Adapted from reference [53].

As seen from the AFM repositioning, there are two methods of rearranging the dimer nano-antennas which lead to a modulation of the maximum electric field intensity and therefore the Purcell factor at the position of the hotspots. One approach, illustrated in Fig.

8.7(a), is the separation of the constituent nano-pillars in the dimer which can be achieved either through AFM repositioning or fabrication. The electric field intensity and Purcell factor in the gap hotspot was numerically studied for an increasing dimer gap in Figs. 8.7(b) and (c). The three different designs were also compared yet each leads to an exponential reduction of both the electric field intensity and the Purcell factor by a factor of one order of magnitude with increasing dimer gap over a range of 100 nm. The hexagonal structure structure yields the highest electric field intensity at small separations yet this changes to the square structure at gap separations of more than 75 nm. For the Purcell factor, the hexagonal structure again results in the highest values for small gaps, however, in this case the square geometry induces the largest Purcell factors at a much lower gap of 20 nm.

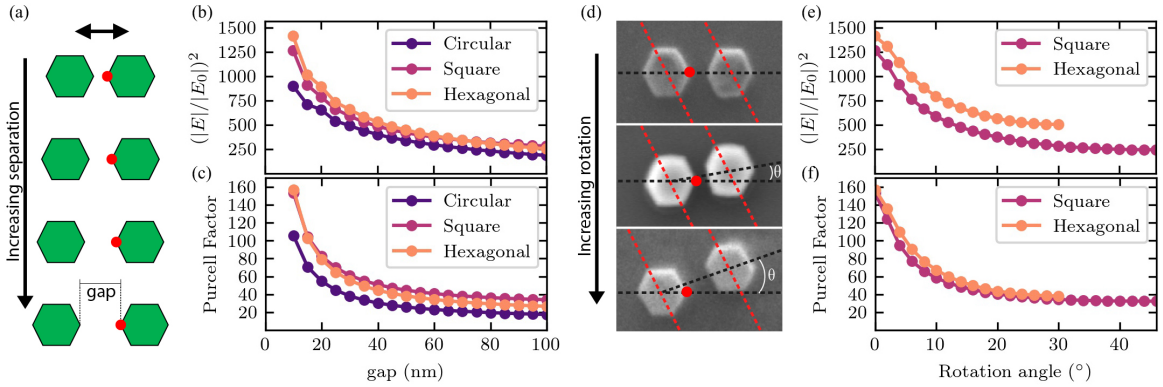

Fig. 8.7 **(a)** Schematic representation of the varied dimer gap used for simulations in **(b)** and **(c)**. **(b)** and **(c)** Simulations of the maximum electric field intensity and Purcell factor in the hotspot of the optimized dimer designs of each geometry respectively for a varying radius at previously used wavelengths. **(d)** SEM images of hexagonal dimer nano-antennas rotated during the EBL patterning step of the fabrication procedure using the symmetry of the WS_2 crystal. **(e)** and **(f)**Simulations of the maximum electric field intensity and Purcell factor in the hotspot of the optimized dimer designs of each geometry respectively for a varying rotation angle at previously used wavelengths. Red circles in **(a)** and **(b)** represent the position of the electric field hotspot and the dipole placement position for all simulations in this figure. Adapted from reference [53].

Another approach to modulating the electric field intensities and Purcell factors only available to hexagonal and square geometries is the rotation of the constituent nano-pillars in the dimer relative to the dimer axis. This aligns their vertices either closer or farther apart from each other. This rotation is straightforward using AFM repositioning, as discussed in the previous chapter, however, a method of achieving this through fabrication is presented in Fig. 8.7(d). Since the chemical etching procedure described in chapter 7 preferentially etches in the armchair crystal axis, this will always lead to nano-antenna sidewalls parallel to the zigzag axis, therefore the orientation of the dimer nano-pillars with respect to the crystal symmetry will always be the same. However, if the pattern defining the midpoint of each pillar is rotated at the EBL patterning stage of the fabrication, the dimer axis can

be rotated which will leave the sidewalls and vertices with a new relative orientation to the dimer axis even though their angle with respect to the crystal axes remains the same. The effect of this rotation on the maximum electric field and Purcell factor induced by the hexagonal and square structures is shown in Fig. 8.7(e) and (f). The exponential decrease by an order of magnitude is again evident, however, the range of available angles is larger for the square structure which leads to a larger modulation range of both the maximum electric field intensity and Purcell factor. For rotations, however, the hexagonal geometry maintains the largest values for both quantities at all the angle.

8.4 Dimer nano-antenna optical trapping simulations

The large electric field intensities seen for the ultra-small gap WS_2 dimer nano-antennas lead to the next logical step of investigating this structure for optical trapping of dielectric nano-particles. To the discern the possibility of such an application, a collaborator from the University of York performed numerical simulations based on the Finite Element Method to determine the Maxwell Stress Tensor (MST) over the surface of a dielectric nano-particle. This MST is then used to calculate attractive forces exerted on the particle by an optical pump and the photonic environment. For these simulations, the optimized WS_2 hexagonal dimer nano-antenna geometry was used with the addition of a nano-sphere (r = 5 nm) of refractive index corresponding to either an approximated colloidal quantum dot (QD) (n = 2.4) [149] or a polystyrene bead (PB) (n = 1.6), which mimics the refractive index and size of a large protein [209]. Since optical trapping experiments are often performed in an environment of water required for the suspension of nano-particles, the background refractive index was set accordingly. For all of these simulations, the experimentally feasible pump power density of 10 mW/μ m^2 was used. A schematic illustration of the simulation geometry is shown in Fig. 8.8(a).

The optical force simulated for the QD and the PB is shown in Fig. 8.8(b) and (c) respectively for a position at the middle of the dimer gap at different points of the vertical z-axis. The geometry is simulated with two gaps (10 nm and 15 nm) leading to attractive (negative) forces maximized at the top surface of the nano-antenna. The maximum expected optical force applied on the QD for a gap of g = 10 nm is 353 fN, whereas the value for the PB at the same gap is 73 fN. With an increase in gap to 15 nm, the maximum optical forces for the QD and PB reduce to 123 fN and 31 fN respectively. The dependence of the dimer gap on the optical trapping forces is studied in Fig. 8.8(d). For both nano-particles, the attractive force exponentially decreases roughly by an order of magnitude with the increase in gap which is expected from the reduction in the hotspot electric field intensity shown in

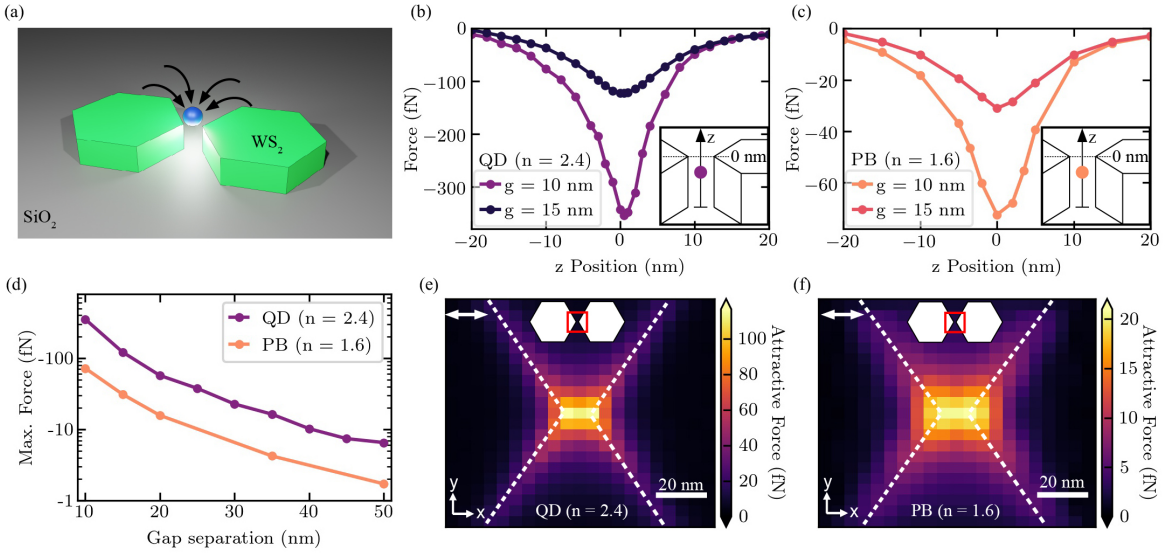

Fig. 8.8 **(a)** Schematic representation of nano-particle optical trapping with the use of hexagonal WS_2 dimer nano-antennas exhibiting ultra-small gaps. **(b),(c)** Simulated optical force for a spherical nano-particle (r = 5 nm) in the dimer (r = 240 nm, h = 200 nm) gap at positions along the z-axis for gaps of 10 nm (bright color) and 15 nm (dark color) The trapping force is simulated at the wavelength of its maximum value for a quantum dot **(b)** (763 nm) and a PB **(c)** (755 nm). Insets illustrates the position of the nano-particle position with zero corresponding to the top surface of the nano-antenna. **(d)** Simulated maximum electric force applied to a QD (purple line) and a PB (yellow line) for a varying dimer gap. **(e),(f)** Trapping force distribution for a QD **(e)** and a PB **(f)** for positions atop the nano-antenna. Excitation polarization is parallel to the white double arrow. Inset highlights the section of the nano-antennas over which the simulation is run with a red square. Dashed white lines represent the physical extent of the structures. The excitation power for all simulations in the figure is 10 mW/μ m^2. Adapted from reference [53].

Fig. 8.7(b). The spatial dependence of the optical trapping forces for the QD and PB are also studied for a position of 5 nm above the top surface of the dimer nano-antenna as shown in Fig. 8.8(e) and (f). This study emulates the optical trapping forces that may be exerted on a 5 nm radius nano-particle which resides on the top of the nano-antenna. The attractive force is maximized at the dimer gap vertices, as expected from the position of the hotspots. The maximum optical forces from this study are more than 100 fN for the QD and 20 fN for the PB.

8.5 Conclusion

In this chapter, I have discussed numerical simulations of WS_2 dimer nano-antennas fabricated and experimentally studied in the previous chapter. Firstly, the electric energy confined to the inside of the dimer nano-antennas was simulated for the two different polarizations resulting from the hybridization and splitting of the anapole resonance. A degree of linear polarization was defined for the enhancement of the SHG signal in dimer nano-antennas

shown in the last chapter. This led to a near-unity degree of linear polarization. Therefore, this WS_2 dimer nano-antenna structure might be advantageous for use in nano-scale optical components which emit linearly polarized second harmonic generated light. Second, FDTD simulations of dimer nano-antennas with the minimum experimentally achieved gap (10 nm) in the last chapter were performed to optimize and plot the spatial distribution of the electric field intensity at the top surface of the nano-antennas and as a vertical cross-sectional cut through the dimer axis. These plots yielded electric field hotspots at the vertices inside the dimer gap with maximum electric field intensities above 10^3. The three different geometries available for fabrication were compared with the hexagonal nano-antenna design leading to the highest electric field intensities. Subsequently, the radius of curvature in hexagonal and square designs was studied so that this could also be included in the simulations and therefore lead to more realistic results. The radius of curvature was measured in many different structures using a geometrical approach to maintain maximum resolution and the minimum values were used in all subsequent simulations. The dependence of the electric field intensity on radius of curvature was also numerically studied. The conclusion derived from this study asserted that a change in radius of curvature does not lead to large changes in the electric field intensity inside the dimer gap hotspots.

The Purcell effect was subsequently simulated for an SPE positioned at the top surface of the nano-antenna comparing the three different dimer geometries. The Purcell factor was maximized at the position of the dimer gap hotspots with values as high as 105, 157 and 153 for the circular, hexagonal and square geometries. This is higher than previous experimentally achieved results for a QD coupled to a micro-meter scale photonic crystal cavity ($F_P \approx 40$, [161]) yet lower than that achieved for a quantum dot coupled to a plasmonic nano-patch antenna ($F_P \approx 540$, [210]). The WS_2 dimer nano-antennas offer a lossless, compared to plasmonics, and nano-scale resonator for Purcell enhancement of single photon emission which is higher than previously achieved for dielectric Mie resonators ($F_P < 100$, [150, 211, 212, 145]). The numerical studies continued with routes to modulation of the electric field intensity and Purcell factor within the hotspots by varying the dimer gap distance as well as the rotation of the individual nano-pillars of a hexagonal or square dimer. These resulted in an order of magnitude modulation of both values for the two approaches. These methods of controlling the emission properties of single photon sources may be utilized for TMD SPES which form at high strain gradients in monolayers as evidenced by the WSe_2 emitters forming in monolayers transferred on gallium phosphide dimer nano-antennas [116]. Similarly the rotation of the quantum emitter polarization with strain topography previously reported [90], may also be feasible with hexagonal or square WS_2 dimer nano-antennas through the use of AFM repositioning as introduced in chapter 7.

Next, the discussion shifted to a study of the optical trapping forces expected for a colloidal quantum dot or a protein-like polystyrene bead positioned in or above the optimised hexagonal WS_2 dimer design. Simulations for a dimer gap of 10 nm yielded attractive forces of up to 353 fN and 73 fN for the QD and PB respectively. These values are more than 83 and 40 times higher than previous dielectric nano-antenna reports for QDs and PBs respectively [148, 149]. The optical trapping force dependence on dimer gaps was also studied yielding an order of magnitude reduction over a range of 10 to 50 nm which is expected from the reduction of the electric field intensity in the hotspot. Lastly, the spatial distribution of the attractive forces which are expected to be exerted on a QD and PB positioned on top of the nano-antenna was also studied leading to maximum forces at the positions of the electric field hotspots. These studies asserted that hexagonal WS_2 dimer nano-antennas may provide stable optical trapping for different nano-particles including colloidal quantum dots and protein-like particles.

In the last chapter of this thesis, I will summarize the research I have completed during my PhD and discuss possible future experiments and the impact of my work.

Chapter 9

Conclusion

In this thesis, I have explored theoretically, experimentally, and numerically the prospect of enhancing single photon emission in 2D materials using nano-scale Mie resonators in the form of monomer and dimer nano-antennas. This was first demonstrated using gallium phosphide (GaP) dimer nano-antennas, yet the drive to fabricate similar resonators from materials in the same family as the quantum emitters led to the numerical study of WS_2 dimer nano-antennas which asserted these as viable structures for Purcell enhancement. In the process of this work, other avenues of research have been revealed including the study of the recombination dynamics and dephasing processes in WSe_2 single photon emitters as well as different applications for WS_2 nano-antennas such as second harmonic generation with near unity degree of linear polarization and optical trapping of nano-particles. I will first provide a summary of the thesis and completed work and finish the chapter with a discussion of future research directions.

9.1 Summary

The overview of transition metal dichalcogenides (TMDs) provided in chapter 2 was the basis of the entire work as the large research interest in their optical properties provided a starting point for the discovery of single photon emitters (SPEs) in these materials as well as the usage of their high refractive indices for the fabrication of photonic resonators. This discussion began with a description of the crystal symmetry as a basis for employing chemical etching in the work presented in chapter 7. Following this, the band structure in bulk and monolayer forms was discussed leading to a description of the strongly bound excitons which account for most of the emission spectrum of these materials. This excitonic description was completed with a brief introduction into dark excitons in tungsten based TMDs which is vital for understanding much of the work in chapter 6.

Chapter 3 introduced quantum states of light as well as the properties of solid state sources which yield such single photon emission. Examples of TMD based SPEs discussed here provided a basis of comparison to previous reports in order to understand the novelty of the work presented in chapter 6. The discussion of the origin of TMD SPEs provided an introduction into strain-induced formation as well as an overview of the theoretical work completed to tie many of the observed optical properties to different recombination processes in WSe_2 used later in descriptions of the investigated behavior of the SPEs recorded in experiments presented in chapter 6.

Mie theory was introduced in chapter 4 including its implications for high refractive index monomer and dimer nano-antennas. This provided a basis for understanding the photonic properties of the GaP and WS_2 nano-antennas employed in the work presented in chapters 6 through 8. The Purcell effect was also discussed here to describe the general method of enhancing SPE emission which was a central focus of this thesis. Finally, a brief introduction into anapole resonances and non-linear light generation was provided in this chapter to enable discussions of the coupling of second harmonic generation to non-radiative resonances presented experimentally as well as numerically in chapter 7 and 8.

Chapter 5 introduces the methods for fabricating 2D materials and nano-resonators as well as experimental and simulation techniques. Mechanical exfoliation followed by identifying monolayers through PL imaging and a transfer procedure was discussed for depositing monolayer WSe_2 onto pre-patterend substrates for the work in chapter 6 as well as simple mechanical exfoliation for the fabrication in chapter 7. Clean room nano-fabrication techniques of SiO_2 nano-pillars, GaP dimers and WS_2 nano-antennas were also discussed. Setups for μ-photoluminescence spectroscopy, time correlated single photon counting, anti-bunching measurements and interferometry were introduced for the various experiments performed in chapter 6. The experimental setups for the work presented in chapter 7, such as dark field spectroscopy and second harmonic generation, were also described. Finally, this chapter discussed the geometry and setup of simulations which played an important role in the work presented in chapters 6, 7 and 8.

In chapter 6, I have demonstrated that high refractive index GaP dimer nano-antennas can be utilized to form and position single photon emitters in monolayer WSe_2 through strain as well as enhance their quantum efficiency and brightness to higher values than previously reported for Purcell enhanced SPEs coupled to plasmonic resonators [98]. The resonant properties of GaP dimer nano-antennas and SiO_2 nano-pillars were compared demonstrating an expected enhancement of photoluminescence by more than two orders of magnitude for emitters forming on the former structures. Subsequently, the optical properties of the SPEs forming in monolayers of WSe_2 deposited on the two nano-structures were

compared yielding photoluminescence intensity enhancements (by 10^2 to 10^4), saturation power reductions (by 10^3) as well as long-lived decay for those emitters forming on GaP dimer nano-antennas. These observations provided evidence for quantum efficiency (*QE*) enhancement from average values of 4% for emitters on SiO_2 structures to 21% for emitters on GaP structures with a maximum of 86%. Very long lived emission lifetimes, attributed to reduced non-radiative processes, provided the first evidence of very long intrinsic radiative recombination times for WSe_2 SPEs. Power dependent PL dynamics studies, enabled by the enhanced quantum efficiency, yielded insight into the relaxation and recombination pathways of WSe_2 dark excitons [79] through the single photon emitting state. This enabled the first report of a dark exciton dwelling time of $\tau_t \approx 1.7$ ns corresponding to the rise time of the PL emission of high *QE* SPEs. The increased intensity and reduced saturation powers for SPEs forming on GaP dimer nano-antennas were found to result from excitation enhancement, quantum efficiency enhancement, and a reduction of Auger processes in the WSe_2 monolayer near the position of the quantum emitters. This provided further insight, suggesting Auger processes may be responsible for observed PL saturation rather than filling of the quantum state. Finally, this chapter provides the first systematic study of the coherence time ($T_2 \approx$ 3.12 ps) of WSe_2 SPEs using an interferometric setup, which led to the conclusion that pure dephasing through phonon interactions may be the dominant dephasing process. The improvement of this coherence time may be achieved by introduction of hBN encapsulating layers.

The work presented in chapter 7 demonstrated the fabrication and optical characterization of monomer and dimer WS_2 nano-antennas in three different geometries, namely circular, hexagonal and square, for use in a variety of nano-photonic applications. The latter two geometries may potentially yield atomically sharp vertices. The novelty of this work focused on the realization of a dimer anapole mode which was utilized for second harmonic generation enhancement as well as the achievement of ultra-small gaps using an atomic force microscopy (AFM) repositioning technique. The fabricated monomer and dimer structures were systematically studied to understand the origin of the observed resonances through dark field spectroscopy and simulations of the scattering cross section which was expanded into multi-pole contributions. A dimer anapole mode was identified through dark field scattering spectroscopy as well as simulations of the confined electric energy inside the nano-structure geometry. The enhancement of second harmonic generation was demonstrated using both monomer and dimer WS_2 nano-antenna anapole resonances with linearly polarized SHG originating from only the dimer structure. Lastly, the use of contact mode AFM was used to translate and rotate one of the constituent nano-pillars forming the dimer structure to yield gaps as low as 10 nm. Previous reports have achieved a similarly small gap only in plasmonic

structures [154]. This work is the first report of such small separations in dielectric resonators using a repeatable, non-damaging technique, as opposed to focused ion beam milling [204], due to the unique van-der-Waals attractive forces inherent to 2D materials.

The simulation results presented in chapter 8 focus on applications which will benefit from the resonances of the WS_2 dimer nano-antennas fabricated and repositioned as shown in chapter 7. These results yielded a near-unity degree of linear polarization of SHG enhancement through coupling to a dimer anapole resonance. Another application studied in simulation was single photon emission of SPEs which yielded Purcell factors higher than 150 for an optimized design of hexagonal WS_2 dimer nano-antennas with the 10 nm gap achieved using post-fabrication AFM repositioning. This result is higher than the largest experimentally achieved Purcell enhancement of a quantum dot in a photonic crystal cavity [161]. The calculated Purcell enhancement of single photon emission is still lower than achieved for a plasmonic nano-patch antenna [210] yet it is the the highest reported for any dielectric Mie resonator with a clear method of fabrication. This resulted from electric field hotspots with intensities higher than 10^3 for the novel hexagonal and square geometries when compared to vacuum. The modulation of the electric field intensity and Purcell enhancement was also explored via an increase in the separation distance or a relative rotation of the constituent dimer nano-pillars, both easily attainable using the novel AFM repositioning method. Simulations of reduced radii of curvature confirmed that the electric field intensity and therefore the Purcell factor will not be detrimentally affected by fabrication imperfections which increase this quantity. The last application which was studied for the use of ultra-small gap WS_2 dimer nano-antennas was optical trapping of dielectric nano-particles. Simulations of the optical trapping force applied to a 5 nm radius colloidal quantum dot and polystyrene bead by a WS_2 hexagonal dimer nano-antenna with a 10 nm gap under an excitation of 10 mW/μ m^2 yielded values higher than 350 fN and 70 fN for the respective nano-particle. This exceeded previous reports by factors of more than 80 [149] and 40 [148] for the quantum dots and protein-like, polystyrene beads respectively.

9.2 Future research directions

Research in 2D materials, and more specifically 2D semiconductors is an expanding field which has not only been studied for its monolayer light emission properties, but also for the formation of single photon emitters as well as the integration with nano-photonic structures which have recently been fabricated in TMDs as well. New and exciting opportunities for novel research applications are opened by the work completed in this thesis. I will briefly propose some further experiments which may arise from this work.

9.2.1 Transition metal dichalcogenide single photon emitters

Single photon emission in TMDs, while only recently discovered, has expanded from WSe_2 to other TMDs with novel and interesting methods of formation of emitters such as with helium ion beam exposure [88] as well as arrays of SPEs enabled by Moire patterns [213]. The origin of the quantum state, however, is still unknown for most emitters and there are outstanding issues of understanding the relaxation and recombination processes. As discussed in chapter 6, Auger recombination was shown to heavily influence the PL dynamics and saturation behavior of WSe_2 SPEs. It is not known, however, which process begins to dominate when approaching the saturation excitation density. Further power dependent time-resolved photoluminescence experiments may provide answers to these questions and even shed some light on the origin of the different single photon emitters observed in this work among others.

The use of high refractive index dielectric nano-antennas have been shown to be advantageous for the study of monolayer TMD optical properties [150, 182] through enhancement of photoluminescence and reduction of non-radiative decay channels. Further work in this direction may provide an opportunity for the measurement of the intrinsic radiative lifetime of all TMD single photon emitters thereby enabling future evidence of Purcell enhancement via comparisons to this inherent value.

Further work to discern the exact mechanism of dephasing responsible for the low coherence time in WSe_2 SPEs is required. Studies of the coherence in single photon emitters formed by other methods also warrant further investigation. These works are vital for the development of a practical single photon source based in 2D semiconductors.

9.2.2 Two dimensional material resonators

Mie resonators have been fabricated in WS_2 using several different approaches for a variety of applications. Other TMD materials used for nano-resonator research have so far been few in number, therefore, the realization of nano-photonic resonators in other 2D materials which have not been thoroughly investigated until now is a possible direction forward. This will provide a new library of materials for the fabrication of photonic resonators suitable for different wavelength ranges or applications and enable the advantages of TMD materials to be utilized for new research directions. Some materials such as the magnetic $NiPS_3$ or $MnPSe_3$ may provide many new and exciting research opportunities for coupling their intrinsic properties to magnetic resonances in nano-antennas.

Other resonant structures may also be fabricated from different 2D materials. While work on hexagonal boron nitride (hBN) has abundantly demonstrated the fabrication of

photonic crystal cavities, nano-beam cavities, ring resonators, circular bragg gratings and waveguides, such structures have yet to be fabricated and demonstrated for other 2D materials. The advantage of fabricating such resonant cavities from TMDs, for instance, is the high refractive index of the material when compared to hBN as well as benefiting from the inherent 2D material compatibility with a variety of substrates. As an extension of the transition from monomer to dimer nano-antennas, arrays of closely spaced nano-antennas which host collective resonances, such as surface lattice resonances which may be bound states in continuum, may also be realized in 2D materials.

9.2.3 Applications of TMD resonators

The use of resonant structures such as the ones explored in this work may prove beneficial for a variety of applications which are not exhausted by the possibilities explored in this work. However, the simulations in the previous chapter highlight some specific directions for further research which have only been presented as simulations in this thesis. The near unity degree of linearly polarized SHG enhancement provides an opportunity for the fabrication of optical elements which yield second harmonic generation with a well defined polarization axis from a nano-meter scale resonator which can be expanded into arrays of such structures for larger excitation densities. The simulations of Purcell enhancements of single photon emission for WS_2 dimer nano-antennas lead to a logical next step of integration with TMD single photon emitters. These structures, similar to the GaP dimers, are expected to yield strain values in monolayer WSe_2 to induce SPE formation at the hotspots of the dimer resonances and lead to even higher levels of photoluminescence intensity due to an increased excitation rate and Purcell enhanced quantum efficiency. The simulations of the expected optical trapping forces also suggest a possible direction for further experiments to be done by trapping colloidal quantum dots in close proximity to the electric field hotspots of WS_2 dimer nano-antennas and provide Purcell enhancement of their single photon emission. Many other applications not mentioned in this thesis will also be enabled by the unique properties of 2D materials for the fabrication of nano-photonic resonators.

References

[1] K. S. Novoselov, A. K. Geim, S V Morozov, D Jiang, Y Zhang, S V Dubonos, I V Grigorieva, A A Firsov, and K. S. Novoselov. Electric Field Effect in Atomically Thin Carbon Films. *Source: Science, New Series Gene Expression: Genes in Action*, 306(5696):183–191, 2004.

[2] L. Landau. Zur Theorie der Phasenumwandlungen. I. *Phys. Z. Sowjetunion*, 11:26–47, 1937.

[3] Andres Castellanos-Gomez. Why all the fuss about 2D semiconductors? *Nature Photonics*, 10:202–204, 2016.

[4] E. Pallecchi, F. Lafont, V. Cavaliere, F. Schopfer, D. Mailly, W. Poirier, and A. Ouerghi. High electron mobility in epitaxial graphene on 4H-SiC(0001) via post-growth annealing under hydrogen. *Scientific Reports*, 4:4558, 2014.

[5] D. A. Bandurin, I. Torre, R. K. Kumar, M. Ben Shalom, A. Tomadin, A. Principi, G. H. Auton, E. Khestanova, K. S. Novoselov, I. V. Grigorieva, L. A. Ponomarenko, A. K. Geim, and M. Polini. Negative local resistance caused by viscous electron backflow in graphene. *Science*, 351(6277):1055–1058, 2016.

[6] Jingang Wang, Fengcai Ma, and Mengtao Sun. Graphene, hexagonal boron nitride, and their heterostructures: properties and applications. *RSC Adv.*, 7:16801–16822, 2017.

[7] R. Bromleyt, R. Murray, and A. Yoffe. The band structures of some transition metal dichalcogenides : 111. Group VI A: trigonal prism materials. *J. Phys. J. Phys. C: Solid State Phys*, 5, 1972.

[8] Kin Fai Mak, Changgu Lee, James Hone, Jie Shan, and Tony F. Heinz. Atomically thin MoS$_2$: A new direct-gap semiconductor. *Physical Review Letters*, 105(13):136805, 2010.

[9] Alejandro Molina-Sánchez, Davide Sangalli, Kerstin Hummer, Andrea Marini, and Ludger Wirtz. Effect of spin-orbit interaction on the optical spectra of single-layer, double-layer, and bulk MoS2. *Physical Review B - Condensed Matter and Materials Physics*, 88(4):1–6, 2013.

[10] Yu-Ming He, Genevieve Clark, John R. Schaibley, Yu-Ming He, Ming-Cheng Chen, Yu-Jia Wei, Xing Ding, Qiang Zhang, Wang Yao, Xiaodong Xu, Chao-Yang Lu, and Jian-Wei Pan. Single quantum emitters in monolayer semiconductors. *Nature Nanotechnology*, 10(6):497–502, 2015.

[11] Philipp Tonndorf, Robert Schmidt, Robert Schneider, Johannes Kern, Michele Buscema, Gary A. Steele, Andres Castellanos-Gomez, Herre S. J. van der Zant, Steffen Michaelis de Vasconcellos, and Rudolf Bratschitsch. Single-photon emission from localized excitons in an atomically thin semiconductor. *Optica*, 2(4):347, 2015.

[12] Ajit Srivastava, Meinrad Sidler, Adrien V. Allain, Dominik S. Lembke, Andras Kis, and A. Imamoğlu. Optically active quantum dots in monolayer WSe2. *Nature Nanotechnology*, 10(6):491–496, 2015.

[13] S. Kumar, A. Kaczmarczyk, and B. D. Gerardot. Strain-Induced Spatial and Spectral Isolation of Quantum Emitters in Mono- and Bilayer WSe$_2$. *Nano Letters*, 15(11):7567–7573, 2015.

[14] Yoonhyuk Rah, Yeonghoon Jin, Sejeong Kim, and Kyoungsik Yu. Optical analysis of the refractive index and birefringence of hexagonal boron nitride from the visible to near-infrared. *Optics Letters*, 44:3797–3800, 2019.

[15] F. Cadiz, E. Courtade, C. Robert, G. Wang, Y. Shen, H. Cai, T. Taniguchi, K. Watanabe, H. Carrere, D. Lagarde, M. Manca, T. Amand, P. Renucci, S. Tongay, X. Marie, and B. Urbaszek. Excitonic linewidth approaching the homogeneous limit in MoS2 based van der Waals heterostructures : accessing spin-valley dynamics. *Physical Review X*, 7:021026, 2017.

[16] Yusuke Hoshi, Takashi Kuroda, Mitsuhiro Okada, Rai Moriya, Satoru Masubuchi, Kenji Watanabe, Takashi Taniguchi, Ryo Kitaura, and Tomoki Machida. Suppression of exciton-exciton annihilation in tungsten disulfide monolayers encapsulated by hexagonal boron nitrides. *Physical Review B*, 95(24):1–6, 2017.

[17] B. Radisavljevic, A. Radenovic, J. Brivio, V. Giacometti, and A. Kis. Single-layer MoS2 transistors. *Nature Nanotechnology*, 6(3):147–150, 2011.

[18] Toan Trong Tran, Kerem Bray, Michael J. Ford, Milos Toth, and Igor Aharonovich. Quantum Emission From Hexagonal Boron Nitride Monolayers. *Nature Nanotechnology*, 11:37–41, 2016.

[19] Andreas W. Schell, Toan Trong Tran, Hideaki Takashima, Shigeki Takeuchi, and Igor Aharonovich. Non-linear excitation of quantum emitters in two-dimensional hexagonal boron nitride. *APL Photonics*, 1:1–091302, 2016.

[20] Toan Trong Tran, Christopher Elbadawi, Daniel Totonjian, Charlene J. Lobo, Gabriele Grosso, Hyowon Moon, Dirk R. Englund, Michael J. Ford, Igor Aharonovich, and Milos Toth. Robust Multicolor Single Photon Emission from Point Defects in Hexagonal Boron Nitride. *ACS Nano*, 10(8):7331–7338, 2016.

[21] John F. Clauser. Experimental Distinction Between the Quantum and Classical Field Theoretic Predictions for the Photoelectric Effect. *Lawrence Berkeley National Laboratory Reports*, pages LBL–202, 1973.

[22] A. I. Ekimov, Al L. Efros, and A. A. Onushchenko. Quantum size effect in semiconductor microcrystals. *Solid State Communications*, 56(11):921–924, 1985.

[23] Rosa Brouri, Alexios Beveratos, Jean-Philippe Poizat, and Philippe Grangier. Photon antibunching in the fluorescence of individual color centers in diamond. *Optics Letters*, 25(17):1294, 2000.

[24] David P. DiVincenzo. The physical implementation of quantum computation. *Fortschritte der Physik*, 48(9-11):771–783, 2000.

[25] Richard P. Feynman. Simulating physics with computers. *International Journal of Theoretical Physics*, 21(6-7):467–488, 1982.

[26] Lov K. Grover. A fast quantum mechanical algorithm for database search. In *Proceedings of the twenty-eight annual ACM symposium on Theory of of Computing*, pages 212–219, 1996.

[27] P.W. Shor. Algorithms for quantum computation: discrete logarithms and factoring. In *Proceedings 35th Annual Symposium on Foundations of Computer Science*, pages 124–134, 1994.

[28] N. Mizuochi, T. Makino, H. Kato, D. Takeuchi, M. Ogura, H. Okushi, M. Nothaft, P. Neumann, A. Gali, F. Jelezko, J. Wrachtrup, and S. Yamasaki. Electrically driven single-photon source at room temperature in diamond. *Nature Photonics*, 6(5):299–303, 2012.

[29] Keyvan Nasirzadeh, Shahram Nazarian, and Seyed Mohammad Gheibi Hayat. Inorganic nanomaterials: A brief overview of the applications and developments in sensing and drug delivery. *Journal of Applied Biotechnology Reports*, 3(2):395–402, 2016.

[30] L. M. Pham, N. Bar-Gill, C. Belthangady, D. Le Sage, P. Cappellaro, M. D. Lukin, A. Yacoby, and R. L. Walsworth. Enhanced solid-state multispin metrology using dynamical decoupling. *Physical Review B - Condensed Matter and Materials Physics*, 86(4):1–5, 2012.

[31] Artur Branny, Santosh Kumar, Raphaël Proux, and Brian D. Gerardot. Deterministic strain-induced arrays of quantum emitters in a two-dimensional semiconductor. *Nature Communications*, 8(May):1–10, 2017.

[32] T. H. Maiman. Stimulated Optical Radiation in Ruby. *Nature*, 187:493–494, 1960.

[33] P. Vogel and V. Ebert. Near shot noise detection of oxygen in the A-band with vertical-cavity surface-emitting lasers. *Applied Physics B: Lasers and Optics*, 72:127–135, 2001.

[34] S. Dufferwiel, T. P. Lyons, D. D. Solnyshkov, A. A. P. Trichet, F. Withers, G. Malpuech, J. M. Smith, K. S. Novoselov, M. S. Skolnick, D. N. Krizhanovskii, and A. I. Tartakovskii. Valley coherent exciton-polaritons in a monolayer semiconductor. *Nature Communications*, 9:4797, 2018.

[35] Hui Deng, Hartmut Haug, and Yoshihisa Yamamoto. Exciton-polariton Bose-Einstein condensation. *Reviews of Modern Physics*, 82:1489, 2010.

[36] Sanfeng Wu, Sonia Buckley, John R. Schaibley, Liefeng Feng, Jiaqiang Yan, David G. Mandrus, Fariba Hatami, Wang Yao, Jelena Vučković, Arka Majumdar, and Xiaodong Xu. Monolayer semiconductor nanocavity lasers with ultralow thresholds. *Nature*, 520:69–72, 2015.

[37] Yongzhuo Li, Jianxing Zhang, Dandan Huang, Hao Sun, Fan Fan, Jiabin Feng, Zhen Wang, and C. Z. Ning. Room-temperature continuous-wave lasing from monolayer molybdenum ditelluride integrated with a silicon nanobeam cavity. *Nature Nanotechnology*, 12(10):987–992, 2017.

[38] Sarah Krämmer, Sanaz Rastjoo, Tobias Siegle, Sentayehu F. Wondimu, Carolin Klusmann, Christian Koos, and Heinz Kalt. Size-optimized polymeric whispering gallery mode lasers with enhanced sensing performance. *Optics Express*, 25(7):7884, 2017.

[39] Mughees Khan, Thomas Babinec, Murray W. McCutcheon, Parag Deotare, and Marko Lončar. Fabrication and characterization of high quality factor silicon nitride nanobeam cavities. *Optics Letters*, 36(3):421–423, 2011.

[40] Gustav Mie. Beiträge zur Optik trüber Medien, speziell kolloidaler Metallösungen. *Annalen der Physik*, 3:377–445, 1908.

[41] Rohit Chikkaraddy, Bart De Nijs, Felix Benz, Steven J. Barrow, Oren A. Scherman, Edina Rosta, Angela Demetriadou, Peter Fox, Ortwin Hess, and Jeremy J. Baumberg. Single-molecule strong coupling at room temperature in plasmonic nanocavities. *Nature*, 535:127–130, 2016.

[42] Tao Cai, Je Hyung Kim, Zhili Yang, Subhojit Dutta, Shahriar Aghaeimeibodi, and Edo Waks. Radiative Enhancement of Single Quantum Emitters in WSe$_2$ Monolayers Using Site-Controlled Metallic Nanopillars. *ACS Photonics*, 5(9):3466–3471, 2018.

[43] Javier Cambiasso, Gustavo Grinblat, Yi Li, Aliaksandra Rakovich, Emiliano Cortés, and Stefan A. Maier. Bridging the Gap between Dielectric Nanophotonics and the Visible Regime with Effectively Lossless Gallium Phosphide Antennas. *Nano Letters*, 17(2):1219–1225, 2017.

[44] Javier Cambiasso, Matthias König, Emiliano Cortés, Sebastian Schlücker, and Stefan A. Maier. Surface-Enhanced Spectroscopies of a Molecular Monolayer in an All-Dielectric Nanoantenna. *ACS Photonics*, 5(4):1546–1557, 2018.

[45] Arseniy I. Kuznetsov, Andrey E. Miroshnichenko, Mark L. Brongersma, Yuri S. Kivshar, Boris Luk'yanchuk, and Boris Luk 'yanchuk. Optically resonant dielectric nanostructures. *Science*, 354(6314), 2016.

[46] Ruggero Verre, Denis G. Baranov, Battulga Munkhbat, Jorge Cuadra, Mikael Käll, and Timur Shegai. Transition metal dichalcogenide nanodisks as high-index dielectric Mie nanoresonators. *Nature Nanotechnology*, 14:679–683, 2019.

[47] Sebastian Busschaert, Moritz Cavigelli, Ronja Khelifa, Achint Jain, and Lukas Novotny. TMDC Resonators for Second Harmonic Signal Enhancement. *ACS Photonics*, 7(9):2482–2488, 2020.

[48] E M Purcell, H C Torrey, and R V Pound. Resonance Absorption by Nuclear Magnetic Moments in a Solid. *Physical Review*, 69(1-2):37–38, 1946.

[49] Sina Najmaei, Zheng Liu, Wu Zhou, Xiaolong Zou, Gang Shi, Sidong Lei, Boris I. Yakobson, Juan Carlos Idrobo, Pulickel M. Ajayan, and Jun Lou. Vapour phase growth and grain boundary structure of molybdenum disulphide atomic layers. *Nature Materials*, 12(8):754–759, 2013.

[50] E. Xenogiannopoulou, P. Tsipas, K. E. Aretouli, D. Tsoutsou, S. A. Giamini, C. Bazioti, G. P. Dimitrakopulos, Ph. Komninou, S. Brems, C. Huyghebaert, I. P. Radu, and A. Dimoulas. High-quality, large-area MoSe$_2$ and MoSe$_2$ /Bi$_2$Se$_3$ heterostructures on AlN(0001)/Si(111) substrates by molecular beam epitaxy. *Nanoscale*, 7(17):7896–7905, 2015.

[51] J. N. Coleman, M. Lotya, A. O'Neill, S. D. Bergin, P. J. King, U. Khan, K. Young, A. Gaucher, S. De, R. J. Smith, I. V. Shvets, S. K. Arora, G. Stanton, H.-Y. Kim, K. Lee, G. T. Kim, G. S. Duesberg, T. Hallam, J. J. Boland, J. J. Wang, J. F. Donegan, J. C. Grunlan, G. Moriarty, A. Shmeliov, R. J. Nicholls, J. M. Perkins, E. M. Grieveson, K. Theuwissen, D. W. McComb, P. D. Nellist, and V. Nicolosi. Two-Dimensional Nanosheets Produced by Liquid Exfoliation of Layered Materials. *Science*, 331(6017):568–571, 2011.

[52] Wei Cao, Jiahao Kang, Wei Liu, and Kaustav Banerjee. A compact current-voltage model for 2D semiconductor based field-effect transistors considering interface traps, mobility degradation, and inefficient doping effect. *IEEE Transactions on Electron Devices*, 61(12):4282–4290, 2014.

[53] Panaiot G. Zotev, Yue Wang, Luca Sortino, Toby Severs Millard, Nic Mullin, Donato Conteduca, Mostafa Shagar, Armando Genco, Jamie K. Hobbs, Thomas F. Krauss, and Alexander I. Tartakovskii. Transition metal dichalcogenide dimer nano-antennas with ultra-small gaps. *arXiv*, 2021.

[54] Yafei Li, Zhen Zhou, Shengbai Zhang, and Zhongfang Chen. MoS 2 Nanoribbons : High Stability and Unusual Electronic and Magnetic Properties. *Journal of the American Chemical Society*, 130(49):16739–16744, 2008.

[55] Shao-long Xiao, Wen-zhe Yu, and Shang-peng Gao. Surface Science Edge preference and band gap characters of MoS$_2$ and WS$_2$ nanoribbons. *Surface Science*, 653:107–112, 2016.

[56] Andrea Splendiani, Liang Sun, Yuanbo Zhang, Tianshu Li, Jonghwan Kim, Chi-yung Chim, Giulia Galli, and Feng Wang. Emerging Photoluminescence in Monolayer. *Nano*, 10:1271–1275, 2010.

[57] Julia Gusakova, Xingli Wang, Li Lynn Shiau, Anna Krivosheeva, Victor Shaposhnikov, Victor Borisenko, Vasilii Gusakov, and Beng Kang Tay. Electronic Properties of Bulk and Monolayer TMDs: Theoretical Study Within DFT Framework (GVJ-2e Method). *Physica Status Solidi (A) Applications and Materials Science*, 214(12):1–7, 2017.

[58] A. Kormányos, G. Burkard, M. Gmitra, J. Fabian, V. Zólyomi, N. D. Drummond, and V. Fal'ko. K · P Theory for Two-Dimensional Transition Metal Dichalcogenide Semiconductors. *2D Materials*, 2(2):022001, 2015.

[59] Di Xiao, Gui Bin Liu, Wanxiang Feng, Xiaodong Xu, and Wang Yao. Coupled spin and valley physics in monolayers of MoS 2 and other group-VI dichalcogenides. *Physical Review Letters*, 108(19):1–5, 2012.

[60] Ting Cao, Gang Wang, Wenpeng Han, Huiqi Ye, Chuanrui Zhu, Junren Shi, Qian Niu, Pingheng Tan, Enge Wang, Baoli Liu, and Ji Feng. Valley-selective circular dichroism of monolayer molybdenum disulphide. *Nature Communications*, 3(May):885–887, 2012.

[61] Chung Huai Chang, Xiaofeng Fan, Shi Hsin Lin, and Jer Lai Kuo. Orbital analysis of electronic structure and phonon dispersion in MoS$_2$, MoSe$_2$, WS$_2$, and WSe$_2$ monolayers under strain. *Physical Review B - Condensed Matter and Materials Physics*, 88:195420, 2013.

[62] K. Komider, J. W. González, and J. Fernández-Rossier. Large spin splitting in the conduction band of transition metal dichalcogenide monolayers. *Physical Review B - Condensed Matter and Materials Physics*, 88(24):1–7, 2013.

[63] Tawinan Cheiwchanchamnangij and Walter R L Lambrecht. Quasiparticle band structure calculation of monolayer , bilayer , and bulk MoS 2. *Physical Review B*, 205302(April):1–4, 2012.

[64] Gang Wang, Alexey Chernikov, Mikhail M. Glazov, Tony F. Heinz, Xavier Marie, Thierry Amand, and Bernhard Urbaszek. Colloquium: Excitons in atomically thin transition metal dichalcogenides. *Reviews of Modern Physics*, 90(2):21001, 2018.

[65] Maurizia Palummo, Marco Bernardi, and Jeffrey C. Grossman. Exciton radiative lifetimes in two-dimensional transition metal dichalcogenides. *Nano Letters*, 15(5):2794–2800, 2015.

[66] C R Zhu, K Zhang, M Glazov, B Urbaszek, T Amand, Z W Ji, B L Liu, and X Marie. Exciton valley dynamics probed by Kerr rotation in WSe$_2$ monolayers. *Physical Review B*, 161302:1–5, 2014.

[67] Kai Hao, Galan Moody, Fengcheng Wu, Chandriker Kavir Dass, Lixiang Xu, Chang-Hsiao Chen, Liuyang Sun, Ming-Yang Li, Lain-Jong Li, Allan H. MacDonald, and Xiaoqin Li. Direct measurement of exciton valley coherence in monolayer WSe2. *Nature Physics*, 12(7):677–682, 2016.

[68] Tomasz Jakubczyk, Valentin Delmonte, Maciej Koperski, Karol Nogajewski, Wolfgang Langbein, Marek Potemski, and Jacek Kasprzak. Radiatively Limited Dephasing and Exciton Dynamics in MoSe$_2$ Monolayers Revealed with Four-Wave Mixing Microscopy. *Nano Letters*, 16(9):5333–5339, 2016.

[69] C. Robert, D. Lagarde, F. Cadiz, G. Wang, B. Lassagne, T. Amand, A. Balocchi, P. Renucci, S. Tongay, B. Urbaszek, and X. Marie. Exciton radiative lifetime in transition metal dichalcogenide monolayers. *Physical Review B*, 93(20):1–10, 2016.

[70] Aaron M. Jones, Hongyi Yu, Nirmal J. Ghimire, Sanfeng Wu, Grant Aivazian, Jason S. Ross, Bo Zhao, Jiaqiang Yan, David G. Mandrus, Di Xiao, Wang Yao, and Xiaodong Xu. Optical generation of excitonic valley coherence in monolayer WSe 2. *Nature Nanotechnology*, 8(9):634–638, 2013.

[71] Kamran Behnia. Condensed-matter physics: Polarized light boosts valleytronics. *Nature Nanotechnology*, 7(8):488–489, 2012.

[72] Yilei Li, Alexey Chernikov, Xian Zhang, Albert Rigosi, Heather M Hill, Arend M Van Der Zande, Daniel A Chenet, En-min Shih, James Hone, and Tony F Heinz. Measurement of the optical dielectric function of monolayer transition-metal dichalcogenides : MoS$_2$, MoSe$_2$, WS$_2$, and WSe$_2$. *Physical Review B*, 90:205422, 2014.

[73] Tsuneya Ando, B Fowler, and Frank Stern. Electronic properties of two-dimensional systems. *Reviews of Modern Physics*, 54(2), 1982.

[74] Alexey Chernikov, Timothy C. Berkelbach, Heather M. Hill, Albert Rigosi, Yilei Li, Ozgur Burak Aslan, David R. Reichman, Mark S. Hybertsen, and Tony F. Heinz. Exciton binding energy and nonhydrogenic Rydberg series in monolayer WS2. *Physical Review Letters*, 113(7):1–5, 2014.

[75] Matthias Florian, Malte Hartmann, Alexander Steinho, Julian Klein, Alexander W Holleitner, Jonathan J Finley, Tim O Wehling, Michael Kaniber, and Christopher Gies. The Dielectric Impact of Layer Distances on Exciton and Trion Binding Energies in van der Waals Heterostructures. *Nano Letters*, 18:2725–2732, 2018.

[76] G. Wang, C. Robert, M. M. Glazov, F. Cadiz, E. Courtade, T. Amand, D. Lagarde, T. Taniguchi, K. Watanabe, B. Urbaszek, and X. Marie. In-Plane Propagation of Light in Transition Metal Dichalcogenide Monolayers: Optical Selection Rules. *Physical Review Letters*, 119(4):1–7, 2017.

[77] M. R. Molas, C. Faugeras, A. O. Slobodeniuk, K. Nogajewski, M. Bartos, D. M. Basko, and M. Potemski. Brightening of dark excitons in monolayers of semiconducting transition metal dichalcogenides. *2D Materials*, 2017.

[78] C. Robert, T. Amand, F. Cadiz, D. Lagarde, E. Courtade, M. Manca, T. Taniguchi, K. Watanabe, B. Urbaszek, and X. Marie. Fine structure and lifetime of dark excitons in transition metal dichalcogenide monolayers. *Physical Review B*, 96(15):1–8, 2017.

[79] Maja Feierabend, Samuel Brem, and Ermin Malic. Optical fingerprint of bright and dark localized excitonic states in atomically thin 2D materials. *Physical Chemistry Chemical Physics*, 21(47):26077–26083, 2019.

[80] H.J. J. Kimble, M. Dagenais, and L. Mandel. Phonon Antibouncing in Resonance Fluoresence. *Physical Review Letters*, 39(11):691–695, 1977.

[81] R. Hanbury Brown and R. Q. Twiss. Correlations between photons in two different beams of light. *Nature*, 177:27–32, 1956.

[82] Charles Santori, Matthew Pelton, Glenn Solomon, Yseulte Dale, and Yoshihisa Yamamoto. Triggered Single Photons from a Quantum Dot. *Physical Review Letters*, 86(8):86–89, 2001.

[83] Mark Fox. *Quantum Optics - An Introduction*. Oxford University Press, 2006.

[84] Karel Lambert, Bram De Geyter, Iwan Moreels, and Zeger Hens. PbTe|CdTe Core|Shell particles by cation exchange, a HR-TEM study. *Chemistry of Materials*, 21(5):778–780, 2009.

[85] Yuan Pu, Fuhong Cai, Dan Wang, Jie Xin Wang, and Jian Feng Chen. Colloidal Synthesis of Semiconductor Quantum Dots toward Large-Scale Production: A Review. *Industrial and Engineering Chemistry Research*, 57(6):1790–1802, 2018.

[86] Suzanne B. van Dam, Michael Walsh, Maarten J. Degen, Eric Bersin, Sara L. Mouradian, Airat Galiullin, Maximilian Ruf, Mark IJspeert, Tim H. Taminiau, Ronald Hanson, and Dirk R. Englund. Optical coherence of diamond nitrogen-vacancy centers formed by ion implantation and annealing. *Physical Review B*, 99:161203(R), 2019.

[87] Mäx Blauth, Marius Jürgensen, Gwenaëlle Vest, Oliver Hartwig, Maximilian Prechtl, John Cerne, Jonathan J. Finley, and Michael Kaniber. Coupling single photons from discrete quantum emitters in WSe$_2$ to lithographically defined plasmonic slot-waveguides. *Nano Letters*, 18(11):6812–6819, 2018.

[88] J. Klein, M. Lorke, M. Florian, F. Sigger, L. Sigl, S. Rey, J. Wierzbowski, J. Cerne, K. Müller, E. Mitterreiter, P. Zimmermann, T. Taniguchi, K. Watanabe, U. Wurstbauer, M. Kaniber, M. Knap, R. Schmidt, J. J. Finley, and A. W. Holleitner. Site-selectively generated photon emitters in monolayer MoS$_2$ via local helium ion irradiation. *Nature Communications*, 10(1):1–8, 2019.

[89] M. Bayer, G. Ortner, O. Stern, A. Kuther, A. A. Gorbunov, A. Forchel, P. Hawrylak, S. Fafard, K. Hinzer, T. L. Reinecke, S. N. Walck, J. P. Reithmaier, F. Klopf, and F. Schäfer. Fine structure of neutral and charged excitons in self-assembled In(Ga)As/(Al) GaAs quantum dots. *Physical Review B - Condensed Matter and Materials Physics*, 65(19):195315, 2002.

[90] Johannes Kern, Iris Niehues, Philipp Tonndorf, Robert Schmidt, Daniel Wigger, Robert Schneider, Torsten Stiehm, Steffen Michaelis de Vasconcellos, Doris E. Reiter, Tilmann Kuhn, and Rudolf Bratschitsch. Nanoscale Positioning of Single-Photon Emitters in Atomically Thin WSe$_2$. *Advanced Materials*, 28:7101–7105, 2016.

[91] Chitraleema Chakraborty, Laura Kinnischtzke, Kenneth M. Goodfellow, Ryan Beams, and A. Nick Vamivakas. Voltage-controlled quantum light from an atomically thin semiconductor. *Nature Nanotechnology*, 10(6):507–511, 2015.

[92] S. C.M. Grijseels, J. Van Bree, P. M. Koenraad, A. A. Toropov, G. V. Klimko, S. V. Ivanov, C. E. Pryor, and A. Yu Silov. Radiative lifetimes and linewidth broadening of single InAs quantum dots in an AlxGa(1-x)As matrix. *Journal of Luminescence*, 176:95–99, 2016.

[93] G. Bacher, R. Weigand, J. Seufert, V. D. Kulakovskii, N. A. Gippius, A. Forchel, K. Leonardi, D. Hommel, K. Leonardi, and D. Hommel. Biexciton versus exciton lifetime in a single semiconductor quantum dot. *Physical Review Letters*, 83(21):4417–4420, 1999.

[94] Nur Baizura Mohamed, Feijiu Wang, Hong En Lim, Wenjin Zhang, Sandhaya Koirala, Shinichiro Mouri, Yuhei Miyauchi, and Kazunari Matsuda. Evaluation of photoluminescence quantum yield of monolayer WSe2 using reference dye of 3-borylbithiophene derivative. *Physica Status Solidi (B) Basic Research*, 254(2), 2017.

[95] Hyungjin Kim, Geun Ho Ahn, Joy Cho, Matin Amani, James P. Mastandrea, Catherine K. Groschner, Der Hsien Lien, Yingbo Zhao, Joel W. Ager, Mary C. Scott, Daryl C. Chrzan, and Ali Javey. Synthetic WSe 2 monolayers with high photoluminescence quantum yield. *Science Advances*, 5(1), 2019.

[96] Shrawan Roy, Anir S. Sharbirin, Yongjun Lee, Won Bin Kim, Tae Soo Kim, Kiwon Cho, Kibum Kang, Hyun Suk Jung, and Jeongyong Kim. Measurement of quantum yields of monolayer tmds using dye-dispersed pmma thin films. *Nanomaterials*, 10(6), 2020.

[97] Pascale Senellart, Glenn Solomon, and Andrew White. High-performance semiconductor quantum-dot single-photon sources. *Nature Nanotechnology*, 12(11):1026–1039, 2017.

[98] Yue Luo, Gabriella D. Shepard, Jenny V. Ardelean, Daniel A. Rhodes, Bumho Kim, Katayun Barmak, James C. Hone, and Stefan Strauf. Deterministic coupling of site-controlled quantum emitters in monolayer WSe$_2$ to plasmonic nanocavities. *Nature Nanotechnology*, 13:1137–1142, 2018.

[99] M. Koperski, K. Nogajewski, A. Arora, J. Marcus, P. Kossacki, and M. Potemski. Single photon emitters in exfoliated WSe2 structures. *Nature Nanotechnology*, 10(6):503–506, 2015.

[100] Santosh Kumar, Mauro Brotóns-Gisbert, Rima Al-Khuzheyri, Artur Branny, Guillem Ballesteros-Garcia, Juan F. Sánchez-Royo, and Brian D. Gerardot. Resonant laser spectroscopy of localized excitons in monolayer WSe$_2$. *Optica*, 3(8):882, 2016.

[101] Carmen Palacios-Berraquero, Matteo Barbone, Dhiren M. Kara, Xiaolong Chen, Ilya Goykhman, Duhee Yoon, Anna K. Ott, Jan Beitner, Kenji Watanabe, Takashi Taniguchi, Andrea C. Ferrari, and Mete Atatüre. Atomically thin quantum light-emitting diodes. *Nature Communications*, 7:12978, 2016.

[102] Igor Aharonovich, Dirk Englund, and Milos Toth. Solid-state single-photon emitters. *Nature Photonics*, 10(10):631–641, 2016.

[103] C. K. Hong, Z. Y. Ou, and L. Mandel. Physical review letters 2. *Physical Review Letters*, 59(November):2044–2046, 1987.

[104] Fabian Cadiz, abdelhak Djeffal, Delphine Lagarde, Andrea Balocchi, Bingshan Tao, Bo Xu, Shiheng Liang, Mathieu Stoffel, Xavier Devaux, Henri Jaffres, Jean-Marie Marie George, Michel Hehn, Stephane Stéphane Mangin, Helene Carrere, Xavier Marie, Thierry Amand, Xiufeng Han, Zhanguo Wang, Bernhard Urbaszek, Yuan Lu, Pierre Renucci, Abdelhak Djeffal, Delphine Lagarde, Andrea Balocchi, Bingshan Tao, Bo Xu, Shiheng Liang, Mathieu Stoffel, Xavier Devaux, Henri Jaffres, Jean-Marie Marie George, Michel Hehn, Stephane Stéphane Mangin, Helene Carrere, Xavier Marie, Thierry Amand, Xiufeng Han, Zhanguo Wang, Bernhard Urbaszek,

Yuan Lu, and Pierre Renucci. Electrical initialization of electron and nuclear spins in a single quantum dot at zero magnetic field. *Nano Letters*, 18(4):acs.nanolett.7b05351, 2018.

[105] A. Thoma, P. Schnauber, M. Gschrey, M. Seifried, J. Wolters, J. H. Schulze, A. Strittmatter, S. Rodt, A. Carmele, A. Knorr, T. Heindel, and S. Reitzenstein. Exploring Dephasing of a Solid-State Quantum Emitter via Time- and Temperature-Dependent Hong-Ou-Mandel Experiments. *Physical Review Letters*, 116(3):1–6, 2016.

[106] K. H. Madsen, S. Ates, J. Liu, A. Javadi, S. M. Albrecht, I. Yeo, S. Stobbe, and P. Lodahl. Efficient out-coupling of high-purity single photons from a coherent quantum dot in a photonic-crystal cavity. *Physical Review B - Condensed Matter and Materials Physics*, 90(15):1–11, 2014.

[107] Bernd Sontheimer, Merle Braun, Niko Nikolay, Nikola Sadzak, Igor Aharonovich, and Oliver Benson. Photodynamics of quantum emitters in hexagonal boron nitride revealed by low-temperature spectroscopy. *Physical Review B*, 96(12):1–5, 2017.

[108] P. M. Petroff and S. P. DenBaars. MBE and MOCVD growth and properties of self-assembling quantum dot arrays in III-V semiconductor structures. *Superlattices and Microstructures*, 15(1):15–21, 1994.

[109] Gabriele Grosso, Hyowon Moon, Benjamin Lienhard, Sajid Ali, Dmitri K. Efetov, Marco M. Furchi, Pablo Jarillo-Herrero, Michael J. Ford, Igor Aharonovich, and Dirk Englund. Tunable and high-purity room temperature single-photon emission from atomic defects in hexagonal boron nitride. *Nature Communications*, 8:705, 2017.

[110] Nicholas R. Jungwirth and Gregory D. Fuchs. Optical Absorption and Emission Mechanisms of Single Defects in Hexagonal Boron Nitride. *Physical Review Letters*, 119(5):1–6, 2017.

[111] Carmen Palacios-Berraquero, Dhiren M. Kara, Alejandro R. P. Montblanch, Matteo Barbone, Pawel Latawiec, Duhee Yoon, Anna K. Ott, Marko Loncar, Andrea C. Ferrari, and Mete Atature. Large-scale quantum-emitter arrays in atomically thin semiconductors. *Nature Communications*, 8:15093, 2017.

[112] Gabriella D. Shepard, Obafunso A. Ajayi, Xiangzhi Li, X. Y. Zhu, James Hone, and Stefan Strauf. Nanobubble induced formation of quantum emitters in monolayer semiconductors. *2D Materials*, 4:021019, 2017.

[113] Matthew R. Rosenberger, Chandriker Kavir Dass, Hsun Jen Chuang, Saujan V. Sivaram, Kathleen M. McCreary, Joshua R. Hendrickson, and Berend T. Jonker. Quantum Calligraphy: Writing Single-Photon Emitters in a Two-Dimensional Materials Platform. *ACS Nano*, 13(1):904–912, 2019.

[114] Raphaël S. Daveau, Tom Vandekerckhove, Arunabh Mukherjee, Zefang Wang, Jie Shan, Kin Fai Mak, A. Nick Vamivakas, Gregory D. Fuchs, A. Nick Vamivakas, and Gregory D. Fuchs. Spectral and spatial isolation of single tungsten diselenide quantum emitters using hexagonal boron nitride wrinkles. *APL Photonics*, 5:096105, 2020.

[115] Simone Bertolazzi, Jacopo Brivio, and Andras Kis. Stretching and breaking of ultrathin MoS 2. *ACS Nano*, 5(12):9703–9709, 2011.

[116] Luca Sortino, Matthew Brooks, Panaiot G. Zotev, Armando Genco, Javier Cambiasso, Sandro Mignuzzi, Stefan A. Maier, Guido Burkard, Riccardo Sapienza, and Alexander I. Tartakovskii. Dielectric nano-antennas for strain engineering in atomically thin two-dimensional semiconductors. *ACS Photonics*, 7(9):2413–2422, 2020.

[117] Yanlong Wang, Chunxiao Cong, Weihuang Yang, Jingzhi Shang, Namphung Peimyoo, Yu Chen, Junyong Kang, Jianpu Wang, Wei Huang, and Ting Yu. Strain-induced direct–indirect bandgap transition and phonon modulation in monolayer WS2. *Nano Research*, 8(8):2562–2572, 2015.

[118] Sujay B. Desai, Gyungseon Seol, Jeong Seuk Kang, Hui Fang, Corsin Battaglia, Rehan Kapadia, Joel W. Ager, Jing Guo, and Ali Javey. Strain-induced indirect to direct bandgap transition in multilayer WSe$_2$. *Nano Letters*, 14(8):4592–4597, 2014.

[119] Xin He, Hai Li, Zhiyong Zhu, Zhenyu Dai, Yang Yang, Peng Yang, Qiang Zhang, Peng Li, Udo Schwingenschlogl, and Xixiang Zhang. Strain engineering in monolayer WS$_2$, MoS$_2$, and the WS$_2$/MoS$_2$ heterostructure. *Applied Physics Letters*, 109(17), 2016.

[120] Joshua O. Island, Agnieszka Kuc, Erik H. Diependaal, Rudolf Bratschitsch, Herre S. J. van der Zant, Thomas Heine, and Andres Castellanos-Gomez. Precise and reversible band gap tuning in single-layer MoSe ₂ by uniaxial strain. *Nanoscale*, 8(5):2589–2593, 2016.

[121] Andres Castellanos-Gomez, Rafael Roldán, Emmanuele Cappelluti, Michele Buscema, Francisco Guinea, Herre S J Van Der Zant, and Gary A. Steele. Local strain engineering in atomically thin MoS2. *Nano Letters*, 13(11):5361–5366, 2013.

[122] Sajedeh Manzeli, Adrien Allain, Amirhossein Ghadimi, and Andras Kis. Piezoresistivity and Strain-induced Band Gap Tuning in Atomically Thin MoS$_2$. *Nano Letters*, 15(8):5330–5335, 2015.

[123] Rui Zhang, Vasileios Koutsos, and Rebecca Cheung. Elastic properties of suspended multilayer WSe2. *Applied Physics Letters*, 108(4), 2016.

[124] Ji Feng, Xiaofeng Qian, Cheng Wei Huang, and Ju Li. Strain-engineered artificial atom as a broad-spectrum solar energy funnel. *Nature Photonics*, 6(12):866–872, 2012.

[125] Pablo San-Jose, Vincenzo Parente, Francisco Guinea, Rafael Roldán, and Elsa Prada. Inverse funnel effect of excitons in strained black phosphorus. *Physical Review X*, 6(3):1–12, 2016.

[126] F. Cadiz, C. Robert, E. Courtade, M. Manca, L. Martinelli, T. Taniguchi, T. Amand, A. C.H. H Rowe, D. Paget, B. Urbaszek, X. Marie, K. Watanabe, T. Amand, A. C.H. H Rowe, D. Paget, B. Urbaszek, and X. Marie. Exciton diffusion in WSe 2 monolayers embedded in a van der Waals heterostructure. *Applied Physics Letters*, 112(15):152106, 2018.

[127] Yue Luo, Na Liu, Bumho Kim, James Hone, and Stefan Strauf. Exciton dipole orientation of strain-induced quantum emitters in WSe$_2$. *Nano Letters*, 20(7):5119–5126, 2020.

[128] Lukas Linhart, Matthias Paur, Valerie Smejkal, Joachim Burgdörfer, Thomas Mueller, and Florian Libisch. Localized inter-valley defect excitons as single-photon emitters in WSe$_2$. *Physical Review Letters*, 123(14):146401, 2019.

[129] Chandriker Kavir Dass, Mahtab A. Khan, Genevieve Clark, Jeffrey A. Simon, Ricky Gibson, Shin Mou, Xiaodong Xu, Michael N. Leuenberger, and Joshua R. Hendrickson. Ultra-Long Lifetimes of Single Quantum Emitters in Monolayer WSe2/hBN Heterostructures. *Advanced Quantum Technologies*, 1900022(5-6):1900022, 2019.

[130] K. Oreszczuk, T. Kazimierczuk, T. Smoleński, K. Nogajewski, M. Grzeszczyk, A. Łopion, M. Potemski, and P. Kossacki. Carrier relaxation to quantum emitters in few-layer WSe2. *Physical Review B*, 102(24):1–5, 2020.

[131] Craig F. Bohren and Donald R. Huffman. *Absorption and Scattering of Light by Small Particles*. Wiley, 1998.

[132] B. E. A. Saleh and M. C. Teich. *Fundamentals of Photonics*. Wiley, 2007.

[133] B. Bleaney and B. I. Bleaney. *Electronicity and Magnetism*. Oxford University Press, 1965.

[134] Tatsuki Hinamoto and Minoru Fujii. MENP: An Open-Source MATLAB implementation of multipole expansion for applications in nanophotonics. *Osa Continuum*, 4:1640–1648, 2021.

[135] Rasoul Alaee, Carsten Rockstuhl, and Ivan Fernandez-Corbaton. Exact Multipolar Decompositions with Applications in Nanophotonics. *Advanced Optical Materials*, 7(1):180783, 2019.

[136] John David Jackson. *Classical Electrodynamics*. Wiley, 1962.

[137] Chao Yu Li, Sai Duan, Bao Ying Wen, Song Bo Li, Murugavel Kathiresan, Li Qiang Xie, Shu Chen, Jason R. Anema, Bing Wei Mao, Yi Luo, Zhong Qun Tian, and Jian Feng Li. Observation of inhomogeneous plasmonic field distribution in a nanocavity. *Nature Nanotechnology*, 15:922–926, 2020.

[138] Alexander E Krasnok, Andrey E Miroshnichenko, Pavel a Belov, and Yuri S Kivshar. All-dielectric optical nanoantennas. *Optics express*, 20(18):20599–604, 2012.

[139] Gustavo Grinblat, Yi Li, Michael P. Nielsen, Rupert F. Oulton, and Stefan A. Maier. Efficient Third Harmonic Generation and Nonlinear Subwavelength Imaging at a Higher-Order Anapole Mode in a Single Germanium Nanodisk. *ACS Nano*, 11(1):953–960, 2017.

[140] Maria Timofeeva, Lukas Lang, Flavia Timpu, Claude Renaut, Alexei Bouravleuv, Igor Shtrom, George Cirlin, and Rachel Grange. Anapoles in Free-Standing III-V Nanodisks Enhancing Second-Harmonic Generation. *Nano Letters*, 18(6):3695–3702, 2018.

[141] Katie E. Chong, Ben Hopkins, Isabelle Staude, Andrey E. Miroshnichenko, Jason Dominguez, Manuel Decker, Dragomir N. Neshev, Igal Brener, and Yuri S. Kivshar. Observation of fano resonances in all-dielectric nanoparticle oligomers. *Small*, 10(10):1985–1990, 2014.

[142] Lei Wang, Sergey Kruk, Hanzhi Tang, Tao Li, Ivan Kravchenko, Dragomir N. Neshev, and Yuri S. Kivshar. Grayscale transparent metasurface holograms. *Optica*, 3(12):1504, 2016.

[143] Son Tung Ha, Yuan Hsing Fu, Naresh Kumar Emani, Zhenying Pan, Reuben M. Bakker, Ramón Paniagua-Domínguez, and Arseniy I. Kuznetsov. Directional lasing in resonant semiconductor nanoantenna arrays. *Nature Nanotechnology*, 13(November), 2018.

[144] Mariano Pascale, Giovanni Miano, Roberto Tricarico, and Carlo Forestiere. Full-wave electromagnetic modes and hybridization in nanoparticle dimers. *Scientific Reports*, 9:14524, 2019.

[145] Pablo Albella, M. Ameen Poyli, Mikolaj K. Schmidt, Stefan A. Maier, Fernando Moreno, Juan José Sáenz, and Javier Aizpurua. Low-loss electric and magnetic field-enhanced spectroscopy with subwavelength silicon dimers. *Journal of Physical Chemistry C*, 117(26):13573–13584, 2013.

[146] Reuben M. Bakker, Dmitry Permyakov, Ye Feng Yu, Dmitry Markovich, Ramón Paniagua-Domínguez, Leonard Gonzaga, Anton Samusev, Yuri Kivshar, Boris Lukyanchuk, and Arseniy I. Kuznetsov. Magnetic and electric hotspots with silicon nanodimers. *Nano Letters*, 15(3):2137–2142, 2015.

[147] Raju Regmi, Johann Berthelot, Pamina M. Winkler, Mathieu Mivelle, Julien Proust, Frédéric Bedu, Igor Ozerov, Thomas Begou, Julien Lumeau, Hervé Rigneault, María F. García-Parajó, Sébastien Bidault, Jérôme Wenger, and Nicolas Bonod. All-Dielectric Silicon Nanogap Antennas to Enhance the Fluorescence of Single Molecules. *Nano Letters*, 16(8):5143–5151, 2016.

[148] Zhe Xu, Wuzhou Song, and Kenneth B. Crozier. Optical Trapping of Nanoparticles Using All-Silicon Nanoantennas. *ACS Photonics*, 5(12):4993–5001, 2018.

[149] Zhe Xu and Kenneth B. Crozier. All-dielectric nanotweezers for trapping and observation of a single quantum dot. *Optics Express*, 27:4034–4045, 2019.

[150] L. Sortino, P. G. Zotev, S. Mignuzzi, J. Cambiasso, D. Schmidt, A. Genco, M. Aßmann, M. Bayer, S. A. Maier, R. Sapienza, and A. I. Tartakovskii. Enhanced light-matter interaction in an atomically thin semiconductor coupled with dielectric nano-antennas. *Nature Communications*, 10:5119, 2019.

[151] M. Kaniber, K. Schraml, A. Regler, J. Bartl, G. Glashagen, F. Flassig, J. Wierzbowski, and J. J. Finley. Surface plasmon resonance spectroscopy of single bowtie nanoantennas using a differential reflectivity method. *Scientific Reports*, 6:23203, 2016.

[152] Anika Kinkhabwala, Zongfu Yu, Shanhui Fan, Yuri Avlasevich, Klaus Müllen, and W. E. Moerner. Large single-molecule fluorescence enhancements produced by a bowtie nanoantenna. *Nature Photonics*, 3:654–657, 2009.

[153] Hyeongrak Choi, Mikkel Heuck, and Dirk Englund. Self-Similar Nanocavity Design with Ultrasmall Mode Volume for Single-Photon Nonlinearities. *Physical Review Letters*, 118:223605, 2017.

[154] Jörg Merlein, Matthias Kahl, Annika Zuschlag, Alexander Sell, Andreas Halm, Johannes Boneberg, Paul Leiderer, Alfred Leitenstorfer, and Rudolf Bratschitsch. Nanomechanical control of an optical antenna. *Nature Photonics*, 2:230–233, 2008.

[155] Estill I. Green. The story of Q. *American Scientist*, 43:584–594, 1955.

[156] J. M. Gérard and B. Gayral. Strong Purcell Effect for InAs Quantum Boxes in Three-Dimensional Solid-State Microcavities. *Journal of Lightwave Technology*, 17(11):2089–2095, 1999.

[157] Russell J. Barbour, Paul A. Dalgarno, Arran Curran, Kris M. Nowak, Howard J. Baker, Denis R. Hall, Nick G. Stoltz, Pierre M. Petroff, and Richard J. Warburton. A tunable microcavity. *Journal of Applied Physics*, 110(5), 2011.

[158] Susumu Noda, Masayuki Fujita, and Takashi Asano. Spontaneous-emission control by photonic crystals and nanocavities. *Nature Photonics*, 1(8):449–458, 2007.

[159] Johannes E. Fröch, Sejeong Kim, Noah Mendelson, Mehran Kianinia, Milos Toth, Milos Toth, Igor Aharonovich, and Igor Aharonovich. Coupling Hexagonal Boron Nitride Quantum Emitters to Photonic Crystal Cavities. *ACS Nano*, 14(6):7085–7091, 2020.

[160] Jacob T. Robinson, Christina Manolatou, Long Chen, and Michal Lipson. Ultrasmall mode volumes in dielectric optical microcavities. *Physical Review Letters*, 95(14):1–4, 2005.

[161] Feng Liu, Alistair J. Brash, John O'Hara, Luis M.P.P. Martins, Catherine L. Phillips, Rikki J. Coles, Benjamin Royall, Edmund Clarke, Christopher Bentham, Nikola Prtljaga, Igor E. Itskevich, Luke R. Wilson, Maurice S. Skolnick, and A. Mark Fox. High Purcell factor generation of indistinguishable on-chip single photons. *Nature Nanotechnology*, 13:835–840, 2018.

[162] L. C. Flatten, L. Weng, A. Branny, S. Johnson, P. R. Dolan, A. A.P. P Trichet, B. D. Gerardot, and J. M. Smith. Microcavity enhanced single photon emission from two-dimensional WSe$_2$. *Applied Physics Letters*, 112(19), 2018.

[163] Xingwang Zhang, Xiaojie Zhang, Wenzhuo Huang, Kedi Wu, Mengqiang Zhao, A. T. Charlie Johnson, Sefaattin Tongay, and Ertugrul Cubukcu. Ultrathin WS2-on-Glass Photonic Crystal for Self-Resonant Exciton-Polaritonics. *Advanced Optical Materials*, 8:1901988, 2020.

[164] Donato Conteduca, Christopher Reardon, Mark G. Scullion, Francesco Dell'Olio, Mario N. Armenise, Thomas F. Krauss, and Caterina Ciminelli. Ultra-high Q/V hybrid cavity for strong light-matter interaction. *APL Photonics*, 2:086101, 2017.

[165] Lukas Novotny and Bert Hecht. *Principles of Nano-Optics*. Cambridge Universty Press, 2012.

[166] Sandro Mignuzzi, Stefano Vezzoli, Simon A. R. Horsley, William L. Barnes, Stefan A. Maier, and Riccardo Sapienza. Nanoscale design of the local density of optical states. *Nano Letters*, 19(3):1613–1617, 2019.

[167] Andrey E. Miroshnichenko, Andrey B. Evlyukhin, Ye Feng Yu, Reuben M. Bakker, Arkadi Chipouline, Arseniy I. Kuznetsov, Boris Luk'yanchuk, Boris N. Chichkov, and Yuri S. Kivshar. Nonradiating anapole modes in dielectric nanoparticles. *Nature Communications*, 6:8069, 2015.

[168] Yuen-Ron Shen. The Principles of Nonlinear Optics, 2002.

[169] Kaiyuan Yao, Nathan R. Finney, Jin Zhang, Samuel L. Moore, Lede Xian, Nicolas Tancogne-Dejean, Fang Liu, Jenny Ardelean, Xinyi Xu, Dorri Halbertal, K. Watanabe, T. Taniguchi, Hector Ochoa, Ana Asenjo-Garcia, Xiaoyang Zhu, D. N. Basov, Angel Rubio, Cory R. Dean, James Hone, and P. James Schuck. Enhanced tunable second harmonic generation from twistable interfaces and vertical superlattices in boron nitride homostructures. *Science Advances*, 7(10):1–8, 2021.

[170] Tony F. Heinz. Second-Order Nonlinear Optical Effects at Surfaces and Interfaces, 1991.

[171] K. S. Novoselov, D. Jiang, F. Schedin, T. J. Booth, V. V. Khotkevich, S. V. Morozov, and A. K. Geim. Two-dimensional atomic crystals. *Proceedings of the National Academy of Sciences of the United States of America*, 102(30):10451–10453, 2005.

[172] Jiadong Zhou, Junhao Lin, Xiangwei Huang, Yao Zhou, Yu Chen, Juan Xia, Hong Wang, Yu Xie, Huimei Yu, Jincheng Lei, Di Wu, Fucai Liu, Qundong Fu, Qingsheng Zeng, Chuang Han Hsu, Changli Yang, Li Lu, Ting Yu, Zexiang Shen, Hsin Lin, Boris I. Yakobson, Qian Liu, Kazu Suenaga, Guangtong Liu, and Zheng Liu. A library of atomically thin metal chalcogenides. *Nature*, 556:355–359, 2018.

[173] Evgeny M. Alexeev, Alessandro Catanzaro, Oleksandr V. Skrypka, Pramoda K. Nayak, Seongjoon Ahn, Sangyeon Pak, Juwon Lee, Jung Inn Sohn, Kostya S. Novoselov, Hyeon Suk Shin, and Alexander I. Tartakovskii. Imaging of Interlayer Coupling in van der Waals Heterostructures Using a Bright-Field Optical Microscope. *Nano Letters*, 17(9):5342–5349, 2017.

[174] Riccardo Frisenda, Efrén Navarro-Moratalla, Patricia Gant, David Pérez De Lara, Pablo Jarillo-Herrero, Roman V. Gorbachev, and Andres Castellanos-Gomez. Recent progress in the assembly of nanodevices and van der Waals heterostructures by deterministic placement of 2D materials. *Chemical Society Reviews*, 47:53–68, 2018.

[175] Shinichiro Mouri, Yuhei Miyauchi, Minglin Toh, Weijie Zhao, Goki Eda, and Kazunari Matsuda. Nonlinear photoluminescence in atomically thin layered WSe2 arising from diffusion-assisted exciton-exciton annihilation. *Physical Review B - Condensed Matter and Materials Physics*, 90(15):1–5, 2014.

[176] Wolfgang Becker. The TCSPC Handbook, 7th ed, 2017.

[177] SPARC cathodeluminescence g$ˆ{(2)}$ imaging technical note.

[178] Alistair J. Brash, Jake Iles-Smith, Catherine L. Phillips, Dara P.S. S. McCutcheon, John O'Hara, Edmund Clarke, Benjamin Royall, Jesper Mørk, Maurice S. Skolnick, A. Mark Fox, Ahsan Nazir, Luke R. Wilson, Jesper Mørk, Maurice S. Skolnick, A. Mark Fox, and Ahsan Nazir. Light Scattering from Solid-State Quantum Emitters: Beyond the Atomic Picture. *Physical Review Letters*, 123(16):167403, 2019.

[179] D. E. Aspnes and A. A. Studna. Dielectric functions and optical parameters of Si, Ge, GaP, GaAs, GaSb, InP, InAs, and InSb from 1.5 to 6.0 eV. *Physical Review B*, 27(2):985, 1983.

[180] Jessica Lindlau, Malte Selig, Andre Neumann, Léo Colombier, Jonathan Förste, Victor Funk, Michael Förg, Jonghwan Kim, Gunnar Berghäuser, Takashi Taniguchi, Kenji Watanabe, Feng Wang, Ermin Malic, and Alexander Högele. The role of momentum-dark excitons in the elementary optical response of bilayer WSe2. *Nature Communications*, 9:1–7, 2018.

[181] Yu Ming He, Oliver Iff, Nils Lundt, Vasilij Baumann, Marcelo Davanco, Kartik Srinivasan, Sven Höfling, and Christian Schneider. Cascaded emission of single photons from the biexciton in monolayered WSe 2. *Nature Communications*, 7:1–6, 2016.

[182] Luca Sortino, Panaiot G. Zotev, Catherine L. Phillips, Alistair J. Brash, Javier Cambiasso, Elena Marensi, A. Mark Fox, Stefan A. Maier, Riccardo Sapienza, and Alexander I. Tartakovskii. Bright single photon emitters with enhanced quantum efficiency in a two-dimensional semiconductor coupled with dielectric nano-antennas. *Nature Communications*, 12:6063, 2021.

[183] A. Femius Koenderink. Single-Photon Nanoantennas. *ACS Photonics*, 4(4):710–722, 2017.

[184] Iris Niehues, Robert Schmidt, Matthias Drüppel, Philipp Marauhn, Dominik Christiansen, Malte Selig, Gunnar Berghäuser, Daniel Wigger, Robert Schneider, Lisa Braasch, Rouven Koch, Andres Castellanos-Gomez, Tilmann Kuhn, Andreas Knorr, Ermin Malic, Michael Rohlfing, Steffen Michaelis De Vasconcellos, and Rudolf Bratschitsch. Strain Control of Exciton-Phonon Coupling in Atomically Thin Semiconductors. *Nano Letters*, 18(3):1751–1757, 2018.

[185] T. Godde, D. Schmidt, J. Schmutzler, M. Aßmann, J. Debus, F. Withers, E. M. Alexeev, O. Del Pozo-Zamudio, O. V. Skrypka, K. S. Novoselov, M. Bayer, and A. I. Tartakovskii. Exciton and trion dynamics in atomically thin MoSe2 and WSe2: Effect of localization. *Physical Review B*, 94:165301, 2016.

[186] Mark Danovich, Viktor Zólyomi, Vladimir I. Fal'ko, and Igor L. Aleiner. Auger recombination of dark excitons in WS2 and WSe2 monolayers. *2D Materials*, 3:035011, 2016.

[187] Fengnian Xia, Han Wang, Di Xiao, Madan Dubey, and Ashwin Ramasubramaniam. Two-dimensional material nanophotonics. *Nature Photonics*, 8:899–907, 2014.

[188] Long Zhang, Rahul Gogna, Will Burg, Emanuel Tutuc, and Hui Deng. Photonic-crystal exciton-polaritons in monolayer semiconductors. *Nature Communications*, 9:713, 2018.

[189] Alex Krasnok, Sergey Lepeshov, and Andrea Alú. Nanophotonics with 2D transition metal dichalcogenides. *Optics Express*, 26(12):15972–15994, 2018.

[190] Nils Bernhardt, Kirill Koshelev, Simon J.U. White, Kelvin Wong Choon Meng, Johannes E. Fröch, Sejeong Kim, Toan Trong Tran, Duk-Yong Yong Choi, Yuri Kivshar, and Alexander S. Solntsev. Quasi-BIC Resonant Enhancement of Second-Harmonic Generation in WS$_2$ Monolayers. *Nano Letters*, 20(7):5309–5314, 2020.

[191] Vasily Kravtsov, Ekaterina Khestanova, Fedor A. Benimetskiy, Tatiana Ivanova, Anton K. Samusev, Ivan S. Sinev, Dmitry Pidgayko, Alexey M. Mozharov, Ivan S. Mukhin, Maksim S. Lozhkin, Yuri V. Kapitonov, Andrey S. Brichkin, Vladimir D. Kulakovskii, Ivan A. Shelykh, Alexander I. Tartakovskii, Paul M. Walker, Maurice S. Skolnick, Dmitry N. Krizhanovskii, and Ivan V. Iorsh. Nonlinear polaritons in a monolayer semiconductor coupled to optical bound states in the continuum. *Light: Science and Applications*, 9:56, 2020.

[192] Kin Fai Mak and Jie Shan. Photonics and optoelectronics of 2D semiconductor transition metal dichalcogenides. *Nature Photonics*, 10:216–226, 2016.

[193] Sejeong Kim, Johannes E. Fröch, Joe Christian, Marcus Straw, James Bishop, Daniel Totonjian, Kenji Watanabe, Takashi Taniguchi, Milos Toth, and Igor Aharonovich. Photonic crystal cavities from hexagonal boron nitride. *Nature Communications*, 9:2623, 2018.

[194] Johannes E. Fröch, Yongsop Hwang, Sejeong Kim, Igor Aharonovich, and Milos Toth. Photonic Nanostructures from Hexagonal Boron Nitride. *Advanced Optical Materials*, 7:1801344, 2019.

[195] H. H. Fang, B. Han, C. Robert, M. A. Semina, D. Lagarde, E. Courtade, T. Taniguchi, K. Watanabe, T. Amand, B. Urbaszek, M. M. Glazov, and X. Marie. Control of the Exciton Radiative Lifetime in van der Waals Heterostructures. *Physical Review Letters*, 123(6):067401, 2019.

[196] G. A. Ermolaev, D. V. Grudinin, Y. V. Stebunov, V. G. Kravets, J. Duan, G. I. Tselikov, K. V. Voronin, D. I. Yakubovsky, S. M. Novikov, D. G. Baranov, A. Y. Nikitin, T. Shegai, P. Alonso-González, A. N. Grigorenko, A. V. Arsenin, K. S. Novoselov, and V. S. Volkov. Giant optical anisotropy in transition metal dichalcogenides for next-generation photonics. *Nature Communications*, 12:854, 2021.

[197] Huiqin Zhang, Bhaskar Abhiraman, Qing Zhang, Jinshui Miao, Kiyoung Jo, Stefano Roccasecca, Mark W. Knight, Artur R. Davoyan, and Deep Jariwala. Hybrid exciton-plasmon-polaritons in van der Waals semiconductor gratings. *Nature Communications*, 11:3552, 2020.

[198] Battulga Munkhbat, Denis G. Baranov, Michael Stührenberg, Martin Wersäll, Ankit Bisht, and Timur Shegai. Self-Hybridized Exciton-Polaritons in Multilayers of Transition Metal Dichalcogenides for Efficient Light Absorption. *ACS Photonics*, 6(1):139–147, 2019.

[199] Xingwang Zhang, Chawina De-Eknamkul, Jie Gu, Alexandra L. Boehmke, Vinod M. Menon, Jacob Khurgin, and Ertugrul Cubukcu. Guiding of visible photons at the ångström thickness limit. *Nature Nanotechnology*, 14:844–850, 2019.

[200] Thomas D. Green, Denis G. Baranov, Battulga Munkhbat, Ruggero Verre, Timur Shegai, and Mikael Käll. Optical material anisotropy in high-index transition metal dichalcogenide Mie nanoresonators. *Optica*, 7:680–686, 2020.

[201] Haonan Ling, Renjie Li, and Artur R. Davoyan. All van der Waals Integrated Nanophotonics with Bulk Transition Metal Dichalcogenides. *ACS Photonics*, 8(3):721–730, 2021.

[202] Naseer Muhammad, Yang Chen, Cheng Wei Qiu, and Guo Ping Wang. Optical Bound States in Continuum in MoS$_2$-Based Metasurface for Directional Light Emission. *Nano Letters*, 21(2):967–972, 2021.

[203] Hasan Ahmed and Viktoriia E. Babicheva. Resonant and scattering properties of tungsten disulfide WS$_2$ nanoantennas. *Proceedings of SPIE*, 11289R, 2020.

[204] Lukas Novotny and Niek Van Hulst. Antennas for light. *Nature Photonics*, 5:83–90, 2011.

[205] Kai Wang, Ethan Schonbrun, Paul Steinvurzel, and Kenneth B. Crozier. Trapping and rotating nanoparticles using a plasmonic nano-tweezer with an integrated heat sink. *Nature Communications*, 2:469, 2011.

[206] Russell A. Jensen, I. Chun Huang, Ou Chen, Jennifer T. Choy, Thomas S. Bischof, Marko Lončar, and Moungi G. Bawendi. Optical Trapping and Two-Photon Excitation of Colloidal Quantum Dots Using Bowtie Apertures. *ACS Photonics*, 3(3):423–427, 2016.

[207] F. A. Bovino, M. Giardina, M. C. Larciprete, A. Belardini, M. Centini, C. Sibilia, M. Bertolotti, A. Passaseo, and V. Tasco. Optical logic functions with nonlinear gallium nitride nanoslab. *Optics Express*, 17(22):19337–19344, 2009.

[208] Yoshihiro Akahane, Takashi Asano, Bong-shik Song, and Susumu Noda. High- Q photonic nanocavity in a two-dimensional photonic crystal. *Nature*, 425(October):944, 2003.

[209] Gavin Young, Nikolas Hundt, Daniel Cole, Adam Fineberg, Joanna Andrecka, Andrew Tyler, Anna Olerinyova, Ayla Ansari, Erik G. Marklund, Miranda P. Collier, Shane A. Chandler, Olga Tkachenko, Joel Allen, Max Crispin, Neil Billington, Yasuharu Takagi, James R. Sellers, Cedric Eichmann, Philip Selenko, Lukas Frey, Roland Riek, Martin R. Galpin, Weston B. Struwe, Justin L.P. Benesch, and Philipp Kukura. Quantitative mass imaging of single molecules in solution. *Science*, 360(6387):423–427, 2017.

[210] Thang B. Hoang, Gleb M. Akselrod, and Maiken H. Mikkelsen. Ultrafast Room-Temperature Single Photon Emission from Quantum Dots Coupled to Plasmonic Nanocavities. *Nano Letters*, 16(1):270–275, 2016.

[211] M. K. Schmidt, R. Esteban, J. J. Sáenz, I. Suárez-Lacalle, S. Mackowski, and J. Aizpurua. Dielectric antennas - a suitable platform for controlling magnetic dipolar emission: errata. *Optics Express*, 20(17):18609, 2012.

[212] Brice Rolly, Betina Bebey, Sebastien Bidault, Brian Stout, and Nicolas Bonod. Promoting magnetic dipolar transition in trivalent lanthanide ions with lossless Mie resonances. *Physical Review B - Condensed Matter and Materials Physics*, 85(24):2–7, 2012.

[213] H Baek, Z X Koong, A Campbell, M Rambach, K Watanabe, and T Takashi. Highly tunable quantum light from moiré trapped excitons. *Science Advances*, 6:eaba8526, 2020.